

ABSTRACT

FUIERER, RYAN RICHARD Probing the Electronic Properties of Materials that Self-Assemble (Under the directions of Drs. Christopher B. Gorman and Daniel L. Feldheim)

Developing methods to control the chemistry of surfaces on the 1–100 nm length scale is a fundamental and exciting challenge in many disciplines of science today because it opens new possibilities in fields ranging from molecular electronics (ME) to biomedicine to catalysis. Scanning probe microscopy techniques have been a key goal in achieving this challenge. This work begins with an exhaustive review of scanning probe lithography techniques using self-assembled monolayer (SAM) systems reported in the literature to date. Experimental study describes the development of a scanning probe lithography technique (termed replacement lithography) in which a scanning tunneling microscopy (STM) tip selectively desorbs organothiolate SAMs in a predefined pattern, allowing a replacement thiol to adsorb onto the exposed gold in the patterned region. The replacement parameters were investigated using electroactive containing replacement thiol species because they displayed large apparent height contrasts in STM images, allowing the efficacy of the pattern to be easily ascertained. These data were subsequently employed to create mesoscale chemical gradients with replacement lithography. The electronic properties of redox active SAMs were also shown to display negative differential resistance in current-voltage measurements, a behavior that has possible utility in the development of ME devices. Temporal investigations monitoring the stochastic variation in apparent height contrasts in STM images of electroactive containing SAM guest species isolated within insulating host SAM matrices was also studied. The observations from these data may lend insight to how ME candidates might behave when sandwiched in a two-electrode configuration (metal-SAM-metal junction).

Probing the Electronic Properties of Materials that Self-Assemble

By

Ryan R. Fuierer

A Dissertation Submitted to the Graduate Faculty of
North Carolina State University
In Partial Fulfillment of the
Requirements for the
Degree of Doctor of Philosophy

Department of Chemistry

Raleigh, North Carolina
May 11, 2004

Approved by:



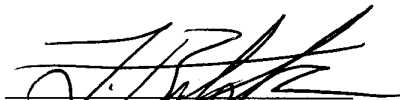
Dr. Christopher B. Gorman, Co-Chair of Advisory Committee



Dr. Daniel L. Feldheim, Co-Chair of Advisory Committee



Dr. Edmond F. Bowden



Dr. T. Brent Gunnoe

Dr. Jan Genzer,
Graduate School Representative

Dedication

This accomplishment is dedicated to my family and friends.

I also would like to dedicate this work to my friend Miles Andersen. I was very sad to hear you passed that day, and will always wish I could have seen you have the chance to prepare a document like this. I think of you often.

Biography

Ryan Richard Fuierer was born in Rochester, NY on October 31, 1971 to Richard and Marianne Fuierer and sister Tristan. He grew up in the satellite suburb of Holley, NY, graduating from the local High School in 1989. During this time he worked for the family home building business as a general laborer and equipment operator. He attended college at St. John Fisher College in Rochester, NY, earning a B.S. in Chemistry in 1993. In 1995 he moved to Chapel Hill, NC where he enrolled part time in graduate classes at UNC-CH to learn about materials science, while earning a living as a finish carpenter. In 1999, he began the graduate program in Chemistry at North Carolina State University under the directions of Drs. D.L. Feldheim and C.B. Gorman. He spent the following five years earning a Ph.D. in Chemistry, studying the electronic properties of self-assembled monolayer systems with scanning probe microscopy, and dabbling in the art of synthetic organic chemistry.

Acknowledgements:

First, I would like to thank my loving family and friends who have been very supportive of me throughout my life. Without their tremendous influences, I would not be the person I am today. I would especially like to thank my immediate family (Marianne, Richard and Tristan) for teaching me the importance of work ethic and perseverance towards one's goals. Thank you for always believing in me. I love you all dearly.

I would like to Dr. Susan Hendrickson. For had it not been for her, I would have never had the opportunity to be introduced to the advisors who would took a chance on me - the guy with the sub-par college GPA. With that, I greatly appreciate the opportunities my advisors Drs. Feldheim and Gorman enabled me to pursue, along with their willingness to allow me to follow my curiosities in science. I can say that I had an overall positive graduate experience because of the two of you.

I would like to gratefully acknowledge my colleagues along the way, who also became great friends: Drs. Lloyd Carroll, Grace Credo, Wyatt McConnell and Stephan Kramer. I appreciate all of you more than I could ever describe because you made my time here very enjoyable, taught me so much about my field of study and the ability to teach myself. I would like to especially acknowledge Stephan for his helpfulness in my research, critical reading of this document, and as my daily latte companion.

I greatly appreciate Dr. Tyson Chasse for his help with my discovery of the art of synthetic chemistry, and more importantly, his side splitting humor and plentiful advice about life over the years- you are a very wise man for your years. Your mom did a great job with you.

I acknowledge Christopher Cameron for his invaluable help in learning synthetic chemistry, general day-to-day discussion and laboratory banter. Thank you Sofi Bin-Salamon for your willingness to field general science questions at any time. Thank you Joe Ryan for friendship and support.

I would like to thank all my other colleagues in the Feldheim and Gorman groups. I appreciate all their help and support over the years aiding in my arrival to this point. I especially would like to acknowledge Drew Wassel for all his help and discussion with our related research.

Last but certainly not least, I gratefully acknowledge my best friend Candice Brannen. You've taught me so much about life in such a short period of time. I knew you were very special from the day our eyes met, and have never thought otherwise since that remarkable day. Your companionship is very dear to me. Thanks for all your understanding, patience and support while I was preparing this document, and your confidence in me. Thank you for all that you do for me. I appreciate you more than I could ever convey. I love you sweet pea.

Table of Contents

| | Page |
|--|-------------|
| List of Figures | ix |
| List of Tables | xxiii |
| List of Schemes | xxiiv |
| | |
| Chapter 1: | |
| Scanning Probe Lithography using Self-Assembled Monolayers | 1 |
| 1.0.0 Introduction | 3 |
| 1.2.0 Elimination Lithography | 8 |
| 1.2.1 STM Modification under Ambient Conditions | 10 |
| 1.2.2 STM Modification in UHV | 21 |
| 1.2.3 Modification with AFM (Mechanical and Electrical) | 24 |
| 1.2.4 Scanning Probe Lithography with NSOM | 43 |
| 1.3.0 Addition Lithography | 45 |
| 1.3.1 Historical Precedent for Addition Lithography | 45 |
| 1.3.2 The Fundamentals of DPN | 47 |
| 1.3.3 Variation of the Ink and Substrate | 58 |
| 1.3.4 DPN Structures as Templates | 72 |
| 1.3.5 Mechanistic Aspects Underlying DPN | 80 |
| 1.4.0 Substitution Lithography | 84 |
| 1.4.1 Substitution Initiated by Removal of SAM Under Elevated Bias | 85 |
| 1.4.2 Substitution Initiated by Removal of SAM via Mechanical Desorption | 98 |
| 1.4.3 Substitution Followed by ex-situ Addition to Patterns | 107 |
| 1.4.4 Substitution via Tip-Induced Terminal Group Modification | 112 |
| 1.5.0 Conclusions and Outlook | 127 |
| 1.6.0 Glossary | 128 |
| 1.7.0 References | 134 |
| Table 1 | 149 |
| | |
| Chapter 2: | |
| Replacement Lithography | 137 |
| 2.1 Introduction | 138 |
| 2.2 Results and Discussion | 141 |
| 2.3 Replacement Lithography with <i>n</i> -Alkylthiolates | 145 |
| 2.4 Replacement Lithography of SAMs with Electroactive Moieties | 149 |
| 2.5 Investigation of Replacement Efficacy | 154 |
| 2.6 Patterning with Other Electroactive SAMs | 161 |
| 2.7 Conclusion | 164 |

| | |
|--|-----|
| 2.8 Experimental | 165 |
| 2.9 References | 166 |
| Chapter 3: | |
| Patterning Mesoscale Gradient Structures with Replacement Lithography | 169 |
| 3.1 Introduction | 170 |
| 3.2 Effect of Replacement Parameter on Gradient Fabrication | 173 |
| 3.3 Multidirectional Gradients | 175 |
| 3.4 Ex-Situ Treatment of Functionalized Gradients | 178 |
| 3.5 Conclusion | 181 |
| 3.6 Experimental | 182 |
| 3.7 Acknowledgement | 183 |
| 3.8 References | 184 |
| Chapter 4: | |
| Tunneling Spectroscopy Measurements of Electroactive Self-Assembled Monolayers via Scanning Tunneling Microscopy | 185 |
| 4.1 Introduction | 186 |
| 4.2 Results and Discussion | 191 |
| 4.3 Current – Voltage Measurements on Patterned FcC ₁₁ S-SAMs in C ₁₂ S-SAMs | 199 |
| 4.4 Further Tunneling Spectroscopy Studies of Electroactive SAMs | 201 |
| 4.5 Conclusion | 204 |
| 4.6 Experimental | 205 |
| 4.7 References | 208 |
| Chapter 5: | |
| Stochastic Variation in Appearance of Electroactive Guests Molecules in Insulating Host Self-Assembled Monolayers | 221 |
| 5.1 Introduction | 222 |
| 5.2 Results and Discussion | 226 |
| 5.3 Stochastic Conductance Variation in FcC ₁₁ S- Guests Isolated in C ₁₂ S-SAMs | 228 |
| 5.4 Stochastic Conductance Variation in GalC ₆ S- Guests Isolated in C ₁₂ S-SAMs | 232 |
| 5.5 Stochastic Conductance Variation in Ru(bpy) ₃ C ₅ S- Guests Isolated in C ₁₂ S-SAMs | 233 |
| 5.6 Conclusion | 235 |
| 5.7 Experimental | 236 |
| 5.8 References | 238 |

| | | |
|---|-----------------|-----|
| Appendix | | |
| A.1 Operation of STM | | 242 |
| A.2 Chapter 2 Lithography Programs | | |
| A.2.1 “Quarterfoil Pattern” | for Figure 2.3 | 258 |
| A.2.2 “NC State Logo” | for Figure 2.4 | 261 |
| A.2.3 “12 lines” | for Figure 2.6 | 262 |
| A.2.4 “6 lines” | for Figure 2.7 | 264 |
| A.2.5 “7 lines” | for Figure 2.8 | 265 |
| A.2.6 “RH lines” | for Figure 2.9 | 266 |
| A.2.7 “Gal” | for Figure 2.10 | 267 |
| A.2.8 “Fc” | for Figure 2.10 | 268 |
| A.3 Chapter 3 Lithography Programs | | |
| A.3.1 “Replacement bias gradient” | for Figure 3.1 | 269 |
| A.3.2 “Lithographic scan rate gradient” | for Figure 3.2 | 273 |
| A.3.3 “L gradient” | for Figure 3.3 | 276 |
| A.3.4 “Y gradient” | for Figure 3.4 | 280 |
| A.4 Synthesis of 11-Ferrocenylundecanethiol | | 286 |

List of Figure Captions

- | | Page |
|---|------|
| Figure 1.1 Schematic diagram illustrating elimination, addition and substitution lithography with a scanning probe. In general, the probe imaged the surface first with non-destructive imaging parameters, in order to find an area suitable for patterning. Elimination was achieved by the removal of the SAM in proximity of the probe by mechanical or electrical means (A). In addition lithography, a probe coated with a molecular ‘ink’ was brought into contact with a nominally ‘bare’ substrate. The ink got transferred from the probe to the surface (B). Substitution lithography could proceed by two different pathways. In the first substitution pathway, the tip removed the SAM while scanning and an <i>in-situ</i> addition of a different molecule into the ‘bare’ region occurred (C, substitution via elimination and <i>in-situ</i> addition). The alternative substitution via SAM terminus modification occurred by the probe modifying the head groups of the SAM through electrochemical or catalytic interaction (D). | 7 |
| Figure 1.2 STM images of four nominally $(50 \text{ nm})^2$ patterns fabricated in a C_{18}S -SAM in air. The tunneling currents were (A) 0.05 nA, (B) 0.15 nA, (C) 1.5 nA and (D) 6 nA, respectively. (<i>z</i> -scale: 2 nm) Reprinted with permission from ref. 91. Copyright 1997 American Chemical Society. | 17 |
| Figure 1.3 SEM images showing a series of features in gold created through STM-based lithography on a MMEA/Au substrate ($i_{\text{set}} = 50 \text{ pA}$, $V_{\text{b}} = 10 \text{ V}$, $15 \text{ }\mu\text{m/s}$), immersing the sample into a solution of C_{16}SH for 30 s, and subsequent etching of the gold. A $(5 \text{ }\mu\text{m})^2$ square resulting from scanning consecutive 1024 lines (A). The lines seen in B, C resulted from 25 and one pass with the tip, respectively. The test grid (D) demonstrated single line patterns several microns in length. No proximity effect was seen at the crossing points. Reprinted with permission from ref. 93. Copyright 1997 American Chemical Society. | 19 |
| Figure 1.4 STM images showing (A) A circular pattern fabricated from voltage pulses of 2.7 V created 11 holes and one protrusion. (B) One of the smallest intentionally created holes (100 ms pulse duration, $V_{\text{b}} = 2.6 \text{ V}$). The SAM order in the periphery of the created pattern was disordered. Reprinted with permission from ref. 96. Copyright 1998 American Chemical Society. | 23 |
| Figure 1.5 Topography (A) and current (B) images of a nominally $(50 \text{ nm})^2$ square in a C_{18}S -SAM on gold (under water saturated toluene, lithographic conditions: ca. 3 nN force, 3 V bias; | 27 |

imaging conditions: 4 nN force, 0.05 V bias). The corresponding cross-section is shown below each image. (C) I-V curves recorded (i) during the patterning inside the square, (ii) just after patterning inside the square and (iii) outside the square (e.g. on C₁₈S-SAM). Reprinted with permission from ref. 102. Copyright 2001 American Chemical Society.

Figure 1.6

29

Schematic diagram of the anodic oxidation of a silane monolayer coated silicon oxide surface. (A) A conductive probe was scanned under an applied bias in a well-defined area on the sample surface. At ambient conditions, a water column formed between the tip and the surface and acted as an electrochemical cell. The pattern appeared as a protruded structure through the volume expansion of the SiO_x. (B) The pattern could be transferred into the silicon substrate via a wet chemical etching treatment.

Figure 1.7

32

Scanning electron microscope image of fluorescent latex nanoparticles immobilized onto a pattern generated by STM ($V_b = +5$ V, 0.2 $\mu\text{m/s}$ scan speed in N₂ with 80% RH) after APS treatment and immersion in latex particle suspension. Reprinted with permission from ref. 106. Copyright 1997 American Chemical Society.

Figure 1.8

33

AFM images showing the results of AFM anodic oxidation and wet etching of a pattern in an ODS-SAM on a multi-layer resist. Scan speed: 10 $\mu\text{m/s}$, probe current: 5 nA, etching steps with 0.5 wt % hydrofluoric acid (0.5 min) and 25 wt % tetraammonium hydroxide (3 min). Reprinted with permission from ref. 109. Copyright 1999 Society of the American Institute of Physics.

Figure 1.9

36

(A) Tapping mode AFM images of an oxide dot array fabricated by anodic oxidation of an OTS/SiO_x sample after backfilling with aminopropyltrimethoxysilane (dot height *ca.* 2.5 nm, diameter 70 nm). (B) The same template after the adsorption of 15 nm gold nanoparticles. Single particles were adsorbed to the oxide patterns. The section analysis data for both images are given below the corresponding image. Reprinted with permission from ref. 112. Copyright 2003 American Chemical Society.

Figure 1.10

37

Schematic diagram of (A) selective anodization of the silicon regions not masked by nanoparticles. (B) The volume expansion of the silicon led to a decreased height contrast between the particles and the substrate. (C) After a wet etching step, silicon columns capped with a nanoparticle were formed.

- Figure 1.11** 38
Non-contact mode AFM image ($7\ \mu\text{m}$)² of a patterned square (*ca.* $(5\ \mu\text{m})^2$) containing silicon columns. Reprinted with permission from ref. 113. Copyright 2000 American Chemical Society.
- Figure 1.12** 42
AFM images showing a lithographically defined pattern in a palmitic acid LB layer adsorbed to a SiO_x/Si substrate. Diamond pattern with protruding lines was written with $-10\ \text{V}$ (A), and with grooves written with $+10\ \text{V}$ applied tip bias (B). (*z*-scale: 6 nm) Reprinted with permission from ref. 121. Copyright 2002 American Institute of Physics.
- Figure 1.13** 44
AFM images of parallel lines of MUA in a C₁₂S-SAM on gold created by NSOM lithography. (A) The topography image showed no contrast. (B) LFM image showed lines with a width of $50 \pm 5\ \text{nm}$. (lithographic conditions: $0.2\ \mu\text{m}/\text{s}$ writing speed, 60 mW laser power) (C) A LFM image of a 30 nm line of C₁₂S- in a MUA-SAM (lithographic conditions: $1\ \mu\text{m}/\text{s}$ writing speed, 20 mW laser power) Reprinted with permission from ref. 125. Copyright 2002 American Chemical Society.
- Figure 1.14** 48
Schematic diagram illustrating dip-pen nanolithography (DPN). A tip coated with ‘ink’ molecules was brought into contact with the substrate. A water meniscus formed between the tip and the substrate, which facilitated the transport of the ink to the substrate.
- Figure 1.15** 49
LFM images of dots fabricated from (A) C₁₈SH and (B) MHA on a gold substrate by DPN. The contact times were 2, 4 and 16 min, respectively. (45% RH, images recorded at 4 Hz scan rate) Reprinted with permission from ref. 141. Copyright 1999 American Association for the Advancement of Science.
- Figure 1.16** 52
AFM images showing polygon shapes written with MHA on an amorphous gold substrate. The writing times per side were 30 s for the triangle, 20 s for the square and 8 s for the pentagon (*ca.* 0.1 nN force, 4 Hz scan speed, 35% RH). The geometric patterns were overwritten with a $(3\ \mu\text{m})^2$ square pattern with a C₁₈SH coated tip (four scans, 0.1 nN, 5 Hz, *ca.* 35% RH). The polygons showed the highest lateral force contrast, while the C₁₈S-SAM showed the lowest. The bare gold outside had an intermediate contrast. Reprinted with permission from ref. 142. Copyright 1999 American Association for the Advancement of Science.

Figure 1.17 54
LFM images of ‘molecular corral’ patterns consisting of two different inks. (A) A cross-shaped structure where the horizontal and vertical lines were written with C₁₈SH. A tip inked with MHA was then brought into contact in the middle of the pattern. The MHA diffused radially and the C₁₈S-SAM lines confined the spreading of the MHA. (B) A cross shape pattern, where the horizontal lines were written with a MHA coated tip and the vertical lines were written with C₁₈SH ink. (C) A tip inked with MHA was brought into contact with the substrate in the middle of the pattern. The MHA diffused radially and could diffuse across the horizontal lines, but not across the vertical lines (C₁₈S-SAM). Reprinted with permission from ref. 143. Copyright 2002 American Association for the Advancement of Science.

Figure 1.18 61
Direct patterning of two different acrylamide-modified oligonucleotide inks by DPN. The DNA was hybridized with their complementary ssDNA, which had different fluorescent labels (Oregon Green 488-X and Texas Red-X). (A) A combined green-red epifluorescence image. (B) Tapping mode images of hybridized ssDNA attached to a AuNP (5 and 13 nm diameter) to the same array structure. (C) The section analysis corresponding to both nanoparticle patterns (start and finish is indicated by arrows). Reprinted with permission from ref. 155. Copyright 2002 American Association for the Advancement of Science.

Figure 1.19 66
(A) AFM image of a ‘V’ shaped structure. The line on the left was drawn by E-DPN of platinum ($V_b = 4$ V, 10 nm/s) and the line on the right was created by anodic oxidation of the silicon substrate ($V_b = -10$ V, 50 nm/s, 58% RH). (B) The same structure after the heating (500 °C) under ethylene in argon for one hour. Reprinted with permission from ref. 190. Copyright 2001 American Chemical Society.

Figure 1.20 68
(A) AFM image of a SiO_x line on the left and an EDOT polymer line created via E-DPN on the right side. (B) The same patterns after the treatment with a 2:1 H₂SO₄:H₂O₂ solution. The polymer line was removed by chemical oxidation, while the SiO_x line was not altered. Reprinted with permission from ref. 162. Copyright 2002 American Chemical Society.

Figure 1.21 76
AFM topography images of magnetic nanoparticles adsorbed onto MHA patterns formed by DPN and backfilled with C₁₈SH. (A) A dot array fabricated by varying the contact time from 0.05 s (45 nm diameter) to 12.8 s (920 nm diameter). (B) Lines generated with different writing speeds (A: 0.1 μm/s (120 nm) to F: 1.6 μm/s (45 nm)). The images were recorded with a scan rate of 1 Hz. (C) Plot of the MHA dot diameter versus the tip-substrate contact time. (D) Plot of the linewidth of MHA versus the writing speed. Reprinted with permission from ref. 176. Copyright 2002 Wiley-VCH.

Figure 1.22 77
Schematic diagram of the orthogonal assembly of DNA nanostructures. In a first step regions containing two different types of ssDNA (strand a and b) were assembled on DPN patterned regions created from MHA (white ellipsoid). A ssDNA (a'b'), where one side was complementary to a and the other side was complementary to b, was hybridized to the surface. Two different sized nanoparticles (either functionalized with ssDNA a or b) were bound to this pattern, resulting in regions containing nanoparticles with different sizes.

Figure 1.23 78
Noncontact AFM image of a nanoparticle array assembled by orthogonal SA as described in Figure 22. (*z*-scale: *ca.* 40 nm) Reprinted with permission from ref. 177. Copyright 2001 Wiley-VCH.

Figure 1.24 88
Schematic diagram of substitution lithography by elimination and *in-situ* addition. (A) The self-assembled monolayer was imaged with non-perturbative tunneling parameters to locate an area suitable for patterning. (B) Upon change of the tunneling parameters (I_t , V_b), the thiolates of the SAM desorbed in proximity of the tip, resulting in removal of the SAM. The replacement molecules in solution assembled into the 'bare' regions. (C) The patterns could be assessed by changing the tunneling parameters to their initial, non-perturbative values.

Figure 1.25 92
STM images showing the bias dependent apparent height contrast of electroactive FcC₁₁S-SAM patterned into a non-electroactive C₁₂S-SAM. At a low bias of 150 mV, the letters 'Fc' were nearly invisible because the two molecules were similar in length. At higher imaging bias (1000 mV), the patterned FcC₁₁S-SAM showed a large apparent height contrast compared to the background SAM. (Imaging conditions: $I_t = 10$ pA, *z*-scale 2 nm, scan speed *ca.* 350 nm/s).

Figure 1.26 93
Schematic diagram for the fabrication of mesoscale chemical gradients. The diffuse (low) coverage end of the gradient was achieved by a non-overlapping lithographic line spacing (e.g. 12 nm) and low replacement voltage or fast lithographic scan speed. During the patterning of the gradient, the line spacing was incrementally decreased to overlap lithographic lines (e.g. 5 nm), while the replacement voltage was increased or the scan speed was decreased, resulting in high replacement coverage.

Figure 1.27 94
STM images of mesoscale chemical gradient fabricated from FcC₁₁SH into a C₁₂S-SAM, either systematically varying the replacement voltage from 2.6 to 3.1 V (A) or the lithographic scan speed from 160 to 20 nm/s (B) (*z*-scale: 6 nm). (C) A chemical gradient of MUA in a C₁₂S-SAM. The replacement bias was changed from 2.5 to 3 V (*z*-scale: 2 nm).

Figure 1.28

96

Schematic and STM images illustrating multi-point complementary hydrogen bonding recognition elements for the addition and removal of electroactive functionalities. (A) The host thiol molecule (diacyl 2,6-diaminopyridine decanethiol (DAP)) was patterned via replacement lithography into a C₁₂S-SAM. An electroactive functionality was added *in-situ* to this structure through non-covalent binding of a ferrocene-terminated uracil (B). The electroactive functionality could be replaced with a non-electroactive dodecyl-uracil (C). STM images after each of these steps taken at 0.5 V imaging voltage showed the change in the apparent height contrast. The replacement region of DAP had a low contrast (D). After the addition of ferrocene-terminated uracil, the apparent height contrast increased due to the electroactive moiety (E). The apparent height contrast was decreased by adding the dodecyl uracil molecule that replaced the electroactive moiety (F). ($I_{\text{set}} = 10 \text{ pA}$, z -scale: 3 nm) Reprinted with permission from ref. 193. Copyright 2002 American Chemical Society.

Figure 1.29

98

Schematic diagram of nanografting. A SAM is imaged with an AFM tip under a non-destructive imaging force to locate an area suitable for patterning (A). With an increased, applied force the monolayer was removed under the tip and the replacement molecules in solution assembled into the ‘bare’ regions (B).

Figure 1.30

100

(A) Topographic AFM image of two squares fabricated from C₁₈SH in a background C₁₀S-SAM (replacement parameters: 5.3 nN force, imaging conditions: 0.3 nN). The cross section showed that the C₁₈S-SAM was ca. 8 Å higher than the background. The edge resolution was 1 nm. Molecular resolution images of the C₁₈S- region (C) and the C₁₀S-SAM (D) revealed a two-dimensional close-packed structure. Reprinted with permission from ref. 195. Copyright 1997 American Chemical Society.

Figure 1.31

102

(A) Topographic AFM image of two rectangles fabricated from C₂₂SH and C₁₈SH in a C₁₀S-SAM matrix (replacement parameters: 15 nN force, writing speed of 50 ms per line). The corresponding cursor profile is shown (B) and revealed a height difference of ca. 1.2 and 0.85 nm for the two different replaced patterns, respectively. Reprinted with permission from ref. 196. Copyright 1999 American Chemical Society.

Figure 1.32

103

Time-dependent AFM images of a C₁₀S-SAM with a nanografted square of hexanethiol-modified oligonucleotide (12 base pairs). After the fabrication of the pattern, the sample was immersed in an enzyme to digest the DNA and imaged. The patterned square was clearly visible in the topography (A) and the friction image (B). The corresponding cross section analysis (C) revealed a height different of ca. 3 nm. After 4 h, the contrast in the topography

image was decreased (D), and the friction image showed the same contrast as before (E). The cross section (F) depicted a decreased height difference to ca. 1 nm. After 20 h, nearly no difference between the nanografted square and the background SAM was visible (G) & (I), while in the LFM image the square was still present (H). Reprinted with permission from ref. 203. Copyright 2002 American Chemical Society.

Figure 1.33 108

(A) AFM topography images ($12\ \mu\text{m}^2$) of a C_8S -SAM with a square replaced with MUA after the binding of rabbit IgG through a coupling agent (EDC). (B) The same square after subsequent exposure to goat anti-rabbit IgG. The corresponding cross section analysis was an average of the lines inside the box. (Imaging conditions: 2 nN force, 6 Hz, z-scale: 30 nm). Reprinted with permission from ref. 209. Copyright 2001 American Chemical Society.

Figure 1.34 111

(A) *In-situ* AFM (z-scale: 10 nm) and (B) corresponding SEM images of lines written on silicon under the presence of $\text{CF}_3(\text{CF}_2)_7\text{CH}=\text{CH}_2$ with different applied forces (ranging from 74 μN (left line) to 5 μN (right line)). (C) Profiles of three different lines (vertical axis was the gray scale value). Reprinted with permission from ref. 212. Copyright 2003 American Institute of Physics.

Figure 1.35 113

Schematic diagram of ligand based substitution lithography. (A) The functional head group of the SAM was altered with a STM. (B) A Pd catalyst reacted with the non-exposed area of the sample. (C) The electroless Ni plating procedure led to metal growth outside of the STM pattern.

Figure 1.36 115

Fluorescence micrographs of a SAM with terminal azide groups after patterning under different parameters. (A) A nominally $(10\ \mu\text{m})^2$ square area was written with a Pt-coated tip in hydrogen-saturated isopropanol and subsequently modified with fluorescently modified latex beads. (B) A square fabricated as in (A) but modified with ATTO-TAG reagent. (C) A nominally $(10\ \mu\text{m})^2$ area scanned and modified under the same conditions as (B) but with an unmodified silicon tip. Reprinted with permission from ref. 217. Copyright 1995 American Association for the Advancement of Science.

Figure 1.37 119

Schematic diagram of substitution lithography through the head group modification under an applied bias. (A) A conductive AFM tip scanned under an applied bias voltage across a SAM and modified the head group without changing the structural integrity of the SAM. (B) The altered functionality was used for the subsequent binding of a second self-assembly molecule.

Figure 1.38

123

Schematic representation of constructive nanolithography as a generic approach to the planned surface self-assembly of diverse organic, metal, and semiconductor nanoentities. Six nanofabrication routes were indicated, starting with an 'inert' silane monolayer (OTS/silicon) that was non-destructively patterned by an electrically biased AFM tip to locally form electrooxidized OTS (OTSeo), followed by the selective self-assembly of a vinyl-terminated silane overlayer (NTS) at the OTSeo polar sites defined by the tip. Subsequently, the terminal ethylenic functions of NTS were photoreacted with H₂S in the gas-phase or chemically oxidized with aqueous (KMnO₂ + KIO₄) to give the corresponding TFSM/OTSeo or NTSox/OTSeo bilayer template. Site-defined surface self-assembly of metallic silver, cadmium sulfide, or a third organic monolayer could be achieved using various template-controlled processes. The possibilities depicted here were: (1, 4) binding of Ag⁺ ions to the thiol or the carboxylic acid surface functions of the TFSM (1) and NTSox (4) template, followed by reduction with aqueous NaBH₄ or gaseous N₂H₄ and further development (if desired) of the silver nanoparticles obtained with a silver enhancer (SE) solution; (2) binding of gold species to the TFSM surface, followed by gold-catalyzed silver metal deposition from the SE solution; (3, 5) binding of Cd²⁺ ions to the TFSM (3) or the NTSox (5) surface, followed by the formation of CdS upon exposure of H₂S; (6) exposure of NTSox to a solution of a self-assembling silane, resulting in the formation of an organic trilayer at the tip inscribed sites.

Figure 1.39

124

AFM phase image of controlled self-assembly of silver nano- and macrostructures on a template produced by AFM lithography. Reprinted with permission from ref. 137. Copyright 2002 Wiley-VCH.

Figure 1.40

125

AFM images of an array of four Au₅₅/thiolated bilayer dots after annealing at 80 °C for 12 h ((A) topography, (B) phase image). Topography (C) and phase image (D) of a pattern combining dots, wires and contact pads. Reprinted with permission from ref. 228. Copyright 2002 American Chemical Society.

Figure 1.41

126

(A) Schematic diagram of the DPN procedure for the Diels-Alder reaction on a SAM. The tip, inked with a reactive molecule (diene), was scanned over a vinyl terminated (alkene) SAM and a Diels-Alder reaction took place. (B) Sketch of the Diels-Alder reaction of 2-(13-hydroxy-2-oxatridecanyl) furan on the alkene terminal headgroup of a silane SAM.

Figure 2.1

158

Typical STM images of dodecanethiol self-assembled monolayers (C₁₂S-SAM) on Au(111). A) A (1.0 μm)² area of C₁₂S-SAM showing large atomically flat Au(111) areas produced with this annealing technique. (Imaging conditions: 1.0 V, 10 pA, 1 Hz, z-scale: 2 nm). B)

(50 nm)² area showing molecular order of the film. (Imaging conditions: 1.0 V, 10 pA, 1 Hz, z-scale: 0.8 nm).

Figure 2.2 161
STM image of C₁₆S-SAM patterned in C₁₂S-SAM using replacement lithography. A) The (400 nm)² area of C₁₂S-SAM before patterning, and B) after patterning. (Imaging conditions: 1.0 V, 10 pA, 1 Hz, z-scale: 2 nm, Replacement conditions: 3.2 V, 10 pA, 1 Hz, RH: 53%).

Figure 2.3 163
A (400 nm)² STM image of a quarterfoil pattern consisting of FcC₁₁S- replaced into a C₁₂S-SAM. (Imaging conditions: 1.2 V, 8 pA, 1 Hz, z-scale: 3 nm, Replacement conditions: 3.1 V, 8 pA, 40 nm/s, RH: 59%).

Figure 2.4 165
Three (500 nm)² STM images demonstrating the apparent height contrast dependence of FcC₁₁S- with imaging bias. A) Image bias 100 mV. B) Image bias 500 mV. C) Image bias 1500 mV. D) Section analysis (depicted by dotted line) showing contrast between patterned FcC₁₁S- SAM and C₁₂S-SAM. (Imaging conditions: 10 pA, 1 Hz, z-scale: 3 nm; Replacement conditions: 3.0 V, 10 pA, 50 nm/s, RH: 57%).

Figure 2.5 167
Two (300 nm)² STM images comparing the amount of adventitiously replaced FcC₁₁S- guest species into a C₁₂S-SAM after a 30 minute incubation. Below each image is a histogram representing the pixel colors contained within image. A) The SAM incubated FcC₁₁SCOCH₃ (thioacetate species). B) The SAM incubated FcC₁₁SH (thiol species). (Imaging conditions: 1.0 V, 10 pA, 1 Hz, z-scale: 2 nm).

Figure 2.6 169
STM image (750 nm)² demonstrating efficacy of thiol replacement with systematic variation of positive substrate replacement bias. (Imaging conditions: 1.0 V, 8 pA, 1 Hz, z-scale: 3 nm; Replacement conditions: 8 pA, 50 nm/s, RH: 57%, bias listed under each patterned line).

Figure 2.7 171
STM images (ca. 900 nm x 300 nm) of six replaced lines demonstrating efficacy of thiol replacement with systematic variation in negative substrate replacement bias. (Imaging conditions: -1.0 V, 8 pA, 1 Hz, z-scale: 3 nm; Replacement conditions: 8 pA, 40 nm/s, RH: 53%, bias listed under each patterned line).

Figure 2.8 172

Two STM images (*ca.* 950 nm x 300 nm) demonstrating efficacy of thiol replacement with systematic variation lithographic scan rate. A horizontal averaged line analysis below each image, whose area is indicated by dotted line in the STM image. (Imaging conditions: 1.0 V, 8 pA, 1 Hz, *z*-scale: 5 nm; Replacement conditions: 3.2 V, 10 pA, RH: 58%, lithographic scan rate listed under each patterned line).

Figure 2.9 174

Schematic of the lithographic pattern indicating replacement bias for each line for relative humidity experiments. A series of six STM images (*ca.* 800 nm x 250 nm) demonstrating the efficacy of thiol replacement with a systematic variation in relative humidity ranging from 38% to 79%. (Imaging conditions: 1.0 V, 10 pA, 1 Hz, *z*-scale: 3 nm; Replacement conditions: 2.7 to 3.2 V, 10 pA, relative humidity listed in each image).

Figure 2.10 176

Two (200 nm)² STM images showing the imaging bias dependence of a (100 nm)² pattern containing galvinol substituted hexanethiolate replaced into C₁₂S-SAM. Averaged line analysis found below each image (Imaging conditions: 1.0 V, 10 pA, 1 Hz, *z*-scale: 4 nm; Replacement conditions: 2.8 V, 10 pA, 1 Hz, RH: 63%).

Figure 2.11 177

STM images (650 x 700 nm) demonstrating the process of patterning two electroactive inks in close proximity to each other. A) A galvinol thiol patterned first (in letters ‘Gal’), image bias 1000 mV, B) Image after ferrocenyl ink patterned (in letters ‘Fc’) in close proximity to the first. C) The apparent height contrast of differing inks at image bias 250 mV. (Imaging conditions: 8 pA, 1 Hz, *z*-scale: 5 nm; Replacement conditions: 3.0 V, 8 pA, 50 nm/s, RH: 59%).

Figure 3.1 180

STM image (*ca.* 400 x 900 nm) of FcC₁₁S- mesoscale chemical gradient in C₁₂S-SAM fabricated by systematically varying the replacement bias from 2.6 V to 3.1 V while keeping the setpoint current (10 pA), scan rate (50 nm/s) and relative humidity (58%) constant. Averaged horizontal line section analysis immediately below the image demonstrating gradient nature of pattern. (Imaging conditions: 1.0 V, 10 pA, 1 Hz, *z*-scale: 5 nm)

Figure 3.2 182

STM image (*ca.* 400 x 900 nm) of FcC₁₁S- mesoscale chemical gradient in C₁₂S-SAM fabricated by systematically varying the lithographic scan rate from 160 nm/s to 20 nm/s while keeping the setpoint current (10 pA), replacement bias (2.8 V) and relative humidity (60%) constant. Averaged horizontal line section analysis immediately below the image demonstrating gradient nature of pattern. (Imaging conditions: 1.0 V, 8 pA, 1 Hz, *z*-scale: 6 nm)

Figure 3.3 183

STM image of a multi-directional gradient (“L” shape) of $\text{FcC}_{11}\text{S-SAM}$ in $\text{C}_{12}\text{S-SAM}$. Structure was fabricated by systematically varying the replacement bias (from 2.95 V to 2.7 V), the lithographic scan rate (from 50 nm/s to 60 nm/s), lithographic line width (150 nm to 70 nm) and raster line spacing (4 nm to 11 nm), while maintaining constant setpoint current (10 pA) and relative humidity (58%) along each leg. (Imaging conditions: 1.0 V, 8 pA, 1 Hz, z-scale: 2 nm)

Figure 3.4 184

STM image of a three-legged gradient (“Y” shape) of $\text{FcC}_{11}\text{S-SAM}$ into $\text{C}_{12}\text{S-SAM}$. Structure was fabricated by systematically varying the replacement bias, the lithographic scan rate, and raster line spacing as depicted in image, while maintaining constant setpoint current (10 pA) and relative humidity (55%) along each leg. Image is annotated to depict replacement conditions along the gradient legs, fabricated in sequential order from Leg 1 to 3 following the direction of dashed arrows. (Imaging conditions: 1.0 V, 8 pA, 1 Hz, z-scale: 5 nm)

Figure 3.5 186

STM image (*ca.* 400 x 900 nm) of 200 nm x 720 nm $\text{HOOC}(\text{CH}_2)_{10}\text{S-}$ mesoscale chemical gradient in $\text{C}_{12}\text{S-SAM}$ fabricated by systematically varying the replacement bias (2.5 V to 3.0 V denoted in image) while keeping setpoint current (10 pA), scan rate (50 nm/s) and relative humidity (51%) constant. Average vertical line section analysis immediately below the image demonstrating gradient nature of pattern. (Imaging conditions: 1.0 V, 10 pA, 1 Hz, z-scale: 2 nm)

Figure 3.6 187

STM Image set demonstrating the successive process fabricating a $\text{HOOC}(\text{CH}_2)_{10}\text{S-}$ mesoscale chemical gradient, and installing amine terminated nanoparticles within. A) Area before gradient fabrication. B) Fabrication of an acid terminated gradient by systematically varying replacement bias and line spacing, while keeping setpoint, lithographic scan rate and relative humidity constant. C) Gradient mesostructure after aqueous incubation in $\text{H}_2\text{N}(\text{CH}_2)_7\text{S-}$ terminated 2 nm AuNPs. All imaging was carried out under dodecane. (Imaging conditions: 1.0 V, 10 pA, 1 Hz, z-scale: 2 nm)

Figure 4.1 200

A) Typical nonlinear I(V) curves from a $\text{FcC}_{11}\text{S-SAM}$ under dodecane displaying negative differential resistance. B) Histogram representing I-V curves that gave NDR responses in a data set of 938 curves. The histogram was fitted to a Gaussian to give NDR peak potentials: negative region -1438 mV; positive region 1539 mV. (500 nm)² scan area, I_{set} : 5 pA, 1000 μs sample period (*ca.* 15.6 V/s).

Figure 4.2 203

A $(500 \text{ nm})^2$ STM image of a $\text{FcC}_{11}\text{S-SAM}$ on Au(111) in dodecane demonstrating the image resolution obtained from a quality tip used for I(V) experiments. Surface features such as substrate vacancy islands and terraces are distinguishable. Notably, the presence of domain boundaries was expectedly absent due to the bulky headgroup of the ferrocenyl terminus, preventing an ordered SAM. The white rectangles depict scanning artifacts in the image. (Imaging conditions: 1.0 V, 5 pA, 1 Hz, z-scale: 2 nm)

Figure 4.3 204

Schematic qualitatively illustrating tunneling current enhancement via molecular state and tip Fermi energy (E_F) alignment (resonant tunneling) through a double tunnel junction containing electroactive ferrocenyl moiety. The result of changing tip-substrate bias (Panels A-E) is depicted on the generic I(V) trace (above). A) The double tunnel junction at 0 V with the HOMO of the ferrocenyl moiety much higher than E_F of substrate and tip. B) An increase in substrate bias causes some overlap of the tip E_F and ferrocenyl molecular state, resulting in an increase in tunneling current. C) Optimal substrate bias gives maximum alignment (resonance) of the tip E_F and molecular state resulting in a peak maximum (NDR). D) A further increase in substrate bias moves the tip E_F and molecular state out of alignment, decreasing tunneling bias. E) A significantly large enough substrate bias causes the tip E_F to surpass the tunnel barrier height of substrate, allowing electrons to cascade over the barrier resulting in an exponential increase in tunneling current.

Figure 4.4 206

Selected I(V) curves obtained from a $\text{FcC}_{11}\text{S-SAM}$ at various sample periods depicted in legend. No trend regarding scan rate was observed suggesting the NDR response proceeds by a resonant process.

Figure 4.5 207

Histogram representing the number of curves containing nonlinear responses from a CITS data set of $\text{HOOC}(\text{CH}_2)_{10}\text{S-SAM}$ on Au(111). This data set consisted of 945 of 1024 curves that weren't rejected as aberrant. The histogram is set to same scale as Figure 4.2B.

Figure 4.6 209

Results of a CITS experiment on a $\text{FcC}_{11}\text{S-SAM}$ patterned in a $\text{C}_{12}\text{S-SAM}$. A) $(500 \text{ nm})^2$ STM image of a $(300 \text{ nm})^2$ $\text{FcC}_{11}\text{S-SAM}$ patterned into a $\text{C}_{12}\text{S-SAM}$ using replacement lithography (Imaging conditions: 1.0 V, 8 pA, 1 Hz, z-scale: 5 nm). B) Four I(V) curves from inside the $\text{FcC}_{11}\text{S-SAM}$ pattern displaying NDR (lines), and four I(V) curves obtained from the outside the ferrocenyl pattern displaying no NDR (open markers), CITS parameters: $(600 \text{ nm})^2$, $I_{\text{set}} = 8 \text{ pA}$, 160 μs sample period.

- Figure 5.1** 227
 (250 nm)² STM image of a C₁₂S- host SAM containing adventitiously adsorbed FcC₁₁S- guest species. The region marked with the square was tracked over time to generate the data seen in Figure 5.3. Imaging conditions: 1 V, 9 pA, 1 Hz, z-scale: 2 nm.
- Figure 5.2** 236
 Analysis protocol used to determine apparent height contrast of guest species in host SAM. Section analysis of vertical, horizontal and diagonal section analysis were obtained and averaged to give an apparent height.
- Figure 5.3** 237
 A) Time-lapse series of images of a collection of FcC₁₁S-guests in C₁₂S-SAM. Image size *ca.* (20 nm)². (Imaging conditions: 1.0 V, 9 pA, 1 Hz, z-scale: 2 nm). B) Apparent height contrast variation with frame number. Time between frames was 8.5 minutes.
- Figure 5.4** 238
 A) Time-lapse series of images of FcC₁₁S-SAM guest in C₁₂S-SAM. Image size *ca.* (20 nm)². (Imaging conditions: 1.0 V, 9 pA, 1 Hz, z-scale: 2 nm). B) Apparent height contrast variation with frame number. Time between frames was 8.5 minutes.
- Figure 5.5** 239
 Schematic illustrating conformation changes (A & B) of a host electroactive containing SAM in an insulating guest SAM, resulting in different apparent height contrasts.
- Figure 5.6** 241
 A) Time-lapse series of images of GalC₆S-SAM guest in C₁₂S-SAM. Image size (15.3 nm)² (Imaging conditions: 1.3 V, 10 pA, 1 Hz, z-scale: 1.5 nm). B) Apparent height contrast variation with frame number. Time between frames was 8.5 minutes.
- Figure 5.7** 242
 A) Time-lapse series of images of Ru(bpy)₃C₆S-SAM guest in C₁₂S-SAM. Image size (22.9 nm)². (Imaging conditions: 1.0 V, 10 pA, 1 Hz, z-scale: 2 nm). B) Apparent height contrast variation with frame number. Time between frames was 8.5 minutes.
- Figure 5.8** 243
 A) Time-lapse series of images of Ru(bpy)₃C₆S-SAM guest in C₁₂S-SAM. Image size (24.1 nm)². (Imaging conditions: 1.0 V, 10 pA, H1 z, z-scale: 2 nm). B) Apparent height contrast variation with frame number. Time between frames was 8.5 minutes.
- Figure A.1** 251
 Schematic of a scanning tunneling microscope (STM).

- Figure A.2** 252
Schematic illustrating the energy levels in the tip and substrate separated by a energy (tunnel) barrier with an applied bias. Energies of the electrons in the electrodes are indicated by the shaded regions. The applied bias is equal to the difference in the Fermi energies (E_F) of the two electrodes.
- Figure A.3** 253
Exponential dependency of voltage and current (respectively) as a function of tip-substrate distance (z).
- Figure A.4** 254
Schematic illustrating the relation between the CITS parameters.
Figure adaptation courtesy of Drs. S. Krämer & W.P. McConnell
- Figure A.5** 256
Peak width vs. cut-off frequency plot as a function of sample period of the CITS experiment. Curves below the cut-off frequency of 1.5 kHz fall within bandwidth of the low current electronics.

List of Tables

| | Page |
|---|------|
| Table I “Surface Chemistry Reaction Schemes” | 149 |
| Table A.1 “Calculated Film Thickness” | 249 |

List of Schemes

Page

Scheme 2.1

156

Schematic of replacement lithography. A) SAM imaged at non-perturbative imaging bias to locate an area free from defects and substrate facet terraces suitable for patterning. B) Upon an increase in substrate bias, the SAM thiulates are desorbed in proximity of the tip, resulting in the removal of the SAM. The replacement molecules in solution assemble in to the freshly exposed regions of the gold. C) The pattern is assessed under imaging bias.

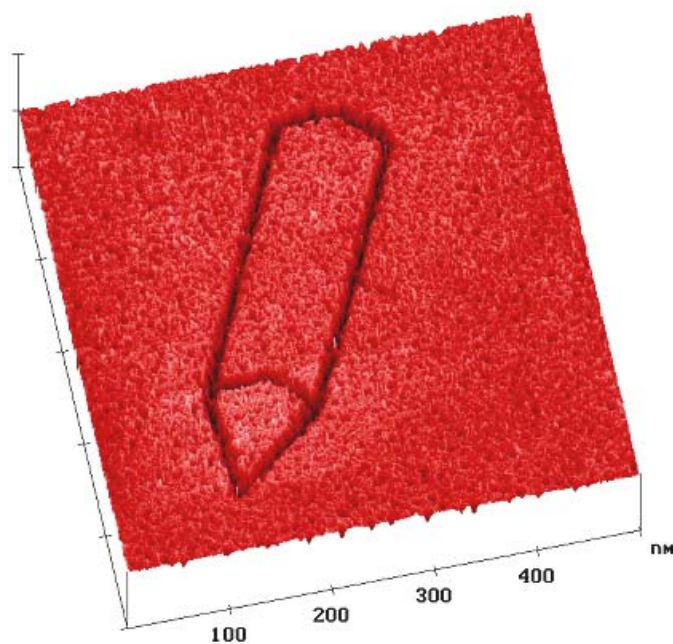
Scheme 3.1

187

Gradient tip raster pattern. In diffuse coverage region, spacing between pattern lines was *ca.* 12 nm and either low replacement bias, fast lithographic scan rate, or both, were employed. These patterning parameters were incrementally varied across the length of the gradient to reach the high coverage region where spacing between pattern lines was *ca.* 4 nm and either higher replacement bias, slow lithographic scan rate, or both were employed. The set point current and relative humidity were kept constant.

Chapter 1

Scanning Probe Lithography using Self-Assembled Monolayers



This work was done in close collaboration with Drs. Stephan Krämer and Christopher Gorman and was the subject of a publication, Krämer, S., Fuierer, R.R., Gorman, C.B., *Chemical Reviews*, **2003**, *103* (11), 4367-4418. Their exhaustive efforts are gratefully appreciated and acknowledged.

| | |
|--|-----|
| 1. Introduction..... | 3 |
| 2. Elimination Lithography..... | 8 |
| 2.1. STM modification under ambient conditions | 10 |
| 2.2. STM modification in UHV | 21 |
| 2.3. Modification with AFM (mechanical and electrical)..... | 24 |
| 2.4. Scanning probe lithography with NSOM | 43 |
| 3. Addition Lithography..... | 45 |
| 3.1. Historical precedent for addition lithography..... | 45 |
| 3.2. The fundamentals of DPN | 47 |
| 3.3. Variation of the ink and substrate | 58 |
| 3.4. DPN structures as templates | 72 |
| 3.5. Mechanistic aspects underlying DPN | 80 |
| 4. Substitution Lithography | 84 |
| 4.1. Substitution initiated by removal of SAM under elevated bias | 85 |
| 4.2. Substitution initiated by removal of SAM via mechanical desorption..... | 98 |
| 4.3. Substitution followed by ex-situ addition to patterns | 107 |
| 4.4. Substitution via tip-induced terminal group modification..... | 112 |
| 5. Conclusions and Outlook..... | 127 |
| 6. Glossary | 129 |
| 7. References..... | 134 |

1. Introduction

The ability to organize matter on the nanometer scale is one of the major enabling principles in the field of nanotechnology. Scanning probe microscopy (SPM) has been a key tool in achieving this goal. SPM serves two important purposes. The probe tip can visualize surfaces at the sub-molecular level. The ability to “see” molecules in this relatively straightforward way undoubtedly facilitated the emergence of molecular nanotechnology. Scanning probes have been employed to visualize many molecular phenomena. A few notable examples include the direct determination of the chirality of adsorbed molecules,¹⁻¹⁰ observation of the conformation of polymers,¹¹⁻¹⁸ dendrimers,¹⁹⁻²² adsorbed supramolecular nanostructures,²³⁻²⁸ and conformational and orientational dynamics of small molecules.²⁹⁻³⁴ In addition, probe tips can be used to manipulate atoms and molecules on surfaces.³⁵ In this mode, the technique is often referred to as scanning probe lithography (SPL). Such demonstrations as writing (of the letters “IBM”)³⁶ with xenon atoms, moving molecules to and fro (the “molecular abacus”)³⁷ and organization of atoms so as to illustrate the quantum nature of electrons (the “quantum corral”)^{38,39} have, at a minimum, piqued our collective curiosity about how we might further expand these ideas to perform useful functions at the molecular scale. Several excellent, recent reviews have treated the basic visualization and manipulation functions of scanning probes in detail.⁴⁰⁻⁴⁴

As one contemplates more complex, molecular scale operations, the need for chemically well-defined surfaces becomes apparent. The term “chemically well-defined” denotes control of the placement, patterning, orientation, and packing of chemical functional groups on a surface. These functionalities will be sites for control of the physical properties of that surface region. Several of these include control of the relative wetting behavior, adhesion, friction and chemical interaction with the environment above the surface. Moreover, these functional groups can facilitate a wide variety of chemical binding and covalent bond formation reactions.⁴⁵ The range of functional, molecular scale elements to be attached in a well-defined way depends only on the imagination, but has already been illustrated (as will be described in detail herein) with such diverse structures as metallic lines, polymers, active biomolecules, and colloids. These functionalities can also facilitate transduction of such a chemical event into an optical or electrochemical signal. Undoubtedly, other functions will be illustrated beyond these.

Self-assembled monolayers (SAMs) have emerged as a prominent, flexible, and convenient way to present functionality at a surface in a chemically well-defined way. The formation, characterization and the properties of SAMs have been described and reviewed extensively.⁴⁶⁻⁵⁰ Several features of SAMs are attractive. First, they provide a simple way to produce relatively ordered structures at the molecular scale. Second, they provide a way of presenting a wide variety of chemically well-defined terminal functional groups to a surface. The roles of these functional groups have been suggested above. Third, variation in the length of the chain between the head and tail groups offers some

control over the interaction between the underlying substrate and the chemical environment above the SAM. Thus, in applications from sensing to building with discrete numbers of molecules, the chemical and structural control offered by SAMs seems critical.

In addition to the elements of SAMs highlighted above, the ability to pattern the chemical functionality presented by SAMs at various length scales has been important in extending their utility. A variety of “soft lithography” methods have been developed to pattern surfaces with SAM regions presenting different chemical functionalities.^{51,52} The most notable of these is the technique of microcontact printing (μ CP). This technique is most easily employed to pattern SAMs at the micrometer scale, although several extensions of it have been described to extend its utility into the nanometer scale regime. The use of stamps to pattern at the nanometer scale has also been exploited in the technique of nanoimprint lithography.^{53,54} However, of the materials to be patterned at the nanometer scale, SAMs have the attractive feature that they present and hold chemical functionality (e.g. functional head groups) at the surface. To exploit this chemical definition afforded by SAMs at the nanometer scale, it is attractive to take advantage of methods that probe and pattern at this length scale.

Thus, it is natural to marry the molecular scale visualization and manipulation capabilities of SPM/SPL with the chemical definition and opportunities for creating patterns afforded by SAMs. This combination is the subject of this introductory chapter.

From a fundamental manufacturing standpoint, simultaneous utilization of these two elements can also be considered as a hybridization of top-down (SPL) and bottom-up (self-assembly) approaches. The importance of self-assembly in nanometer-scale construction has been highlighted.^{55,56} Yet, as there are no general paradigms for the artificial construction of arbitrary objects exclusively via self-assembly, the use of SPL to direct the patterning of self-assembled structures has enabled their use in nano-synthesis.

Indeed, it is attractive (at least to chemists) to view the creation of nanometer-scale constructs as an extension of molecular-scale chemical synthesis. In this vein, the efforts in this area have been categorized in a fashion analogous to the classification of chemical reactions. Nearly all chemical reactions can be divided into three major categories: eliminations, where a specific group is cleaved from a molecule ($AB \rightarrow A + B$); additions, where functional groups are added to a present structure ($A + B \rightarrow AB$); and substitutions, where one functional group is replaced by another ($AB + C \rightarrow AC + B$). As lithography on SAMs ultimately is about transforming chemical functionality presented at a surface, the lithographic approaches can also be categorized in this way. Specifically, techniques grouped in 'Elimination' denote SAM patterns that were created by removing the film from the substrate. Figure 1.1A depicts this process. The probe images the surface first in order to find an area suitable for patterning under conditions that do not perturb the SAM. Elimination involves the removal of the SAM in proximity of the probe by mechanical or electrochemical means. Chronologically, this was the focus of much of the early SPL work done on SAMs. As will be described, material is often added in

subsequent, *ex-situ* treatments of the patterned substrate. ‘Addition’ of a SAM precursor to a substrate denotes delivery of molecular ‘inks’ that formed patterns on bare surfaces

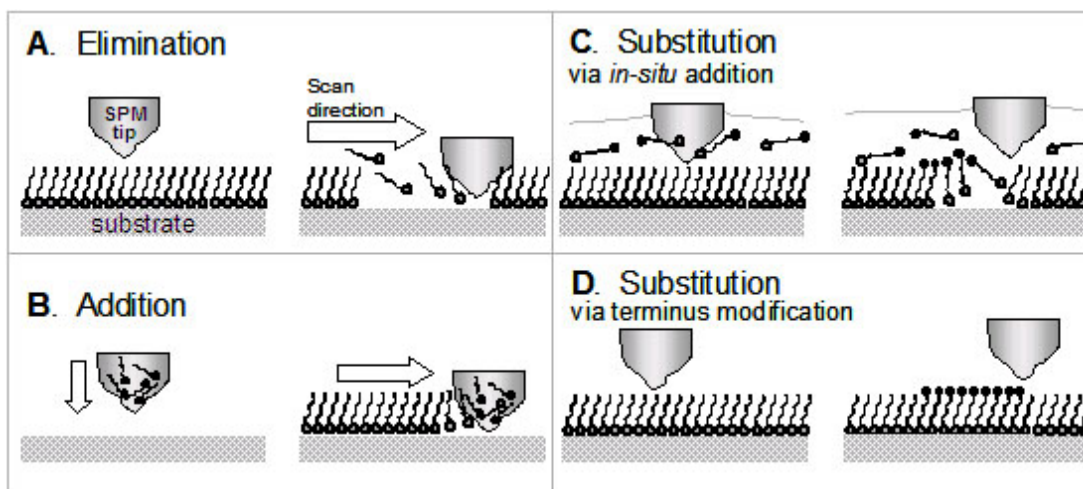


Figure 1.1: Schematic diagram illustrating elimination, addition and substitution lithography with a scanning probe. In general, the probe imaged the surface first with non-destructive imaging parameters, in order to find an area suitable for patterning. Elimination was achieved by the removal of the SAM in proximity of the probe by mechanical or electrical means (A). In addition lithography, a probe coated with a molecular ‘ink’ was brought into contact with a nominally ‘bare’ substrate. The ink got transferred from the probe to the surface (B). Substitution lithography could proceed by two different pathways. In the first substitution pathway, the tip removed the SAM while scanning and an *in-situ* addition of a different molecule into the ‘bare’ region occurred (C, substitution via elimination and *in-situ* addition). The alternative substitution via SAM terminus modification occurred by the probe modifying the head groups of the SAM through electrochemical or catalytic interaction (D).

(Figure 1.1B). A probe coated with molecular ‘ink’ is brought into contact with a nominally ‘bare’ substrate. The ‘ink’ gets transferred from the probe to the surface. ‘Substitution’ denotes *in-situ* mechanical or electrochemical pattern fabrication strategies. Substitution approaches are further subdivided into two categories: (1) initial elimination of the SAM film, followed by *in-situ* addition of self-assembly (SA) precursor to the

exposed substrate (Figure 1.1C) and (2) chemical change to the terminal functional group of the SAM, which can be used for further localized chemistry (Figure 1.1D). The use of scanning probes to perform lithography has been the subject of several prior reviews.^{42,57-}

⁶¹ These include some discussion of lithography on SAMs. This review intends to provide a comprehensive description of all types of SPL on SAMs and covers the literature up to the first part of 2004.

SAMs have also been used in other types of nanometer-scale patterning efforts that do not involve scanning probes. In addition to the microcontact printing and nano-printing applications mentioned above, SAMs have also been employed as electron-beam and UV patterning resists⁶² including examples where the chemical functionality presented by the SAM is modified upon this type of exposure.⁶³ Other examples include the patterning of a substrate followed by monolayer formation,⁶⁴ bottom-up patterning by using SAM-based multi-layers to bridge gaps between previously defined elements.⁶⁵ The conductivity of individual molecules has been probed by inserting them into defect sites in a SAM,^{41,66-68} and polymer growth from adventitiously inserted initiator molecules into a SAM has been investigated.⁶⁹

2. Elimination Lithography

A natural idea for the creation of structures is the removal of material from a surface in a controlled manner. The carving of symbols and letters into stone or the scratching of wax with a quill are some early examples. The basis of these techniques can be categorized as elimination. A part of a canvas is removed and results in a pattern. This type of nanometer scale scraping or ploughing had previously been demonstrated on a variety of surfaces including polymers, liquid crystals, bilayers and other types of resists.⁷⁰⁻⁷⁹

Elimination lithography on self-assembled monolayers has emerged from two different directions of research. One came from the investigation of resists for electron beam lithography. In pushing the resolution limit of electron beam lithography, thinner and thinner resist layers became important. This led to the investigation of thin polymer films and self-assembled monolayers as resist materials. The use of scanning tunneling microscopes (STM) emerged from these results, because STM produces a current of low energy electrons, and it thus can induce processes reminiscent of those induced by the electron beam. The second direction emerged shortly after the invention of scanning probe techniques. It was quickly noted that under certain conditions of imaging, the tip perturbed the sample. Thus, scanning probes act as some combination of probe and stylus. Determining the conditions under which the tip alternately acted as a non-destructive probe, and as a stylus, initiated the field of scanning probe lithography. Scanning probe lithography has been explored on virtually every class of substrate. Excellent general overview reviews of these efforts have been published by Penner and

Quate.^{42,60} The research reviewed in this introductory chapter focuses specifically on the use of SAMs in scanning probe lithography.

In this section, modification by STM under ambient conditions is described first. This is followed by a discussion of work performed in ultrahigh vacuum (UHV). Then elimination lithography using an atomic force microscope (AFM) is then reviewed. A few SPL examples with scanning electrochemical probe microscopy and near-field scanning probe microscopy have also emerged and will be described. The results of elimination lithography were often evaluated by some type of subsequent modification of the pattern.

2.1. STM Modification Under Ambient Conditions

An early example of SPL was demonstrated by Kim and Bard who described the modification of *n*-octadecanethiolate-SAMs (C₁₈S-SAM) on Au(111) with an STM operated in ambient conditions.⁸⁰ The surface modifications were observed upon the repeated scanning of a specific area with a setpoint bias voltage of 1 V and a setpoint tunneling current of 1 nA. The surface pits (e.g. vacancy islands), typically observed in STM images of SAMs, were seen to expand laterally during this process.^{50,81-84} This observation was attributed to a strong interaction between the STM tip and the surface. Purposeful modification of the SAM occurred by increasing the set-point current and lowering the bias, which effectively brought the tip closer to the surface. The removal of

the SAM was termed ‘etching’, and was presumed to be physical removal of the thiolate molecules by the tip. This assumption was supported by STM images that revealed the formation of holes in the SAM with material accumulation at the periphery of the scan area. Control experiments described the repeated scanning of a bare (e.g. unmodified) gold substrate under “etching” conditions that did not change the Au(111) surface. SAM modification could also be accomplished by applying a voltage pulse of $\pm(3 \text{ to } 5) \text{ V}$ to the tip (termed ‘voltage excursions’). The pulses resulted in material transfer between the tip and the substrate or vice versa, depending on the polarity of the applied voltage.

Crooks and co-workers established some of the early considerations in STM-based elimination lithography of SAMs under ambient conditions.⁷³ Their first report demonstrated the fabrication of geometrically well-defined patterns through removal of a C_{18}S -SAM from a Au(111) surface by applying a large substrate bias (+3 to +8 V) and repeated scanning. One experiment created $60 \text{ nm} \times 60 \text{ nm}$ sized squares by scanning the area four successive times under an applied substrate bias of +3 V, 110 pA tunneling current and at 31.25 Hz scan frequency ($1.875 \mu\text{m/s}$). To ensure complete SAM removal, the bias was lowered to +300 mV for a series of four scans, while the other parameters were held constant. The decrease of the bias voltage resulted in a smaller tip-substrate distance to remove SAM material mechanically. Scan line analysis of the preferentially removed areas showed more shallow depths (*ca.* 0.7 nm) than the reported ellipsometric thickness of a C_{18}S -SAM (2.2 to 2.8 nm). The authors attributed the finding to the fact that STM measures apparent height based on relative conductance of different regions of

the surface. Thus, the apparent topography of a pattern imaged by STM differs from its real topography. The extent of SAM removal was characterized with cyclic voltammetry (CV) employing the patterns as ultramicroelectrodes. Using $\text{Ru}(\text{NH}_3)_6^{3+}$ as an electrochemical probe, one $5\ \mu\text{m} \times 5\ \mu\text{m}$ pattern gave a current response in CVs corresponding to a round electrode with a radius of $3.6\ \mu\text{m}$. The current response scaled linearly when the number of similar sized patterns generated was increased. The authors concluded from these results that the removal of nearly all of the organic material in the patterned areas occurred.

Lercel and co-workers used STM as a low-energy electron source for SPL of C_{18}S -SAMs on gold and gallium-arsenide.⁸⁵ The tip was biased negative with potentials between 1 and 10 V over a range of tunneling currents of 10 nA to 110 pA. Square-shaped grating patterns (sizes between 2 and $140\ \mu\text{m}$) were formed by scanning the tip over an entire raster scan area. Non-contact mode AFM images of the resulting patterns on gold and on GaAs revealed the modifications resulted in raised features of *ca.* 2 to 4 nm in height. The mechanism for the fabrication of the raised features was not clear. The authors suggested that the electron beam was damaging the molecules, and parts of the molecules were drawn towards the tip by the electric field, creating bonds in the damaged layer that could combine with oxygen. Mechanical removal of the SAM and the substrate also occurred by bringing the tip in close contact with the sample using low bias and high tunneling current parameters. The smallest structures fabricated were 15 nm on GaAs and 20 nm on gold. The line widths on gold were usually larger, which the authors attributed

to the higher density of states in gold dictating a larger tip-substrate gap. This resulted in a larger diameter of the electron beam from the tip. The lines on gold could be transferred into the underlying substrate with a wet etching step, while transfer results on GaAs were inconclusive.

In a similar approach, Xu and Allee used C₁₈S-SAMs on GaAs and Langmuir-Blodgett (LB) films of a polymer (PMMA) and octadecanol on various substrates for STM based lithography.⁸⁶ A line pattern was written in the C₁₈S-SAM on GaAs with a tunneling current of 0.5 nA and a bias voltage of 10 V. AFM images after the patterning process revealed ca. 15 nm wide protruding lines, which could not be dissolved in organic solvents. The patterns could be transferred into the GaAs substrate by a wet etching step with either aqueous ammonium hydroxide or a citric acid etch. The observed line width increased to 25 nm as the result of this etching procedure. The authors observed substantial surface roughening of the SAM after etching, which was attributed to defects in the monolayer.

Lercel *et al.* compared the pattern transfer of various SAM systems modified with electron beams (e⁻-beams) of various energies (10 eV to 50 keV).⁸⁷ SAMs were prepared from octadecyltrichlorosilane (OTS, CH₃(CH₂)₁₇SiCl₃) on silicon dioxide and titanium dioxide, and octadecanethiol (C₁₈SH) on gold and GaAs. Electron beam exposure of the SAMs was manifested with a high-energy electron beam lithography system (50 keV), scanning electron microscope e⁻ beams with 1 keV to 25 keV exposures, and low energy

e^- beams generated from an STM tip (up to 10 eV for the conducting substrates). The patterns were imaged by an AFM in contact and non-contact modes and were also visualized using various types of wet and dry etches. Patterns generated from high-energy e^- beams yielded resolution of *ca.* 25 nm, while the minimum line size achieved with an STM was *ca.* 15 nm.

Sugimura and Nakagiri patterned silane layers on silica substrates.⁸⁸ Trimethylsilyl (TMS) monolayers were prepared by the vapor deposition of hexamethyldisilazane (HMDS, $(\text{CH}_3)_3\text{Si-NH-Si}(\text{CH}_3)_3$) onto a thin silicon oxide layer. The authors investigated the patterning of the TMS-layers under ambient conditions in air, oxygen or nitrogen atmospheres. Patterns were achieved by scanning an area at a sample bias of +5 V and a tunneling current of 200 pA. The structures were visualized by oxidation of the underlying substrate via a H_2O_2 treatment followed by the condensation of atmospheric water. Optical microscope images showed that the patterned area was hydrophilic, while AFM images revealed slight protrusions (*ca.* 0.5 nm) from the surrounding areas. Further proof for the degradation of the TMS-layer was obtained by immersing the samples in wet chemical etching solutions ($\text{NH}_4\text{F}/\text{H}_2\text{O}_2$), and the resulting structures were investigated by optical microscopy and AFM. Both microscopy techniques revealed that the TMS-SAM effectively protected the unpatterned areas from the wet chemical etchant. AFM images of patterns after etching showed the lithographic regions appeared as depressions in the Si substrate, with the narrowest line resolution of *ca.* 80 nm. The chemistry of the surface reaction was concluded to be primarily an anodic oxidation of

the silicon induced by the STM. An adventitiously adsorbed water layer effectively facilitated this electrochemical event. The atmosphere itself did not alter the patterning result if the humidity was kept constant. Water electrolysis and related electrochemical reactions induced beneath the tip were reckoned to be responsible for the degradation mechanism of the organosilane layer under the atmospheric conditions in the experiment.

Shortly after the first demonstrations of elimination lithography of SAMs on gold or silicon surfaces, the Crooks group described the use of these patterns in an *ex-situ* modification of the substrate. Schoer *et al.* reported the subsequent low temperature chemical vapor deposition (CVD) of copper into patterns generated by STM.⁸⁹ The researchers removed the C₁₈S-SAM as described above, and subsequently treated the sample with a copper CVD precursor (hexafluoroacetylacetonatocopper(I)-(1,5-cyclooctadiene), (hfac)Cu-(1,5-COD)) which decomposed at temperatures between 120 - 200°C. This temperature range was found to be compatible with the thermal tolerances of the C₁₈S-SAM resist (*ca.* 140°C). It was observed that the copper grew selectively only in the exposed (patterned) areas. XPS measurements confirmed the high purity of the deposited copper, while areas outside of the pattern gave negligible signals for copper. A second demonstration of the selective CVD deposition connected two larger patterns with a single SPL scan line. Scanning electron micrographs after the CVD process showed a 50 nm wide copper line between the larger pads. The authors observed that even patterns with incomplete removal of the SAM were sufficient to produce nucleation sites for the copper precursor, and enabled the separated copper grains to grow together.

Crooks and co-workers proposed that the patterning mechanism for the SPL induced removal (or deposition) of material from organic films in air was electrochemical in nature.⁹⁰ The inherent, thin water layer that covers film surfaces in ambient conditions was suggested to act as a thin layer electrochemical cell, and that adventitious impurities served as an electrolyte for a low current electrochemical process. By fabricating patterns in nonanethiolate- (C_9S -) and $C_{18}S$ -SAMs at various relative humidity (RH) and atmospheres (N_2 and air), it was reasoned that the atmosphere played little role in the desorption event, but the relative humidity was a crucial factor. At RHs below *ca.* 25%, no thiolates were removed, while larger RHs induced desorption. At this time, Schoer *et al.* produced the smallest known, intentionally created features in a SAM with a diameter below 10 nm, and a volume of less than 100 nm^3 . The creation of the features on the surface was independent of the tunneling current, which led to the assumption that bombardment with high-energy electrons was not responsible for the patterns. The authors showed that the created patterns could be transferred into the underlying substrate by an etching step. The etched structures from patterns in a C_9S -SAM were deeper and more irregularly shaped compared to the $C_{18}S$ -SAM, but showed the similar dependence on the relative humidity as the longer alkanethiolates. The effect on patterning of reverse bias polarity was also addressed, indicating ‘mounds’ of material were deposited on the SAM. Removal of this accumulated surface material could only be achieved when normal patterning conditions were applied.

Schoer and Crooks later showed that the created patterns were also dependent on the total amount of current (Coulomb dose), which again supported the hypothesis of an electrochemical process for the removal of the SAM.⁹¹ The authors investigated the shape of the created patterns' dependence on the applied bias and the tunneling current used for the lithography. Figure 1.2 shows four patterns created with different biases (different coulomb doses). The depth of the patterned squares increased with larger applied bias,

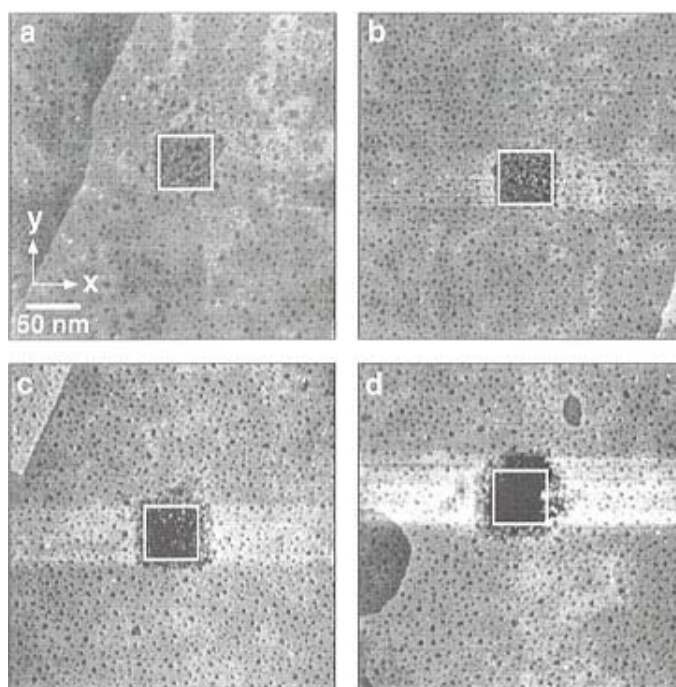


Figure 1.2: STM images of four nominally $(50 \text{ nm})^2$ patterns fabricated in a C_{18}S -SAM in air. The tunneling currents were (A) 0.05 nA, (B) 0.15 nA, (C) 1.5 nA and (D) 6 nA, respectively. (z-scale: 2 nm) Reprinted with permission from ref. 91. Copyright 1997 American Chemical Society.

depicted by incrementally darker patterned regions in the images. Studies with increased number of scans (equal to an increase in the coulomb dose) led to similar results.

Additionally, the authors discussed the mechanical effect caused by the tip. The authors assumed that at the standard imaging conditions (SIC: $V_b = +0.3$ V; $I_t = 150$ pA; 0.4 to 5 $\mu\text{m/s}$) the tip was already penetrating the surface of the SAM and impurities were inserted into the film. This assumption was consistent with later findings by the Weiss group on the relative height of the tip above SAMs of various thickness.⁹² STM images revealed distortions in the order of the SAM and some deposited material on the periphery of the scanned region in the fast scan direction. Patterns formed under standard patterning conditions (SPC: $V_b = 3$ V; $I_t = 150$ pA; 2.05 to 8.2 $\mu\text{m/s}$) created a disordered region surrounding the primary pattern. This effect resulted from long-range interactions between the tip and the surface, and was believed to be due to faradaic electrochemical processes. The size of this disordered region was dependent on the relative humidity and could reach as far as hundreds of nanometers around the primary pattern. Additionally, debris from the removed monolayer was deposited onto the tip, decreasing the resolution of the images after the patterning process.

Delamarche *et al.* compared the results of patterning SAM resists with high and low energy e^- beams.⁹³ High-energy electrons were generated from a transmission electron microscope (TEM, 100 keV) or scanning electron microscope (SEM, 1, 10, or 35 keV) under a moderately high vacuum, while low energy e^- beams patterns could be created with an STM. A self-assembled monolayer of mercaptomethylethylamine (MMEA, $\text{HSCH}_2\text{CONHCH}_2\text{CH}_3$), known to produce homogeneous, dense and stable monolayers

were formed on gold substrates. The molecule protected the gold from further thiol adsorption, but did not function as a protective layer against cyanide etch (post treatment). After patterning, the substrate was washed in different solvents (water, ethanol, heptane) and exposed to hexadecanethiol ($C_{16}SH$) solution to create $C_{16}S$ -SAMs in the patterned areas. These regions were resilient to a post treatment etch solution of aqueous KOH/HCN. Empirically, the authors determined that an electron dose from high-energy electron beams of three electrons per MMEA molecule was sufficient for the patterning. The MMEA-SAM could also be chemically converted to an effective etch stop without $C_{16}SH$ treatment with larger electron doses. Two possible explanations for the phenomena were discussed. One suggestion was that at high doses, the MMEA

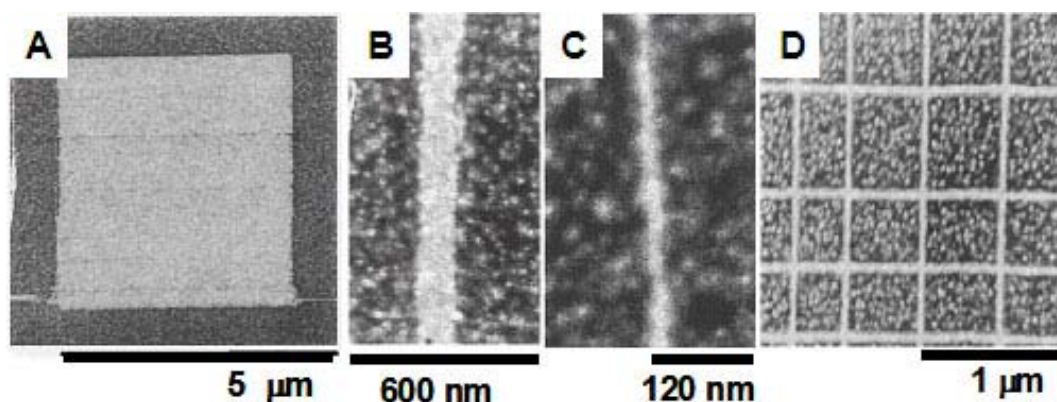


Figure 1.3: SEM images showing a series of features in gold created through STM-based lithography on a MMEA/Au substrate ($I_{set} = 50$ pA, $V_b = 10$ V, 15 mm/s), immersing the sample into a solution of $C_{16}SH$ for 30 s, and subsequent etching of the gold. A $(5 \mu\text{m})^2$ square resulting from scanning consecutive 1024 lines (A). The lines seen in B, C resulted from 25 and one pass with the tip, respectively. The test grid (D) demonstrated single line patterns several microns in length. No proximity effect was seen at the crossing points. Reprinted with permission from ref. 93. Copyright 1997 American Chemical Society.

monolayer itself was converted into a form that was resistant to the etching solution. A second possibility suggested that “contaminants” accumulated on top of the SAM functioned as a resist layer. The authors observed the high-energy electron beam irradiated MMEA resists required much larger doses than the exposure of a 50 nm thick PMMA resist, presumably due to the thinness (transparency) of the MMEA-SAMs. Therefore, the authors changed their focus to the lower electron energy regime created by STM. The researchers determined the non-perturbative parameters for scanning the monolayer in ambient conditions to be 1 V bias and 50 pA tunneling current. The threshold voltage for patterning of the MMEA resist was determined to be 4 V, with the most reproducible structures achieved at 10 V bias, 50 pA tunneling current and a scan speed of 15 $\mu\text{m/s}$ in an argon atmosphere. Gold patterns up to 5 μm long and 40 nm wide were created over large areas. Figure 1.3 shows a series of SEM images of features in gold created using the lithography process described above, followed by transfer into the substrate. Figure 1.3A displays a square resulting from scanning 1024 lines consecutively. The line pattern seen in Figure 1.3B was created by scanning 25 lines, while Figure 1.3C resulted from only one pass of the tip. The test grid (Figure 1.3D) demonstrates single line patterns several microns in length. The exact mechanism for the patterning scheme was not known and why 50000 electrons per molecule were required to pattern with a STM also remained unclear. Regardless, compared to the results achieved with the high-energy e^- beam experiments, this STM based lithography proved to be easier because it could be operated at ambient conditions. The higher energies of

standard electron beam lithography, which allowed much faster movement of the probe, proved to be non-advantageous for the use of SAM-resists.

Self-assembled layers of chemically bound nanoparticles were mechanically patterned by Yang *et al.* via STM.⁹⁴ Hexanedithiolate/decanethiolate-capped gold clusters were deposited onto gold on mica. Lithography was performed at greater than 2.55 V bias and 15.6 $\mu\text{m/s}$ scan speed to locally remove the gold particles in squares corresponding to the scan dimensions. A complete removal of all particles within the pattern usually required four consecutive scans. No effect of humidity was reported, but the tunneling current played an important role. Tunneling currents of 0.5 nA and a 10 mV bias removed surface bound particles. The authors assumed that this was a clear indication that the removal was not due to an electrochemical effect and was based on mechanical scratching.

2.2. STM modification in UHV

Müller *et al.* investigated the patterning of C_{16}S -SAMs and *n*-docosanethiolate (C_{22}S -) SAMs on gold with an STM operated in field emission mode in ultrahigh vacuum (UHV).⁹⁵ In this technique, high bias voltages (greater than 30 V) created tip-sample distances that were much larger (10 to 100 nm) than in normal STM imaging modes. The ultra-sharp field emission tips were electrochemically etched single crystalline tungsten

wires that yielded a line resolution of 20 nm at 10 $\mu\text{m/s}$ scan speeds. The resulting patterns were transferred into the substrate by wet etching treatments. The researchers found no significant difference in the performance between the different chain-lengths used.

Mizutani *et al.* investigated molecular scale patterning and the subsequent ‘healing’ of C_9S -SAMs on gold (created by gas-phase deposition in UHV), and reported some of the smallest SPL generated features to date.⁹⁶ The researchers worked under UHV conditions to avoid possible ‘uncharacterized’ electrochemical processes that might occur due to the surface water layer in ambient conditions. Patterns were created through voltages pulses (between +2.6 to +3 V, 70 to 200 ms in duration). The smallest created feature of *ca.* 2 nm was achieved with a pulse of +2.6 V of 100 ms duration. Figure 1.4A shows an example of a circular pattern of these pulsed SAMs with a magnified image of one pulse region in Figure 1.4B. The most important observation in this paper was that the monolayer underwent changes after the applied pulse. Under continuous scanning, a self-healing process was observed in less than five minutes. The authors suggested that the molecules may adsorb at the tip during the voltage pulses, and were ‘re-supplied’ during the imaging process. This assumption was supported by the fact that the self-healing process did not occur when the tip was retracted from the surface. Nevertheless, some of the created structures did not recover completely.

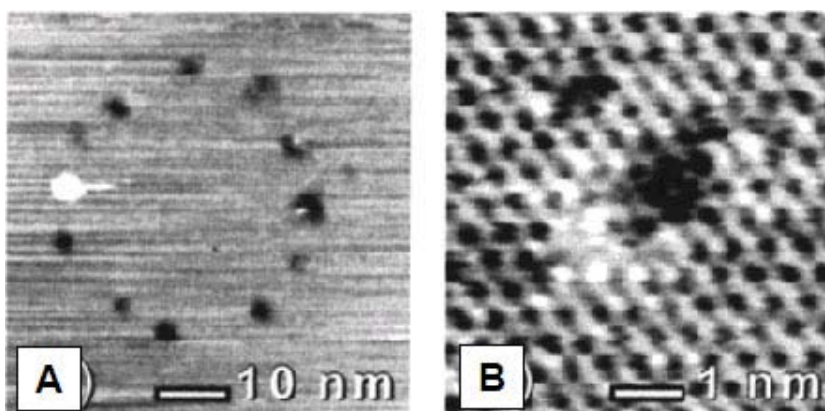


Figure 1.4: STM images showing (A) A circular pattern fabricated from voltage pulses of 2.7 V created 11 holes and one protrusion. (B) One of the smallest intentionally created holes (100 ms pulse duration, $V_b = 2.6$ V). The SAM order in the periphery of the created pattern was disordered. Reprinted with permission from ref. 96. Copyright 1998 American Chemical Society.

Keel *et al.* described the removal of the top gold layers from Au(111) surfaces modified with $C_{12}S$ -SAMs.⁹⁷ Using an UHV-STM with tunneling parameters of 0.1 V and 1 nA (etching conditions), the surface was modified in a manner that coalesced the characteristic surface vacancy islands after one patterning scan. Irregularly shaped deposition of debris (the height of one layer of gold atoms) outside the scanned region was observed. Temperatures above 320 K showed more drastic changes in the surface morphology during the ‘etching’ process, which were attributed to the higher mobility of the surface molecules and the surface gold atoms at elevated temperatures. Experiments performed under ambient conditions with a tunneling current of 1.2 nA required voltages between 0.1 to 0.4 V, and altered the surface more than observed in vacuum. It was concluded that the SAM played an important role. The binding of thiol molecules to the gold surface altered the bond strength between the top two gold layers significantly. No

alteration in the morphology of a bare gold surface was observed under the same etching conditions.

2.3. Modification with AFM (mechanical and electrical)

During an investigation of the structure and stability of decanethiolate ($C_{10}S^-$) and $C_{18}S^-$ SAMs on gold, Liu and Salmeron observed that molecules could be displaced on the surface when the sample was scanned with an AFM tip under a high applied load (up to 100 nN).⁹⁸ After this displacement was observed, the molecules near these “defect” sites appeared to diffuse laterally back and subsequently ‘repaired’ the initial SAM. Later, a similar study for alkylsilanes on mica was reported.⁹⁹ The force needed to displace silanes was higher than for the alkylthiolates of the same carbon chain length, but the actual value was dependent on the radius of the tip. Sharper tips decreased the required load by a factor of ten. This work illustrates the first step in the nanografting and nanoshaving processes discussed below in the section describing substitution lithography.

Kelley *et al.* described the mechanical removal of thiol modified double stranded DNA (dsDNA) by an AFM.¹⁰⁰ The DNA on a Au(111) substrate was imaged under a very low force (smaller than 200 pN). To remove the dsDNA, both the force applied to the AFM tip and the scan speed was increased. This resulted in the formation of squares exposing the underlying gold. The depth of these depressions was measured and taken to be the

film thickness. By performing this process in an electrochemical cell, subsequent variation in the potential applied to the surface caused changes in thickness of the dsDNA layer, attributed to the orientation of the dsDNA molecules with applied bias.

Zhou *et al.*¹⁰¹ investigated changes in the surface morphology of thiol functionalized DNA SAMs upon exposure to complementary single-stranded DNA (ssDNA) or mercaptohexanol (HOC_6SH). The modified ssDNA was self-assembled to a flat gold surface and imaged with an AFM. By increasing the force applied to the tip (30 to 50 nN) the DNA was mechanically scraped away in square shaped patterns. In this way, the researchers measured the thickness of the organic layer. When the patterned SAMs of ssDNA were immersed into complementary ssDNA, an increase in the thickness of the SAM was observed. The authors attributed this result to the formation of dsDNA, which had a more vertical conformation than the ssDNA. The same method was used to alter the height differences of patterned regions. After the writing of square patterns into a SAM composed of dsDNA, a second oligonucleotide with more bases (longer molecule) was assembled into the holes. Initially the AFM images showed that the height of the squares decreased, but was still below the film thickness of the dsDNA background. When this sample was reacted with complementary DNA, the depressions changed to protruding squares.

Uosaki and Zhao employed a current sensing AFM (CSAFM) for localized removal of a SAM. This instrument consisted of a conductive cantilever that could collect surface

information/morphology the same way as a traditional AFM. This instrument had the added ability to monitor current in a two-electrode configuration (similar to STM) to selectively remove C₁₈S-SAMs from Au(111). The researchers investigated the patterning dependence on applied bias, applied force and the effect of water on patterning efficacy in an inert solvent (toluene).¹⁰² The CSAFM enabled the authors to simultaneously compare topography and current images of the resulting pattern. The removal of SAM in patterned regions was supported by the appearance of *ca.* 1 nm (measured) depressions in the topography image, while the current sensing image showed high apparent height contrast between the 'bare' substrate and the background SAM. This result suggested that the resist layer was no longer present, resulting in higher currents passing through the patterned regions. Figure 1.5 shows the topography (Figure 1.5A) and current images (Figure 1.5B) of a C₁₈S-SAM pattern generated by 3 nN applied force and 3 V substrate bias. Figure 1.5C shows I-V curves during patterning (i), after patterning (ii) and outside the pattern (iii). Current voltage measurements revealed that the patterned areas gave resistance values of $1.7 \times 10^9 \Omega$; much lower than an unmodified substrate (metal), but higher than a C₁₈S-SAM resist (insulator). From these data, the authors concluded that the desorbed material or contaminants from solution most likely re-adsorbed to the gold substrate. A series of experiments was conducted to investigate the patterning parameters for the CSAFM based negative lithography. A systematic variation in applied bias under constant force yielded a critical threshold voltage of 2.0 V to remove the C₁₈S-SAMs. Application of the opposite bias (substrate negative) showed that a larger magnitude (-2.6 V) was required for the removal of the SAM. The applied

force needed for elimination was observed to decrease with increasing bias. At biases larger than 2.9 V, no force dependence with applied bias was found. The authors suggested that the process was

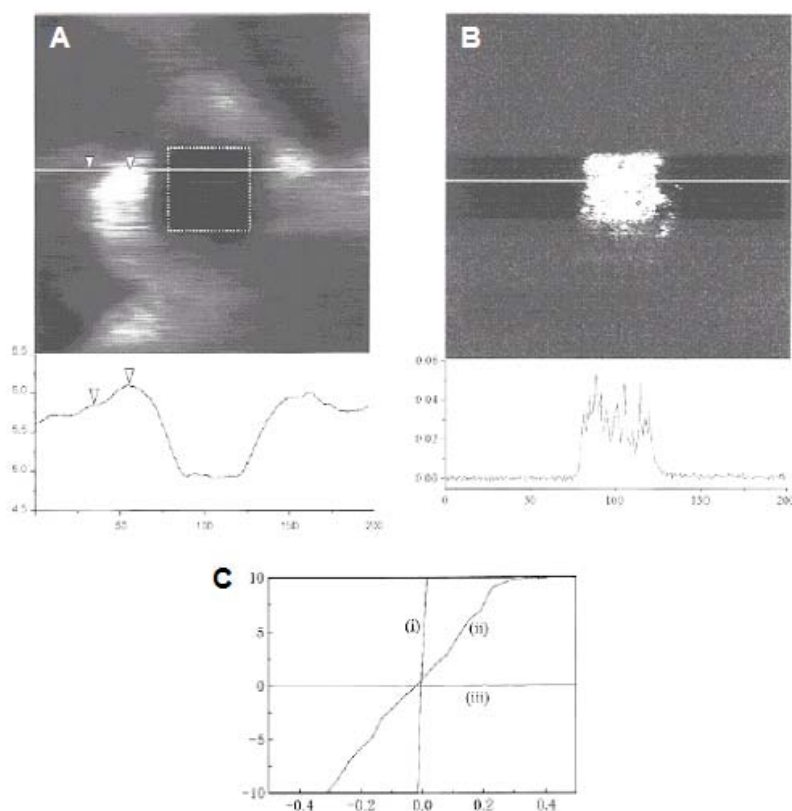


Figure 1.5: Topography (A) and current (B) images of a nominally $(50 \text{ nm})^2$ square in a $\text{C}_{18}\text{S-SAM}$ on gold (under water saturated toluene, lithographic conditions: *ca.* 3 nN force, 3 V bias; imaging conditions: 4 nN force, 0.05 V bias). The corresponding cross-section is shown below each image. (C) I-V curves recorded (i) during the patterning inside the square, (ii) just after patterning inside the square and (iii) outside the square (e.g. on $\text{C}_{18}\text{S-SAM}$). Reprinted with permission from ref. 102. Copyright 2001 American Chemical Society.

dominated by an electrochemical event at higher applied bias. Studies on the influence of water also revealed that lower bias was required to pattern under water-saturated toluene, whereas patterning performed under dry toluene required larger biases. This result supported that trace amounts of water facilitated the electrochemistry at the tip - substrate interface. The researchers concluded that the mechanism for the removal of organothiolate from the gold surface was electrochemical in nature, similar to the mechanism proposed by Crooks *et al.* for elimination lithography with a STM (*vide supra*).

A large body of work has described and exploited probe-based lithography to produce patterns involving the anodic oxidation of silicon. These experiments all employ silicon or a silica layer on silicon covered with a SAM as a resist. As will be illustrated below, the type of SAM has a large effect on the threshold bias and resolution of this process. Oxidation could be viewed as “adding” to the surface due to the silicon expansion. However, since the SAM is likely locally removed or “eliminated”, these techniques are discussed in this section.

Similar to previous (anodic oxidation) patterning demonstrations with an STM,⁸⁸ Sugimura *et al.* employed a conducting AFM for the nano-oxidative patterning of TMS-SAMs on silica that was based on tip-induced electrochemistry.¹⁰³ As illustrated in Figure 1.6, the conductive probe was connected to the substrate by a water meniscus (termed a ‘water column’) that was attributed to capillary condensation in ambient conditions. The

silane-based monolayer was degraded and the native oxide silica surface once again became hydrophilic, (e.g. hydroxyl terminated). In a similar approach, the authors showed with optical microscopy that the anodized patterns were hydrophilic from the condensation of water on chilled substrates.¹⁰⁴ The patterned regions protruded slightly above the surrounding SAMs. This protrusion was believed to be a volume expansion from the anodization of the (SiO_2) substrate by the incorporation of oxygen. After patterning, the structure was transferred into the substrate by a wet etching process with $\text{NH}_4\text{F}/\text{H}_2\text{O}_2/\text{H}_2\text{O}$. The narrowest line width obtained was 30 nm,

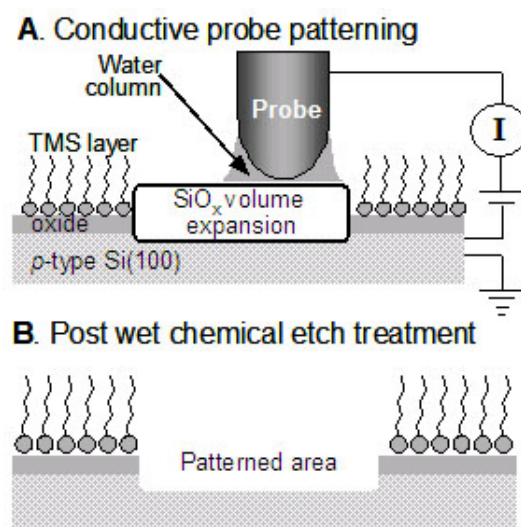


Figure 1.6: Schematic diagram of the anodic oxidation of a silane monolayer coated silicon oxide surface. (A) A conductive probe was scanned under an applied bias in a well-defined area on the sample surface. At ambient conditions, a water column formed between the tip and the surface and acted as an electrochemical cell. The pattern appeared as a protruded structure through the volume expansion of the SiO_x . (B) The pattern could be transferred into the silicon substrate via a wet chemical etching treatment.

but the isotropic etching process resulted in a widening of the lines. Patterning with positive biases required more than +3 V for complete patterning, while negative voltages needed was at least -5 V. Larger biases led to more complete degradation of the TMS-SAMs and therefore, a more effective etching procedure. The researchers observed a difference in the onset of the degradation threshold voltage in the positive and negative polarities that was believed to be due to the asymmetric nature of the tip-sample junction.

The exact mechanism of the degradation of the silane-based layer was unknown and the number of electrons needed to remove a molecule was calculated to be several hundred. The authors assumed that not all of these electrons were necessary for an electrochemical process associated with the degradation of the TMS layer. The authors speculated that tunneling or field emission currents passing through the molecule were responsible for these results. Leakage current through the water column by lateral electron hopping or electrons contributed to/from other reactions not related to the degradation of the organic monolayer also could cause these results. The amount of current injected per unit area was also observed to decrease as the patterning scan speed increased. To further understand the role electrons played in the degradation of organic monolayers, Sugimura *et al.* performed AFM lithography in constant current mode and observed that an injected electron density of several pC/ μm fabricated clear etched features in the SAMs.¹⁰⁵ When this current density was applied, scan speeds up to 5000 $\mu\text{m/s}$ could be used. However, the limits of the mechanical stability of the AFM system were reached and created irregular patterns. At injections of 1000 pC/ μm , the area surrounding the scanned region

was altered, and LFM images suggested contaminants could be present due to different friction contrasts than previously obtained of silicon oxide. Relative humidity studies strongly suggested that the degradation rate was also accelerated with increased humidity. Scan rate studies revealed that the depth and width of the line transferred into the substrate by etching increased with decreased scan rate. The researchers explanation was that the amount of injected current per unit time was changing.

In an *ex-situ* approach to generate chemically heterogeneous patterns, Sugimura *et al.* lithographically prepared a TMS-SAM as described above, but added a second silane (3-aminopropyltriethoxysilane (APS, $\text{H}_2\text{N}(\text{CH}_2)_3\text{Si}(\text{OCH}_2\text{CH}_3)_3$)) that reacted to the surface hydroxyl groups generated in the anodic oxidized patterns.¹⁰⁶ To confirm the selective growth of the APS layer, aldehyde-modified, fluorescently-tagged, latex nanoparticles were reacted with amine functionalities in the patterns. Fluorescence optical micrographs (Figure 1.7) confirmed that the latex nanoparticles were bound only in the patterned areas. Further experiments revealed that the amine groups of the confined APS areas could be reacted with the amine groups of proteins (e.g. horse radish peroxidase) with the help of a glutaraldehyde cross linker. Tapping mode (non-contact mode AFM) and phase contrast AFM images revealed the adsorption of protein to the APS confined regions with no apparent non-specific binding to the TMS regions of the SAM. Another *ex-situ* addition approach reacted heptadecafluoro-1,1,2,2-tetrahydro-decyl-1-trimethoxysilane (FAS) by chemical vapor deposition (CVD) to the SiO_2 structures created from anodic oxidation in an OTS-SAM.¹⁰⁷

The samples were monitored before and after with topographic AFM images and Kelvin probe force microscopy (KFM). The large molecular dipole of FAS contributed to

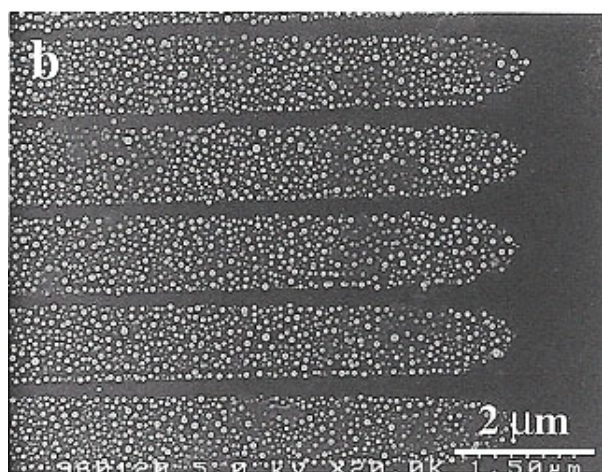


Figure 1.7: Scanning electron microscope image of fluorescent latex nanoparticles immobilized onto a pattern generated by STM ($V_b = +5$ V, 0.2 mm/s scan speed in N_2 with 80% RH) after APS treatment and immersion in latex particle suspension. Reprinted with permission from ref. 106. Copyright 1997 American Chemical Society.

surface potentials that were 50 mV higher in the patterned lines than in the surrounding OTS-SAM, which showed up clearly in KFM images. Patterns generated by anodic oxidation transferred into the oxide layer by a wet chemical process served as a template for the electroless plating of Au.¹⁰⁸ Here, the plating proceeded selectively on the Si surface due to the galvanic displacement between Si and Au ions, while the OTS-SAM surface remained free of deposits. The line resolution of the electroless plating achieved was 200 nm, confirmed with SEM and Auger spectroscopy.

Sugimura *et al.* also used localized current injection (from a conducting AFM tip) to pattern insulating SiO₂ substrates by utilizing a multi-layered resist containing a conductive layer.¹⁰⁹ An amorphous silicon resist was thermally grown on SiO₂ and cleaned by ultraviolet light-generated ozone, which created a thin silicon oxide layer. This layered structure was then coated with an octadecylsilyl SAM (ODS-SAM). The SPL patterning parameters were similar to those described previously by this group. A two-step wet chemical development process transferred the structures to the underlying thermal oxide film. First, etching in dilute hydrofluoric acid led to the removal of the exposed photochemical oxide. A second wet etch step with tetramethylammonium hydroxide (TMAH, 25 wt %) was performed and the pattern mask for the further etching of the thermal oxide was achieved. By immersion of the substrate into hydrofluoric (HF)

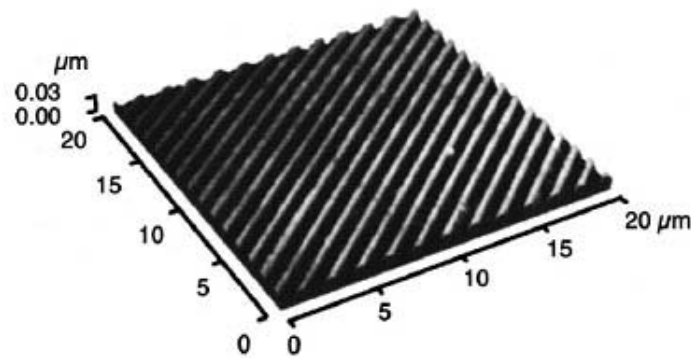


Figure 1.8: AFM images showing the results of AFM anodic oxidation and wet etching of a pattern in an ODS-SAM on a multi-layer resist. Scan speed: 10 μm/s, probe current: 5 nA, etching steps with 0.5 wt % hydrofluoric acid (0.5 min) and 25 wt % tetraammonium hydroxide (3 min). Reprinted with permission from ref. 109. Copyright 1999 Society of the American Institute of Physics.

acid, the oxide was structured with the same patterns written with the AFM probe. An example of Si structures created with this process is shown in Figure 1.8.

Sugimura *et al.* also described the influence of SPL parameters on the patterning of organosilane SAMs on silicon substrates.¹¹⁰ The effect of the pulse duration on the size, height of patterns created in SAMs composed from octadecyltrimethoxysilane (ODS-SAMs) was investigated by lateral force contrast. By comparing the results from the different measured parameters, the authors concluded that the surface modification was a multiple step process and electrochemical reactions between the tip and the sample in the water column took place. The line width was dependent on the writing speed with a lower width limit of 20 nm, but the authors believed this value to be convoluted with the shape and size of the probe.

Zheng and co-workers chemically positioned Au nanoparticles on a silicon surface using a nano-oxidation technique for the preparation of quasi-one-dimensional lines.¹¹¹ After SPL patterning (*ca.* 8 V, 4 $\mu\text{m/s}$) of a SAM prepared from octadecyltrichlorosilane on silica (OTS-SAM), amine-terminated silanes were self-assembled into the oxidized, patterned areas. Then, 12 nm diameter gold nanoparticles were electrostatically bound to these amine-terminated SAM regions. SEM images showed the particles were exclusively immobilized on the predefined patterns.

Using a similar methodology as described above, Li *et al.* presented the fabrication of lithographic patterns that could trap single gold colloids.¹¹² The researchers investigated the role of the humidity, pulse duration and pulse voltage on the diameter of the oxidized (patterned) spots. Prior to patterning, OTS-SAMs were incubated in the presence of small silane molecules (phenyltrichlorosilane or 3-chloropropyltrichlorosilane) to avoid colloidal binding in the defect sites of the SAM when exposed to the gold nanoparticle (AuNP) solution. By controlling the size of the SPL pattern, the number of particles adsorbed could be controlled. With a spot diameter of 100 nm, the efficiency for binding 15 nm particles was determined to be 100%. As the diameter was decreased to 28 nm, only 30% of the oxidized/functionalized spots on the surface were found to bind a colloid. The authors believed that the effective area where the adsorption took place was smaller than the measured diameter of the oxidized area due to an inhomogeneous degradation of the OTS layer. As the spot diameters became smaller, the number of OTS molecules remaining in the patterned region increased, effectively decreasing the number of binding possibilities for the gold nanoparticles. The non-planar shapes of the oxidized silicon patterns were also believed to contribute to the lower efficiency for binding. Nevertheless, the authors demonstrated the ability to control the number of particles down to the binding of a single Au particle in a single oxidized dot. Figure 1.9A shows an AFM image of the original oxide patterns, and Figure 1.9B depicts 15 nm diameter AuNPs absorbed onto this structure.

Nanoparticles patterned on a silica surfaces have also been used by Zheng *et al.* as masks in the anodization of a silica substrate. This strategy facilitated the fabrication of silicon nanopillars under ambient conditions (Figure 1.10).¹¹³ Gold colloids (18 nm) were initially anchored to the surface with a mercaptopropyltriethoxysilane SAM (MPTS-

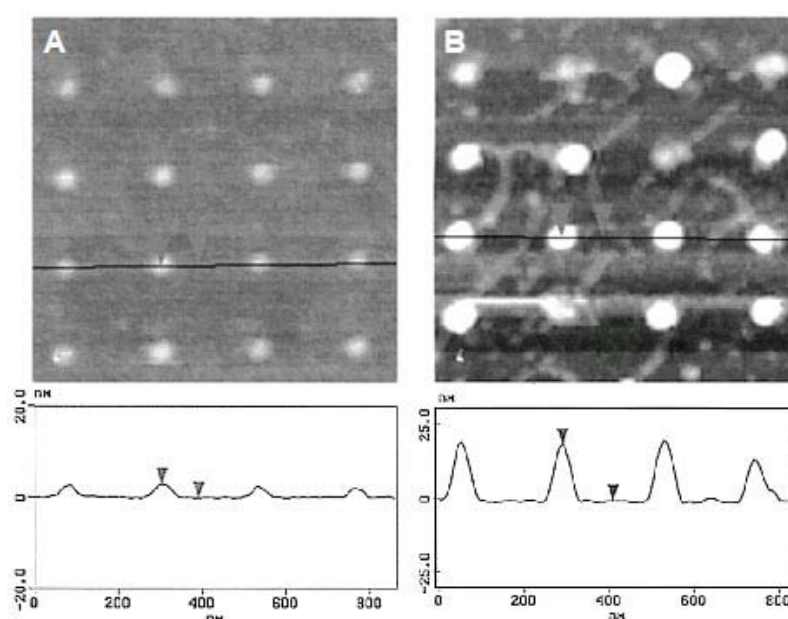


Figure 1.9: (A) Tapping mode AFM images of an oxide dot array fabricated by anodic oxidation of an OTS/SiO_x sample after backfilling with aminopropyltrimethoxysilane (dot height *ca.* 2.5 nm, diameter 70 nm). (B) The same template after the adsorption of 15 nm gold nanoparticles. Single particles were adsorbed to the oxide patterns. The section analysis data for both images are given below the corresponding image. Reprinted with permission from ref. 112. Copyright 2003 American Chemical Society.

SAM) as illustrated schematically in Figure 1.10A. An area was scanned with an applied bias of +9 V to oxidize the silicon in this region (Figure 1.10B). By comparing the height of the nanoparticles before and after the anodization, the measured height of the

nanoparticles decreased slightly from 18 nm to 15 nm, which supported the assumption that the silicon around the nanoparticles oxidized and slightly expanded (Figure 1.10B). After wet etching of the sample, columns remained under the nanoparticles (Figure 1.10C). The measured

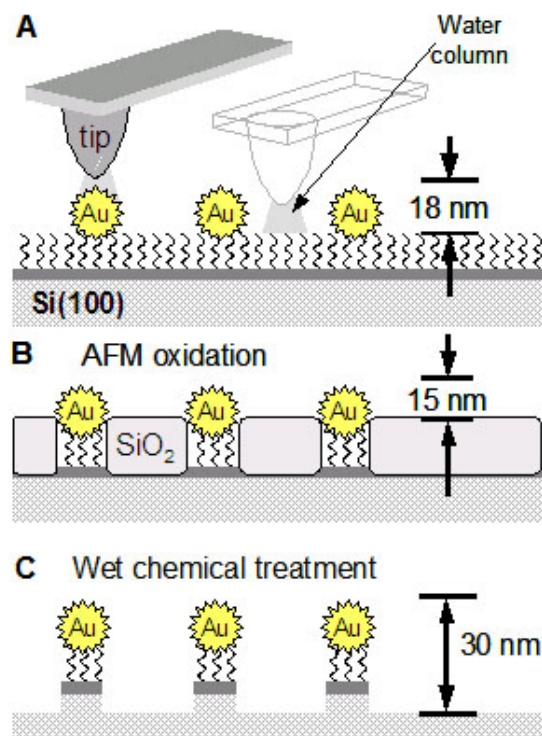


Figure 1.10: Schematic diagram of (A) selective anodization of the silicon regions not masked by nanoparticles. (B) The volume expansion of the silicon led to a decreased height contrast between the particles and the substrate. (C) After a wet etching step, silicon columns capped with a nanoparticle were formed.

diameter of these columns (in the lithographically patterned area) was 71 nm with a height (including the AuNP) of 30 nm (Figure 1.11). The real lateral dimension of the

features could be smaller due to the convolution of the tip shape and the columns. This experiment showed that nanoparticles could be used as masks for the electrochemical modification of a silicon surface.

Kim *et al.* followed the same silicon anodization approach as Sugimura *et al.* reporting the use of octadecyldimethylmethoxysilane (ODMS) as an organic resist for lithography with a conductive AFM (cAFM).¹¹⁴⁻¹¹⁶ The organic monolayer was degraded under a constant force

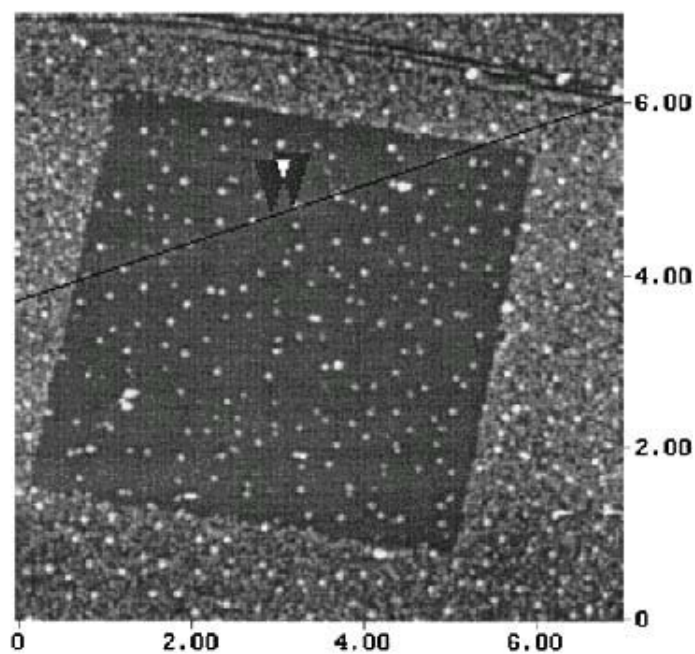


Figure 1.11: Non-contact mode AFM image ($7 \mu\text{m}^2$) of a patterned square (*ca.* $(5 \mu\text{m})^2$) containing silicon columns. Reprinted with permission from ref. 113. Copyright 2000 American Chemical Society.

and an applied negative voltage of -10 to -30 V. The authors assumed that the voltages used resulted in field emission from the tip. This patterning resulted in protruded features caused by the volume expansion of the silicon during the anodization. It was shown that the patterns could be transferred into the substrate by a wet etching step with buffered oxide etch (BOE). This etching process was selective and the organic layer was nearly unaffected, while the oxide layer was removed. The smallest reported line width was *ca.* 70 nm written at a scan speed of 120 $\mu\text{m/s}$.

Several efforts studied the effect of various types of surface monolayers and multi-layers with this type of patterning via anodic oxidation of silicon. Kim *et al.* anodized silicon terminated with multi-layered structures based on zirconium phosphonate chemistry.¹¹⁷ During the course of multi-layer formation, it was observed that lines patterned on a Zr^{4+} terminated surface were smaller than lines patterned on a phosphonate terminated surface. The researchers concluded that the surface charge of the Zr^{4+} was enhancing the effect of the anodization. This group extended their efforts by later investigating the effect of surface charge on the efficacy of patterning.¹¹⁸ The films were fabricated by the sequential adsorption of phosphoric acid and metal ions (Zr^{4+} or Ca^{2+}), in which the adsorption of Zr^{4+} resulted in a net positive charge, while Ca^{2+} led to neutral surfaces. Film preparation was confirmed by ellipsometry and AFM. The authors reported the effect of systematically changing the applied bias voltages and scan speeds during patterning, and compared the resulting line widths and heights of the silicon protrusions. It was observed that the positively charged film could be patterned at lower applied

voltages and higher scan speeds than the neutral surface. The authors concluded that the positive charge (on Zr^{4+} films) led to an enhancement of the lithographic process by altering the electron transfer process, causing the Zr^{4+} films to be patterned at lower voltages.

In a similar vein, Lee *et al.* investigated the silicon protrusions generated on charged amphiphilic layers physisorbed on silicon surfaces.¹¹⁹ The bipolar amphiphiles, 1,12-diaminododecane (DAD-2HCl) and *n*-tridecylamine (TDA-HCl), were adsorbed onto a negatively charged silicon wafer creating ammonium chloride modified and methyl-terminated films, respectively. Various AFM anodizations were performed at a relative humidity of 50% with different scan speeds (30 to 480 $\mu\text{m/s}$), applied voltages (10 to 25 V), and currents (13 to 14 nA). The ammonium chloride modified surface led to broader and higher protruding lines than the surface terminated with methyl groups. The authors attributed this to an enhancement effect by the charged ammonium ions.

Mixed monolayers of the above mentioned amphiphiles were used to investigate terminal surface group effects on the efficacy of anodic patterning of silicon wafers with this AFM lithography.¹²⁰ It was shown that the mixing ratio on the surface was strictly related to the ratio of the molecules in solution and played an important role for the threshold voltage necessary to produce lines of a predetermined height. Under fixed anodization parameters, as the amount of DAD-2HCl in solution was increased, the voltage for creating a line of 10 nm in width decreased. However, it was observed that the current

during the patterning process was nearly constant for the different mixtures, which supported a faradaic process for the anodic oxidation. Increased ratios of DAD-2HCl resulted in increased line widths. The amount of ammonium chloride groups present on the surface was believed to be responsible for this phenomenon. The authors argued that when the surface was more hydrophilic, the water meniscus present was larger, leading to wider lines.

The effect of polarity change applied to the AFM cantilever was the focus of a report by Lee *et al.* who patterned Langmuir Blodgett (LB) resists / films prepared from palmitic acid ($C_{15}COOH$) physisorbed on a silicon oxide surface.¹²¹ Under positive substrate biases, protruding lines in silicon were generated. Under reverse biases, grooves with a smaller width were found. The depth of the groove correlated with the thickness of the LB layer. The authors supplied two possible explanations for the selective removal of the molecules from the surface under reverse bias. The first hypothesis was based on the dissociation reaction of the palmitic acid. The second hypothesis described the degradation of the resist under a strong electric field, which was concluded to be the dominant process based on the increase in groove depth with increasing bias. At -5 V, the negative-tone pattern was just half the depth of the film thickness, and increased with increasing bias. This work was the first example for the creation of protruding lines or grooves by merely changing the polarity of the applied bias. Figure 1.12 shows an example of a diamond pattern generated with a -10 V bias to create a protrusion (Figure

1.12A), and a similar pattern created with a bias of +10 V resulted in a groove (Figure 1.12B).

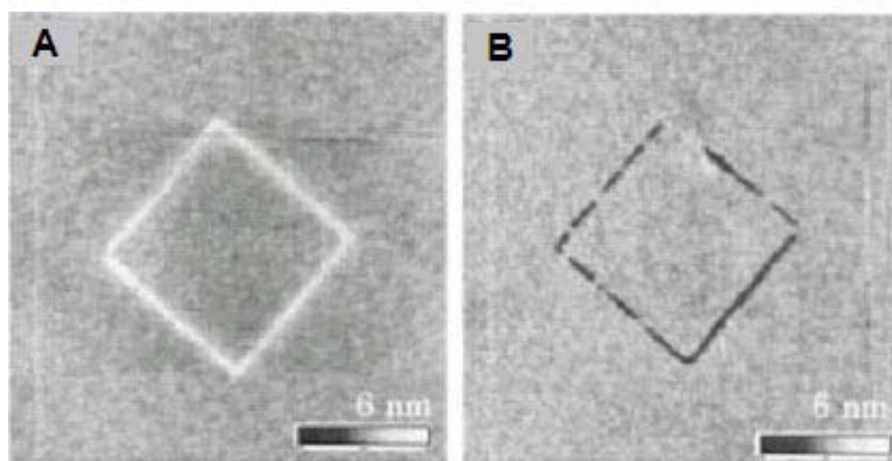


Figure 1.12: AFM images showing a lithographically defined pattern in a palmitic acid LB layer adsorbed to a SiO_x/Si substrate. Diamond pattern with protruding lines was written with -10 V (A), and with grooves written with $+10$ V applied tip bias (B). (z-scale: 6 nm) Reprinted with permission from ref. 121. Copyright 2002 American Institute of Physics.

She *et al.* described the effect of applied force on the groove formation in LB films of OTS on freshly cleaved mica substrates.¹²² All measurements and mechanical modifications were done in 40% to 70% relative humidity at room temperature. The OTS monolayer was removed between applied forces of 400 nN to 800 nN. Forces above 800 nN formed deeper holes, which indicated that the mica substrate was affected. The narrowest lines (50 nm) could be written with a large applied force of 700 nN.

Ara and co-workers used alkyl monolayers covalently bound to silicon as resists for nanolithography.¹²³ Again, this process was proposed to oxidize the underlying silicon as described above. Alkyl monolayers were created by the reaction of 1-alkenes with hydrogen-terminated silicon. The authors showed that these layers could be anodized with an applied bias of +5V. It was pointed out that the voltage necessary for pattern formation was roughly half of that needed for the patterning of alkylsiloxane (alkylsilane) monolayers on silica. The researchers showed that the anodized lines could either be etched away or modified with another alkyl silane. With this technique, letters with a line width of 40 nm were produced.

2.4. Scanning probe lithography with NSOM

Sun *et al.* employed near field optical microscopy (NSOM) to pattern C₁₂S-, mercaptoundecanoic acid (MUA) and mercaptoundecanol SAMs on gold substrates.^{124,125} The light from a frequency-doubled argon ion laser ($\lambda = 244$ nm) was coupled into a fused silica fiber, which had an Al-coated tip with an aperture of *ca.* 50 nm. The fiber was scanned at a distance of 5 to 10 nm above the surface. The UV-light photooxidized the surface bound thiolate molecules to sulfonate species, which were much more weakly bound to the substrate. The patterned surface could either be dipped into a solution with a different thiol, replacing the weakly bound sulfonate from the surface, or dipped into an etching solution for structuring the gold. In one example, the patterned substrate was

immersed into mercaptoundecanoic acid. As can be observed in Figure 1.13, the topography image (Figure 1.13A) showed no difference between the two SAM regions, while the friction image (Figure 1.13B) clearly showed the patterned lines. The line width was 50 nm, corresponding to the size of the probe aperture, which seemed to be the limiting factor for scanning near-field photolithography (SNP). However the size of the gold grains from the substrate also played an important role. Nevertheless, a feature size of 30 nm corresponded to a resolution of ca. $\lambda/9$. It was also shown that it was possible to use the patterned SAMs as an etch mask for the

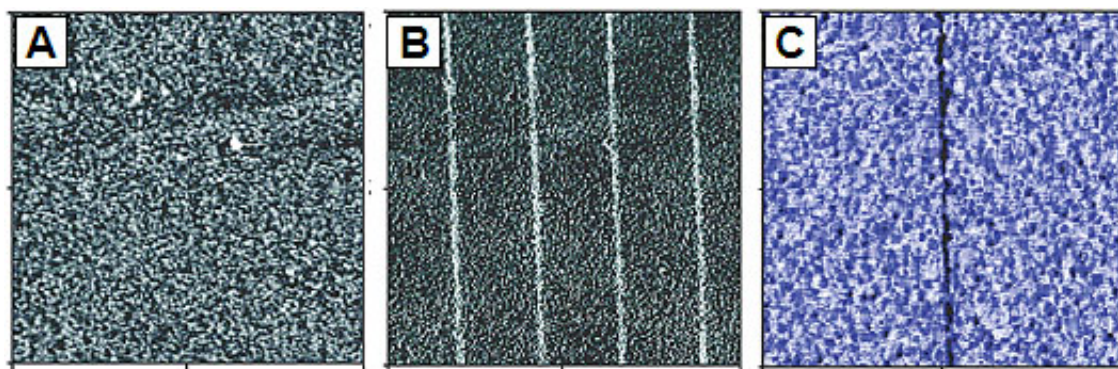


Figure 1.13: AFM images of parallel lines of MUA in a $C_{12}S$ -SAM on gold created by NSOM lithography. (A) A $(1400 \text{ nm})^2$ topography image showed no contrast. (B) A $(1400 \text{ nm})^2$ LFM image showed lines with a width of $50 \pm 5 \text{ nm}$. (lithographic conditions: 0.2 mm/s writing speed, 60 mW laser power) (C) A $(1450 \text{ nm})^2$ LFM image of a 30 nm line of $C_{12}S$ - in a MUA-SAM (lithographic conditions: 1 $\mu\text{m/s}$ writing speed, 20 mW laser power) Reprinted with permission from ref. 125. Copyright 2002 American Chemical Society.

gold substrates. A ferri/ferrocyanide etch solution was used to etch exclusively the part of the SAM that had previously been illuminated. The unexposed regions were resistant to

the etchant. The reaction time for creating structures in the gold substrate was longer than in the case of bare gold suggesting that the oxidized SAM was not immediately collapsing in the etch solution. This optical lithographic technique required the same time frame (scan speed of 200 nm/s) as the AFM and STM type approaches discussed previously. However, it was observed that the scan speed could be increased if an acid terminated self-assembled monolayer was used. It was suggested that the oxidation occurred much faster with this SAM. A disadvantage of the acid terminated SAM was that it had less resistance to etching solutions compared to the methyl terminated SAMs. This behavior was possibly due to less order within the MUA-SAM.

3. Addition Lithography

3.1. Historical Precedent for Addition Lithography

The most natural idea about writing is the application of ink to paper. The class of lithographic methods that are termed addition lithography resembles this process. Prior to the use of SAMs in this scanning probe-based lithography category, various other types of materials were applied to a substrate under the action of a scanning probe. An example is the deposition of copper clusters onto gold from an atomic force microscope (AFM) tip.^{124,125} Moreover, several efforts have focused on the patterning of SAMs via addition using techniques other than scanning probes. These approaches include μ CP,^{51,52,126}

micropens and nanopipettes. In an early example, Lopez *et al.* demonstrated the use of a micropen to create 50 μm wide lines of a C_{16}S -SAM on gold.¹²⁷ More recently, these approaches have been expanded to deposit a wider range of materials. For example, materials deposited with nanopipettes include DNA, proteins, enzymes, reactive gases, etchants and photoresists.¹²⁸⁻¹³⁴

The fundamental scheme behind this type of lithography is diagrammed in Figure 1.1B. To a (nominally) bare substrate, a reactive molecule is applied via some type of pen. In the case of SPL-based lithography, the pen is the sharp tip of an atomic force microscope cantilever. The ink is composed of molecules and a metal or semiconductor surface is the paper. In reviewing this strategy, early papers are described first, and later the types of inks and substrates are treated in kind.

In 1995, Jaschke and Butt reported the creation of aggregates of octadecanethiol on mica by the transfer of these molecules from an AFM tip to the surface.¹³⁵ The authors noted that the deposits displayed a relatively homogeneous height of 1.2 ± 0.3 nm in ambient conditions. However, little control was illustrated in fabricating patterns – irregularly shaped islands were typically deposited. Moreover, the apparent heights measured were too short to attribute them to a well-ordered crystalline SAM. The authors rationalized this appearance by suggesting that these molecules were physisorbed to the substrate resulting in disorder in the observed domains and/or a large molecular tilt with respect to the substrate. Nevertheless, the first lithographically defined pattern (a star shaped

structure) was formed. Notably, these patterns were only obtained on the high energy surface of mica and the authors stated, "...we do not find any deposits on glass or gold." This early report can be seen as the first example of transfer of molecules from a tip to a substrate.

Two years later, Piner and Mirkin published a paper on transport of water to and from polymer and mica substrates as effected and observed by lateral force microscopy (LFM).¹³⁶ The authors concluded that this transport occurred via the meniscus formed between the AFM tip and the sample. At low humidity, water was transported from the tip to the substrate. Under high humidity (95%), water was transported from the surface to the tip. This effect was based on capillary condensation. Although the principal goal of this work was to characterize the effects of water on LFM measurements, the authors recognized that this effect could be used for lithography. Patterns of letters composed of water were written onto a mica substrate under low humidity conditions. After a detailed discussion of the phenomena, it was concluded that the transport of water was a dynamic phenomena and was dependent on humidity, hydrophobicity of the substrate and the dynamics of the tip motion. This work set the stage for the subsequent development of the dip-pen nanolithography technique.

3.2. The Fundamentals of DPN

Dip-Pen Nanolithography (DPN) is illustrated in Figure 1.14 and is performed as follows. AFM tips are ‘inked’ with a material known to self-assemble on a solid substrate. The tip is then contacted to the surface. A water meniscus is formed and the ink, which is adsorbed on the tip, is transferred to the substrate when the probe is held in contact or moved along the surface below a certain linear velocity. The material immobilizes on the surface in a subsequent chemical or electrochemical event. DPN can often use commercially available tips, which are not modified prior to the adsorption of the ink. This technique has been highlighted in several overview articles.¹³⁷⁻¹⁴⁰ Here, the different types of ink, substrate and method are discussed in detail.

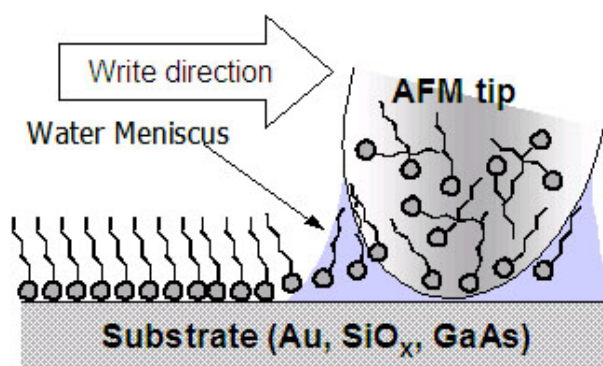


Figure 1.14: Schematic diagram illustrating dip-pen nanolithography (DPN). A tip coated with ‘ink’ molecules was brought into contact with the substrate. A water meniscus formed between the tip and the substrate, which facilitated the transport of the ink to the substrate.

The first report of DPN demonstrated fabrication of organic patterns of dot arrays or lines with thiol-based molecular inks on polycrystalline gold and Au(111).¹⁴¹ Both octadecanethiol ($\text{CH}_3(\text{CH}_2)_{17}\text{SH}$, abbreviated C_{18}SH) and mercaptohexadecanoic acid

($\text{HO}_2\text{C}(\text{CH}_2)_{15}\text{SH}$, abbreviated MHA) were chosen because they were known to create stable SAMs. Patterned features were routinely produced with widths that were less than 100 nm and as narrow as 30 nm. Circular patterns of C_{18}S - and MHA-SAMs on polycrystalline gold were made by bringing the tip into contact with the substrate, the resulting pattern can be seen in Figure 1.15. The size of the dots was dependent on the contact time. Molecular resolution LFM images indicated that the C_{18}S -SAM on Au(111) was densely packed. The use of Au(111) deposited onto mica did suffer some disadvantage. Specifically, it was not possible to draw long (*ca.* micrometer-scale), continuous lines. This problem was attributed to the deep valleys surrounding the small Au(111) facets. On the much rougher polycrystalline gold, contiguous lines could be

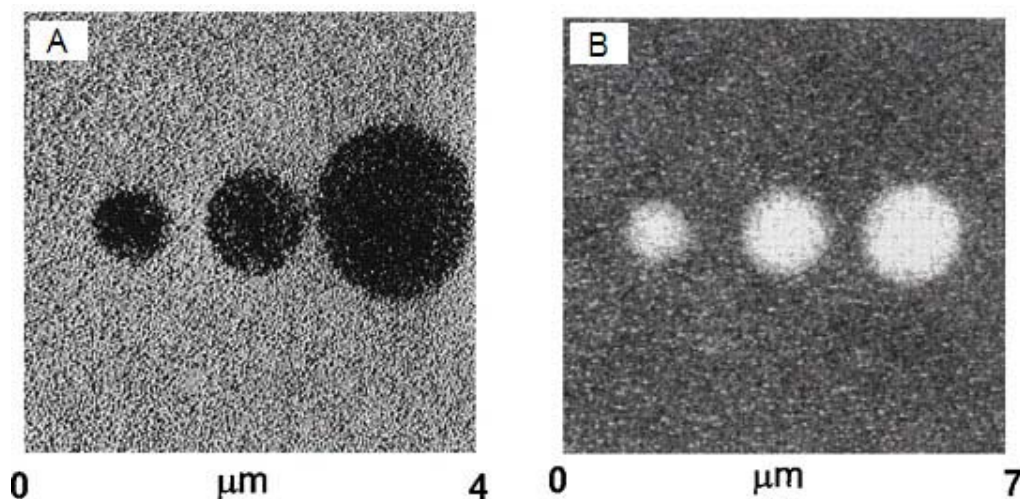


Figure 1.15: LFM images of dots fabricated from (A) C_{18}SH and (B) MHA on a gold substrate by DPN. The contact times were 2, 4 and 16 min, respectively. (45% RH, images recorded at 4 Hz scan rate) Reprinted with permission from ref. 141. Copyright 1999 American Association for the Advancement of Science.

written with micrometer length and 30 nm in width. The line width was dependent on the average size of the grains much as the resolution of an ink pen is dependent on the grain size of the paper.

Humidity plays an important role in DPN. Optimal results were obtained at 30 to 50% RH with a scan rate of 1 Hz. This rate allowed sufficient transport time for the ink to reach the surface. With increasing humidity, the feature size also increased, which was attributed to the change in the size of the water meniscus. A second important parameter was the contact time between the tip and the substrate. Longer contact times (e.g. slow scan speeds) led to larger feature sizes.

An attractive feature of DPN was that the structures could be imaged *in-situ* immediately after the lithography operation to assess the quality of the pattern. The same modified tip was scanned at higher rates (greater than 4 Hz) in LFM mode to provide images showing generally high contrast between the SAM and the Au substrate. Notably, neither different SAMs nor unfunctionalized gold regions can typically be distinguished by contact mode (e.g. normal force) AFM. Thus, friction (e.g. lateral) force is typically used to characterize DPN-fashioned patterns. It was hypothesized that imaging can be achieved without further functionalization of the surface because, during imaging, the tip moves at rates greater than the time required for ink transport from the tip to the substrate. Later, a water meniscus was argued to be responsible for ink transport. This meniscus was

disrupted at a sufficiently high rate of tip travel. A more detailed discussion about this process will follow later in this section.

The second paper on DPN demonstrated the fabrication of nanostructures with multiple organothiols and spatial separation of 5 nm.¹⁴² To achieve these results, registry marks were employed so that when the tip was retracted and re-inked, it could be repositioned close to the previously established pattern. Thus, two molecular inks were lithographically patterned in an area that was defined within these registry marks. Specifically, a second pattern of dots was written in between a pattern of dots with a spatial resolution of *ca.* 15 nm. Another novel demonstration in this paper was the ability to ‘overwrite’ a nanostructure by scanning a tip modified with a second ink over the initial pattern. This procedure had the effect of creating a second SAM around the first with no apparent exchange between molecules in the respective SAMs (as detected by LFM, Figure 1.16) shows the result of this process. Three geometric structures were written using MHA. To backfill around this set of patterns, a tip inked with C₁₈SH was raster scanned four times at *ca.* 12 μm/s (4 Hz) over a scan area encompassing these three structures. The image illustrates the dependence of writing the rate upon the width of the line. By writing each side of the triangle, square, and pentagon at 30 s, 20 s, and 8 s respectively, line widths varying from 80 nm to 30 nm were observed. The image in Figure 1.16 was collected with an unmodified tip to prevent further thiol exchange. The MHA functionalized regions appeared bright (indicating higher tip friction), the ODT

backfill region appeared dark (indicating lower tip friction) and the surrounding ‘unmodified’ gold substrate appeared intermediate in friction.

It has been recognized that the inherent serial nature of SPL results in undesirably slow writing. In an effort to demonstrate a more parallel approach to DPN writing, a linear array of AFM tips (up to eight) were employed.¹⁴³ Two types of writing were

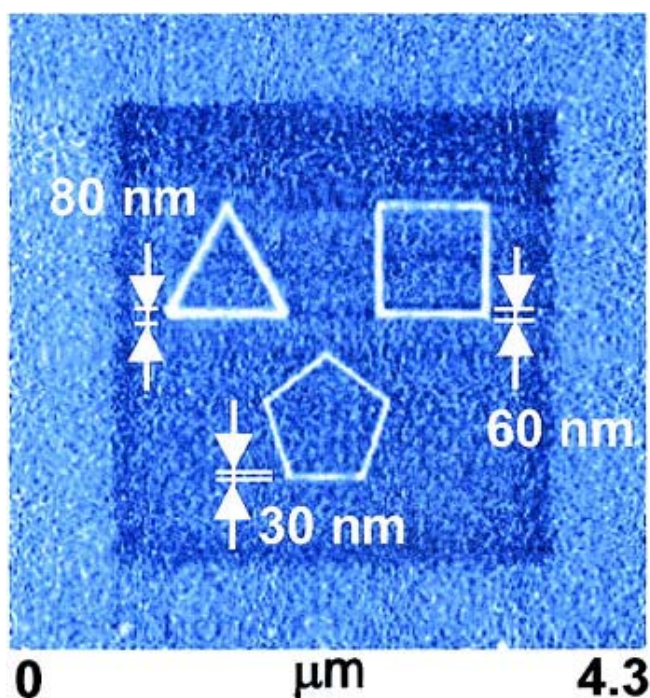


Figure 1.16: AFM images showing polygon shapes written with MHA on an amorphous gold substrate. The writing times per side were 30 s for the triangle, 20 s for the square and 8 s for the pentagon (ca. 0.1 nN force, 4 Hz scan speed, 35% RH). The geometric patterns were overwritten with a (3 mm)² square pattern with a C₁₈SH coated tip (four scans, 0.1 nN, 5 Hz, ca. 35% RH). The polygons showed the highest lateral force contrast, while the C₁₈S-SAM showed the lowest. The bare gold outside had an intermediate contrast. Reprinted with permission from ref. 142. Copyright 1999 American Association for the Advancement of Science.

demonstrated. A set of AFM tips was inked with thiol and simultaneously engaged onto the surface. Using this cantilever array, a set of patterned SAMs was drawn. Each tip drew the same pattern in a region separated, in this case, by several hundred microns from the others. In a second demonstration, each tip was inked with a different molecule. To produce a multiple ink pattern, each tip was used individually in series positioning each subsequent tip in the same region as the first. In both of these demonstrations, multiple cantilevers were obtained by removing several contiguous cantilever-containing segments from a commercially available wafer block. Only the lead tip was monitored with the feedback system to position it, while the others in the array followed in a passive manner. Feedback systems were not found to be necessary for each individual tip because line width and required scan rate for patterning were found to be independent of the tip contact force.

The next advancement in the area of multiple pen DPN was the development of a MEMS nanoplotter with a high density of probes.¹⁴⁴ In this work, linear arrays of tips (up to 32) were fabricated via photolithography. These patterns generated from these linear arrays were nearly identical. The resolution achieved was not quite as high as that observed previously with commercially available single tips. Recently, Zou *et al.* developed a conductivity based sensing technique to control the contact between the tips of a multiple tip array and the substrate. This method used the change in the conductivity between the sample and a metal-coated tip, when the tip contacted the sample surface.¹⁴⁵ More recently, Belaubre, *et al.* developed a technique based on electrostatics to increase the

overall ink loading of biological solutions onto arrays of passivated aluminum cantilevers. The structure sizes generated with these arrays were reported to be on the micrometer scale.¹⁴⁶

DPN has also proved to be an interesting tool for the investigation of monolayer growth and interfacial diffusion using multiple thiol inks.¹⁴³ In one example, the ability of a patterned SAM to corral a second molecular ink was investigated. The fabrication and behavior of the ‘molecular corral’ is illustrated in Figure 1.17. A cross structure

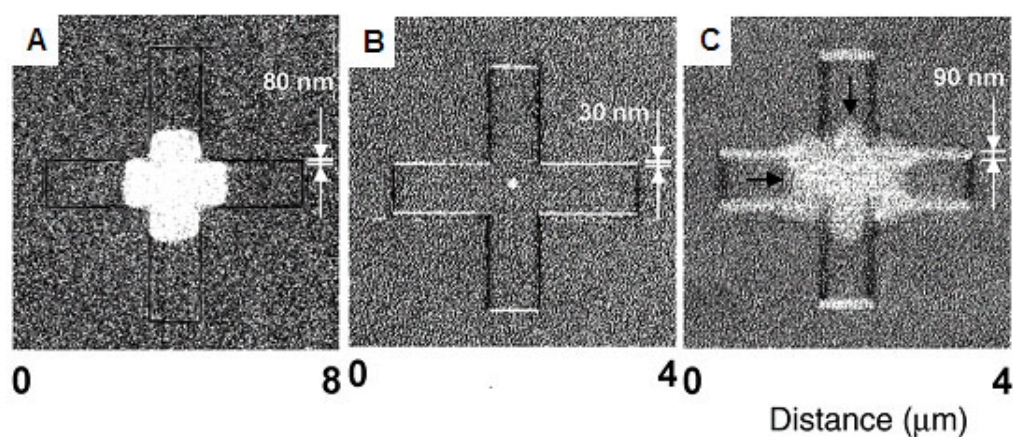


Figure 1.17: LFM images of ‘molecular corral’ patterns consisting of two different inks. (A) A cross-shaped structure where the horizontal and vertical lines were written with $C_{18}SH$. A tip inked with MHA was then brought into contact in the middle of the pattern. The MHA diffused radially and the $C_{18}S$ -SAM lines confined the spreading of the MHA. (B) A cross shape pattern, where the horizontal lines were written with a MHA coated tip and the vertical lines were written with $C_{18}SH$ ink. (C) A tip inked with MHA was brought into contact with the substrate in the middle of the pattern. The MHA diffused radially and could diffuse across the horizontal lines, but not across the vertical lines ($C_{18}S$ -SAM). Reprinted with permission from ref. 143. Copyright 2002 American Association for the Advancement of Science.

consisting of 80 nm wide lines composed of C₁₈S-SAM was fabricated on unmodified gold and a second tip coated with MHA was brought into contact inside the corral, allowing radial delivery of the MHA at the point of contact on the substrate. Figure 1.17A shows that the MHA-SAM was contained inside the barrier created by the C₁₈S-SAM. In a second experiment, a similar pattern was drawn except two inks were used. The horizontal lines of the cross were composed of MHA-SAM while the vertical lines were composed of C₁₈S-SAM (Figure 1.17B). Again, a tip delivered MHA to the center of the pattern, but in this case, the MHA could be observed to diffuse across the MHA-SAM but not across the C₁₈S-SAM (Figure 1.17C). This behavior could be explained in two ways. The C₁₈S-SAM could have hindered the diffusion of the ink, or it could have confined the water meniscus delivering the molecules.

In a second investigation of SAM growth using DPN,¹⁴⁷ a series of LFM images was obtained using an inked tip. By monitoring the change in lateral force over time, the authors were able to make statements about the growth mechanism. The growth of C₁₈S-SAM and MHA-SAM had two distinctly different characteristics. During the growth of a C₁₈S-SAM, small nucleation sites appeared first, grew larger over time and subsequently coalesced. In contrast, during the growth of MHA-SAM, the friction of the scanned region changed nearly linearly as a function of time – no nucleation phenomenon was observed. Molecular resolution images of the resulting monolayers indicated that they were highly ordered and did not show a difference compared to SAMs prepared by solution or gas-phase deposition.

Ivanisevic *et al.* studied the exchange processes between four different molecules/SAMs – MHA-SAM, C₁₈S-SAM, 11-mercaptoundecylferrocenyl SAM (FcC₁₁S-SAM), and 11-mercapto-1-oxoundecylferrocenyl SAM (FcCOC₁₀S-SAM).¹⁴⁸ First, DPN-derived patterns of each SAM were created on polycrystalline gold and exposed to a solution of C₁₈SH. This molecule was observed to exchange both FcC₁₁S-SAM and FcCOC₁₀S-SAM within a matter of seconds to minutes, respectively. This result could be rationalized based on the lower packing density of these two SAMs as the result of the bulky ferrocenyl head groups.

To get a better insight, the exchange process was also performed under continuous scanning with a thiol ink coated AFM tip. The chemical structure of the molecules influenced the rate of exchange, but the size of the structure was also found to be important. Larger regions exchanged more slowly than smaller regions. This result was interpreted to suggest that exchange took place mainly in defect sites of the SAM (i.e. boundaries). A smaller region had a greater percentage of the SAM at boundary sites. Because exchange was observed mainly at the set boundaries, they were presumably less ordered than the center of the region. If the experiment was carried out with a tip coated with MHA, similar results were observed. Based on the relative ability to exchange one thiol for another, it was concluded that the overall relative stability of the SAMs could be ranked as MHA-SAM > C₁₈S-SAM > FcCOC₁₀S-SAM > FcC₁₁S-SAM. If the substrate was changed to Au(111), the exchange process was found to be much slower and could

be nearly neglected. Even after nine hours of continuous scanning over a C₁₈S-SAM with a MHA coated tip, the dot diameter was reduced only by 12%. Thus, the stability of a SAM was strongly dependent on the quality of the substrate.

Partial electrochemical desorption at the edge of DPN-generated SAM patterns was used to reduce the dimensions of DPN patterned features.¹⁴⁹ In this case, a pattern of MHA-SAM was written, the substrate was mounted in an electrochemical cell, and the gold surface was used as the working electrode. By applying a potential of -750 mV vs. Ag/AgCl, the structures decreased in size. The potential was an important factor for the control of this process. The regime between -750 mV and -800 mV was found to be optimal and the rate of shrinking was very controllable and linear with time. With a less negative potential, no change in the size was observed. The electrochemical desorption process started on the outside of the features, considered to be defect sites (due to lower order). The smallest feature size fabricated on polycrystalline gold reported was 30 nm. Such feature sizes were otherwise difficult to achieve (without desorption). This electrochemical shrinking method did not appear to alter the structural integrity of the SAM. Upon exposure to a gold etchant, the shrunken and unmodified SAM features resisted etching.

Additional papers have reported the use of DPN to create etch masks with SAMs.

Weinberger *et al.* patterned C₁₈SH on gold evaporated onto silicon (e.g,

Au/Ti/SiO₂/Si(100)).¹⁵⁰ The pattern was used as a resist against gold etching for a

subsequent anisotropic HF etch that patterned the underlying silicon. Mirkin and co-workers showed that it is possible to create large, nearly homogeneous arrays of dots.¹⁵¹ DPN patterns were written on Au/Ti/SiO_x/Si using MHA ink and the unprotected gold was etched away using ferri/ferrocyanide etchant. An array of 40,000 dots with a diameter of 50 nm and a spacing of 100 nm was produced. In addition, nanogaps between 12 and 100 nm wide were also fabricated. Because of diffusion of ink on the surface, these gaps were smaller than would be accounted for by the positioning of the tip. Recently, Zhang and Mirkin extended this etching process to Ag and Pd surfaces, observing that ODT was the superior resist for Pd substrates.¹⁵²

3.3. Variation of the Ink and Substrate

The first DPN investigations employed thiol-based inks and gold substrates. However, the technique is not limited to this system. DPN has been employed with other ink and substrate combinations. Ivanisevic and Mirkin reported the use of DPN to write lines on semiconductor (silicon and gallium arsenide) substrates using disilazane molecules as inks.¹⁵³ Two potentially important features of disilazane inks were highlighted compared to trichloro- or trialkoxysilanes. First, they did not polymerize appreciably in the water meniscus. Second, the secondary amine base functionality within them catalyzed the chemisorption of the molecules to the substrate. The authors observed that patterning on these semiconductor surfaces required much longer time periods to produce similar sized

structures than the thiol/gold systems under similar conditions. However, a slight temperature increase, generated from a fiber optic light, was observed to increase the rate. The authors attributed this faster patterning rate to contributions from increased ink diffusion or the increased reaction kinetics of disilazanes at elevated temperatures. Pattern features as small as 50 nm in width were obtained. Silane structures on Si/SiO_x were purportedly resilient to three successive acetonitrile washes, suggesting that they were irreversibly chemisorbed to the substrate.

Since this aforementioned report, researchers have demonstrated the ability to reduce the degree of silane polymerization in order to pattern these precursors on silica substrates. Collier and co-workers were able to immobilize fluorescently labeled Cy3-streptavidin via covalent attachment of biotin on glass substrates.¹⁵⁴ To do this, they patterned a silane with a pendant thiol group (3'-mercaptopropyltrimethoxysilane (MPTMS)) that would not interfere with the silane anchoring group, yet could be used to conjugate a biotin-maleimide group for further surface chemistry. To decrease the degree of silane polymerization during patterning, silane inks were vapor deposited onto the tip under anhydrous conditions, while patterning occurred at a carefully controlled relative humidity (22%), and temperature (22–23 °C), and negative cantilever force constants (-0.04 nN). Under these conditions, line widths of 110 nm were achieved. Notably, larger relative humidity (25–30%) gave much poorer results, presumably due to the formation of disordered polymeric films. Above 30%, adhesive forces between tip and substrates made silane patterning impossible. When patterning dots, it was observed that there was

no dependence of dot size with contact time at RH of 22%, presumably due to cross linking of the silane ink that occurred in the inherent thin water film on the surface which limited the isotropic diffusion of the pattern. However, at *ca.* 0% RH, dot size increased with contact time, but caused irregular dot patterns. The researchers also showed that fluorescently tagged streptavidin could be immobilized to biotin conjugated through maleimide groups to the surface in fluorescent images.

A number of inks that represent increasing chemical diversity have subsequently been employed with the DPN technique. The direct writing of modified oligonucleotides has been illustrated with a pattern resolution of 50 nm on Au and silicon substrates.¹⁵⁵ On gold, various oligonucleotides functionalized with a hexanethiol linker were employed as inks. Writing of oligonucleotides on silica was accomplished by first preparing a thiol-terminated surface by reacting the silica with mercaptopropyltrimethoxysilane. Then, oligonucleotides functionalized with acrylamide moieties were applied to the surface as ink. The acrylamide underwent Michael addition with the thiol-terminated surface to covalently attach the oligonucleotides. It was also noted that in order to achieve the physisorption of the oligonucleotide inks to the tip, it first had to be coated with a hydrophilic silane.

After writing patterns of oligonucleotides, the non-patterned area of the array was passivated with C₁₈SH (for gold) or buffered acrylic acid monomer (for silica) to hinder nonspecific binding. The biological activity was confirmed by exposure of the structures

to a solution of complementary and non-complementary fluorophore labeled DNA. Only the fluorescent signal of the complementary DNA was observed via fluorescence microscopy after washing. The hybridization was also performed with complementary oligonucleotides attached to gold nanoparticles. In this way, the authors fabricated arrays of dots that were 1.6×10^5 times smaller than conventional micro arrays. In an area of $100 \mu\text{m} \times 100 \mu\text{m}$, *ca.* 1.0×10^5 nucleotide spots could be formed on a timescale comparable with known micro-robotic spotting procedures.

This work also demonstrated a multiple ink experiment. Two oligonucleotide inks were patterned on silica as described above. This surface was then exposed to DNA-conjugated gold nanoparticles that contained two labels. Each type of DNA was labeled

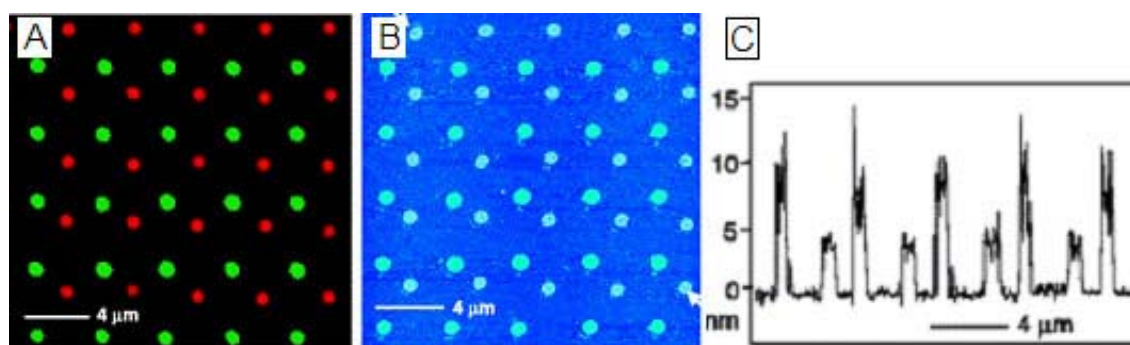


Figure 1.18: Direct patterning of two different acrylamide-modified oligonucleotide inks by DPN. The DNA was hybridized with their complementary ssDNA, which had different fluorescent labels (Oregon Green 488-X and Texas Red-X). (A) A combined green-red epifluorescence image. (B) Tapping mode images of hybridized ssDNA attached to a AuNP (5 and 13 nm diameter) to the same array structure. (C) The section analysis corresponding to both nanoparticle patterns (start and finish is indicated by arrows). Reprinted with permission from ref. 155. Copyright 2002 American Association for the Advancement of Science.

with a fluorophore. Moreover, the nanoparticles to which each type of DNA was attached were of different sizes. The particles assembled in the expected locations with little nonspecific binding outside the pattern. Fluorescence microscopy showed the expected colors of the complementary fluorophore-labeled DNA (Figure 1.18A). In addition, tapping mode AFM was used to image the array and displayed the two different sizes of nanoparticles in their expected positions (Figure 1.18B & C).

Wilson *et al.* showed that collagen and a model peptide-like collagen could be written on gold surfaces via DPN.¹⁵⁶ The binding of these molecules to gold was facilitated by native cysteine (e.g. thiol-containing) units in the protein/peptide. The feature sizes observed ranged from 30 nm in width to hundreds of micrometers in length. The writing was performed in tapping mode (e.g. non-contact AFM with a resonating cantilever) and not in contact mode as in prior DPN work. This imaging mode was employed nominally because of the soft character of the biopolymer. Closer investigation with tapping mode AFM revealed a helical structure of the patterned molecules on the surface consistent with the structure of collagen. Notably, collagen deposited onto gold from solution did not show this order. The authors suggested that the tip was important in inducing order to the collagen patterns. Moreover, collagen written onto a gold surface displayed biological activity as evidenced by the binding of primary and secondary antibodies.

Stone and co-workers also reported DPN using tapping mode to write patterns of short, cysteine-containing peptides on gold.¹⁵⁷ Interestingly, the drive amplitude of the

resonating cantilever played an important role and had to be increased during the course of writing. This behavior was attributed to depletion of the peptide ink at the terminus of the cantilever – presumably, the increase in drive amplitude facilitated continued transfer of the ink to the probe apex. The peptide employed contained a histidine tag on the C-terminus, and these authors originally attempted to write this peptide onto a commercially obtained nickel nitrilotriacetic acid (Ni-NTA) functionalized slide. However, despite the known propensity of binding histidine tags to Ni-NTA, no deposition was found.

The papers about DPN discussed so far rely on chemical interaction for the binding of the ink to the substrate, but DPN can also be used to apply other inks that do not chemisorb to the surface. This extension has expanded the range of materials that can be patterned. Most of the efforts described below do not employ SAMs. However, as they represent evolution of the DPN technique and as they represent efforts to create chemically well-defined patterns, they are treated here. Noy *et al.* showed that a luminescent dye, fluorescently-labeled proteins and luminescent polymer nanowires could be written onto modified glass surfaces.¹⁵⁸ With a home-built instrument combining AFM and scanning confocal microscopy, the luminescence of the patterns was observed. The line width observed (600 nm) by confocal microscopy was attributed to the limit of the resolution of the instrument. It was suggested that the true line width of the patterns was smaller.

Su and Dravid followed a similar approach employing four different organic dyes (two anionic, cationic and neutral) as DPN writing inks.¹⁵⁹ The idea of using dyes stemmed

from their binding to ionic groups contained within biological materials commonly used in many industrial /clinical applications. All the dyes (rhodamine 6G (R6G), coumarin 6 (C6), acid red 8 (AR8) and fluorescein (FITC)) adsorbed on Si/SiO_x surfaces. This result indicated that a variety of non-covalent interactions played a role in the process. Because the resulting features could be imaged by contact-mode AFM, it was concluded that the dye was bound strongly to the substrate. The neutral organic C6 dye was observed to have the highest rate of diffusion on the surface creating the largest features in the shortest time. The topographic height of these features was larger than the size of the molecules, suggesting that aggregates had formed on the surface. The fluorescence emission was uniform over the pattern indicating that the dye molecules were uniformly distributed. Dot patterns were also formed with C6 and R6G that followed the $t^{1/2}$ dependence with dot diameter, consistent with results previously reported.

McKendry *et al.* used dendrimer inks in DPN for writing on silica.¹⁶⁰ The influence of the molecular weight (e.g. dendrimer generation) and type of functional group within the dendrimer (which interact with the substrate) were varied. The authors showed that with increasing generation the delivery rate to the surface slowed. The number of functional head groups did not appear to influence the results. However, if the functionality of these groups was changed from amine to hydroxyl, the delivery rate was much faster. Lines as narrow as 100 nm were written, corresponding to approximately 20 dendrimer molecules.

Lim and Mirkin also investigated fabrication of patterns of polymers by DPN.¹⁶¹ Negatively charged, self-doped polyaniline and positively charged, doped polypyrrole were patterned on silica substrates that were functionalized to present a complementary charge to that of the polymer. It was also shown that no writing was observed when the surface and the polymer had the same charge. Differential pulse voltammetry confirmed that the patterns imaged by LFM were electroactive polymers. The cathodic peaks matched with the values tabulated in the literature. The kinetics of the writing process was found to be similar for these high molecular weight polymers as for small alkanethiols. The transport rate was proportional to the square root of time ($t^{1/2}$), consistent with a radial diffusion process previously reported.

More recently, proteins have been directly written to various substrates with DPN. Utilizing electrostatic interactions between the positively charged parts of proteins and negatively charged SiO_x , or through the covalent bonding between aldehyde modified SiO_x and amine groups on proteins, Lim *et al.* patterned nanostructures of immunoglobulin-gamma (IgG). In this approach, the cantilevers were first modified with a silane-PEG to inhibit non-specific binding of the protein to the tip.¹⁶² In a similar approach, Lee, *et al.* patterned nanostructure dots arrays consisting of two different proteins (rabbit IgG and lysozyme) proteins to gold surfaces.¹⁶³

The DPN technique has been further extended to involve the deposition of materials concomitant with electrochemical oxidation or reduction. The first example of

electrochemical DPN (or E-DPN) was reported by Li, Maynor and Liu to directly fabricate several types of metal nanostructures on silicon-based surfaces.^{164,165} Patterned materials included gold, germanium, silver, copper, and palladium. In this method, the tip was “inked” with a metal salt and the meniscus at the tip-substrate interface served as an electrochemical ‘reaction vessel’ that limited the area where deposition could occur. By applying an appropriate bias to the substrate, the metal ions dissolved within the meniscus were reduced in the proximity of the tip, creating metallic structures. It was suggested that the native surface oxide present on the silicon wafers was conductive enough to facilitate the completion of the electrochemical circuit required to reduce the precursor ion ink to allow the deposition of the metal. As in all DPN experiments reported so far, the control of relative humidity was essential to maintain the meniscus,

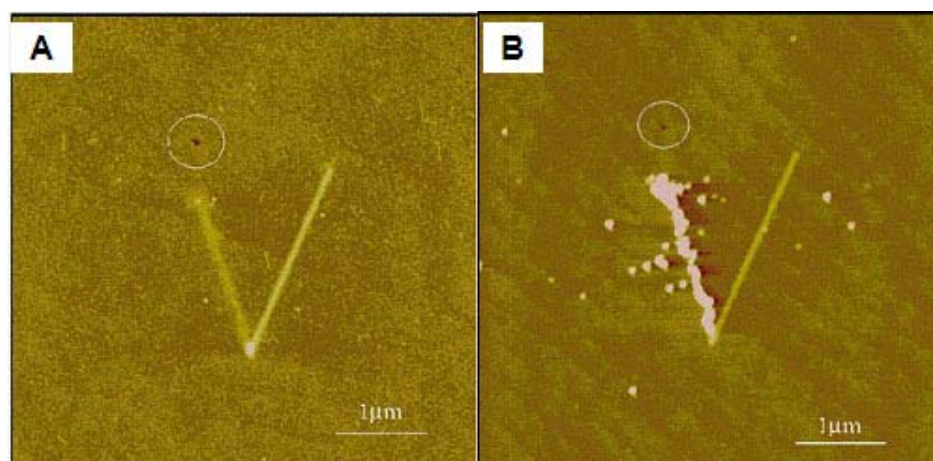


Figure 1.19: (A) AFM image of a ‘V’ shaped structure. The line on the left was drawn by E-DPN of platinum ($V_b = 4$ V, 10 nm/s) and the line on the right was created by anodic oxidation of the silicon substrate ($V_b = -10$ V, 50 nm/s, 58% RH). (B) The same structure after the heating (500 °C) under ethylene in argon for one hour. Reprinted with permission from ref. 164. Copyright 2001 American Chemical Society.

and was kept between 35 and 60% in these experiments. Likewise, the lithographic dimensions were found to be dependent on scan rate and applied bias. To confirm that the lines are composed of metal, the following experiment was performed. The letter “V” was fabricated with a Pt line on the left ($V_b = 4$ V, 10 nm/s) and SiO₂ line on the right ($V_b = -10$ V, 50 nm/s), shown in Figure 1.19A. After elevating the substrate temperature to 500 °C in an ethylene/argon atmosphere, the Pt line showed a large amount of deposited material and the authors suggested that this material was carbon from the Pt-catalyzed thermal decomposition of ethylene. It was further observed that as the metal line melted, it reconstructed into metal spheres (nominally) confined along the original line, while the SiO₂ line was unaffected (Figure 1.19B).

E-DPN was also used to fabricate nanostructures composed of a conducting polymer on silicon substrates.¹⁶⁶ The conductive AFM tip was coated with a monomer reactant (3,4-ethylenedioxythiophene, EDOT) that was soluble in the water meniscus. By applying a cathodic voltage, patterns of conducting polymer immobilized on the substrate were created. In an experiment to confirm that the lines were composed of organic material, a SiO₂ line was drawn (left line) adjacent to a poly EDOT line ($V_b = -12$ V, 10 nm/s, 48% RH; right line), shown in Figure 1.20A. After the patterned lines were treated with 2:1 H₂SO₄/H₂O₂, the polymer line was removed through oxidation, while the SiO₂ line was unaffected (Figure 1.20B). Polymerization on thick (*ca.* 500 nm) thermally grown oxide on silicon was also reported by applying high negative substrate biases (e.g. -130 V). It was hypothesized that the mechanism of polymer synthesis and deposition was caused by

an electric-field-induced polymerization under the high electric field found at the apex of the sharp tip.

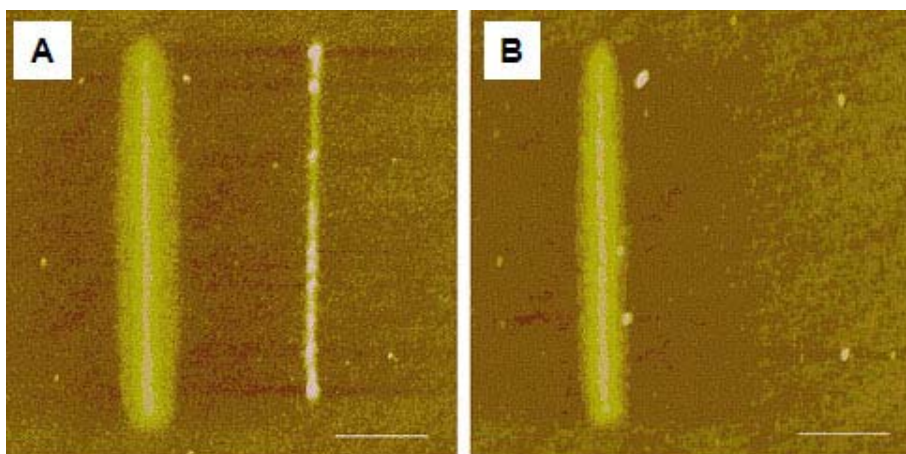


Figure 1.20: (A) AFM image of a SiO_x line on the left and an EDOT polymer line created via E-DPN on the right side. (B) The same patterns after the treatment with a 2:1 H₂SO₄:H₂O₂ solution. The polymer line was removed by chemical oxidation, while the SiO_x line was not altered. Reprinted with permission from ref. 166. Copyright 2002 American Chemical Society.

More recently, Agarwal *et al.* created patterns on nickel surfaces with histidine-tagged proteins and free-base porphyrins via E-DPN in tapping mode. Under a negative tip bias, the nickel surface was ionized and the His-tagged peptide (or porphyrin) ink was subsequently attached to the surface. Optimum delivery was found to occur between -2 and -3 V. Interestingly, it was reported that upon static tip-substrate contact, no radial delivery (i.e. dots structures) of peptide occurred. The researchers found that only a

scanning, negatively biased tip ionized an area in order for the deposition of peptide to occur via histidine binding to ionized Ni.¹⁶⁷

Chilkoti and co-workers have recently developed 'enzyme DPN' that directly patterned enzymes to oligonucleotide SAMs and subsequently locally cleaved the SAM by activating the enzyme with a Mg^{2+} buffer.¹⁶⁸ In a proof of concept report, DNase I (an enzyme that digests double or single stranded DNA into nucleotide fragments) was patterned onto 5'-GGTATACC-(CH₂)₃-SH-3' on evaporated gold surfaces under the relative humidities of 35% to 55% and writing speeds of up to 0.2 $\mu\text{m/s}$. Line widths of 116 nm (fwhm) were obtained, with pattern heights consistent for one layer of the DNase I molecules (3.6 nm). After incubation in a Mg^{2+} buffer solution, the activated enzyme locally digested the oligonucleotide SAM, decreasing the patterned line features by 3 nm (as measured with TMAFM) relative to the background SAM, which was consistent with near-complete digestion of the SAM. It was also observed that the line width of the patterned features increased to more than 100 nm of the originally predigested pattern, indicative of lateral diffusion of the enzyme. Control experiments were performed to confirm the validity of these patterning experiments.

In another report by Liu and co-workers, it was demonstrated that the Au(III) ink could undergo a surface induced reduction on *n*-type Si(100) without an applied potential.¹⁶⁹ The tips were inked from a dilute H₂AuCl₄ aqueous solution, and translated along the surface in a predefined pattern. Unlike previously reported DPN of organic materials, the

same tip was not used to probe the structures immediately after the lithographic operation. The nanostructures were subsequently imaged with a different tip using tapping mode AFM. A line resolution of *ca.* 100 nm was illustrated and found to be dependent on the geometry of the tip, the scan rate, and the relative humidity. A series of experiments were performed to explore the stability of the nanostructures written, and to support that these structures were fabricated of gold. Among these, repeated washing and heating to 300 °C did not degrade the written structures, suggesting that they were not composed of adventitious organics. Heating to 500 °C resulted in the metal structures melting and reconstructing to form spherical shapes confined to the pattern. Resistance to HF etching suggested that the structures were not composed of silicon oxide. In a similar approach by Buriak and co-workers, the same type of writing with HAuCl₄ solution (or a palladium containing salt) was employed to prepare patterns on a Ge(100) surface coated with native oxide.¹⁷⁰ Recently, Fu *et al.* reported patterning a BaFe precursor with DPN on Si/SiO_x substrates, with subsequent post treatment at elevated temperatures, which created ‘hard’ magnetic nanostructures consisting of barium hexaferrite (BaFe₁₂O₁₉). The precursor ink consisted of a mixture of iron nitrate, and barium carbonate in ethylene glycol; the latter solvated and stabilized the inorganic reagents and aided wetting of the hydroxylated SiO_x substrate. The structures were characterized with AFM, magnetic force microscopy (MFM) and XPS.¹⁷¹

Another patterning method that relied on chemical reaction within the meniscus was reported by Su and Dravid in which the direct patterning of organic/inorganic, composite

solid-state nanostructures (SiO_x , Al_2O_3 , SnO_2) was achieved on silicon and silicon oxide substrates.¹⁷² The ink consisted of a metal precursor ($M = \text{Si}, \text{Al}, \text{Sn}$) salt and a commercial block copolymer surfactant. The hydrolysis of metal precursors occurred in the tip – substrate interface meniscus. The amphiphilic block copolymer surfactant was employed to disperse the ink (solution) and increase its fluidity, but also contributed to the mesoporosity of the final nanostructure. The latter mentioned organic moiety could be combusted to create metal oxide mesoporous nanostructures. The metal oxide structures were stable to repeated scanning and remained intact even one month after fabrication. This process was different from the ones described previously because it could be employed on an insulating surface and patterned non-organic surfaces. The speed of the deposition was comparable with the writing of alkanethiols on gold. The nanostructures created have potential applications in the field of catalysis and waveguides due to their large surface areas.

Nanoparticles have also been an alternate ink used in conjunction with DPN has been nanoparticles. Liao *et al.* fabricated patterns of gold nanoparticles on a surface using a nanoparticle solution as the ink.¹⁷³ Specifically, DPN was performed on a silicon surface modified with (3-mercaptopropyl)-triethoxysilane. The ink consisted of citrate capped gold nanoparticles (10 nm diameter) in an aqueous solution. By scanning a predefined area, it was observed that the particles could be immobilized only in the scanned area. A high-resolution AFM image showed that the patterns were composed of loosely packed particles. In a separate effort, Ben Ali *et al.* used an AFM modified with a second

independently controllable tip on a separate nanopositioning stage for the deposition of gold nanoparticles on an insulator surface.¹⁷⁴ One tip controlled by a nanopositioning system was used as the pen, while a second tip controlled by an AFM imaged the structures. By inking the tip with an evaporated nanoparticle solution, the authors showed that they could create small dots (diameters ranging from *ca.* 70 to 200 nm) on the surface with a height comparable to the diameter of the nanoparticles. TEM images were obtained that resolved individual clusters within an island. The solvent and the chain length of the capping ligand on the particles were also found to play an important role for the successful deposition.

3.4. DPN Structures as Templates

An alternative to direct deposition of a material was to employ a DPN-derived pattern as a template. In this way, SAM precursors whose patterning properties were well understood could be used as thethers for more complex materials could be reacted with the pattern in a second, often *ex-situ* step. The first reports using DPN to pattern complex structures such as those consisting of nanoparticles, DNA or proteins often employed this strategy.

Lee *et al.* created protein nanoarrays by DPN.¹⁷⁵ Dot array patterns of -COOH terminated thiol (MHA) were fashioned on gold. The acid sites were designed to be the connection

points for protein and cellular adhesion. The area between the dots was passivated with triethyleneglycol-terminated thiol, known to hinder nonspecific adsorption of proteins on surfaces. In a first step lysozyme, an ellipsoidal shaped protein, was assembled on the dots of the array. No binding was observed in passivated areas on the array, as evidenced in a series of AFM micrographs. In a similar fashion, rabbit immunoglobulin G (IgG) was attached to the array. To demonstrate the selectivity of the binding, this array was incubated in a mixture of proteins that were not expected to bind to IgG. AFM detected no changes in appearance of the array. However, when a similar rabbit IgG array was exposed to a mixture of proteins containing rabbit anti-IgG, the AFM measured a doubling in height (*ca.* 5.5 nm) of the dots in the array, consistent with specific antigen/antibody binding. In another experiment, the adhesion of cells patterned on features was investigated. An array contained dots of MHA with a diameter of 200 nm and spaced by 700 nm. This reduced array size was novel. Prior reports employing patterned surfaces for cell binding were limited to feature sizes larger than 1 μm . This pattern was exposed to a solution containing fibroblast cells and the resulting slides were investigated by optical microscopy. It was observed that the cells only attached to the patterned areas and did not spread. This result showed that sub-micron surface features could promote cell adhesion.

A similar approach pursued by Hyun *et al.* also fabricated patterns of mercaptohexadecanoic acid SAMs (MHA-SAMs) and backfilled around the features with triethylene glycol terminated thiol to hinder non-specific binding.¹⁷⁶ The carboxylic acid

head groups were converted into *N*-hydroxysuccinimide esters (NHS) (with the aid of the coupling agent 1-ethyl-3-(3-dimethylaminopropyl)carbodiimide hydrochloride, (EDAC)), which were active for further binding events. The NHS groups were then reacted with NH₂-terminated biotin or biotin conjugated bovine serum albumin. Fluorescently-labeled streptavidin was subsequently bound to the biotin moieties. All steps were characterized by AFM and fluorescence microscopy. The authors performed control experiments, where it was shown that the binding was specific to the patterned features. No non-specific binding occurred on the NHS-ester patterns or on the passivated background. The reason for choosing the biotin-streptavidin binding strategies was that this was a nearly universal, flexible method and many biotin-linked reagents were commercially available.

Multiple groups have reported attaching cysteine labeled cowpea mosaic virus (cys-CPMV) to surfaces using the highly selective thiol-maleimide reactions. DeYoreo and coworkers demonstrated patterning gold surfaces with an amine terminated, PEG containing SAM precursor employing DPN and nanografting techniques, and subsequently linking/tethering the CPMV viron with 3-maleimidopropionate *N*-hydroxysuccinimide (MPS) linker¹⁷⁷. Smith *et al.* patterned a mixture of two dialkyl PEG containing disulfides inks in arrays of 150 nm dots on gold with DPN. The pattern inks used were a symmetric 11-mercaptoundecyl-penta(ethylene glycol) disulfide (98%) and mixed disulfide substituted with one maleimide group (2%), and the remaining surface was subsequently passivated with 11-mercaptoundecyl-(triethyleneglycol). The

researchers then attached cys-CPMV icosaheral structures and observed height measurement increases in the patterned areas with TMAFM that were consistent with the virus diameter (*ca.* 27 nm).¹⁷⁸

One major effort that has been demonstrated with DPN experiments has been the ability to fabricate patterns of dots or grids to serve as templates for the organization of various types of particles. DPN with functionalized thiol inks was used to generate a pattern with some ‘sticky ink’ on a substrate, which afforded particle binding in a subsequent step. This step was typically followed by passivation of the non-patterned areas with a ‘non-sticky ink’ (generally C₁₈S-SAM) to inhibit non-specific binding of nanoparticle assemblies. Subsequent incubation in a functionalized nanoparticle assembly solution resulted in chemical or physical immobilization of these assemblies on the patterned areas of interest. These architectures have potential applications in the development and study of molecular electronic devices, photonic band gap arrays, biosensors and protein arrays for proteomics research.

In one report, MHA was patterned on gold into dot arrays of varying diameters, the unpatterned areas were passivated, and the sample was exposed to charged polymer beads.¹⁷⁹ The polymer beads were exclusively immobilized on the patterned areas of the substrate. This combinatorial approach enabled the researchers to find the optimum dot diameter that effectively immobilized the particles without significant desorption during rinsing. In another report, magnetic nanoparticles (Fe₃O₄) were attached to templates in a

similar manner.¹⁸⁰ In this paper, the size of the nanoparticle dots could be controlled by changing the contact time of the modified tip with the substrate or by changing the writing speed for the creation of lines. Figure 1.21 shows the change in dot size over the

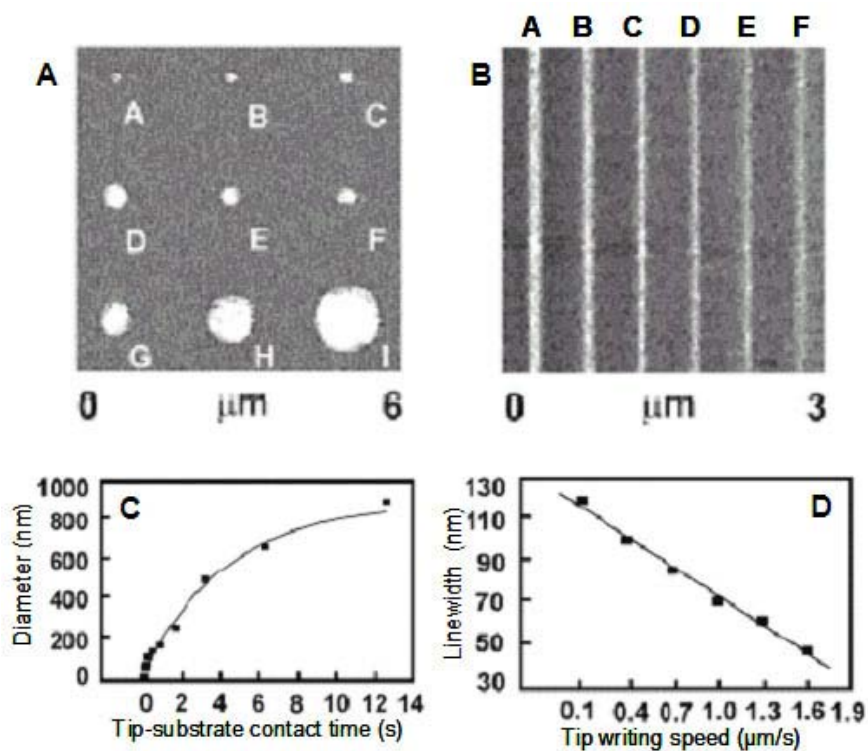


Figure 1.21: AFM topography images of magnetic nanoparticles adsorbed onto MHA patterns formed by DPN and backfilled with C_{18}SH . (A) A dot array fabricated by varying the contact time from 0.05 s (45 nm diameter) to 12.8 s (920 nm diameter). (B) Lines generated with different writing speeds (A: 0.1 $\mu\text{m/s}$ (120 nm) to F: 1.6 $\mu\text{m/s}$ (45 nm)). The images were recorded with a scan rate of 1 Hz. (C) Plot of the MHA dot diameter versus the tip-substrate contact time. (D) Plot of the linewidth of MHA versus the writing speed. Reprinted with permission from ref. 180. Copyright 2002 Wiley-VCH.

tip-substrate contact time and the decrease in the line width with increasing writing speed after the adsorption of the iron oxide nanoparticles.

Orthogonal approaches have also been studied in which multicomponent nanoparticle assemblies were guided to their intended positions with the help of DPN patterned features.¹⁸¹ The procedure (Figure 1.22) began with the writing of an MHA-SAM array on a gold surface. The pattern was backfilled with C₁₈S-SAM in order to prevent non-

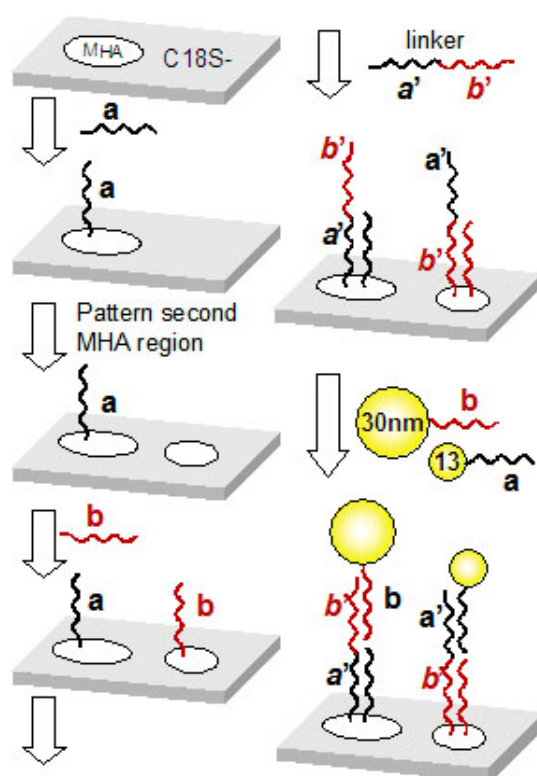


Figure 1.22: Schematic diagram of the orthogonal assembly of DNA nanostructures. In a first step regions containing two different types of ssDNA (strand *a* and *b*) were assembled on DPN patterned regions created from MHA (white ellipsoid). A ssDNA (*a'b'*), where one side was complementary to *a* and the other side was complementary to *b*, was hybridized to the surface. Two different sized nanoparticles (either functionalized with ssDNA *a* or *b*) were bound to this pattern, resulting in regions containing nanoparticles with different sizes.

specific binding. The carboxylic head group was activated with a coupling agent EDAC. A first alkylamine modified DNA was then reacted with the surface (ink *a*). Taking advantage of the fact, that C₁₈S-SAM regions could be over-written (replaced) with MHA, a second set of dots was patterned, activated, and reacted with a different DNA-based ink (*b*). This process created two arrays comprising two distinct oligonucleotide sequences. The surface was then incubated with a linker (*a'*-*b'*) that was partly complementary to strand *a* and *b*. The next step exposed the surface to a solution containing two different sizes of particles (13 and 30 nm), each modified with a DNA (*a* or *b*) structured to bind only to one of the two complimentary oligonucleotide patterns. The results could be visualized using AFM (Figure 1.23). In this way, arrays of two different particles and oligonucleotides were produced.

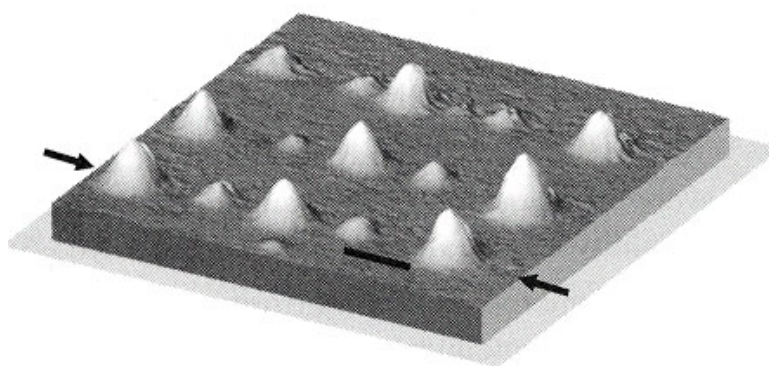


Figure 1.23: Noncontact AFM image of a nanoparticle array assembled by orthogonal SA as described in Figure 1.22. (*z*-scale: *ca.* 40 nm) Reprinted with permission from ref. 181. Copyright 2001 Wiley-VCH.

Another strategy for the orthogonal assembly of oligonucleotide-modified gold nanoparticles on a template surface was performed on gold substrates patterned with ω -functionalized ferrocene (Fc) tagged alkyl and acylthiol inks.¹⁸² These electrochemically active materials had a redox potential difference of 255 mV, allowing for non-overlapping redox processes between the two molecular inks. Appropriate changes in applied substrate potential resulted in oxidation of one or both of the patterned regions. This oxidation (to ferrocinium) made the region positively charged. Subsequent assembly of oppositely charged, polyanionic oligonucleotide coated gold colloids of two different sizes occurred onto the region of interest depending on the applied potential.

Oligonucleotide modified gold nanoparticles did not display non-specific binding on the neutral Fc species, suggesting they did not readily adsorb to non-ionic patterned regions.

Zhang *et al.* described a different approach for the preparation of colloid-functionalized oligonucleotide nanostructures.¹⁸³ DPN was used to generate dot arrays and lines of MHA-SAM on gold evaporated on top of the thermally grown oxide of a silicon wafer. After the patterning with DPN, the unmodified gold was etched away. The bare silica was coated afterwards with *n*-octadecyltrimethoxysilane (OTS) and the MHA was removed by illumination with UV-light. The now bare gold nanostructures were reacted with disulfide-functionalized oligonucleotides. A passivation step with a C₁₈SH solution enhanced the hybridization efficiency and removed non-specifically bound DNA.

3.5. Mechanistic Aspects Underlying DPN

The mechanism governing dip-pen nanolithography is still not fully understood. The importance of water (via humidity in the air) has been cited in most DPN-based demonstrations. Several mechanistic investigations are based on the presence of a water meniscus between the AFM tip and the substrate, and it has been suggested that the water mediates the transport of the ink to the substrate. As there is no obvious way to characterize the size and shape of the water meniscus, its exact role in the mechanism is not specifically determined. The transport of the ink to the substrate is only one part of the DPN process. Assuming a water meniscus is important in the mechanism, the complete mechanistic description must involve desorption of ink molecules from the tip into the water, diffusion through the water, desolvation of the molecules onto the substrate and their simultaneous or subsequent ordering to form a SAM. As will be discussed below, the importance of a meniscus in facilitating ink transport has been debated. In any event, the role of water is likely complex. For example, the way in which hydrophobic hydrocarbons are transferred through the water meniscus and if/how the presence of water on the surface affects the transfer and diffusion of the ink molecules are issues of current investigation.

Theoretical efforts by Ratner and co-workers modeled two important features of the DPN model. The study of the dynamics of ink self-assembly on the surface in DPN was performed through a diffusion model of the molecular ink on the surface. The role of the

tip was described as an infinite source of ink, which avoided the discussion whether a water meniscus is important for the ink transport to the surface.¹⁸⁴ An important issue in this paper was the relative rates of 'ink' diffusion from the source versus diffusion along the surface to an open binding site. Dot patterns were modeled showing that the radii grew proportionate to the square root of tip-substrate contact time ($t^{1/2}$), in agreement with the experimental results. When the tip was moved for the creation of lines, the patterns were dependent on the translation speed of the tip and the deposition rate.

Ratner and co-workers subsequently described a theoretical investigation of the condensation of the water meniscus between the tip and the substrate.¹⁸⁵ A grand canonical Monte Carlo simulation of a two dimensional lattice gas model described the meniscus condensation within the context of tip shape, tip-substrate distance, and tip wettability. A smaller tip radius and a larger tip-substrate distance led to a smaller meniscus diameter, and the instability of the meniscus increased. The smallest meniscus diameter found was 2.3 nm, which may suggest the limit of resolution of DPN. The real resolution limit was suggested to be larger because the effect of surface diffusion during deposition and after tip retraction was not considered. Similarly this group recently expanded their theoretical investigations of DPN to a description of the capillary force cause by the inherent water meniscus between the tip and a flat substrate.¹⁸⁶ The qualitative behaviour was in accordance with experimental data found, but the force was at least one order of magnitude to low, which the researchers explained through the two-dimensional approach. The force was increasing if a three dimensional meniscus was

assumed. Other theoretical efforts by this group determined that the limit of line width formation in DPN could be 5 molecular widths (1.9 nm, one ink molecule wide) with the sharpest tip possible, which was determined by a subtle interplay between vapor saturation and tip substrate distance.¹⁸⁷ More recently, Jang and coworkers used a lattice gas constant model to calculate the capillary force due to the water meniscus for both hydrophobic and hydrophilic tips at various relative humidities.¹⁸⁸ Using a well defined geometry to emulate the AFM, the effects of tip hydrophilicity on the pull off force were simulated.

De Yoreo and co-workers described the effect of dissolution kinetics on feature size with DPN assuming a liquid meniscus was necessary.¹⁸⁹ They proposed a three-step process where thiol molecules dissolve from the tip into the meniscus, diffuse through the meniscus and attach to the surface. Their model predicted the dependency of feature size on dwell (contact) time and tip speed that were in agreement with the measured dependencies. At short contact times, the concentration of thiol in the meniscus was nearly zero and the deposition was dominated by the dissolution kinetics for the detachment of the ink from the tip. For longer contact times, the transfer process of the ink (diffusion) to the surface was the dominating factor.

In contrast, Sheehan *et al.* argued that a meniscus is not important in the DPN writing process by experimentally and theoretically investigating the role of humidity upon surface diffusion of thiol. DPN was conducted at 0% RH and C₁₈S-SAM pattern was

formed under these conditions. It was argued that, in the absence of any humidity in the environment, no meniscus was present.¹⁹⁰ For the theoretical description of the empirical data, a two-dimensional diffusion equation was used. This equation was solved using an analytical approach including a parameter for the kinetics of molecular transport from the tip to the surface. The surface diffusion coefficient for C₁₈SH was determined to be 8400 ± 2300 nm²/s. This value was claimed to be independent of humidity.

In another investigation, Schwartz also concluded from successful DPN patterning experiments at 0% RH, using both C₁₈SH and MHA inks, that a meniscus was not responsible for the ink transport to the surface.¹⁹¹ The modeled molecular diffusion rate was found to be independent of humidity, but the deposition depended on the write speed and the temperature. The author proposed two different diffusion models for the nonpolar C₁₈SH and polar MHA molecular inks.

Mirkin *et al.* most recently investigated the role of humidity in dip-pen nanolithography and presented new experimental evidence for the importance of a meniscus.¹⁹² Two elementary processes were identified: molecular transport from the tip to the substrate via a meniscus (e.g. dissolution of ink and transport through the meniscus to the substrate), and adsorption of the ink on the substrate. These processes were dependent on temperature, humidity, the physicochemical properties of ink and surface, writing speed and the tip-substrate contact force. It was observed that the deposition was still possible if the sample and the tip were kept in 0% humidity for 24 h. To support that a meniscus

was still present under these conditions, two experiments were performed. The first held a tip in contact with a sodium chloride (NaCl) crystal for a certain period of time. The images then obtained on the crystal showed wells whose size was dependent on the contact time and the humidity. Even at 0% RH, a depression was observed. The authors suggested that at 0% RH, residual water on the surface formed the meniscus. If the same experiments were performed under UHV conditions, no changes on the surface of the NaCl crystal were observed. In their discussion the authors assumed that the transport was occurring from the tip to the substrate in the presence of water. Higher temperatures raised the number of solvated molecules, and the diffusion rate in the meniscus and on the surface increased. The patterning process was described as a competition between surface diffusion and solvation of the ink in the meniscus. The adsorption of the ink onto the substrate required displacement of water. At higher humidity, more molecules were solvated because a larger meniscus was formed, however a thicker water layer on the surface was also present that was proposed to impede ink deposition.

4. Substitution Lithography

Substitution lithography involves a process whereby a SAM covers the entire surface both before and after the patterning step. This type of approach has the advantages that all regions retain chemical definition during the entire procedure, and that the behavior of any patterned region installed can be directly compared to that of a “background” SAM

that was not intended to display this behavior. From a semantic viewpoint, several of the papers already discussed could be grouped into this category. In particular, lithographic processes classified as elimination followed by *ex-situ* addition do result in net substitution. However, here, we restrict our discussion to processes that effect substitution in “one pot” without multiple formal steps. Two distinct types of substitution lithography processes on SAMs can be identified. In the first, localized elimination of the SAM occurs by physical or electrochemical means followed by subsequent *in-situ* addition of a different molecule into the exposed surface. In the second, a functional head group is chemically transformed into a different functionality under the action of a probe tip. Each of these types of lithographic processes is treated below in turn.

4.1.Substitution Initiated by Removal of SAM Under Elevated Bias

In the section of this review on elimination, work by the Crooks group was discussed in which a SAM was locally removed under the influence of a biased STM tip. These authors extended this to originate an *in-situ* approach for the formation of metal structures. This procedure involved initial SAM removal followed by electrochemical deposition of a metal from a Pt/Ir STM tip.¹⁹³ Prior to the patterning, the tip was coated with a thin layer of electrodeposited silver metal. The surface of a C₁₆S-SAM on gold was scanned at an applied bias of +400 mV (substrate) without apparent destruction of the monolayer. When the bias was elevated to ca. 3 V, the monolayer and some gold

layers were removed in the scanned area. Subsequent scanning of a larger area around the pattern at a negative bias (−600 to −1000 mV) oxidized the silver at the tip, which was redeposited only in the exposed gold regions. No silver deposition was found outside the patterned region, and the researchers believed that the highly ordered and unperturbed SAM hindered the electrochemical (metalization) process. If the silver patterns were scanned again with a high positive bias, a partial removal of the previously deposited silver occurred. The authors suggested the lithographic scheme was electrochemical because it was dependent on relative humidity. Control experiments with bare Pt/Ir tips at high humidity or Ag-coated tips at low humidity resulted in no significant deposition of silver onto the surface.

An *in-situ* replacement in a SAM of one organic component by another was reported by Chen *et al.* who used STM to replace conjugated molecules into a C₁₂S-SAM on a gold surface.¹⁹⁴ Initial experiments reported creation of pits in a C₁₂S-SAM by moving the tip close to the surface ($V_b = 0.1$ V; $I_t = 0.5$ nA), and applying voltage pulses between 1.8 to 3.6 V. This experiment was performed with a coated tip and the substrate immersed in 1,4-dioxane. The probability for the creation of pits was shown to depend on the amplitude of the pulse and the distance between the tip and the substrate as controlled by the set-point current. The researchers observed that positive voltage pulses had to be used; otherwise mounds of material were created on the surface. They next added a conjugated molecule (2'-ethyl-4:1'-ethylphenyl-4'': 1'-ethylphenyl-1,4'-thioacetylbenzene) and deprotecting agent (NH₄OH) to the solution. STM images showed

that areas originally displaying a depression in the SAM from the elimination step subsequently showed a larger apparent height than the background SAM. This result was rationalized by pointing out that, although the thickness of the SAM composed of the conjugated molecule and the C₁₂S-SAM were nearly the same, the conductivity through the SAM composed of the conjugated molecule should be higher. This two-step patterning could also be done *in-situ* with similar results when the replacement molecule and deprotecting agent were present in solution during the pit formation. The smallest created dots had a diameter of around 10 nm, which was equivalent to the replacement of *ca.* 400 molecules.

The Gorman group has reported a similar approach to a chemically well-defined, scanning tunneling microscope based-lithography.¹⁹⁵ SAMs composed of *n*-alkanethiol on Au(111) were locally removed under the action of a biased STM tip. The mechanism of this removal was argued to be similar to that reported by Crooks *et al.* (as described in the section on elimination lithography⁷³). A low current STM (*ca.* 10 pA set-point current) was employed to minimize the mechanical interaction between the tip and the SAM and replacement was effected under the application of an increased set-point bias (*ca.* 3 V). The removal was performed in a fluid solvating a second ‘replacement’ thiol, which presumably adsorbed to the freshly exposed gold. This approach employed a low dielectric, nonpolar solvent (dodecane, mesitylene) to avoid the use of coated tips that would normally have to be employed to avoid a high leak current (greater than 1 pA) from the tip into the surrounding solution. Avoiding a coated tip eliminated concerns

about the reproducibility of tip coating and potential problems with contaminations from the organic tip coating material. Figure 1.24 illustrates this replacement lithography

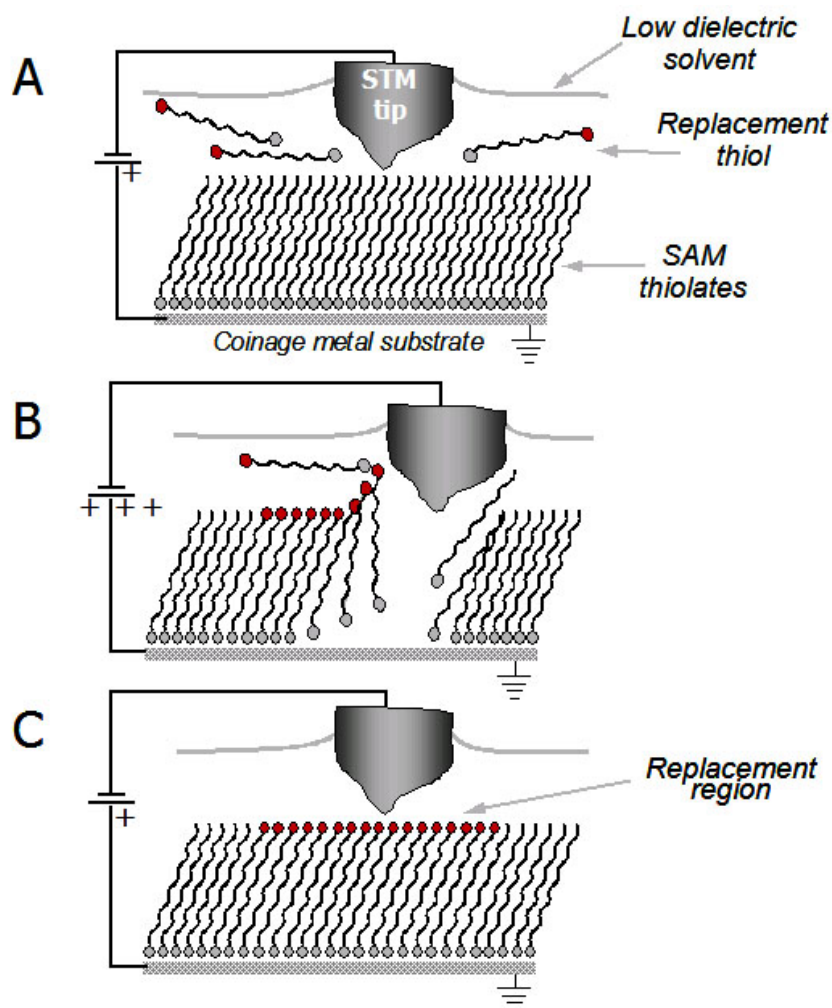


Figure 1.24: Schematic diagram of substitution lithography by elimination and *in-situ* addition. (A) The self-assembled monolayer was imaged with non-perturbative tunneling parameters to locate an area suitable for patterning. (B) Upon change of the tunneling parameters (I_{set} , V_b), the thiolates of the SAM desorbed in proximity of the tip, resulting in removal of the SAM. The replacement molecules in solution assembled into the 'bare' regions. (C) The patterns could be assessed by changing the tunneling parameters to their initial, non-perturbative values.

approach. Under standard imaging conditions (SIC: $V_b = 1$ V, $I_t = 5$ to 10 pA), an appropriate region of the SAM on Au(111) was identified for patterning that was free of terraces or defects (Figure 1.24A). Desorption in the proximity of the tip was effected by elevating the applied bias (positive substrate) to the replacement conditions (RC: $V_b = 3$ to 4 V, $I_t = 5$ to 10 pA, Figure 1.24B). In the presence of a replacement thiol in solution, this region was observed to fill in promptly. After returning to SIC, the pattern could be subsequently imaged (Figure 24C). This technique resulted in patterns with line widths of *ca.* 10 nm.

In a first demonstration of thiol replacement, *n*-alkanethiolate SAM patterns were created composed of regions of different chain lengths. A $C_{10}S$ -SAM pattern was written into a $C_{12}S$ -SAM matrix. The apparent height of the shorter $C_{10}S$ -SAM pattern appeared taller than the background $C_{12}S$ -SAM matrix in the STM images. When $C_{12}SH$ was patterned into a $C_{10}S$ -SAM matrix, the patterned $C_{12}S$ -SAM had a lower apparent height in the STM images. Here, the tunneling gap in fluid solution had a higher transconductance than that of the SAM itself, resulting in a reversal of the apparent heights of these regions compared to those anticipated. This apparent height contrast reversal had been predicted previously by Weiss *et al.*⁹² Relative humidity also was found to play a role in the relative ability to effect replacement. When the humidity of the surrounding atmosphere was below approximately 40%, the set-point voltage required for the replacement increased and the formation of pits in the gold substrate was observed. In the range of 60 to 80% RH the replacement occurred at lower voltages and the pit formation was nearly

completely suppressed. The effect of humidity suggested that the removal of the SAM was electrochemical in nature. A similar conclusion was drawn earlier by Crooks *et al.*⁷³ It was argued that mechanical effects in this process should be negligible because the tip was further away (e.g. higher voltage) from the SAM during replacement than under the standard imaging conditions. The line width of the replaced SAM region was *ca.* 7 nm at full width half maximum, and a spatial line resolution of *ca.* 15 nm was observed.

Replacement lithography was subsequently employed to create SAM regions composed of electroactive headgroups within insulating C₁₂S-SAMs. Investigation of these patterns showed bias dependent image contrasts, and allowed the current-voltage (I-V) behavior of electroactive tip/SAM/substrate junctions to be directly compared against an electroinactive SAM background. Replacement lithography was used to create (400 nm)² patterns of ferrocenylundecanethiolate SAM (FcC₁₁S-SAM) and galvinolphenoxyhexanethiolate SAM (GalC₆S-SAM) within a C₁₂S-SAM background. Notably, the SAM precursor inks employed were ferrocenylundecanthioacetate (FcC₁₁SAc) and phenoxygalvinol-substituted hexanethioacetate (GalC₆SAc) instead of the thiol derivatives. It has been observed that when thiols were used in replacement lithography, a larger amount of adventitious replacement (that is, replacement not stimulated by the action of the tip) occurred at defect sites in the SAM. The mechanistic differences between the use of thiols and thioacetates remain unclear. It is speculated that either a small amount of the thioacetate molecules were adventitiously deprotected

resulting in a low concentration of free thiol, or somehow the elevated bias of the STM tip promoted the deprotection reaction. This work will be discussed in detail in Chapter 2.

Using the STM tip, current vs. voltage (I-V) curves were collected over different regions (e.g. C₁₂S-SAM versus FcC₁₁S-SAM). Within the regions containing a SAM with electroactive headgroups, non-linear I-V curves displaying negative differential resistance (NDR) were measured, while in the regions of C₁₂S-SAM no NDR was observed. This experiment facilitated a direct comparison of the electronic behavior between two different types of molecules (electroactive, non-electroactive) and was, in this regard, an ideal way to investigate molecular structure-property relationships relevant to molecular electronics. The relative transconductance of the electroactive SAM regions increased (compared to the insulating C₁₂S-SAM background) with increased imaging bias. As observed in Figure 1.25, at low bias ($V_b = 150$ mV), the relative transconductance between the FcC₁₁S-SAM and C₁₂S-SAM regions was similar, and the pattern of the electroactive molecules (the letters 'Fc') was almost indistinguishable from the C₁₂S-SAM. At higher applied bias ($V_b = 1000$ mV), the electroactive thiolate pattern had a much higher relative transconductance compared to the C₁₂S-SAM background. It was hypothesized that both the nonlinear I-V behavior and bias-dependent difference in relative transconductance occurred via resonant tunneling through the electroactive ferrocenyl moiety. This work also illustrated sequential replacement with two different

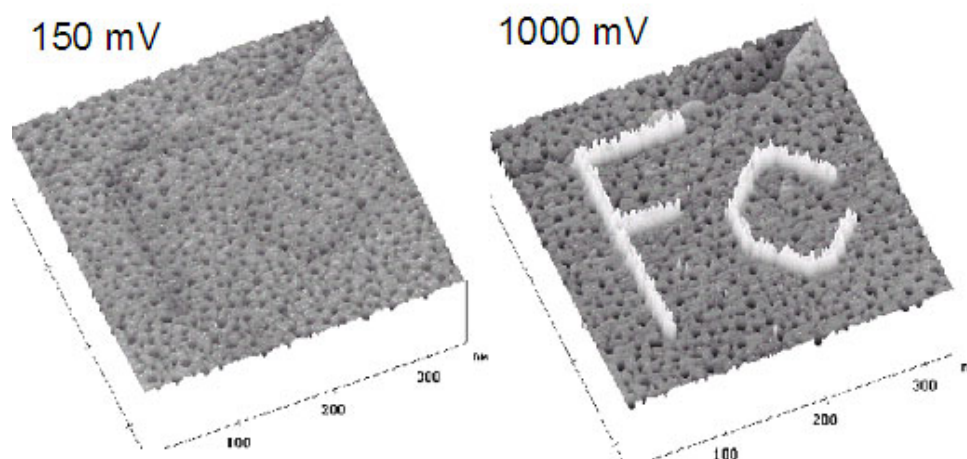


Figure 1.25: STM images showing the bias dependent apparent height contrast of electroactive $\text{FcC}_{11}\text{S-SAM}$ patterned into a non-electroactive $\text{C}_{12}\text{S-SAM}$. At a low bias of 150 mV, the letters 'Fc' were nearly invisible because the two molecules were similar in length. At higher imaging bias (1000 mV), the patterned $\text{FcC}_{11}\text{S-SAM}$ showed a large apparent height contrast compared to the background SAM. (Imaging conditions: $I_{\text{set}} = 10 \text{ pA}$, $z\text{-scale: } 2 \text{ nm}$, scan speed *ca.* 350 nm/s).

thiol inks to compare simultaneously two SAM regions with different electroactive headgroups against a $\text{C}_{12}\text{S-SAM}$ background. This work will be discussed in more detail in Chapter 4. SAMs constructed from these electroactive thiols provided excellent image contrast against a $\text{C}_{12}\text{S-SAM}$ background, and this contrast was employed to correlate various experimental parameters (applied bias, scan rate, and RH) with the efficacy of replacement.¹⁹⁶ It was observed that there was a window of optimal replacement bias for a constant set point current and RH. There was a threshold bias that afforded complete replacement (3.2 to 3.4 V). Below that bias, incomplete or no replacement occurred, while a larger applied bias produced replacement with inconsistent line widths, damage to the surrounding $\text{C}_{12}\text{S-SAM}$ regions and/or etching of the Au(111) substrate beneath the tip. There also was found to be an optimal lithographic scan rate (30 to 50 nm/s) under constant bias (3.2 V) and constant RH (58%). Very slow scan rates (10 to 20 nm/s)

produced inconsistent line widths, and very fast scan rates resulted in incomplete and diffuse replacement.

Using the findings that the manipulation of replacement parameters could affect the degree of replacement, mesoscale chemical gradient structures were fabricated. These structures were created via a systematic variation in scan rate, bias and line spacing (Figure 1.26). The high replacement coverage at one end of the gradient was achieved by a close spacing (e.g. 5 nm) between the scan lines (to overlap replaced lines), a slow scan rate (broad replacement lines) and/or a higher replacement bias (broader lines). The variation in the coverage resulted from the change of one of more of these parameters.

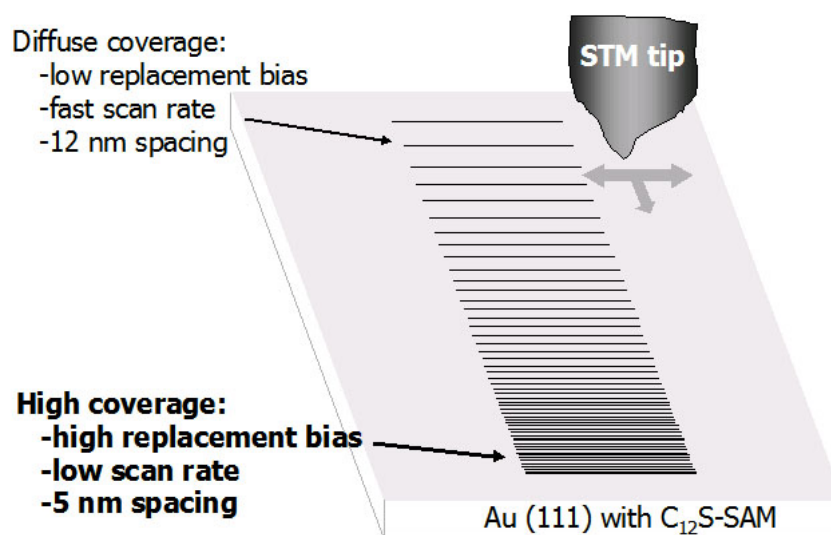


Figure 1.26: Schematic diagram for the fabrication of mesoscale chemical gradients. The diffuse (low) coverage end of the gradient was achieved by a non-overlapping lithographic line spacing (e.g. 12 nm) and low replacement voltage or fast lithographic scan speed. During the patterning of the gradient, the line spacing was incrementally decreased to overlap lithographic lines (e.g. 5 nm), while the replacement voltage was increased or the scan speed was decreased, resulting in high replacement coverage.

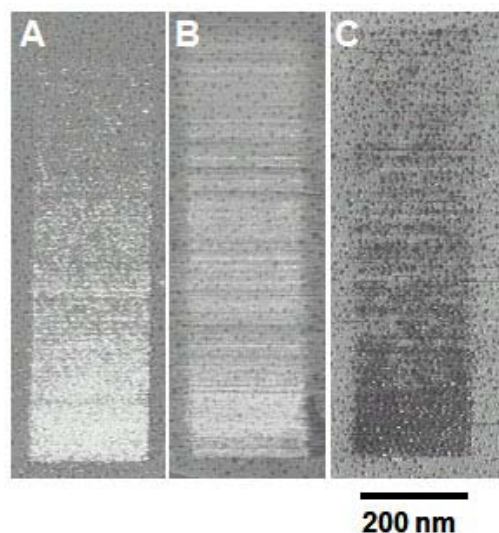


Figure 1.27: STM images of mesoscale chemical gradient fabricated from FcC_{11}SH into a C_{12}S -SAM, either systematically varying the replacement voltage from 2.6 to 3.1 V (A) or the lithographic scan speed from 160 to 20 nm/s (B) (z-scale: 6 nm). (C) A chemical gradient of MUA in a C_{12}S -SAM. The replacement bias was changed from 2.5 to 3 V (z-scale: 2 nm).

The diffuse end of the gradient was created by a combination of increased line spacing faster scan rate and/or lower replacement bias. The chemical gradient structures shown in Figure 1.27 were fabricated by systematically varying the replacement bias (from $V_b = 3.1$ V to 2.6 V, line spacing 4 nm to 12 nm, Figure 1.27A) or the lithographic scan rate (from 20 to 160 nm/s, line spacing 4 nm to 12 nm, Figure 1.27B). Figure 1.27C shows a chemical gradient consisting of mercaptoundecanoic acid-SAM (from $V_b = 3.0$ V to 2.5 V, line spacing 4 nm to 12 nm) and illustrates that gradients could be written with other inks than $\text{FcC}_{11}\text{-SAc}$. This work will be discussed in more detail in Chapter 3.

Another report utilizing replacement lithography demonstrated the novel use of hydrogen bonding to add and remove electroactive functionality from a mesoscale molecular assembly in a reversible fashion.¹⁹⁷ Multi-point, complementary hydrogen bonding recognition elements mediated the assembly steps depicted in Figure 1.28. The host thiol, diacyl 2,6-diaminopyridine decanethiol (DAP), was patterned via replacement lithography into a C₁₂S-SAM matrix on Au(111) from a mesitylene solution (Figure 1.28A). Addition of an electroactive functional moiety through a non-covalent binding event was subsequently achieved by incubation of the DAP-SAM pattern in a solution containing the complementary ferrocene-terminated uracil (Fc-uracil, Figure 1.28B). Subsequent replacement of the electroactive Fc-uracil by a non-electroactive dodecyl uracil “eraser” (C₁₂-uracil) was effected by exposure of the replacement region to a solution of C₁₂-uracil (Figure 1.28C). STM images taken after each step are shown in Figure 1.28D-F. Under an imaging bias of 0.5 V, the DAP replacement region within the canvas C₁₂S-SAM had low apparent contrast (Figure 1.28D). When the DAP-SAM region of the surface was functionalized with the electroactive Fc-uracil, the apparent height of this region increased (Figure 1.28E). This contrast change was decreased with the *in-situ* addition of the C₁₂-uracil ‘eraser’ molecule (Figure 1.28F). The non-covalent host-guest binding events observed in STM images were further characterized on monocomponent SAMs via cyclic voltammetry and XPS.

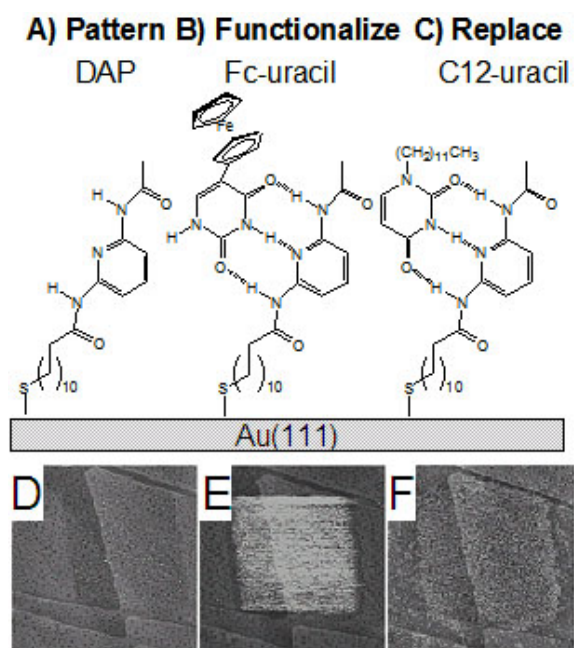


Figure 1.28: Schematic and STM images illustrating multi-point complementary hydrogen bonding recognition elements for the addition and removal of electroactive functionalities. (A) The host thiol molecule (diacyl 2,6-diaminopyridine decanethiol (DAP)) was patterned via replacement lithography into a C₁₂S-SAM. An electroactive functionality was added *in-situ* to this structure through non-covalent binding of a ferrocene-terminated uracil (B). The electroactive functionality could be replaced with a non-electroactive dodecyl-uracil (C). STM images after each of these steps taken at 0.5 V imaging voltage showed the change in the apparent height contrast. The replacement region of DAP had a low contrast (D). After the addition of ferrocene-terminated uracil, the apparent height contrast increased due to the electroactive moiety (E). The apparent height contrast was decreased by adding the dodecyl uracil molecule that replaced the electroactive moiety (F). ($I_{\text{set}} = 10 \text{ pA}$, z-scale: 3 nm) Reprinted with permission from ref. 197. Copyright 2002 American Chemical Society.

A replacement lithography technique employing a current sensing AFM (CSAFM) was demonstrated. The strategy of effecting local removal of a SAM under elevated tip-substrate bias followed by replacement was similar to that described above. The authors reported the replacement of a series of shorter chain alkylthiolate (C₆S-, C₈S- and C₁₀S-) into C₁₈S-SAMs.¹⁹⁸ When the tip was scanned over the canvas SAM with an applied voltage of 4 to 5 V, the replacement occurred. The scanning parameters used were similar

to those employed for the preparation of structures in which the SAM was locally removed without the addition of a second thiol.¹⁰² Topographic images showed height changes smaller than expected theoretically, but the authors speculated this behavior was due to the applied load of the cantilever during imaging. Current images captured at 0.5 V showed the reverse contrast in fluids compared to those in air (similar to that previously observed by our group¹⁹⁵). The edge resolution of the structures was observed to be higher in current mode images than in the topography images. The authors rationalized this result by indicating that the apparent height in the current mode images arose from the exponential behavior of the tunneling current with height. In contrast, a more linear relationship between force and height would be found in topography images. The linear portion of the I-V curves yielded resistance measurements of each patterned area as $(1.8 \pm 1.2) \times 10^{10} \Omega$, $(2.5 \pm 1.0) \times 10^9 \Omega$ and $(2.5 \pm 1.5) \times 10^8 \Omega$ for C₁₀S-, C₈S- and C₆S-SAMs, respectively. These values corresponded well with those predicted from a tunneling model (e.g. exponential increase in resistance with chain length). The exponential distance decay parameter for tunneling (β) calculated based on these data agreed well with previously published values. A final experiment in which C₁₈SH was patterned into a C₁₀S-SAM matrix was demonstrated with a reported topography height difference of *ca.* 1 nm between SAM regions. Current images indicated that the patterned area appeared as a depression, which was expected because the C₁₈S-SAM had a lower transconductance than the C₁₀S-SAM.

4.2. Substitution initiated by removal of SAM via mechanical desorption

The substitution lithography techniques described thus far have relied on the removal of the SAM under an applied voltage. Alternatively, SAMs can be removed by mechanical means followed by *in-situ* replacement with a second component. Mechanical displacement of SAMs with an AFM tip under a solution containing a replacement thiol was developed by Liu and co-workers.¹⁹⁹ Typically, the SAM was first imaged with a low force (smaller than 0.5 nN) in order to find an area suitable for the surface modification, as is depicted in Figure 1.29. Early experiments demonstrated the localized elimination of the molecules of the SAM in solution (2-butanol). This approach was later termed ‘nanoshaving’. When a similar experiment was performed under a solution of a replacement thiol, the blank sites reacted with the thiol in solution and formed a region of

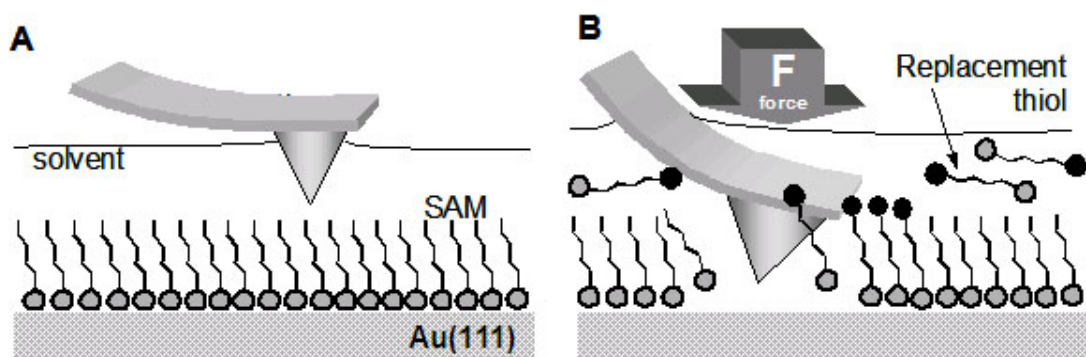


Figure 1.29: Schematic diagram of nanografting. A SAM was imaged with an AFM tip under a non-destructive imaging force to locate an area suitable for patterning (A). With an increased, applied force the monolayer was removed under the tip and the replacement molecules in solution assembled into the ‘bare’ regions (B).

replacement (Figure 1.29B). After patterning, the force was reduced to the initial imaging force, and the structure could be directly imaged with the same tip used for the surface modification. The authors named this replacement procedure ‘nanografting’.

The first nanografting experiments were performed on a $C_{10}S$ -SAM, and patterns consisting of $C_{18}S$ -SAMs were generated (Figure 1.30A & B) with corresponding section analysis (Figure 1.30C). High-resolution images of the canvas (Figure 1.30D) and the replaced region (Figure 1.30E) revealed a very high order with a two-dimensional close-packed structure. This structure was consistent with the well-known structure of monocomponent SAMs formed from solution self-assembly. A multiple thiol ink experiment was also demonstrated in which the solution was exchanged after each fabrication step. In this way, a $C_{18}S$ -SAM line structure was created, subsequently erased by nanografting with the same thiol precursor as the matrix ($C_{10}S$ -SAM), and a third line consisting of $C_{18}S$ -SAM in close proximity to the original nanostructure was written. This experiment illustrated both the fabrication and alteration of structures on the nanoscale.

The rate of replacement and degree of order in the replaced regions was, under some circumstances, observed to be different from self-assembly onto a bare surface. This point was addressed by Xu *et al.* in a comparison of the self-assembly process onto a bare

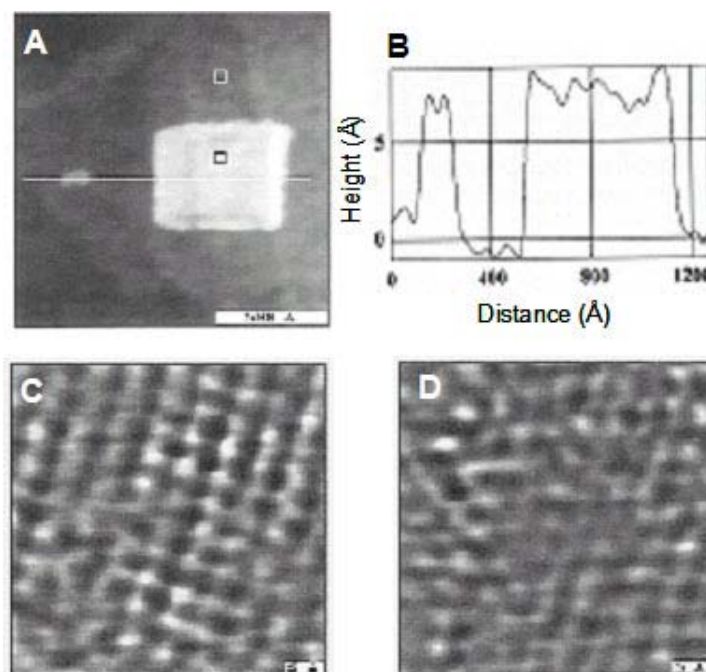


Figure 1.30: (A) Topographic AFM image of two squares fabricated from $C_{18}SH$ in a background $C_{10}S$ -SAM (replacement parameters: 5.3 nN force, imaging conditions: 0.3 nN). The cross section showed that the $C_{18}S$ -SAM was *ca.* 8 Å higher than the background. The edge resolution was 1 nm. Molecular resolution images of the $C_{18}S$ - region (C) and the $C_{10}S$ -SAM (D) revealed a two-dimensional close-packed structure. Reprinted with permission from ref. 199. Copyright 1997 American Chemical Society.

surface with that into nanografted regions using time resolved AFM measurements.²⁰⁰

Here, it was speculated that replacement molecules were spatially confined, having limited area to insert into the exposed gold surface region. The researchers found that the assembly time for the nanografted patterns was at least one order of magnitude faster than the film formation from solution that showed higher order with less defect sites. It was suggested that the more rapid assembly into nanografted regions occurred because a lying-down to standing-up transition found in the reaction on a bare gold surface was avoided. During the first step of thiol self-assembly on gold, a phase was initially

observed where the molecules lie flat on the surface.⁴⁷ At a higher surface coverage (above the saturation coverage of this first phase), a solid-solid phase transition occurred resulting in domains of molecules standing up. Consistent with this observation, nanografted structures formed slowly when their dimensions were larger than the size of the molecules and when nanografting occurred at a rate of scanning that was faster than that of assembly. Conversely, when the dimensions of the nanografted structure were smaller than the size of the molecules and when nanografting occurred at a rate of scanning that was slower than that of assembly, the rate of structure formation was much faster.

Several additional interesting demonstrations have been described to illustrate the range of possible nanostructures that can be created using nanografting. Xu *et al.* used a wide variety of inks with various chain lengths and functional head groups, and showed topography and LFM images of MHA grafted into a C₁₈S-SAM, C₁₈SH grafted into 2-mercaptoethanol-based SAM (HOC₂S-SAM), and HO₂CC₂SH grafted into a C₁₀S-SAM.²⁰¹⁻²⁰⁴ Another example in which two different inks were sequentially employed can be observed in Figure 1.31. Two rectangular nanoislands patterned from C₂₂SH and C₁₈SH, respectively, were created in a C₁₀S-SAM background matrix. In another report, complex patterns and complete sentences were fabricated. These structures were made possible through the combination of vector-scanning probe lithography combined with computer-assisted design.²⁰⁵

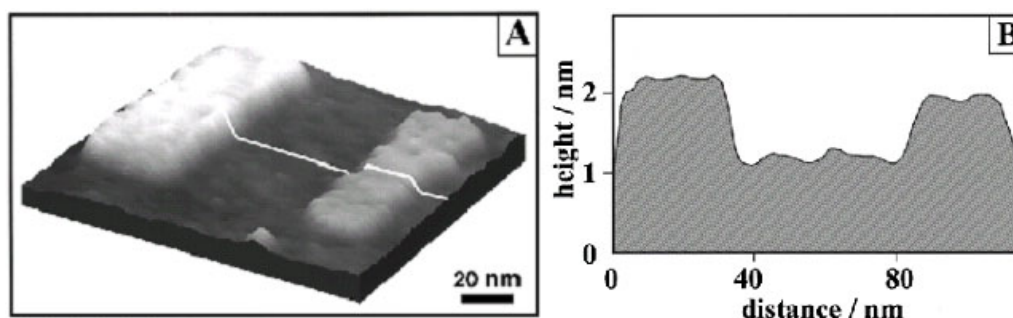


Figure 1.31: (A) Topographic AFM image of two rectangles fabricated from $C_{22}SH$ and $C_{18}SH$ in a $C_{10}S$ -SAM matrix (replacement parameters: 15 nN force, writing speed of 50 ms per line). The corresponding cursor profile is shown (B) and revealed a height difference of *ca.* 1.2 and 0.85 nm for the two different replaced patterns, respectively. Reprinted with permission from ref. 204. Copyright 1999 American Chemical Society.

Another application of nanografting reported was the characterization of the shape of AFM tips.²⁰⁶ Due to the previously mentioned spatial confinement effect of self-assembly in nanografting, the edges of patterned lines were sharp and straight. The observed line profile width was in direct correlation with the shape of the top portion of the tip, and the sides of the line profile represented the shape of the tip.

The nanografting of thiol modified single stranded DNA (ssDNA) has been illustrated by Liu *et al.*²⁰⁷ An 18 or 12 base oligomer with hexanethiol linker was grafted into a hexanethiolate-(C_6S -) matrix under a force of 20 nN and a scan speed of 800 nm/s. The patterns showed a height that correlated with the theoretical height (84 Å for the 18 base and 59 Å for the 12 base oligomer). This observation led the authors to conclude that the DNA SAM region adopted a nearly standing up configuration. The periodicity of SAMs

routinely observed under AFM was not obtained for the ssDNA patterns, leading to the conclusion that the DNA molecules did not form an ordered and close-packed structure on the gold surface. To confirm that the structures were made out of DNA, the authors used an enzyme that cleaved the ssDNA to leave a terminal hydroxyl group. In a time

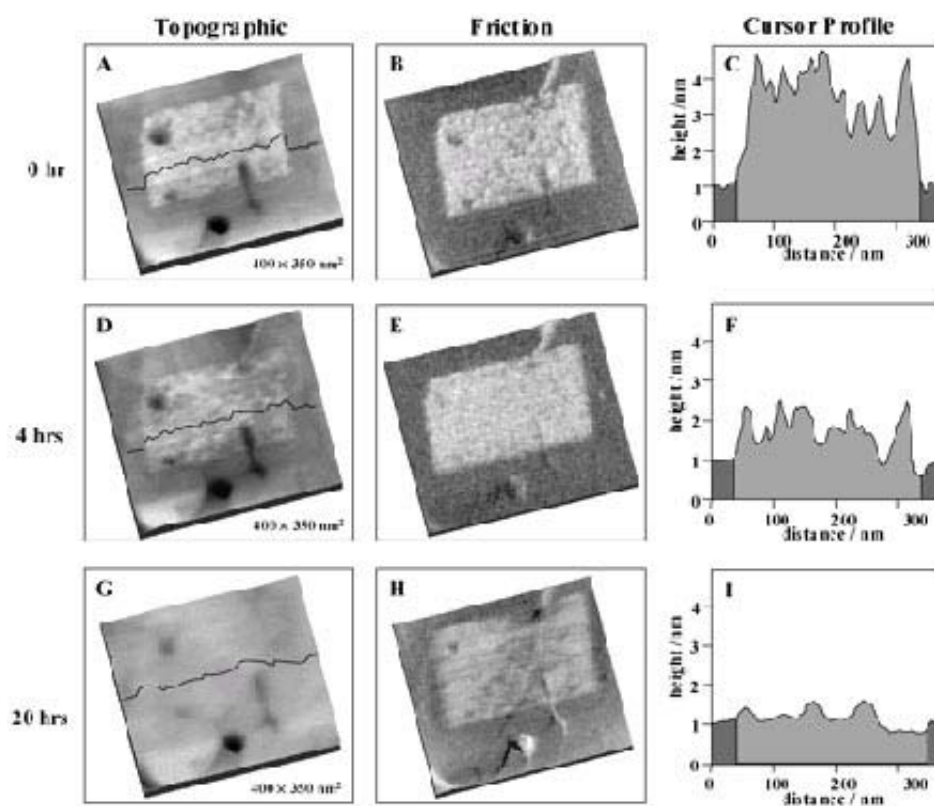


Figure 1.32: Time-dependent AFM images of a $C_{10}S$ -SAM with a nanografted square of hexanethiol-modified oligonucleotide (12 base pairs). After the fabrication of the pattern, the sample was immersed in an enzyme to digest the DNA and imaged. The patterned square was clearly visible in the topography (A) and the friction image (B). The corresponding cross section analysis (C) revealed a height difference of *ca.* 3 nm. After 4 h, the contrast in the topography image was decreased (D), and the friction image showed the same contrast as before (E). The cross section (F) depicted a decreased height difference to *ca.* 1 nm. After 20 h, nearly no difference between the nanografted square and the background SAM was visible (G) & (I), while in the LFM image the square was still present (H). Reprinted with permission from ref. 207. Copyright 2002 American Chemical Society.

resolved AFM experiment, the change in the topographic images was easily seen as shown in Figure 1.32A, D and G (corresponding cursor profiles shown in Figure 1.32C, F and I), while friction images (Figure 1.32B, E and H) showed little difference in appearance (the 3' end of the original oligomer was also terminated in a hydroxyl group). After 4 hours, the initial height was decreased and the density of the ssDNA was lower, which was due to the enzyme cleaving the patterned DNA randomly. After twenty hours, the pattern was nearly invisible in the topography image. The enzyme digested only the DNA, but did not cleave the C–C bond of the linker. The region where the ssDNA had been was still visible in the friction mode because the surface was terminated with a hydroxyl groups, compared to the methyl groups of the background SAM. These experiments showed that the structures were indeed composed of DNA and were accessible to enzymatic reactions.

Case *et al.* designed a protein to bind to a gold surface and employed it in nanografting experiments.²⁰⁸ A tertiary parallel three-helix bundle complexed to iron (on one end) with a D-cysteine residue (on the other) provided a thiol for chemisorption on the gold substrate. By choosing the appropriate buffer, the helicity in the protein was enhanced, resulting in the average height of the protein structures that compared well with the height predicted from molecular models. The authors observed forces applied to the tip that exceeded 40 nN disrupted the grafted proteins and showed a decrease in the measured height. The grafting had to be done under a very slow scan speed, presumably due to the slow diffusion coefficient of the large protein in solution. If the scan speed was

too large, bare gold areas were observed that were slowly filled by the protein, resulting in lower coverage in the nanografted regions.

Amro *et al.* developed an ambient condition technique that combined nanografting and DPN, termed “nanopen reader and writer” (NPRW).²⁰⁹ As an AFM tip coated with a thiol ink (e.g. DPN) scanned the thiolate matrix under an elevated force, it removed the SAM molecules (e.g. nanoshaving), while the molecules from the tip were subsequently transferred into the vacant areas. The factors governing the resolution were the same as those reported for nanografting, and the patterning was independent of the humidity and the texture of the substrate. In a proof-of-concept experiment, a C₁₀S-SAM was used as the matrix and the tip was coated with C₁₈SH. The rectangular pattern of the longer alkyl chain thiolate was created and found to be ca. 8 Å higher than the background thiolates. Other thiols with different chain lengths and functional groups were also described, including CF₃(CF₂)₁₁(CH₂)₂SH, as well as thiols with terminal aldehyde, carboxylic acid, thiol and hydroxyl groups.

Garno *et al.* presented the precise positioning of nanoparticles by nanoshaving with subsequent nanoparticle adsorption.²¹⁰ A second approach with the aforementioned NPRW technique was also employed. During nanoshaving, gold nanoclusters with mixed thiolate shells (dithiol and thiol) were present in solution to fill in the bare gold region exposed as the AFM tip locally removed a C₁₀S-SAM. In contrast to nanografting of thiolate SAMs, the adsorption process of the nanoparticles was much slower. The authors

attributed the slow speed of replacement to the low concentration of the gold particles (AuNPs) in solution (10^{13} /mL AuNPs compared to *ca.* 10^{18} /mL for thiols) and the size of particles, which decreased the rate of colloid diffusion. An AFM image showed a 150×300 nm² area where 51 nanoparticles with an average diameter of 3.8 nm had adsorbed. In the NPRW approach, colloids were physisorbed to the tip prior to patterning. The high-applied force during the writing process resulted in the removal of the thiolate SAM from the substrate and the transfer of the nanoparticles to the substrate. The authors claimed that the writing process was highly selective because the transfer of the particles to the substrate required the removal of the underlying SAM and therefore, required a high-applied load. The reported coverage of nanoparticles in the patterned regions was lower than for a densely packed layer.

Schwartz reported an approach for creating structures of a thiol-modified molecule in a preformed matrix that was termed “meniscus force nanografting”.²¹¹ Thiol-modified DNA was patterned onto a gold surface that was covered with shorter, thiol modified DNA strands. A drop of the patterning solution served to simultaneously wet the hydrophilic resist on the gold as well as the AFM tip. It was argued that the surface tension of this drop supplied enough force for the tip to locally remove the resist allowing the DNA to attach to the gold surface. Narrow line widths (*ca.* 15 nm) and very high linear writing speeds (*ca.* 320 $\mu\text{m/s}$) were featured. These DNA-based nanostructures were then hybridized to a complementary strand that had been grafted to metal nanoparticles, illustrating a complementary self-assembly process.

4.3. Substitution Followed by *ex-situ* Addition to Patterns

The examples discussed to this point involve substitution in which a monolayer-based pattern is the object of interest. Opportunities have been illustrated to exploit the monolayer pattern as a template for the growth or immobilization of another material. Often, this templated growth or deposition is performed in a second, *ex-situ* step. These types of investigations are treated in this section.

Wadu-Mesthrige *et al.* bound the protein lysozyme to nanografted squares of mercaptopropionic acid-based SAM ($\text{HO}_2\text{C}(\text{CH}_2)_2\text{S-SAM}$) patterns surrounded by a $\text{C}_{12}\text{S-SAM}$ matrix.²¹² This binding was from electrostatic interaction between the carboxylate head groups of the SAM region and the protein. The authors noted that in order to prevent non-specific binding of the protein to the $\text{C}_{12}\text{S-SAM}$ matrix, very specific concentrations and incubation times had to be employed. More stable protein patterns could be realized if covalent binding schemes or specific chemical interactions were used. Aldehyde functional groups were suitable for binding of proteins containing amino groups through the formation of imide bonds. Patterns of aldehyde-terminated, $\text{OHC}(\text{CH}_2)_2\text{S-SAM}$ were created in a $\text{C}_{10}\text{S-SAM}$ background, and the protein immunoglobulin G (IgG) was adsorbed selectively in these patterned regions. The researchers showed that at least 50% of the protein remained biologically active as

evidenced by their ability to bind antibodies. By using different molecules for nanografting, the creation of multi-ink patterns expanded the use of this method.

Protein patterns fabricated with various SPL strategies were reported by Kenseth *et al.*²¹³ In the first example, 5 μm MUA-SAM square patterns were nanografted into a C₈S-SAM on gold. Notably, the threshold force for nanografting of this pattern was higher than that reported by Liu and co-workers. The authors attributed this fact to the larger feature size and the faster scan speeds (greater than 20 $\mu\text{m}/\text{s}$). Rabbit IgG antibody was bound to the MUA patterns by a reaction via carbodiimide coupling. The results of this binding was observed in the topography image and cross / line section analysis (Figure 1.33A). Non-

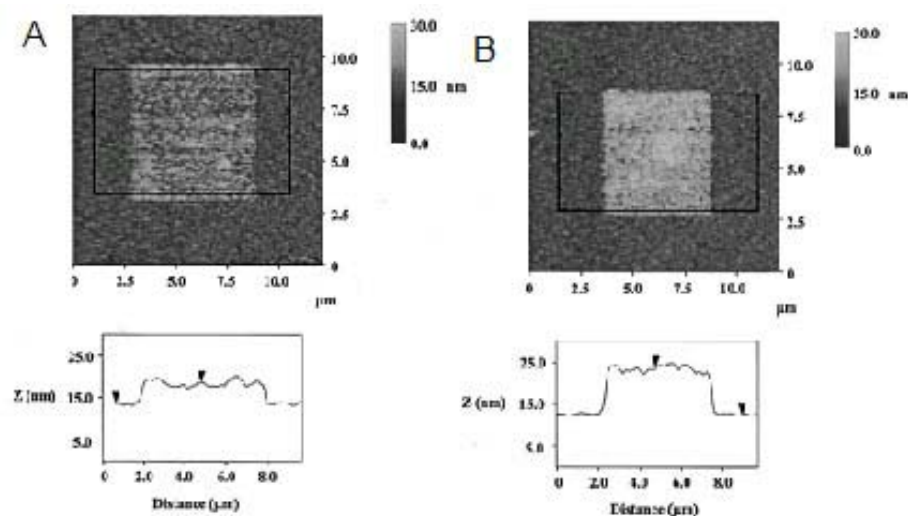


Figure 1.33: (A) AFM topography images ($12 \mu\text{m}$)² of a C₈S-SAM with a square replaced with MUA after the binding of rabbit IgG through a coupling agent (EDC). (B) The same square after subsequent exposure to goat anti-rabbit IgG. The corresponding cross section analysis was an average of the lines inside the box. (Imaging conditions: 2 nN force, 6 Hz, z-scale: 30 nm). Reprinted with permission from ref. 213. Copyright 2001 American Chemical Society.

specific protein binding to the C₈S-matrix was very low and was removed by scanning the surface with a force of 15 nN, which did not alter the covalently bound structures on the surface. The pattern could be further exposed to the complimentary Rabbit IgG antigen (Figure 1.33B). In both cases, measured topography heights corresponded to the expected size of the molecules.

The second technique demonstrated was based on nanoshaving a pattern into a (undec-11-mercapto-1-yl) triethylene glycol methyl ether (EG3-OMe) SAM. The resist layer was scraped away from the gold surface by applying a high force, and indirect (adsorption of coupling agent and subsequent binding of a protein) and direct (adsorption of thiol modified protein) procedures for the attachment of proteins to the gold surface were demonstrated.

Liu's group fabricated three-dimensional nanostructures through nanografting, pursuing two different schemes.²¹⁴ In the first scheme, mercaptoundecanol (MUD) was patterned in a C₁₈S-SAM. The hydroxyl-groups were reacted with the trichlorosilane head group of octadecyltrichlorosilane (OTS) to form a Si-O network. This structure had a larger height than the surrounding MUD-SAM. This type of pattern transfer was termed 'positive'. Conversely, a negative pattern transfer was based on nanografting a C₁₈SH into a MUD monolayer. The sample was then exposed to OTS which self-assembled on the background SAM. In both experiments, the silane layer had a smaller height than it would be expected from the size of the molecule. The authors concluded that the packing

density was not as good as a thiolate SAM, and therefore the bilayer structure was more susceptible to compression from the tip.

Jang *et al.* created small patterns of enzymes by subsequent adsorption of acetylcholinesterase (AChE) to a nanografted poly(ethylene glycol)-containing SAM pattern composed from $\text{HS}(\text{CH}_2)_{11}(\text{OCH}_2\text{CH}_2)_6\text{OCH}_2\text{CO}_2\text{H}$ within a $\text{HO}(\text{OCH}_2\text{CH}_2)_3(\text{CH}_2)_{11}\text{S-SAM}$ background.²¹⁵ The triethylene glycol groups within each SAM region were present to resist non-specific protein adsorption. Small, bare Au patches (termed ‘trapping sites’) were then created by removal of the background SAM via nanoshaving. Acetylthiocholine (ATCh) was added with the intention that the trapped enzymes would cleave this molecule to form thiocholine, which contains a free thiol group. Indeed, after the addition of ATCh, bright spots on the trapping sites were apparent in AFM images consistent with the binding of the thiocholine to these bare gold regions. In a control experiment, it was shown that, if only the trap was created and the surface was brought into contact with ATCh, no change in the surface morphology occurred. These experiments led to the conclusion that the change in the pattern was due to the enzyme.

Wacaser *et al.* used a chemomechanical approach, similar to ‘nanografting’, to simultaneously pattern and functionalize a silicon surface.²¹⁶ A hydrogen terminated silicon surface was immersed into one of three reactive compounds (heptadecafluoro-1-decene, 1-hexadecene or 1-octanol). The mechanical action of the AFM tip was proposed

to facilitate chemical reaction of these compounds with the surface. Figure 1.34 shows SEM and AFM images as well as an AFM section analysis of the same area that had been patterned with heptadecafluoro-1-decene using this technique. The line width achieved depended on the applied force (e.g. a force of 5 μN produced 30 nm wide lines). It was observed from SEM images that a force of 0.25 μN (i.e. AFM imaging force) was nondestructive to the hydrogen-termination layer. Besides lines and squares, the

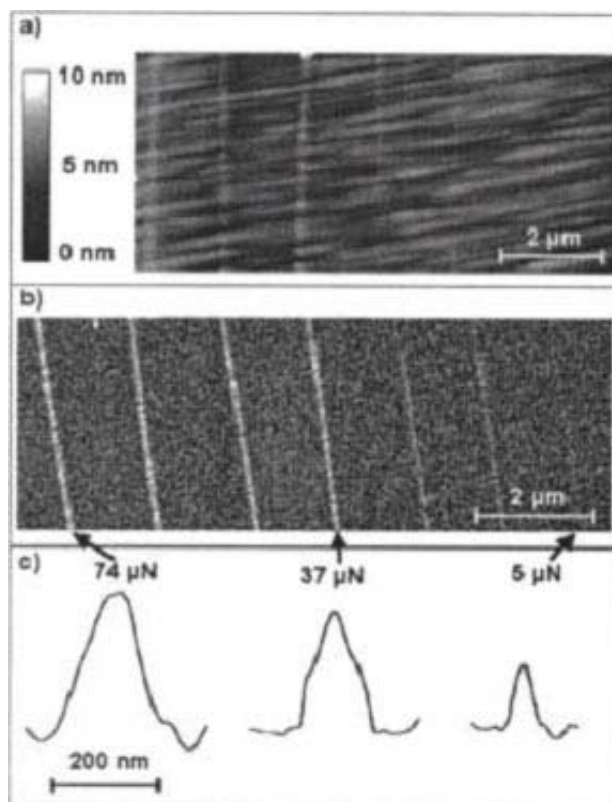


Figure 1.34: (A) *In-situ* AFM (z-scale: 10 nm) and (B) corresponding SEM images of lines written on silicon under the presence of $\text{CF}_3(\text{CF}_2)_7\text{CH}=\text{CH}_2$ with different applied forces (ranging from 74 μN (left line) to 5 μN (right line)). (C) Profiles of three different lines (vertical axis was the gray scale value). Reprinted with permission from ref. 216. Copyright 2003 American Institute of Physics.

researchers also showed that they could write letters. Further characterization of the structures was performed with TOF-SIMS showing higher fluorine content and lower signals from Si-H⁺ and Si⁺ in the patterned areas. Thus, by using the AFM probe to break Si-H and Si-Si bonds in the presence of reactive molecules chemical patterns could be created.

4.4.Substitution via Tip-Induced Terminal Group Modification

A second classification of substitutive lithography involves the chemical modification of the terminal functional headgroup of the SAM. This type of modification has been stimulated by both mechanical and electrochemical means. In these approaches, it was intended to maintain the structural integrity of the SAM throughout the process. This approach has allowed the fabrication of multi-layers through subsequent iterative addition processes, or the immobilization of functionalized particles to the locally modified SAM.

Marrian, Calvert and Perkins employed an STM tip in UHV (10^{-7} to 10^{-8} Torr) as a low energy e⁻-beam lithography source to chemically modify amine terminated organosilane resists on silicon covered with native oxide.²¹⁷ Unlike conventional e⁻-beam lithography, the STM was an attractive alternative because it could generate low energy electrons (smaller than 50 eV) with a beam diameter on the order of 10 nm. After the high-

resolution e^- -beam lithography (Figure 1.35A), the samples were treated with an aqueous Pd^{2+} catalyst solution (Figure 1.35B), followed by *ex-situ* incubation in an electroless Ni plating bath (Figure 1.35C). The Pd^{2+} catalyst bound only to the non-exposed areas and the Ni was selectively deposited in these regions. The authors assumed that the amino groups were locally deactivated, eliminating their affinity for the Pd^{2+} complex catalyst that promoted electroless plating of Ni films. Two different organosilane resist layers were patterned by applied tip biases of -4 to -35 V (scan rates of 0.2 to 2 $\mu\text{m/s}$). One

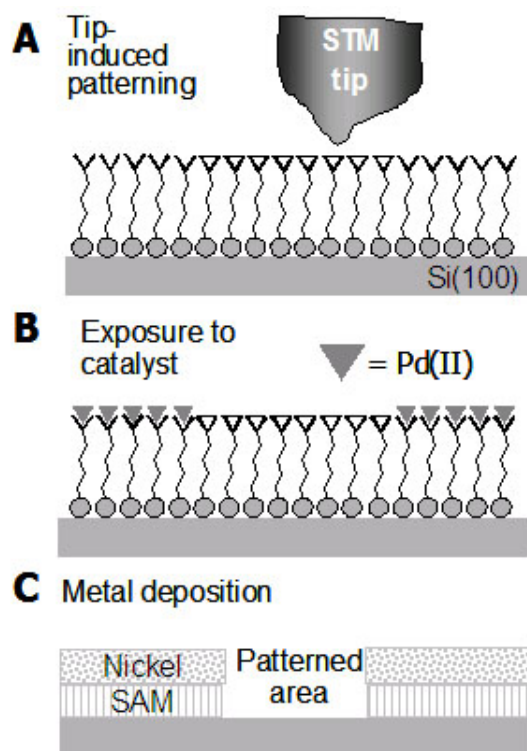


Figure 1.35: Schematic diagram of ligand based substitution lithography. (A) The functional head group of the SAM was altered with a STM. (B) A Pd catalyst reacted with the non-exposed area of the sample. (C) The electroless Ni plating procedure led to metal growth outside of the STM pattern.

resist terminated with a functional amine head group, aminoethylaminomethylphenethyltrimethoxysilane ($\text{NH}_2\text{-(CH}_2\text{)}_2\text{-NH-CH}_2\text{-C}_6\text{H}_4\text{-(CH}_2\text{)}_2\text{-Si(OCH}_3\text{)}_3$, PEDA), was reported to have a patterning threshold voltage of -8 V. The second resist, 4-chloromethylphenyltrichlorosilane ($\text{Cl-CH}_2\text{-C}_6\text{H}_4\text{-SiCl}_3$, CMPTS), was reported to have a threshold bias of -4 V. CMPTS contained no ligating amino group and had to be treated after patterning with a grafting agent (lithium ethylenediamine, Li-EDA) to install an amine functionality. For both silanes, larger exposure voltages were explored (more negative than -35 V), but were observed to increase feature sizes. The smallest created metal features were *ca.* 30 nm wide. The resolution of the metal pattern was not limited by the lithographic step itself. Electroless plating of Ni caused the growth of grains with diameters of *ca.* 30 nm. A later report extended the work to octadecyltrichlorosilane (OTS) as a resist.²¹⁸ The patterning threshold using OTS was -10 V, and patterns could also be transferred into the underlying substrate by wet etching techniques. The PEDA resist was later used on hydrogen passivated silicon and improved the resolution to 15 nm.²¹⁹

Clausen-Schaumann *et al.* functionalized an AFM tip with an enzyme and used this to locally hydrolyze a phospholipid in a bilayer. The AFM tip was functionalized with the enzyme phospholipase A_2 and was used to create patterns in a dipalmitoylphosphatidylcholine (DPPC) bilayer supported on a gel. A line resolution of *ca.* 100 nm was achieved. It was suggested that the mechanical pressure of the AFM tip induced defects in the bilayer to allow entry of the enzyme molecules.²²⁰

An AFM tip coated with a catalyst can also be employed to induce a localized chemical reaction at the terminal functional groups of a SAM. Müller *et al.* illustrated how the azide-terminal groups of a monolayer ($\text{N}=\text{N}=\text{N}-\text{R}-\text{Si}-\text{O}-$) on glass could be locally reduced to amino groups using a Pt coated AFM tip as a catalyst.²²¹ This reaction occurred without any applied potential between the tip and substrate. To facilitate the hydrogenation of the azide groups, the lithographic pattern was performed in hydrogen-saturated isopropanol, and patterning was performed under a force of *ca.* 400 nN with a scan speed of 1 $\mu\text{m}/\text{s}$. By exploiting the reactivity between amino groups and aldehydes, fluorescently-labeled latex microspheres functionalized with aldehydes were immobilized in the patterned areas of the

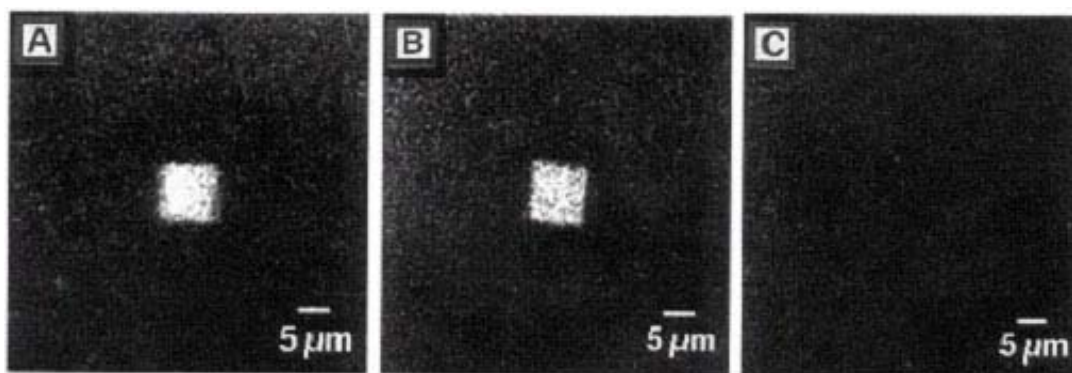


Figure 1.36: Fluorescence micrographs of a SAM with terminal azide groups after patterning under different parameters. (A) A nominally $(10\ \mu\text{m})^2$ square area was written with a Pt-coated tip in hydrogen-saturated isopropanol and subsequently modified with fluorescently modified latex beads. (B) A square fabricated as in (A) but modified with ATTO-TAG reagent. (C) A nominally $(10\ \mu\text{m})^2$ area scanned and modified under the same conditions as (B) but with a unmodified silicon tip. Reprinted with permission from ref. 221. Copyright 1995 American Association for the Advancement of Science.

of the amide groups with 3-(2-furoyl)quinoline-2- carboxaldehyde (ATTO-TAG) was SAM with little non-specific binding (Figure 1.36A). In a second example, the modification illustrated. This compound was not fluorescent by itself, but after the binding to primary amines, the highly fluorescent isoindiol was formed (Figure 1.36B). This demonstration also illustrated that the surface was modified through the Pt coated AFM tip. When the scanning was done with uncoated or Au coated tips, no subsequent binding of the fluorescent labels occurred (Figure 1.36C).

Blasdel *et al.* reported the use of an AFM tip coated with a hydride reducing agent to selectively reduce *in-situ* a spatial region in a monolayer of imines (Table IA).²²² A cystamine SAM (e.g. $\text{H}_2\text{N-CH}_2\text{CH}_2\text{S-SAM}$) was reacted with cyclopentanone to form terminal imine. Micrometer-sized ‘chunks’ of the reducing agent sodium triacetoxyborohydride ($\text{Na(OAc)}_3\text{BH}_4$) were attached to a gold coated tip using a thin film of UV-curable glue. The tip was then scanned over the SAM to locally reduce the imine terminal groups to secondary amines. The scans were run in intermittent contact (tapping) mode in anhydrous methanol (under vigorous water exclusion) to avoid degradation of the reducing agent and the hydrolysis of the imine groups. After scanning, the wafers were washed with water and placed into a NaOH solution to hydrolyze the remaining imine terminal groups back to primary amines. A chloranil test was used to detect the secondary amines in the scanned region; this region appeared as a blue-colored area in bright field optical micrographs. The authors claimed that a $(50 \mu\text{m})^2$ area had to

be scanned for 1.5 h with a speed of 60.4 $\mu\text{m/s}$ to achieve complete reduction. Thus, while this technique was slow and the spatial resolution was low, it did serve to illustrate how a tip could be used to selectively induce a chemical reaction.

Untreated AFM probes can also assist in the reaction of a functional head group. Porter and co-workers reported the tip-assisted base hydrolysis of an ester-terminated alkanethiol monolayer on gold (Table IB).²²³ The researchers self-assembled dithiobis(succinimido undecanoate) (DSU) on Au(111), and scanned the sample in 10 mM KOH solution with a force of 25 nN. The scanned area exhibited a higher friction than the surrounding regime, as observed in LFM images. The authors suggested that the tip induced a local disorder in the outer regime of the self-assembled layer, permitting better access of hydroxide ions to the acyl carbon of the DSU-SAM. A control experiment performed in deionized water showed no modification, but after the addition of alkaline solution, the scanned area showed the expected contrast in friction mode images.

Blackledge and co-workers pursued a similar approach to that reported by Müller in which a Pd-coated AFM tip was used to alter the chemical functionality of the head groups of self-assembled monolayers.²²⁴ The Pd-tip-catalyzed hydrogenation was illustrated in which azide terminal groups of a SAM were reduced to form amines (Table IC). The Pd-tip-catalyzed hydrogenation of *n*-benzyloxycarbonyl (CBZ) protected amino-terminal groups to free amines was also illustrated (Table ID). The third approach

showed the localized, tip-induced hydrosilation of aminobutyldimethylsilane (ASiH) from solution to the alkene head groups of a SAM (Table IE). This process resulted in a pattern terminated with amino groups. These amino groups were labeled by reaction with fluorescence probes (5- and 6-carboxytetramethyl-rhodamine succinimidyl ester or 6-((biotinoyl)amino)hexanoic acid succinimidyl ester). For the detection of the patterns on the substrate, the authors used confocal microscopy and various AFM techniques. The forces needed for these conversions were higher than the ones reported by Müller *et al.*²²¹ The authors concluded that the best results were obtained with the reduction of azide terminated SAMs. The conversion of the azide groups into amines was specific and nearly no nonspecific binding of the fluorescence labels occurred. The other two approaches were more problematic. The terminal CBZ groups appeared to spontaneously hydrolyze, and this process may have been enhanced by the deposition of palladium from the tip. The use of ASiH suffered from partial decomposition of this reaction in solution. The resulting species were postulated to chemisorb to the silanol groups present on the substrates.

Sagiv and co-workers developed a different type of substitution lithography, which they termed ‘constructive lithography’. In this method, a conducting AFM tip was utilized to selectively induce nanoscale electrochemical oxidation to the terminal functional groups (methyl, (-CH₃) or vinyl, (-CH=CH₂)) of SAMs on silicon. Figure 1.37 illustrates the steps involved to fabricate a structure. The headgroup of a silane-based SAM is subject to a localized redox event initiated by a conducting AFM tip (Figure 1.37A). Subsequent *in-*

situ chemistry was used to form organic bi- and multi-layers or inorganic nanostructures (Figure 1.37B). The patterned nanostructures could be observed with AFM height and friction imaging modes. Linewidths as low as 10 nm were illustrated; although the surface roughness of the silicon dictated that most clear demonstrations occur at larger length scales. Locally modified surfaces could then be used to induce site selective self-assembly of a number of different materials (organic, metal, semiconducting).

The selective oxidation of terminal vinyl groups in a nonadecenyltrichlorosilane (NTS) SAM yielded patterns of terminal hydroxyl groups.²²⁵ The modification occurred under

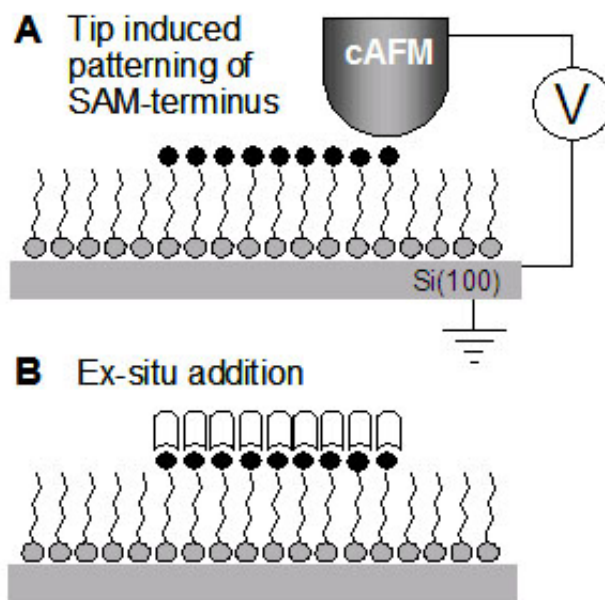


Figure 1.37: Schematic diagram of substitution lithography through the head group modification under an applied bias. (A) A conductive AFM tip scanned under an applied bias voltage across a SAM and modified the head group without changing the structural integrity of the SAM. (B) The altered functionality was used for the subsequent binding of a second self-assembly molecule.

an applied tip bias *ca.* 9 V with no measurable current (smaller than 0.5 nA) flowing in ambient conditions. Topography images showed no change in height, however the friction images suggested a different functionality in the patterned area relative to surrounding unmodified NTS SAM. After *in-situ* addition of OTS, which reacted with the hydroxyl groups of the oxidized NTS, the topography data showed an area of higher apparent height relative to the surrounding SAM, consistent with the expected height of the bilayer structure fabricated. The friction data suggested that the patterned area and surrounding SAM were composed of similar low friction surfaces (hydrophobic functionality). The authors noted that disordered monolayers seemed to contribute to a lack of oxidation control, creating patches of SiO₂ in the defects of the SAM. To unambiguously correlate microscopic features, macroscopic structures were created through dipping procedures whose chemical identity and structural integrity was confirmed by IR spectroscopy.

Starting with OTS-SAMs, the authors showed that it was possible to oxidize the -CH₃ terminal group with an AFM tip in a specific regime of applied bias. The researchers observed that between 8.5 to 10 V, three different regimes were observed. Below a certain threshold voltage nearly no conversion occurred, while above a certain value, the underlying silicon surface was oxidized. The optimal values were dependent on the relative humidity and the required patterning bias increased with decreasing humidity. Using SAMs prepared by exposure of 1-octadecene to hydrogenated silicon surfaces, Pignataro *et al.* studied a similar, tip-induced nanoelectrochemical modification by TOF-

SIMS and LFM.²²⁶ The authors observed two different regimes dependent on the absolute value of the applied bias. It was suggested that, at low bias, a redox event at the head group occurred, while at higher bias, the underlying silicon substrate was affected.

Recently, Pavlovic *et al.* described the local oxidation of thiol-derivatized SAMs (3-mercaptopropyltrimethoxysilanes (3-MPTMS) on p-doped silica) to thiolsulfonates or thiolsulfonates with a cAFM tip. The patterns were used to (covalently) immobilize a thiol rich protein (β -galactosidase) through disulfide bonds. Optimal potentials for patterning were reported to be between 2 and 4V; higher voltages compromised the SAM.²²⁷

The next demonstration of constructive lithography involved the site selective reduction of chemisorbed silver ions generating surface-bound elemental silver nanoparticles atop a thiol terminated SAM.²²⁸ The vinyl headgroups of an NTS-SAM were photochemically converted by radical addition of H₂S to form thiol and/or disulfide functionalities. The addition of a silver acetate solution terminated the SAM with silver thiolate groups, which could be converted to metallic silver if the surface was scanned under a reductive applied bias. Upon the addition of a silver enhancer solution, silver nano-islands were further developed. A negative tip bias formed no site selective Ag islands, nor did a positive tip bias followed by rewriting with a negative tip bias. Constructive nanolithography did not modify local surface sites at 0% RH regardless of tip bias, suggesting the water condensing from the atmosphere was essential in the faradic process occurring at the tip. These observations were all consistent with the authors' proposal of a

reduction process in which the sulfur-silver headgroup was converted into a thiol and silver under the influence of water. By applying locally well-defined drops of a NaBH_4 solution to a silver-thiolate terminated SAM, macroscopic sized areas were converted into metallic silver as confirmed by AFM imaging, UV-Vis spectroscopy and XPS.

The novelty of constructive nanolithography is based upon the ability of the technique to create templating patterns atop inert, stable monolayers. Many different chemical strategies with the reactive sites could be employed.²²⁹ This technique had the advantage that the surrounding non-patterned SAMs were not reactive to many *in-situ* wet chemical treatments. From these templates, organic (insulator), metal and semiconducting architectures could be created on highly ordered, inert monolayer scaffolds. An example of the schematic steps is shown in Figure 1.38.²²⁹ CdS nanoparticles were fabricated on top of organic bi-layer architectures, realized by two different chemical paths. Elemental silver structures were constructed by four different chemical pathways, while organic tri-layers were fabricated with iterations (layer-by-layer hierarchical treatment) of NTS and subsequent oxidation treatments, followed by a final ‘capping’ with OTS.

Constructive nanolithography was also employed to connect macroscopic with nanoscopic patterns.²³⁰ Macroscopic electrodes were generated with a multi-step process that involved the masking of headgroups with gallium metal, subsequent conversion of adjacent unmasked headgroups by UV irradiation followed by the guided self-assembly

of new organic layers and ions. Between the millimeter sized contact pads created, nanometer wide connecting lines were drawn using constructive nanolithography that

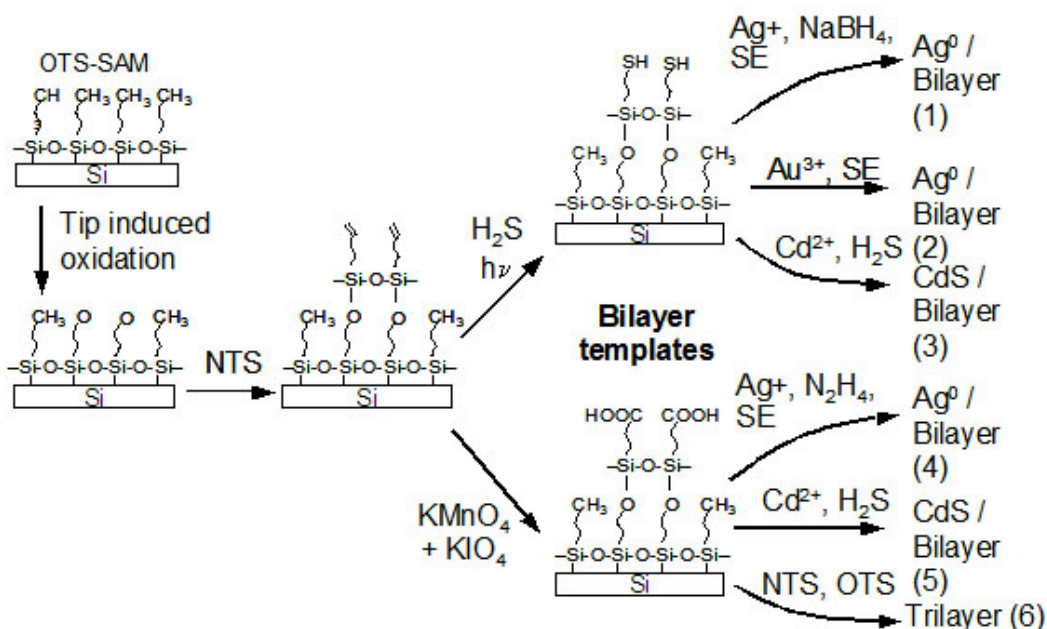


Figure 1.38: Schematic representation of constructive nanolithography as a generic approach to the planned surface self-assembly of diverse organic, metal, and semiconductor nanoentities. Six nanofabrication routes were indicated, starting with an ‘inert’ silane monolayer (OTS/silicon) that was non-destructively patterned by an electrically biased AFM tip to locally form electrooxidized OTS (OTSeO), followed by the selective self-assembly of a vinyl-terminated silane overlayer (NTS) at the OTSeO polar sites defined by the tip. Subsequently, the terminal ethylenic functions of NTS were photoreacted with H₂S in the gas-phase or chemically oxidized with aqueous (KMnO₂ + KIO₄) to give the corresponding TFMS/OTSeO or NTSOx/OTSeO bilayer template. Site-defined surface self-assembly of metallic silver, cadmium sulfide, or a third organic monolayer could be achieved using various template-controlled processes. The possibilities depicted here were: (1, 4) binding of Ag⁺ ions to the thiol or the carboxylic acid surface functions of the TFMS (1) and NTSOx (4) template, followed by reduction with aqueous NaBH₄ or gaseous N₂H₄ and further development (if desired) of the silver nanoparticles obtained with a silver enhancer (SE) solution; (2) binding of gold species to the TFMS surface, followed by gold-catalyzed silver metal deposition from the SE solution; (3, 5) binding of Cd²⁺ ions to the TFMS (3) or the NTSOx (5) surface, followed by the formation of CdS upon exposure of H₂S; (6) exposure of NTSOx to a solution of a self-assembling silane, resulting in the formation of an organic trilayer at the tip inscribed sites.

defined the sites for the silver ion reduction procedure described above. An AFM phase image (Figure 1.39) of a structure, created by this combined effort, revealed the successful combination of micro- and nanoscale patterns.

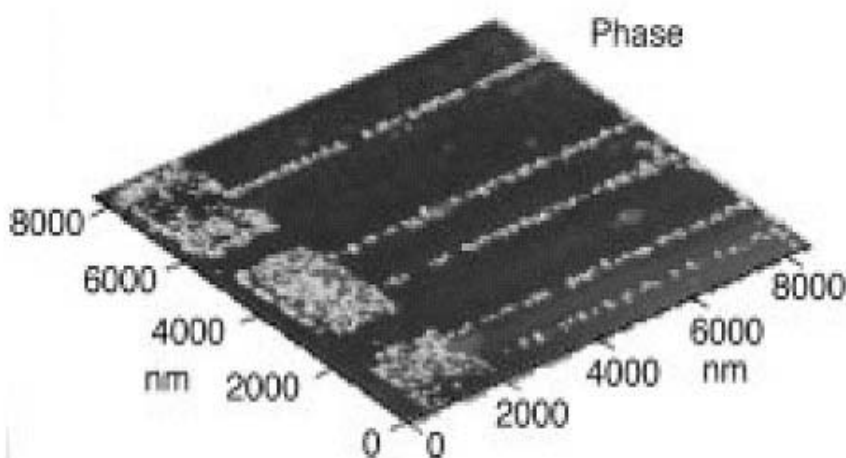


Figure 1.39: AFM phase image of controlled self-assembly of silver nano- and macrostructures on a template produced by AFM lithography. Reprinted with permission from ref. 230. Copyright 2002 Wiley-VCH.

Recently, this group expanded constructive lithography to the micro- and millimeter range employing TEM grids as a rigid stamp. The conductive grids were used as anodes to oxidize the SAM headgroups under the stamp, provided there was a sufficient water bridge between stamp and SAM to facilitate the electrochemical transformation. This new approach may be a practical means to parallel patterning at much larger length scales than the limited range inherent to SPL.²³¹ Constructive nanolithography was also employed to fabricate an organic bilayer terminated with top thiol functionality to immobilize

selectively triphenyl phosphine ligand-stabilized Au₅₅ nanoparticles (1.4 nm core diameter) through a ligand exchange process.²³² The initial procedure was identical to the one described previously. After the fabrication of a thiol-terminated bilayer, the Au nanoparticles were adsorbed. The authors prepared metal-organic hybrid architectures with feature sizes from *ca.* 10 nm to 2000 nm, which were stable even after heating at 120 °C for an hour in vacuum. Figure 1.40A& B presents the topography and phase images of the patterned nanoparticle islands, while Figure 40C& D shows Au particle wires connecting larger Au pads.

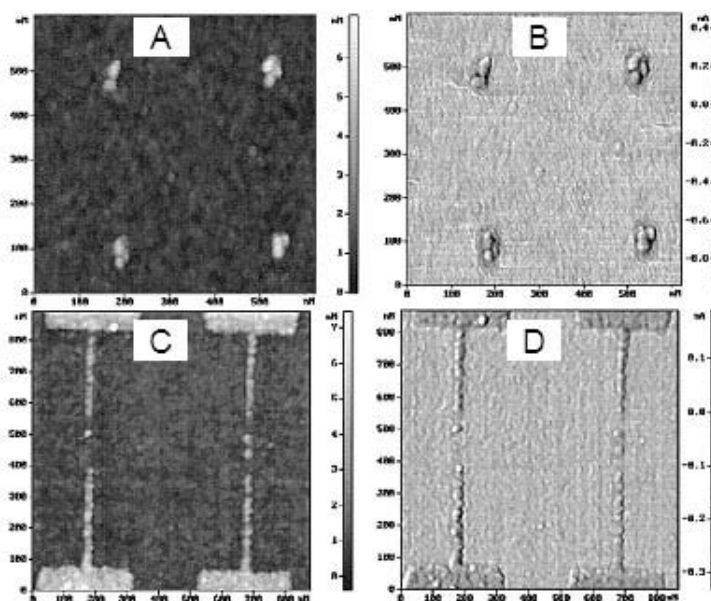


Figure 1.40: AFM images of an array of four Au₅₅/thiolated bilayer dots after annealing at 80 °C for 12 h ((A) topography, (B) phase image). Topography (C) and phase image (D) of a pattern combining dots, wires and contact pads. Reprinted with permission from ref. 232. Copyright 2002 American Chemical Society.

Matsubara *et al.* combined DPN with the type of substitution lithography approach discussed here to perform a Diels-Alder reaction at a vinyl terminated SAM.²³³ Triethoxy(10-undecenyl)silane was self-assembled onto thermally oxidized silicon, and the AFM tip was coated with a diene reactant (2-(13-hydroxy-2-oxatridecanyl)furan) (Figure 1.41A). As the tip was brought into contact with the surface, the 1-undecene underwent a reaction with the furan derivative (Figure 1.41B). The authors observed that initial contact of the tip with the surface produced larger structures than the following patterning attempts, and this result was ascribed to an initial excess of diene molecules on the coated tip. Once the excess was removed, the writing process was dependent on the applied pressure to the tip. With a force of 32 nN, the expected height (2.5 nm) was

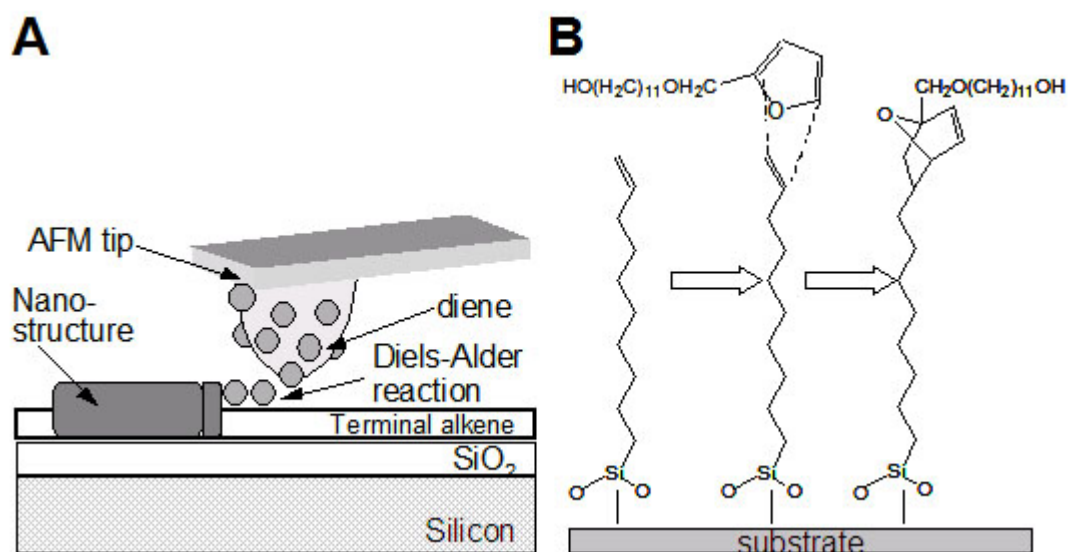


Figure 1.41: (A) Schematic diagram of the DPN procedure for the Diels-Alder reaction on a SAM. The tip, inked with a reactive molecule (diene), was scanned over a vinyl terminated (alkene) SAM and a Diels-Alder reaction took place. (B) Sketch of the Diels-Alder reaction of 2-(13-hydroxy-2-oxatridecanyl)furan on the alkene terminal headgroup of a silane SAM.

achieved. Higher forces resulted in very large structures, assumed to be oligomerized furan. Control experiments on methyl terminated SAMs created no structures.

5. Conclusions and Outlook

This review has shown that there is a diverse array of approaches to scanning probe lithography on SAMs. Scanning probe lithography emerges as one of the most expedient methods for making nanometer-scale patterns, at least in a laboratory setting. Other techniques do exist – for example, microcontact printing of SAMs has been extended to the *ca.* 50 nm scale.¹²⁶ Arguably, however, generation of stamps with features in this size regime requires some skill and has not been employed as routinely in the published literature.

SAMs are perhaps the ideal patterning elements as they offer the most convenient means to define the chemical functionality presented at a surface. Chemical definition is particularly important when the patterned regions have size features in the nanometer range, as these features display “countable” numbers of chemical functional groups. A wide variety of different chemical structures have been patterned. The range of materials described here includes silicon, coinage metals, thiols, silanes, proteins, DNA, nanoparticles and others.

Several basic issues are still unresolved with respect to these techniques. Mechanistically, many questions remain as to how these lithographic processes occur. For example, some of the details of the mechanism of ink transport and SAM formation in dip-pen nanolithography are still unclear. The ultimate resolution of these techniques is still ambiguous. Can other, sharper probes (e.g. carbon nanotubes) make smaller structures? Other issues that require clarification are reproducibility and the stability of the patterned nanostructures over time and in various environments.

There are opportunities in the further study and application of scanning probe lithography techniques. From an applications perspective, scanning probe lithography will always suffer from the problem that it is a serial and thus slow technique. Efforts have been made^{204,234,235} to make parallel arrays of tips. These may obviate this concern. In any event, these techniques may serve to create functional patterns to make, for example, sensor element arrays and interconnects of macroscopic contact pads with nanoscopic metal lines. From the perspective of advancing basic scientific investigations, scanning probe lithography has much promise. Nanometer-scale patterns can facilitate the study of molecular recognition processes, electronic behaviors in small collections of molecules, and the manipulation and organization of biomolecules. Arguably, we have just begun to use this technique to prepare and to explore new functional architectures.

6. Glossary

| | |
|-------------------------|---|
| AChE | acetylcholinesterase |
| AFM | atomic force microscope |
| APS | aminopropyltriethoxysilane |
| AR8 | acid red 8 |
| ASiH | aminobutyldimethylsilane |
| ATCh | acetylthiocholine |
| ATTO-TAG | 3-(2-furoyl)quinoline-2-carboxaldehyde |
| Au(111) | crystal phase of gold with Miller indices 1,1,1 |
| AuNP | gold nanoparticles |
| BOE | buffered oxide etch |
| C ₆ SH | hexanethiol (CH ₃ (CH ₂) ₅ SH) |
| C ₆ S-SAM | hexanethiolate (CH ₃ (CH ₂) ₅ S-) self-assembled monolayer |
| C ₉ SH | nonanethiol (CH ₃ (CH ₂) ₈ SH) |
| C ₉ S-SAM | nonanethiolate (CH ₃ (CH ₂) ₈ S-) self-assembled monolayer |
| C ₁₀ SH | decanethiol (CH ₃ (CH ₂) ₉ SH) |
| C ₁₀ S-SAM | decanethiolate (CH ₃ (CH ₂) ₉ S-) self-assembled monolayer |
| C ₁₂ SH | dodecanethiol (CH ₃ (CH ₂) ₁₁ SH) |
| C ₁₂ S-SAM | dodecanethiolate (CH ₃ (CH ₂) ₁₁ S-) self-assembled monolayer |
| C ₁₂ -uracil | dodecyl uracil |

| | |
|-----------------------|---|
| C ₁₆ SH | hexadecanethiol (CH ₃ (CH ₂) ₁₅ SH) |
| C ₁₆ S-SAM | hexadecanethiolate (CH ₃ (CH ₂) ₁₅ S-) self-assembled monolayer |
| C ₁₈ SH | octadecanethiol (CH ₃ (CH ₂) ₁₇ SH) |
| C ₁₈ S-SAM | octadecanethiolate (CH ₃ (CH ₂) ₁₇ S-) self-assembled monolayer |
| C6 | coumarin 6 |
| CAFM | conductive AFM |
| CBZ | <i>n</i> -benzyloxycarbonyl |
| CMPTS | 4-chloromethylphenyltrichlorosilane (Cl-CH ₂ -C ₆ H ₄ -SiCl ₃) |
| CSAFM | current sensing AFM |
| CV | cyclic voltammetry |
| CVD | chemical vapor deposition |
| DAD-2HCl | 1,12-diaminododecane |
| DAP | diacyl 2,6-diaminopyridine decanethiol |
| DPN | dip-pen nanolithography |
| dsDNA | double stranded deoxyribonucleic acid |
| DSU | dithiobis(succinimido undecanoate) |
| EDC | 1-ethyl-3-(3-dimethylaminopropyl) carbodiimide hydrochloride |
| EDOT | 3,4-ethylenedioxythiophene |

| | |
|--------------------------|---|
| E-DPN | electrochemical dip-pen nanolithography |
| FAS | heptadecafluoro-1,1,2,2-tetrahydro-decyl-1-trimethoxysilane |
| Fc | ferrocene |
| FcC ₁₁ SAc | ferrocenylundecanthioacetate |
| Fc-C ₁₁ SH | 11-mercapto-1-undecylferrocene |
| Fc-C ₁₁ S-SAM | 11-mercapto-1-undecylferrocenyl self-assembled monolayer |
| FcCOC ₁₀ SH | 11-mercapto-1-oxoundecylferrocene |
| Fc-uracil | ferrocene-terminated uracil |
| FITC | fluorescein |
| GaAs | gallium arsenide |
| GalC ₆ SAc | galvinolphenoxyhexanethiolacetate |
| GalC ₆ SH | galvinolphenoxyhexanethiol |
| GalC ₆ S-SAM | galvinolphenoxyhexanethiolate self-assembled monolayer |
| HMDS | hexamethyldisilazane |
| HOC ₆ SH | mercaptohexanol |
| IgG | immunoglobulin gamma |
| I _t | tunneling current set point |
| KFM | Kelvin probe force microscopy |
| LB | Langmuir Blodgett |
| LFM | lateral force microscopy |
| Li-EDA | lithium ethylenediamine |

| | |
|---------|---|
| MHA | mercaptohexadecanoic acid ($\text{HS}(\text{CH}_2)_{15}\text{COOH}$) |
| MMEA | mercaptomethylethaneamide |
| MPTS | mercaptopropyltriethoxysilane |
| 3-MPTMS | 3-mercaptopropyltrimethoxysilane |
| MUA | mercaptopundecanoic acid ($\text{HS}(\text{CH}_2)_{10}\text{COOH}$) |
| NADH | reduced nicotinamide adenine dinucleotide |
| NHS | N-hydroxysuccinimide ester |
| Ni-NTA | nickel nitrilotriacetic acid |
| NPRW | nanopen reader and writer |
| NSOM | near-field scanning optical microscope |
| NTS | nonadecenyltrichlorosilane |
| ODS | octadecyltrimethoxysilane ($\text{CH}_3(\text{CH}_2)_{17}\text{Si}(\text{CH}_3)_3$) |
| ODS-SAM | octadecyltrimethoxysilane ($\text{CH}_3(\text{CH}_2)_{17}\text{Si}(\text{CH}_3)_3$) based self-assembled monolayer |
| OTS | octadecyltrichlorosilane ($\text{CH}_3(\text{CH}_2)_{17}\text{SiCl}_3$) |
| OTS-SAM | octadecyltrichlorosilane ($\text{CH}_3(\text{CH}_2)_{17}\text{SiCl}_3$) based self-assembled monolayer |
| PEDA | aminoethylaminomethyl-phenethyltrimethoxysilane (NH_2 - (CH_2) ₂ -NH-CH ₂ -C ₆ H ₄ -(CH ₂) ₂ -Si(OCH ₃) ₃) |
| PMMA | polymethylmethacrylate |
| R6G | rhodamine 6G |

| | |
|----------------|---|
| RH | relative humidity |
| SAM | self-assembled monolayer |
| SECM | scanning electrochemical microscope |
| SEM | scanning electron microscope |
| SIC | standard imaging conditions |
| SPC | standard patterning conditions |
| SPL | scanning probe lithography |
| SPM | scanning probe microscope |
| ssDNA | single stranded deoxyribonucleic acid |
| STM | scanning tunneling microscope |
| TDA-HCl | <i>n</i> -tridecylamine |
| TEM | transmission electron microscope |
| TFSM | thiol functionalized NTS |
| TMAH | tetramethylammonium hydroxide |
| TMS-SAM | trimethylsilyl ((CH ₃) ₃ Si-) self-assembled monolayer |
| TOF-SIMS | time-of-flight secondary ion mass spectrometry |
| UHV | ultra high vacuum |
| V _b | bias voltage |
| XPS | x-ray photoelectron spectroscopy |

7. References

- (1) De Feyter, S.; Grim, P. C. M.; Rücker, M.; Vanoppen, P.; Meiners, C.; Sieffert, M.; Valiyaveetil, S.; Müllen, K.; Schryver, F. C. D. *Angewandte Chemie-International Edition* **1998**, *37*, 1223.
- (2) Lopinski, G. P.; Moffatt, D. J.; Wayner, D. D. M.; Wolkow, R. A. *Nature* **1998**, *392*, 909-911.
- (3) Fang, H.; Giancarlo, L. C.; Flynn, G. W. *Journal of Physical Chemistry B* **1998**, *102*, 7311.
- (4) De Feyter, S.; Gesquiere, A.; Grim, P. C. M.; DeSchryver, F. C.; Valiyaveetil, S.; Meiners, C.; Sieffert, M.; Mullen, K. *Langmuir* **1999**, *15*, 2817.
- (5) Ohtani, B.; Shintani, A.; Uosaki, K. *Journal of the American Chemical Society* **1999**, *121*, 6515.
- (6) Giancarlo, L. C.; Flynn, G. W. *Accounts of Chemical Research* **2000**, *33*, 491.
- (7) Lim, R.; Li, J.; Li, S. F. Y.; Feng, Z.; Valiyaveetil, S. *Langmuir* **2000**, *16*, 7023.
- (8) Yablon, D. G.; Giancarlo, L. C.; Flynn, G. W. *Journal of Physical Chemistry B* **2000**, *104*, 7627.
- (9) Böhringer, M.; Morgenstern, K.; Schneider, W.-D.; Berndt, R. *Angewandte Chemie-International Edition* **1999**, *38*, 821.
- (10) Stevens, F.; Dyer, D. J.; Walba, D. M. *Angewandte Chemie-International Edition* **1996**, *35*, 900.
- (11) Mena-Osteritz, E.; Meyer, A.; Langeveld-Voss, B. M. W.; Janssen, R. A. J.; Meijer, E. W.; Bäuerle, P. *Angewandte Chemie-International Edition* **2000**, *39*, 2680.
- (12) Lio, A.; Reichert, A.; Ahn, D. J.; Nagy, J. O.; Salmeron, M.; Charych, D. H. *Langmuir* **1997**, *13*, 6524.
- (13) Grim, P. C. M.; De Feyter, S.; Gesquiere, A.; Vanoppen, P.; Rücker, M.; Valiyaveetil, S.; Moessner, G.; Müllen, K.; De Schryver, F. C. *Angewandte Chemie-International Edition* **1997**, *36*, 2601.

- (14) Takami, T.; Ozaki, H.; Kasuga, M.; Tsuchiya, T.; Mazaki, Y.; Fukushi, D.; Ogawa, A.; Uda, M.; Aono, M. *Angewandte Chemie-International Edition* **1997**, *36*, 2755.
- (15) Kumaki, J.; Hashimoto, T. *Journal of the American Chemical Society* **1998**, *120*, 423.
- (16) Karim, A.; Slaweck, T. M.; Kumar, S. K.; Douglas, J. F.; Satija, S. K.; Han, C. C.; Russell, T. P.; Liu, Y.; Overney, R.; Sokolov, J.; Rafailovich, M. H. *Macromolecules* **1998**, *31*, 857.
- (17) Dziezok, P.; Sheiko, S. S.; Fischer, K.; Schmidt, M.; Möller, M. *Angewandte Chemie-International Edition* **1997**, *36*, 2812.
- (18) Kumaki, J.; Nishikawa, Y.; Hashimoto, T. *Journal of the American Chemical Society* **1996**, *118*, 3321.
- (19) Huisman, B. H.; Schonherr, H.; Huck, W. T. S.; Friggeri, A.; van Manen, H. J.; Menozzi, E.; Vancso, G. J.; van Veggel, F. C. J. M.; Reinhoudt, D. N. *Angewandte Chemie-International Edition* **1999**, *38*, 2248.
- (20) Takada, K.; Díaz, D. J.; Abruña, H. D.; Cuadrado, I.; Casado, C.; Alonso, B.; Morán, M.; Losada, J. *Journal of the American Chemical Society* **1997**, *119*, 10763.
- (21) Prokhorova, S. A.; Sheiko, S. S.; Mourran, A.; Azumi, R.; Beginn, U.; Zipp, G.; Ahn, C. H.; Holerca, M. N.; Percec, V.; Möller, M. *Langmuir* **2000**, *16*, 6862.
- (22) Zhang, H.; Grim, P. C. M.; Foubert, P.; Vosch, T.; Vanoppen, P.; Wiesler, U. M.; Berresheim, A. J.; Müllen, K.; De Schryver, F. C. *Langmuir* **2000**, *16*, 9009.
- (23) Barth, J. V.; Weckesser, J.; Cai, C. Z.; Günter, P.; Burgi, L.; Jeandupeux, O.; Kern, K. *Angewandte Chemie-International Edition* **2000**, *39*, 1230.
- (24) Semenov, A.; Spatz, J. P.; Moller, M.; Lehn, J. M.; Sell, B.; Schubert, D.; Weidl, C. H.; Schubert, U. S. *Angewandte Chemie-International Edition* **1999**, *38*, 2547.
- (25) Huisman, B. H.; van Veggel, F. C. J. M.; Reinhoudt, D. N. *Pure and Applied Chemistry* **1998**, *70*, 1985.
- (26) Böhringer, M.; Morgenstern, K.; Schneider, W. D.; Berndt, R.; Mauri, F.; De Vita, A.; Car, R. *Physical Review Letters* **1999**, *83*, 324.
- (27) Eichhorst-Gerner, K.; Stabel, A.; Moessner, G.; Declerq, D.; Valiyaveetil, S.; Enkelmann, V.; Müllen, K.; Rabe, J. P. *Angewandte Chemie-International Edition* **1996**, *35*, 1492.

- (28) Manne, S.; Gaub, H. E. *Science* **1995**, *270*, 1480.
- (29) Gimzewski, J. K.; Joachim, C.; Schlittler, R. R.; Langlais, V.; Tang, H.; Joahanssen, I. *Science* **1998**, *281*, 531.
- (30) Jung, T. A.; Schlittler, R. R.; Gimzewski, J. K. *Nature* **1997**, *386*, 696.
- (31) De Feyter, S.; Grim, P. C. M.; van Esch, J.; Kellogg, R. M.; Feringa, B. L.; De Schryver, F. C. *Journal of Physical Chemistry B* **1998**, *102*, 8981.
- (32) Yamakoshi, Y.; Schlittler, R. R.; Gimzewski, J. K.; Diederich, F. *Journal of Materials Chemistry* **2001**, *11*, 2895-2897.
- (33) Stevens, F.; Beebe, T. P. *Langmuir* **1999**, *15*, 6884.
- (34) Stipe, B. C.; Rezaei, M. A.; Ho, W. *Science* **1998**, *280*, 1732.
- (35) Cavallini, M.; Biscarini, F.; Leo'n, S.; Zerbetto, F.; Bottari, G.; Leigh, D. A. *Science* **2003**, *299*, 662.
- (36) Eigler, D. M.; Schweizer, E. K. *Nature* **1990**, *344*, 524.
- (37) Shigekawa, H.; Miyake, K.; Sumaoka, J.; Harada, A.; Komiyama, M. *Journal of the American Chemical Society* **2000**, *122*, 5411.
- (38) Stroschio, J. A.; Eigler, D. M. *Science* **1991**, *254*, 1319.
- (39) Crommie, M. F.; Lutz, C. P.; Eigler, D. M. *Science* **1993**, *262*, 218.
- (40) Hecht, S. *Angewandte Chemie-International Edition* **2003**, *42*, 24.
- (41) McCarty, G. S.; Weiss, P. S. *Chemical Reviews* **1999**, *99*, 1983.
- (42) Nyffenegger, R. M.; Penner, R. M. *Chemical Reviews* **1997**, *97*, 1195.
- (43) Hla, S. W.; Bartels, L.; Meyer, G.; Rieder, K. H. *Physical Review Letters* **2000**, *85*, 2777.
- (44) Hla, S. W.; Meyer, G.; Rieder, K. H. *ChemPhysChem* **2001**, *2*, 361.
- (45) Sullivan, T. P.; Huck, W. T. S. *European Journal of Organic Chemistry* **2003**, 17.
- (46) Ulman, A. In *An Introduction to Ultrathin Organic Films from Langmuir-Blodgett to Self-Assembly*; Academic Press, Inc.: New York, 1991.

- (47) Schreiber, F. *Progress in Surface Science* **2000**, *65*, 151.
- (48) Dubois, L. H.; Nuzzo, R. G. *Annual Review of Physical Chemistry* **1992**, *43*, 437.
- (49) Ulman, A. *Chemical Reviews* **1996**, *96*, 1533.
- (50) Poirier, G. E. *Langmuir* **1997**, *13*, 2019.
- (51) Xia, Y. N.; Whitesides, G. M. *Annual Review of Materials Science* **1998**, *28*, 153.
- (52) Xia, Y. N.; Rogers, J. A.; Paul, K. E.; Whitesides, G. M. *Chemical Reviews* **1999**, *99*, 1823.
- (53) Torres, C. M. S.; Zankovych, S.; Seekamp, J.; Kam, A. P.; Cedeno, C. C.; Hoffmann, T.; Ahopelto, J.; Reuther, F.; Pfeiffer, K.; Bleidiessel, G.; Gruetzner, G.; Maximov, M. V.; Heidari, B. *Materials Science & Engineering C-Biomimetic and Supramolecular Systems* **2003**, *23*, 23.
- (54) Chou, S. Y. *M.R.S. Bulletin* **2001**, *26*, 512.
- (55) Whitesides, G. M.; Mathias, J. P.; Seto, C. T. *Science* **1991**, *254*, 1312.
- (56) Whitesides, G. M.; Grzybowski, B. *Science* **2002**, *295*, 2418.
- (57) Kondo, S.; Heike, S.; Lutwyche, M.; Wada, Y. *Journal of Applied Physics* **1995**, *78*, 155.
- (58) Majumdar, A.; Lindsay, S. M. In *Technology of Proximal Probe Lithography*; Marrian, C. R. K., Ed.; SPIE Optical Engineering Press: Washington, 1993; Vol. IS 10.
- (59) Marrian, C. R. K.; Dobisz, E. A.; Dagata, J. A. In *Technology of Proximal Probe Lithography*; Marrian, C. R. K., Ed.; SPIE Optical Engineering Press: Washington, 1993; Vol. IS 10.
- (60) Quate, C. F. *Surface Science* **1997**, *386*, 259.
- (61) Wiesendanger, R. In *SPIE Optical Engineering Press*; Marrian, C. R. K., Ed. Washington, 1993; Vol. IS 10.
- (62) Lercel, M. J.; Craighead, H. G.; Parikh, A. N.; Seshadri, K.; Allara, D. L. *Applied Physics Letters* **1996**, *68*, 1504.

- (63) Götzhäuser, A.; Eck, W.; Geyer, W.; Stadler, V.; Weimann, T.; Hinze, P.; Grunze, M. *Advanced Materials* **2001**, *13*, 806.
- (64) Inoue, A.; Ishida, T.; Choi, N.; Mizutani, W.; Tokumoto, H. *Applied Physics Letters* **1998**, *73*, 1976.
- (65) Hatzor, A.; Weiss, P. S. *Science* **2001**, *291*, 1019.
- (66) Bumm, L. A.; Arnold, J. J.; Cygan, M. T.; Dunbar, T. D.; Burgin, T. P.; Jones II, L.; Allara, D. L.; Tour, J. M.; Weiss, P. S. *Science* **1996**, *271*, 1705.
- (67) Cygan, M. T.; Dunbar, T. D.; Arnold, J. J.; Bumm, L. A.; Shedlock, N. F.; Burgin, T. P.; II, L. J.; Allara, D. L.; Tour, J. M.; Weiss, P. S. *Journal of the American Chemical Society* **1998**, *120*, 2721.
- (68) Dunbar, T. D.; Cygan, M. T.; Bumm, L. A.; McCarty, G. S.; Burgin, T. P.; Reinerth, W. A.; Jones, L.; Jackiw, J. J.; Tour, J. M.; Weiss, P. S.; Allara, D. L. *Journal of Physical Chemistry B* **2000**, *104*, 4880.
- (69) Weck, M.; Jackiw, J. J.; Rossi, R. R.; Weiss, P. S.; Grubbs, R. H. *Journal of the American Chemical Society* **1999**, *121*, 4088.
- (70) Jung, T. A.; Moser, A.; Hug, H. J.; Brodbeck, D.; Hofer, R.; Hidber, H. R.; Schwarz, U. D. *Ultramicroscopy* **1992**, *42-44*, 1446.
- (71) Böhme, O.; Ziegler, C.; Göpel, W. *Advanced Materials* **1994**, *6*, 587.
- (72) Elkaakour, Z.; Aime, J. P.; Bouchacina, T.; Odin, C.; Masuda, T. *Physical Review Letters* **1994**, *73*, 3231.
- (73) Ross, C. B.; Sun, L.; Crooks, R. M. *Langmuir* **1993**, *9*, 632.
- (74) Sumomogi, T.; Endo, T.; Kuwahara, K.; Kaneko, R. *Journal of Vacuum Science & Technology* **1995**, *13*, 1257.
- (75) Yamamoto, S.-i.; Yamada, H.; Tokumoto, H. *Journal of Applied Physics* **1995**, *34*, 3396.
- (76) Green, J.-B. D.; McDermott, M. T.; Porter, M. D.; Siperko, L. M. *Journal of Physical Chemistry* **1995**, *99*, 10960.
- (77) Sohn, L. L.; Willett, R. L. *Applied Physics Letters* **1995**, *67*, 1552.
- (78) Zhou, L.; Zhang, P. C.; Ho, P. K. H.; Xu, G. Q.; Li, S. F. Y.; Chan, L. *Journal of Materials Science Letters* **1996**, *15*, 2080.

- (79) Kunze, U.; Klehn, B. *Advanced Materials* **1999**, *11*, 1473.
- (80) Kim, Y. T.; Bard, A. J. *Langmuir* **1992**, *8*, 1096.
- (81) Schöenenberger, C.; Sondag-Huethorst, J. A. M.; Jorritsma, J.; Fokkink, L. G. J. *Langmuir* **1994**, *10*, 611.
- (82) Touzov, I.; Gorman, C. B. *Journal of Physical Chemistry B* **1997**, *101*, 5263.
- (83) Poirier, G. E. *Chemical Reviews* **1997**, *97*, 1117.
- (84) McCarley, R. L.; Dunaway, D. J.; Willicut, R. J. *Langmuir* **1993**, *9*, 2775.
- (85) Lercel, M. J.; Redinbo, G. F.; Craighead, H. G.; Sheen, C. W.; Allara, D. L. *Applied Physics Letters* **1994**, *65*, 974.
- (86) Xu, L. S.; Allee, D. R. *Journal of Vacuum Science & Technology B* **1995**, *13*, 2837.
- (87) Lercel, M. J.; Rooks, M.; Tiberio, R. C.; Craighead, H. G.; Sheen, C. W.; Parikh, A. N.; Allara, D. L. *Journal of Vacuum Science & Technology B* **1995**, *13*, 1139.
- (88) Sugimura, H.; Nakagiri, N. *Langmuir* **1995**, *11*, 3623.
- (89) Schoer, J. K.; Ross, C. B.; Crooks, R. M.; Corbitt, T. S.; Hampden-Smith, M. J. *Langmuir* **1994**, *10*, 615.
- (90) Schoer, J. K.; Zamborini, F. P.; Crooks, R. M. *Journal of Physical Chemistry* **1996**, *100*, 11086.
- (91) Schoer, J. K.; Crooks, R. M. *Langmuir* **1997**, *13*, 2323.
- (92) Weiss, P. S.; Bumm, L. A.; Dunbar, T. D.; Burgin, T. P.; Tour, J. M.; Allara, D. L. *Proceeding of the New York Academy of Sciences* **1998**, *852*, 145.
- (93) Delamarche, E.; Hoole, A. C. F.; Michel, B.; Wilkes, S.; Despont, M.; Welland, M. E.; Biebuyck, H. *Journal of Physical Chemistry B* **1997**, *101*, 9263.
- (94) Yang, W.; Chen, M.; Knoll, W.; Deng, H. L. *Langmuir* **2002**, *18*, 4124.
- (95) Müller, H. U.; David, C.; Volkel, B.; Grunze, M. *Journal of Vacuum Science & Technology B* **1995**, *13*, 2846.
- (96) Mizutani, W.; Ishida, T.; Tokumoto, H. *Langmuir* **1998**, *14*, 7197.

- (97) Keel, J. M.; Yin, J.; Guo, Q.; Palmer, R. E. *Journal of Chemical Physics* **2002**, *116*, 7151.
- (98) Liu, G.-Y.; Salmeron, M. B. *Langmuir* **1994**, *10*, 367.
- (99) Xiao, X. D.; Liu, G. Y.; Charych, D. H.; Salmeron, M. *Langmuir* **1995**, *11*, 1600.
- (100) Kelley, S. O.; Barton, J. K.; Jackson, N. M.; McPherson, L. D.; Potter, A. B.; Spain, E. M.; Allen, M. J.; Hill, M. G. *Langmuir* **1998**, *14*, 6781.
- (101) Zhou, D.; Sinniah, K.; Abell, C.; Rayment, T. *Langmuir* **2002**, *18*, 8278.
- (102) Zhao, J. W.; Uosaki, K. *Langmuir* **2001**, *17*, 7784.
- (103) Sugimura, H.; Okiguchi, K.; Nakagiri, N.; Miyashita, M. *Journal of Vacuum Science & Technology B* **1996**, *14*, 4140.
- (104) Sugimura, H.; Nakagiri, N. *Journal of Vacuum Science & Technology B* **1997**, *15*, 1394.
- (105) Sugimura, H.; Nakagiri, N. *Nanotechnology* **1997**, *8*, A15.
- (106) Sugimura, H.; Nakagiri, N. *Journal of the American Chemical Society* **1997**, *119*, 9226.
- (107) Sugimura, H.; Hanji, T.; Hayashi, K.; Takai, O. *Advanced Materials* **2002**, *14*, 524.
- (108) Sugimura, H.; Takai, O.; Nakagiri, N. *Journal of Electroanalytical Chemistry* **1999**, *473*, 230.
- (109) Sugimura, H.; Takai, O.; Nakagiri, N. *Journal of Vacuum Science & Technology B* **1999**, *17*, 1605.
- (110) Sugimura, H.; Hanji, T.; Hayashi, K.; Takai, O. *Ultramicroscopy* **2002**, *91*, 221.
- (111) Zheng, J. W.; Zhu, Z. H.; Chen, H. F.; Liu, Z. F. *Langmuir* **2000**, *16*, 4409.
- (112) Li, Q.; Zheng, J. W.; Liu, Z. F. *Langmuir* **2003**, *19*, 166.
- (113) Zheng, J. W.; Chen, Z. C.; Liu, Z. F. *Langmuir* **2000**, *16*, 9673.
- (114) Kim, J.; Oh, Y.; Lee, H.; Shin, Y.; Park, S. *Japanese Journal of Applied Physics Part I* **1998**, *37*, 7148.

- (115) Oh, Y.; Kim, J.; Lee, H. *Molecular Crystals and Liquid Crystals* **1999**, 337, 7.
- (116) Oh, Y.; Kim, J.; Lee, H. *Journal of the Korean Physical Society* **1999**, 35, S1013.
- (117) Kim, S. H.; Oh, Y.; Lee, H. *Molecular Crystals and Liquid Crystals* **2000**, 349, 175.
- (118) Kim, S. M.; Ahn, S. J.; Lee, H.; Kim, E. R. *Ultramicroscopy* **2002**, 91, 165.
- (119) Lee, W. B.; Oh, Y.; Kim, E. R.; Lee, H. *Synthetic Metals* **2001**, 117, 305.
- (120) Lee, W. B.; Kim, E. R.; Lee, H. *Langmuir* **2002**, 2002, 8375.
- (121) Lee, H.; Kim, S. A.; Ahn, S. J. *Applied Physics Letters* **2002**, 81, 138.
- (122) She, J.; Song, J. Q.; Wang, Y. C.; Liu, Z. F. *Molecular Crystals and Liquid Crystals* **1999**, 337, 313.
- (123) Ara, M.; Graaf, H.; Tada, H. *Applied Physics Letters* **2002**, 80, 2565.
- (124) Sun, S. Q.; Chong, K. S. L.; Leggett, G. J. *Journal of the American Chemical Society* **2002**, 124, 2414.
- (125) Sun, S. Q.; Leggett, G. J. *Nano Letters* **2002**, 2, 1223.
- (126) Odom, T. W.; Thalladi, V. R.; Love, J. C.; Whitesides, G. M. *Journal of the American Chemical Society* **2002**, 124, 12112.
- (127) Lopez, G. P.; Biebuyck, H. A.; Frisbie, C. D.; Whitesides, G. M. *Science* **1993**, 260, 647.
- (128) Hong, M. H.; Kim, K. H.; Bae, J.; Jhe, W. *Applied Physics Letters* **2000**, 77, 2604.
- (129) Bruckbauer, A.; Ying, L. M.; Rothery, A. M.; Zhou, D. J.; Shevchuk, A. I.; Abell, C.; Korchev, Y. E.; Klenerman, D. *Journal of the American Chemical Society* **2002**, 124, 8810.
- (130) Lewis, A.; Kheifetz, Y.; Shambrodt, E.; Radko, A.; Khatchatryan, E.; Sukenik, C. *Applied Physics Letters* **1999**, 75, 2689.
- (131) Gaspar, S.; Mosbach, M.; Wallman, L.; Laurell, T.; Csoregi, E.; Schuhmann, W. *Analytical Chemistry* **2001**, 73, 4254.
- (132) Voigt, J.; Shi, F.; Edinger, K.; Guthner, P.; Rangelow, I. W. *Microelectronic Engineering* **2001**, 57-8, 1035.

- (133) Smith, J. T., Viglianti, B.L., Reichert, W.M. *Langmuir* **2002**, *18*, 6289.
- (134) Smith, J. T., Reichert, W.M. *Langmuir* **2003**, *19*, 3078.
- (135) Jaschke, M.; Butt, H. J. *Langmuir* **1995**, *11*, 1061.
- (136) Piner, R. D.; Mirkin, C. A. *Langmuir* **1997**, *13*, 6864.
- (137) Mirkin, C. A. *Inorganic Chemistry* **2000**, *39*, 2258.
- (138) Mirkin, C. A. *M.R.S. Bulletin* **2001**, *26*, 535.
- (139) Mirkin, C. A.; Hong, S. H.; Demers, L. *ChemPhysChem* **2001**, *2*, 37.
- (140) Ginger, D. S., Zhang, H., Mirkin, C.A. *Angewandte Chemie-International Edition* **2004**, *43*, 30.
- (141) Piner, R. D.; Zhu, J.; Xu, F.; Hong, S. H.; Mirkin, C. A. *Science* **1999**, *283*, 661.
- (142) Hong, S. H.; Zhu, J.; Mirkin, C. A. *Science* **1999**, *286*, 523.
- (143) Hong, S.; Mirkin, C. A. *Science* **2000**, *288*, 1808.
- (144) Zhang, M.; Bullen, D.; Chung, S. W.; Hong, S.; Ryu, K. S.; Fan, Z. F.; Mirkin, C. A.; Liu, C. *Nanotechnology* **2002**, *13*, 212.
- (145) Zou, J., Bullen, D., Wang, X., Liua, C., Mirkin, C.A. *Applied Physics Letters* **2003**, *83*, 581.
- (146) Belaubre, P., Guirardel, M., Garcia, G., Pourciel, J. B., Leberre, V. ,
Dagkessamanskaia, A., Tre' visiol, E., Francois, J. M., Bergaud, C. *Applied Physics Letters* **2003**, *82*, 3122.
- (147) Hong, S.; Zhu, J.; Mirkin, C. A. *Langmuir* **1999**, *15*, 7897.
- (148) Ivanisevic, A.; McCumber, K. V.; Mirkin, C. A. *Journal of the American Chemical Society* **2002**, *124*, 11997.
- (149) Zhang, Y.; Salaita, K.; Lim, J. H.; Mirkin, C. A. *Nano Letters* **2002**, *2*, 1389.
- (150) Weinberger, D. A.; Hong, S. G.; Mirkin, C. A.; Wessels, B. W.; Higgins, T. B. *Advanced Materials* **2000**, *12*, 1600.

- (151) Zhang, H.; Chung, S. W.; Mirkin, C. A. *Nano Letters* **2003**, *3*, 43.
- (152) Zhang, H.; Mirkin, C. A. *Chemistry of Materials* **2004**, *16*, 1480.
- (153) Ivanisevic, A.; Mirkin, C. A. *Journal of the American Chemical Society* **2001**, *123*, 7887.
- (154) Jung, H., Kulkarni, R., Collier, C.P. *Journal of the American Chemical Society* **2003**, *125*, 12096.
- (155) Demers, L. M.; Ginger, D. S.; Park, S.-J.; Li, Z.; Chung, S.-W.; Mirkin, C. A. *Science* **2002**, *296*, 1836.
- (156) Wilson, D. L.; Martin, R.; Hong, S.; Cronin-Golomb, M.; Mirkin, C. A.; Kaplan, D. L. *Proceedings of the National Academy of Sciences of the United States of America* **2001**, *98*, 13660.
- (157) Agarwal, G.; Sowards, L. A.; Naik, R. R.; Stone, O. *Journal of the American Chemical Society* **2003**, *125*, 580.
- (158) Noy, A.; Miller, A. E.; Klare, J. E.; Weeks, B. L.; Woods, B. W.; DeYoreo, J. J. *Nano Letters* **2002**, *2*, 109.
- (159) Su, M.; Dravid, V. P. *Applied Physics Letters* **2002**, *80*, 4434.
- (160) McKendry, R.; Huck, W. T. S.; Weeks, B.; Florini, M.; Abell, C.; Rayment, T. *Nano Letters* **2002**, *2*, 713.
- (161) Lim, J. H.; Mirkin, C. A. *Advanced Materials* **2002**, *14*, 1474.
- (162) Lim, J. H., Ginger, D.S., Lee, K.B., Heo, J., Nam, J.M., Mirkin, C.A. *Angewandte Chemie-International Edition* **2003**, *42*, 2309.
- (163) Lee, K.-B., Lim, J.-H., Mirkin, C.A. *Journal of the American Chemical Society* **2003**, *125*, 5588.
- (164) Li, Y.; Maynor, B. W.; Liu, J. *Journal of the American Chemical Society* **2001**, *123*, 2105.
- (165) Li, Y.; Ben, M.; Liu, J. *Chinese Journal of Inorganic Chemistry* **2002**, *18*, 75.
- (166) Maynor, B. W.; Filocamo, S. F.; Grinstaff, M. W.; Liu, J. *Journal of the American Chemical Society* **2002**, *124*, 522.

- (167) Agarwal, G., Naik, R.R., Stone, M.O. *Journal of the American Chemical Society* **2003**, *125*, 7408.
- (168) Hyun, J., Kim, J., Craig, S.L., Chilkoti, A. *Journal of the American Chemical Society* **2004**, *ASAP*.
- (169) Maynor, B. W.; Li, Y.; Liu, J. *Langmuir* **2001**, *17*, 2575.
- (170) Porter, L. A.; Choi, H. C.; Schmeltzer, J. M.; Ribbe, A. E.; Elliott, L. C. C.; Buriak, J. M. *Nano Letters* **2002**, *2*, 1369.
- (171) Fu, L., Liu, X., Zhang, Y., Dravid, V.P., Mirkin, C.A. *Nano Letters* **2003**, *3*, 757.
- (172) Su, M.; Liu, X. G.; Li, S. Y.; Dravid, V. P.; Mirkin, C. A. *Journal of the American Chemical Society* **2002**, *124*, 1560.
- (173) Liao, J. H.; Huang, L.; Gu, N. *Chinese Physics Letters* **2002**, *19*, 134.
- (174) Ben Ali, M.; Ondarcuhu, T.; Brust, M.; Joachim, C. *Langmuir* **2002**, *18*, 872.
- (175) Lee, K. B.; Park, S. J.; Mirkin, C. A.; Smith, J. C.; Mrksich, M. *Science* **2002**, *295*, 1702.
- (176) Hyun, J.; Ahn, S. J.; Lee, W. K.; Chilkoti, A.; Zauscher, S. *Nano Letters* **2002**, *2*, 1203.
- (177) Cheung, C., Camarero, J.A., Woods, B.W., Lin, T., Johnson, J.E., De Yoreo, J.J. *Journal of the American Chemical Society* **2003**, *125*, 6848.
- (178) Smith, J. C., Lee, K.-B., Wang, Q., Finn, M. G., Johnson, J.E., Mrksich, M., Mirkin, C.A. *Nano Letters* **2003**, *3*, 883.
- (179) Demers, L. M.; Mirkin, C. A. *Angewandte Chemie-International Edition* **2001**, *40*, 3069.
- (180) Liu, X. G.; Fu, L.; Hong, S. H.; Dravid, V. P.; Mirkin, C. A. *Advanced Materials* **2002**, *14*, 231.
- (181) Demers, L. M.; Park, S. J.; Taton, T. A.; Li, Z.; Mirkin, C. A. *Angewandte Chemie-International Edition* **2001**, *40*, 3071.
- (182) Ivanisevic, A.; Im, J. H.; Lee, K. B.; Park, S. J.; Demers, L. M.; Watson, K. J.; Mirkin, C. A. *Journal of the American Chemical Society* **2001**, *123*, 12424.

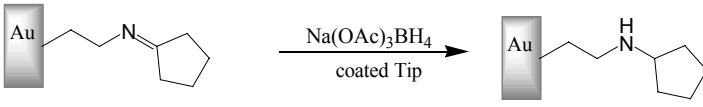
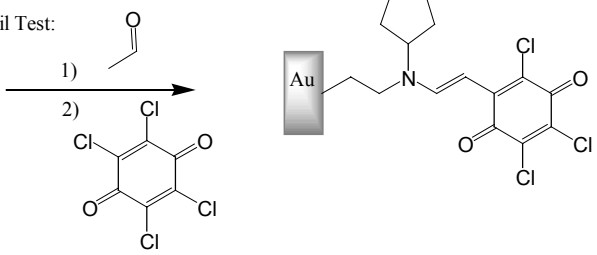
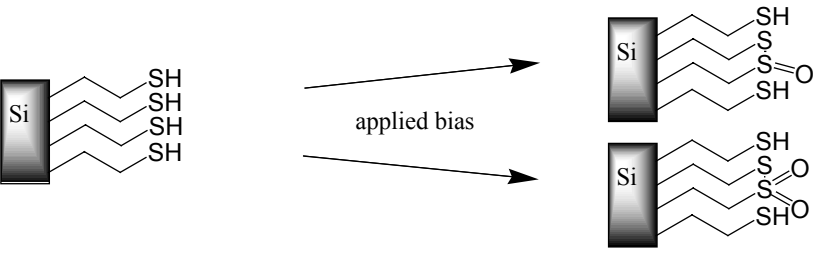
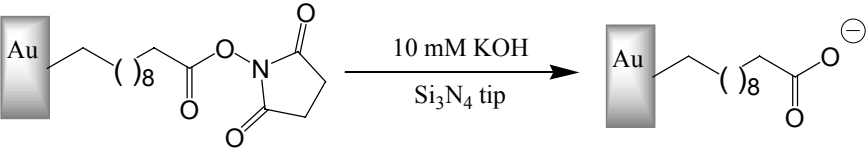
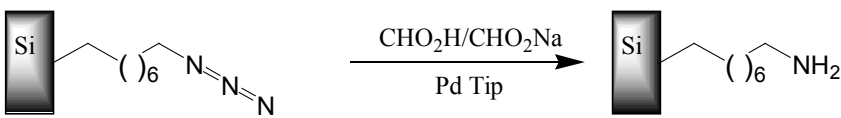
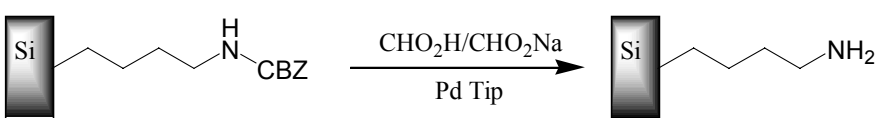
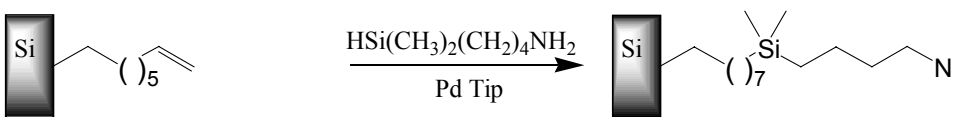
- (183) Zhang, H.; Li, Z.; Mirkin, C. A. *Advanced Materials* **2002**, *14*, 1472.
- (184) Jang, J. Y.; Hong, S. H.; Schatz, G. C.; Ratner, M. A. *Journal of Chemical Physics* **2001**, *115*, 2721.
- (185) Jang, J. Y.; Schatz, G. C.; Ratner, M. A. *Journal of Chemical Physics* **2002**, *116*, 3875.
- (186) Jang, J., Schatz, G. C., Ratner, M. A. *Physical Review Letters* **2003**, *90*, Art. #156104.
- (187) Jang, J., Schatz, G. C., Ratner, M. A. *Physical Review Letters* **2004**, *92*, #085504-1.
- (188) Jang, J., Schatz, G.C., Ratner, M.A. *Journal of Chemical Physics* **2004**, *120*, 1157.
- (189) Weeks, B. L.; Noy, A.; Miller, A. E.; De Yoreo, J. J. *Physical Review Letters* **2002**, *88*, 255505.
- (190) Sheehan, P. E.; Whitman, L. J. *Physical Review Letters* **2002**, *88*, 156104.
- (191) Schwartz, P. V. *Langmuir* **2002**, *18*, 4041.
- (192) Rohzok, S.; Piner, R. D.; Mirkin, C. A. *Journal of Physical Chemistry B* **2003**, *107*, 751.
- (193) Zamborini, F. P.; Crooks, R. M. *Journal of the American Chemical Society* **1998**, *120*, 9700.
- (194) Chen, J.; Reed, M. A.; Asplund, C. L.; Cassell, A. M.; Myrick, M. L.; Rawlett, A. M.; Tour, J. M.; Van Patten, P. G. *Applied Physics Letters* **1999**, *75*, 624.
- (195) Gorman, C. B.; Carroll, R. L.; He, Y. F.; Tian, F.; Fuierer, R. R. *Langmuir* **2000**, *16*, 6312.
- (196) Fuierer, R. R.; Carroll, R. L.; Feldheim, D. L.; Gorman, C. B. *Advanced Materials* **2002**, *14*, 154.
- (197) Credo, G. M.; Boal, A. K.; Das, K.; Galow, T. H.; Rotello, V. M.; Feldheim, D. L.; Gorman, C. B. *Journal of the American Chemical Society* **2002**, *124*, 9036.
- (198) Zhao, J. W.; Uosaki, K. *Nano Letters* **2002**, *2*, 137.
- (199) Xu, S.; Liu, G. Y. *Langmuir* **1997**, *13*, 127.

- (200) Xu, S.; Laibinis, P. E.; Liu, G. Y. *Journal of the American Chemical Society* **1998**, *120*, 9356.
- (201) Liu, G. Y.; Xu, S.; Qian, Y. L. *Accounts of Chemical Research* **2000**, *33*, 457.
- (202) Liu, G. Y.; Amro, N. A. *Proceedings of the National Academy of Sciences of the United States of America* **2002**, *99*, 5165.
- (203) Wadu-Mesthrige, K.; Amro, N. A.; Garno, J. C.; Xu, S.; Liu, G. Y. *Biophysical Journal* **2001**, *80*, 1891.
- (204) Xu, S.; Miller, S.; Laibinis, P. E.; Liu, G. Y. *Langmuir* **1999**, *15*, 7244.
- (205) Cruchon-Dupeyrat, S.; Porthun, S.; Liu, G. Y. *Applied Surface Science* **2001**, *175*, 636.
- (206) Xu, S.; Amro, N. A.; Liu, G.-Y. *Applied Surface Science* **2001**, *175*, 649.
- (207) Liu, M. Z.; Amro, N. A.; Chow, C. S.; Liu, G. Y. *Nano Letters* **2002**, *2*, 863.
- (208) Case, M. A.; McLendon, G. L.; Hu, Y.; Vanderlick, T. K.; Scoles, G. *Nano Letters* **2003**, *3*, 425.
- (209) Amro, N. A.; Xu, S.; Liu, G. Y. *Langmuir* **2000**, *16*, 3006.
- (210) Garno, J. C.; Yang, Y.; Amro, N. A.; Cruchon-Dupeyrat, S.; Chen, S.; Liu, G. Y. *Nano Letters* **2003**, *3*, 389-395.
- (211) Schwartz, P. V. *Langmuir* **2001**, *17*, 5971.
- (212) Wadu-Mesthrige, K.; Xu, S.; Amro, N. A.; Liu, G. Y. *Langmuir* **1999**, *15*, 8580.
- (213) Kenseth, J. R.; Harnisch, J. A.; Jones, V. W.; Porter, M. D. *Langmuir* **2001**, *17*, 4105.
- (214) Liu, J. F.; Cruchon-Dupeyrat, S.; Garno, J. C.; Frommer, J.; Liu, G. Y. *Nano Letters* **2002**, *2*, 937.
- (215) Jang, C. H.; Stevens, B. D.; Carlier, P. R.; Calter, M. A.; Ducker, W. A. *Journal of the American Chemical Society* **2002**, *124*, 12114.
- (216) Wacaser, B. A.; Maughan, M. J.; Mowat, I. A.; Niederhauser, T. L.; Linford, M. R.; Davis, R. C. *Applied Physics Letters* **2003**, *82*, 808.

- (217) Marrian, C. R. K.; Perkins, F. K.; Brandow, S. L.; Koloski, T. S.; Dobisz, E. A.; Calvert, J. M. *Applied Physics Letters* **1994**, *64*, 390.
- (218) Perkins, F. K.; Dobisz, E. A.; Brandow, S. L.; Koloski, T. S.; Calvert, J. M.; Rhee, K. W.; Kosakowski, J. E.; Marrian, C. R. K. *Journal of Vacuum Science & Technology B* **1994**, *12*, 3725.
- (219) Perkins, F. K.; Dobisz, E. A.; Brandow, S. L.; Calvert, J. M.; Kosakowski, J. E.; Marrian, C. R. K. *Applied Physics Letters* **1996**, *68*, 550.
- (220) Clausen-Schaumann, H.; Grandbois, M.; Gaub, H. E. *Advanced Materials* **1998**, *10*, 949.
- (221) Müller, W. T.; Klein, D. L.; Lee, T.; Clarke, J.; McEuen, P. L.; Schultz, P. G. *Science* **1995**, *268*, 272.
- (222) Blasdel, L. K.; Banerjee, S.; Wong, S. S. *Langmuir* **2002**, *18*, 5055.
- (223) Wang, J.; Kenseth, J. R.; Jones, V. W.; Green, J.-B. D.; McDermott, M. T.; Porter, M. D. *Journal of the American Chemical Society* **1997**, *119*, 12796.
- (224) Blackledge, C.; Engebretson, D. A.; McDonald, J. D. *Langmuir* **2000**, *16*, 8317.
- (225) Maoz, R.; Cohen, S.; Sagiv, J. *Advanced Materials* **1999**, *11*, 55.
- (226) Pignataro, B.; Licciardello, A.; Cataldo, S.; Marletta, G. *Materials Science & Engineering C-Biomimetic and Supramolecular Systems* **2003**, *23*, 7.
- (227) Pavlovic, E.; Oscarsson, S.; Quist, A. P. *Nano Letters* **2003**, *3*, 779.
- (228) Maoz, R.; Frydman, E.; Cohen, S. R.; Sagiv, J. *Advanced Materials* **2000**, *12*, 424.
- (229) Maoz, R.; Frydman, E.; Cohen, S. R.; Sagiv, J. *Advanced Materials* **2000**, *12*, 725.
- (230) Hoepfener, S.; Maoz, R.; Cohen, S. R.; Chi, L. F.; Fuchs, H.; Sagiv, J. *Advanced Materials* **2002**, *14*, 1036.
- (231) Hoepfener, S. M., R.; Sagiv, J. *Nano Letters* **2003**, *3*, 761.
- (232) Liu, S.; Maoz, R.; Schmid, G.; Sagiv, J. *Nano Letters* **2002**, *2*, 1055.
- (233) Matsubara, S.; Yamamoto, H.; Oshima, K.; Mouri, E.; Matsuoka, H. *Chemistry Letters* **2002**, 886.

- (234) Vettiger, P.; Despont, M.; Drechsler, U.; Durig, U.; Haberle, W.; Lutwyche, M. I.; Rothuizen, H. E.; Stutz, R.; Widmer, R.; Binnig, G. K. *IBM Journal of Research and Development* **2000**, *44*, 323.
- (235) Wilder, K.; Soh, H. T.; Atalar, A.; Quate, C. F. *Review of Scientific Instruments* **1999**, *70*, 2822.

Table I "Surface Chemistry Reaction Schemes"

| | Reaction Scheme | Reference |
|---|---|-----------|
| |  | 222 |
| A | <p>Chloranil Test:</p>  | |
| B |  | 227 |
| C |  | 223 |
| D |  | 224 |
| E |  | 224 |
| F |  | 224 |

Chapter 2

Replacement Lithography



This work was done in close collaboration with Drs. Lloyd Carroll, Yufan He and Fang Tian. Their efforts are much appreciated and gratefully acknowledged. I also acknowledge the critical reading of this chapter by Drs. S. Krämer and T.L. Chasse.

This work was the subject of the publications, Ryan R. Fuierer, R. Lloyd Carroll, Daniel L. Feldheim, and Christopher B. Gorman, "Patterning Mesoscale Gradient Structures with Self-Assembled Monolayers and Scanning Tunneling Microscopy Based Replacement Lithography" *Advanced Materials*, **2002**, *14* (2) 154-157, and Christopher B. Gorman, R. Lloyd Carroll, Ryan R. Fuierer, "Negative Differential Resistance in Patterned Electroactive Self-Assembled Monolayer" *Langmuir*, **2001**, *17* (22) 6923-6930.

2.1 Introduction:

The requirement to fabricate at the meso- and nanometer (10^{-7} to 10^{-9} m) length scales will be essential for the future miniaturization of electronic and sensing devices. The spatial arrangement of functional materials on solid surfaces with artificial control has attracted attention for the construction of novel, surface-bound chemical systems. Potential applications range from fundamental scientific research in micro- and nanoscale surface chemistry, to practical applications such as chemical sensors and electronic or optical devices.

One promising candidate for the further miniaturization of electronics are materials that self-assemble. One particular type of molecular self-assembly involves a chemical process in which amphiphilic precursor molecules chemisorb to surfaces, producing films that are chemically bonded to that surface and are of monomolecular thickness. These materials are often organic in nature and are frequently termed soft materials.¹⁻⁴

Self-assembled monolayers (SAMs) have attracted considerable attention as patterning materials because of their spontaneous adsorption on certain surfaces, their excellent uniformity in molecular order, and their resistivity to various types of chemical etchants. SAM precursors can be considered bi-functional molecules that can bind to the substrate at one end (head), and an organic group that imparts a desired chemical functionality to the modified surface at the other end (tail).^{1,4} The surface reactions are thermodynamically

driven to completion, lowering the free energy of the system when chemisorbed to the surface creating stable two-dimensional films of high order. The amphiphilic nature of these precursors has allowed them to be chemically tailored to perform specific functions on a variety of substrates.⁵ Organothiols (R-SH) are one such family of materials that self-assembles to coinage metals (Au, Ag, Cu, Pt, Pd) through the formation of covalent bonds.^{4,6,7}

Self-assembled monolayers are excellent candidates for preparing template architectures at the molecular scale or as resist layers, however spatial resolution and rational placement at the molecular scale is often considered challenging. SAMs have been used with longer length scale lithography techniques ($> 1\ \mu\text{m}$), however there are some limitations with these more traditional techniques. Speculation exists that photolithography will not be able to create patterned features at the nanoscale (1 – 100 nm) cost effectively.⁸⁻¹⁰ Electron beam lithography is an alternative but does not permit definition of chemistry without subsequent processing steps.¹¹⁻¹³ Micro-contact printing offers a promising alternative to parallel lithography of self-assembling materials, however, has only begun to reach the sub-100 nm length scales at the present day.¹⁴⁻¹⁷ These methods are unable to replace one type of SAM system for a differing SAM at the molecular length scale. Scanning probe microscopy techniques appear particularly well suited for surface nanopatterning.¹⁸⁻²³

Scanning probe microscopy (SPM) is a family of surface based interface techniques that have been employed for investigating and manipulating materials from the molecular to

micrometer length scales. SPM techniques have emerged as a premier surface analysis methodology. Surface science on the sub-micro to atomic scale has certainly been advanced because of these tools. It was not long after the initial SPM development that the probe tips were used for lithographic applications on the atomic scale^{18,24-26} becoming some of the earliest demonstrations of scanning probe lithography (SPL). It was quickly observed during the characterization of SAMs that under certain instrument parameters the tip could modify the films, and thus the probe could additionally act as a stylus. Determining parameters in which the tip could image the film non-destructively, and alternatively act as a stylus to pattern the film, initiated the nanoscale probe lithography of SAM systems. For the work presented within, scanning tunneling microscopy (STM) has been the instrument employed for the patterning described. A basic description of STM operation, as well as more detailed information about the specific instrument used, can be found in Appendix A.1.

An early demonstration described by Bard and Kim consisted of the degradation of organothiolate resists ($C_{18}S$ -SAMs) on polycrystalline gold at ambient conditions under repeated scanning in the same area of the resist film, or through ‘voltage excursions’ by varying STM substrate bias and set point current parameters.²⁷ In the aforementioned experiment, a specific region of the SAM was scanned with the STM tip at constant bias and setpoint current (1.0 V and 1 nA, respectively), and the researchers observed a temporal modification in the appearance of the SAM. In another demonstration the tip was rastered close to the surface through decreasing the substrate bias, mechanically desorbing the SAM. This observation was supported by an apparent accumulation of material at the periphery of

the patterned area. Voltage pulses of 3 to 5 V were also observed to modify the SAMs. Crooks and co-workers produced patterns in C₁₈S-SAMs on gold by selectively removing the alkanethiolates with a large bias (*ca.* 3 V) and large tunneling currents (*ca.* 10 nA) applied to a STM tip with repeated scanning, creating patterns within resist layers. Their work clearly demonstrated how to controllably remove the resist layer, and supported the localized SAM removal by using exposed patterns as ultramicroelectrodes to detect an electrochemical probe (Ru(NH₃)₆) using cyclic voltammetry.²⁸ Later reports by the group provided experimental evidence which suggested a desorption process that was electrochemical in nature by varying the relative humidity in the patterning environment. Other groups have reported organosilane resist layers patterned with STM,^{19,29-31} and atomic force microscopy.^{19,32-35} Subsequent *ex-situ* treatments to patterned substrates such as metallization, wet chemical etching or the addition of a second self-assembly material to prepare nano- and mesostructures have also been reported.³⁶⁻³⁸

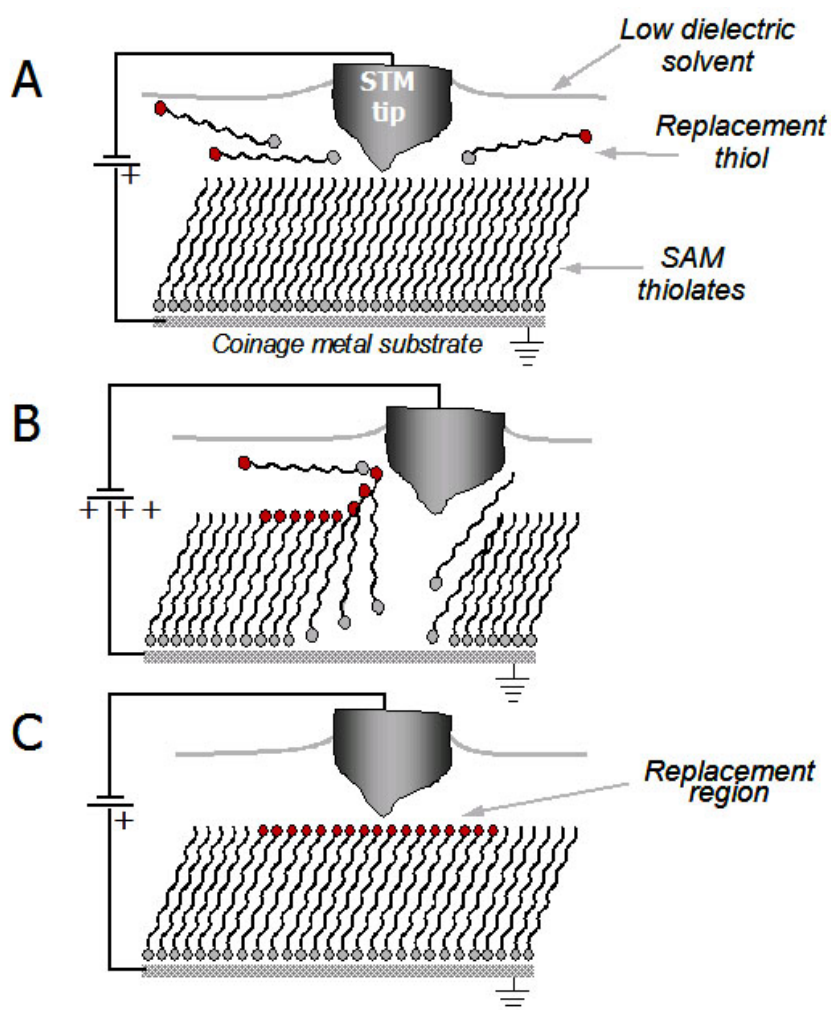
2.2 Results and Discussion:

The patterning described within involves an STM based replacement lithography technique in which SAM thiolates are selectively desorbed from a gold substrate and replaced with a second alkanethiol contained in the surrounding solution. The impetus of this patterning was to investigate the current *vs.* voltage (I-V) properties of electroactive moieties installed into alkylthiolate SAMs, the results of which will be discussed with more detail in Chapter 4. Electroactive species are interesting because of their potential to exhibit non-linear current

flow with applied voltage, which can provide potential bi-stability in a material for possible device applications. It was recognized that there was a need to perform measurements in a system that allows direct comparison to some other non-electroactive species. This required the ability to routinely pattern different thiol species at the nanometer length-scale. Once this was achieved, many other interesting film property investigations including I-V measurements, diffusion of thiolate species in or around the nanostructure (both laterally and with solution), and the stability of structures fabricated could be performed. This chapter focuses on the development of the optimal conditions needed to produce well-defined regions of the replaced thiol into dodecanethiolate SAMs ($C_{12}S$ -SAMs), which will often be referred to as the ‘canvas’ SAM.

A schematic of the replacement lithography methodology used to pattern SAMs is illustrated in Scheme 2.1 and has been described in detail elsewhere.³⁹⁻⁴² The process was performed in dodecane ($C_{12}H_{26}$), a non-polar low dielectric fluid ($\epsilon = 2.002$)⁴³ which served as a solvent for the replacement thiol of interest, and also facilitated imaging with negligible leak currents (typically *ca.* -0.003 nA at 1.0 V bias) into the solvent. The latter avoided the coating of the STM tip to limit leak currents, a task that proves difficult to reproduce with the concomitant possibility of the organic tip coating material contaminating the imaging fluid and surface. Prior to replacement (Scheme 2.1, Panel A), the substrate was imaged in order to locate an area free of defects and substrate terraces that were suitable in size for the desired pattern. Thiolate desorption from the Au (111) substrate was induced by elevating the substrate bias to *ca.* +3 V (Scheme 2.1, Panel B). This localized desorption in proximity of the tip allowed

the replacement SAM precursor molecules in solution to adsorb into the freshly exposed gold regions, creating a new monolayer within the patterned region. Generally, the lithographic pattern (lateral excursion) was produced under computer software control with no user interference, however square patterns could also be produced by simply desorbing the monolayer within a specific sized scan area under replacement conditions. Once the desired



Scheme 2.1: Schematic of replacement lithography. A) SAM imaged at non-perturbative imaging bias to locate an area free from defects and substrate facet terraces suitable for patterning. B) Upon an increase in substrate bias, the SAM thiolates are desorbed in proximity of the tip, resulting in the removal of the SAM. The replacement molecules in solution assemble into the freshly exposed regions of the gold. C) The pattern is assessed under imaging bias.

lithographic pattern was complete, the STM parameters were returned to the lower imaging bias parameters to ascertain the nanostructure (Scheme 2.1, Panel C).

The ‘canvas’ monolayer in this work was typically a dodecanethiolate SAM ($C_{12}S$ -SAM) assembled on a Au (111) substrate. Atomically flat surfaces of Au (111) were prepared by melting the end of a 0.5 mm diameter of Au wire in a H_2 flame, forming a Au bead that was subsequently zone refined to yield facets along its equatorial region, a process previously described in the literature.^{28,42,44,45} The $C_{12}S$ -SAMs were typically produced by incubating the Au substrate in refluxing 1mM dodecanethiol ethanolic solutions for approximately 1 hour, allowed to cool to room temperature, rinsed with absolute EtOH (AAPER Alcohol and Chemical Co.), and dried in a stream of N_2 . The advantage of using a $C_{12}S$ -SAM was that the alkyl chain is long enough to promote stable, well ordered monolayers, but short enough to employ low current STM imaging parameters (1.0 V, 10 pA). These parameters permitted the tip to reside just outside the monolayer during imaging, as suggested by Weiss and co-workers.^{46,47} The advantages of using this particular Au(111) surface was in its ease of preparation, and large areas of atomically flat terraces on the order of $(1.0 \mu m)^2$ could be routinely obtained (Figure 2.1A). Areas of this size were more than sufficient for patterning on the length scales described below. A typical high resolution STM image illustrating the molecular order of these films can be seen in Figure 2.1B. Long-range molecular order is visible in the corrugation /packing of the $C_{12}S$ - molecules within the domains. The film also possesses defects such as domain boundaries, surface vacancy islands,^{1,4,45,46,48-52} and even individual thiolates missing within the ordered domain regions.

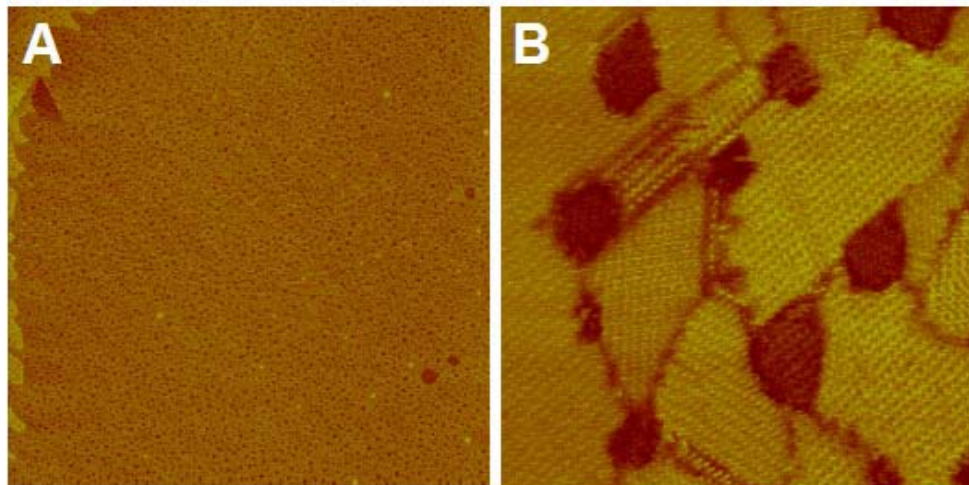


Figure 2.1: Typical STM images of dodecanethiol self-assembled monolayers ($C_{12}S$ -SAM) on Au(111). A) $(1.0 \mu\text{m})^2$ area of $C_{12}S$ -SAM showing large atomically flat Au(111) areas produced with this annealing technique. (Imaging conditions: 1.0 V, 10 pA, 1 Hz, z -scale: 2 nm). B) $(50 \text{ nm})^2$ area showing molecular order of the film. (Imaging conditions: 1.0 V, 10 pA, 1 Hz, z -scale: 0.8 nm).

These defects were typically on a length scale much smaller than that of the intended pattern, and were not considered to inhibit the overall lithography quality.

2.3 Replacement Lithography with *n*-Alkylthiolates:

Scanning tunneling microscopy images are inherently a convolution of the topography and the electronic properties of the surface. The setpoint current and voltage used to establish the tunneling gap in STM images (obtained in constant current mode) are directly influenced by the surface properties. It is also known that the electron tunneling current through vacuum or air decreases exponentially with distance.⁵³ When imaging *n*-alkylthiolate films with STM, there exists a double tunnel junction that consists of the resistance of the gap between the tip

and film (R_{gap} , established by the imaging parameters), and that of the monomolecular film (R_{film}) which is an intrinsic property of that material.⁴⁶ These combined resistances give the total resistance (R_{total}) of the double tunnel junction. Weiss and coworkers demonstrated that when imaging SAM systems that were composed of *n*-alkylthiolates of differing chain lengths ($C_{10}S-$ & $C_{12}S-$) in vacuum at 1.0 V and 10 pA, changes in the apparent height between the different chain lengths did not yield accurate height differentials due to the two film resistance components.^{46,47} They contended that this result occurred because the R_{film} was lower than that of R_{gap} . This observation was supported by a film height differential between $C_{10}S-$ and $C_{12}S-$ of 1.1 Å, however the calculated difference between these two films is 2.2 Å.

In contrast to the previously described system, imaging in dodecane produced an apparent height contrast reversal in STM images of SAMs containing differing *n*-alkylchain lengths. The phenomena was also anticipated by Weiss,^{46,54} and experimentally shown by Gorman.^{40,42} Weiss hypothesized that when the two films are immersed in a medium that has a R_{gap} lower than the films (R_{film}), the apparent height would be inverted. Empirically, this would imply that as the tip passes over a film of higher conductance to lower conductance (i.e. shorter to longer alkyl chain length), the tip must approach the surface to maintain the setpoint current due to the higher resistance of the film.

In the first replacement lithography report by our group, this contrast reversal was demonstrated in a series of eloquent experiments.⁴⁰ In one demonstration, mixed monolayer

systems of *n*-alkylthiols were employed with 10:1 molar ratios to unambiguously assign the minority species in STM images. A mixed monolayer containing a 10:1 ratio of C₁₂SH to decanethiol (C₁₀SH) showed the minority species displayed a higher apparent height relative to the majority C₁₂S-SAM when imaged under dodecane. The higher conductance of C₁₀S-alkylthiolate caused the STM feedback to retract from the surface to maintain the setpoint current, depicting a larger apparent height (brighter) in the STM images collected under dodecane. A control experiment of the same mixed monolayer system imaged in air showed the (expected) opposite result. When the ratios of the mixed monolayer were reversed (10:1 C₁₀SH to C₁₂SH), the C₁₂S- minority species displayed a lower apparent height relative to the majority C₁₀S- species, as expected. A second experiment demonstrated the contrast reversal by patterning two alkylthiols of differing chain lengths in a canvas SAM of medium length. Within a C₁₂S-SAM, C₁₀SH was patterned in the form of the letters ‘NCSU’, which displayed a larger apparent height relative to the ‘canvas’ C₁₂S-SAM. Above this, C₁₆SH was patterned in the same letter pattern, and appeared to have a lower apparent height relative to the canvas SAM. This experiment demonstrated the apparent height contrast reversal of the short (C₁₀S-) and longer (C₁₆S-) alkylthiols side by side within the medium length canvas C₁₂S-SAM. This report empirically supported the hypothesis of contrast reversal in STM images,⁵⁵ and also demonstrated the ability to pattern with multiple alkylthiolate ‘inks’ using this lithography technique. A depiction of contrast reversal can be seen in Figure 2.2. Starting with a C₁₂S-SAM (Figure 2.2A), a 200 nm x 200 nm hexadecanethiol (C₁₆S-SAM) square mesostructure was installed into the canvas SAM (Figure 2.2B) by attenuating the scan area

and operating under replacement conditions of 3.2 V, 10 pA and a relative humidity of 53%.

The longer $C_{16}S$ - molecule (20.1 Å) has a lower conductance than the $C_{12}S$ -SAM (15.1 Å),

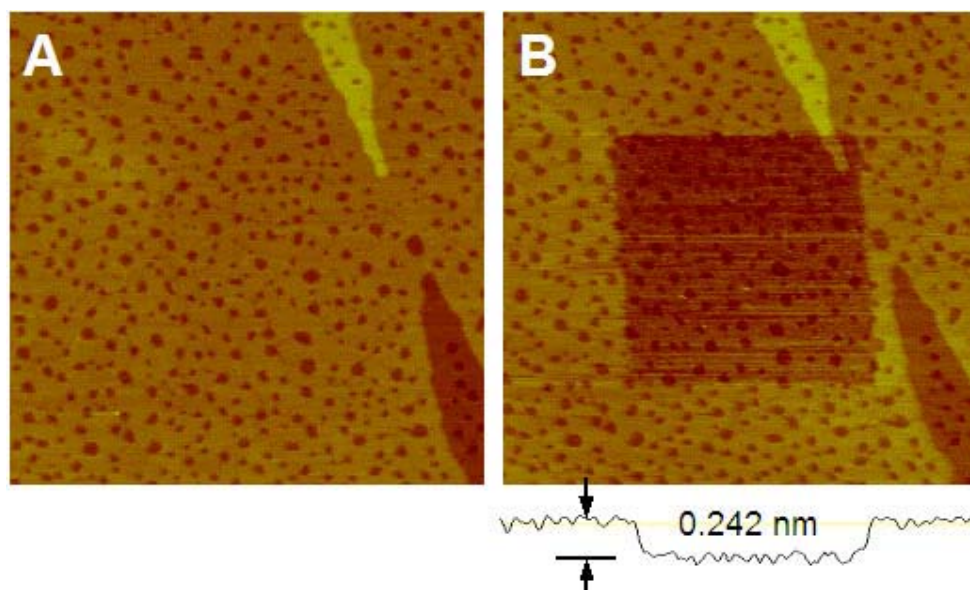


Figure 2.2: STM image of $C_{16}S$ -SAM patterned in $C_{12}S$ -SAM using replacement lithography. A) The $(400 \text{ nm})^2$ area of $C_{12}S$ -SAM before patterning, and B) after patterning. (Imaging conditions: 1.0 V, 10 pA, 1 Hz, z -scale: 2 nm, Replacement conditions: 3.2 V, 10 pA, 1 Hz, RH: 53%).

attenuating the tunneling current through the longer alkyl chain in the replaced region. This in turn caused the microscope feedback loop to decrease the tip-substrate distance to maintain the low set point current resulting in an appearance of depth (smaller z -scale value) in the topographic image. As seen in the averaged section analysis below Panel B, a height differential of -2.42 \AA was measured between the two SAMs. From Table A.1, the calculated film thickness difference is $+5.0 \text{ \AA}$. This gives a film height difference of 7.42 \AA , which is a result of the convolution of electronic properties and topography in STM images. This large

film height differential at these imaging conditions (1.0 V, 10 pA) may be a result of the tip being buried within the C₁₆S- monolayer as suggested by Weiss,⁵⁵ further convoluting the current measurement. Also noted in this image was the vacancy islands did not seem to be affected during the desorption process, suggesting that only the SAM thiolates were desorbed during patterning and no damage to the underlying gold occurred. Table A.1 shows the molecular structures and calculated length of the organothiol species used in the work presented.^{4,6}

2.4 Replacement Lithography of SAMs with Electroactive Moieties:

Other two component SAM systems have been studied in which the different organothiolates are of similar film thickness gave different apparent height contrasts because one of the SAM molecules contained a terminal electroactive moiety. In my own contribution to the development of the replacement lithography patterning technique described within, the electroactive replacement species most often used was ferrocenyl-undecanethioacetate (FcC₁₁SAc). The synthetic details of this molecule can be found in Appendix A.4. The use of this replacement molecule has many advantages, one of which included large apparent height contrasts relative to the canvas SAM. If the replacement molecule did not contain an electroactive moiety, it would not have been expected to display such height contrast due to the similar lengths of the two molecules (Table A.1). An example of the large apparent height contrast can be seen in Figure 2.3, which shows a 400 nm x 400 nm image of a quarter-foil pattern,^{A.2.1} fabricated under the replacement conditions of 3.1 V, 8 pA, 40 nm/s

and relative humidity (RH) of 59% (the importance of the replacement parameters will be discussed in detail below). Typical concentrations of the ferrocenyl species within the fluid cell containing the substrate was on the order of 10 μM . Under the imaging conditions of 1.2 V and 8 pA, the apparent height contrast was large relative to the C_{12}S -SAM, allowing the

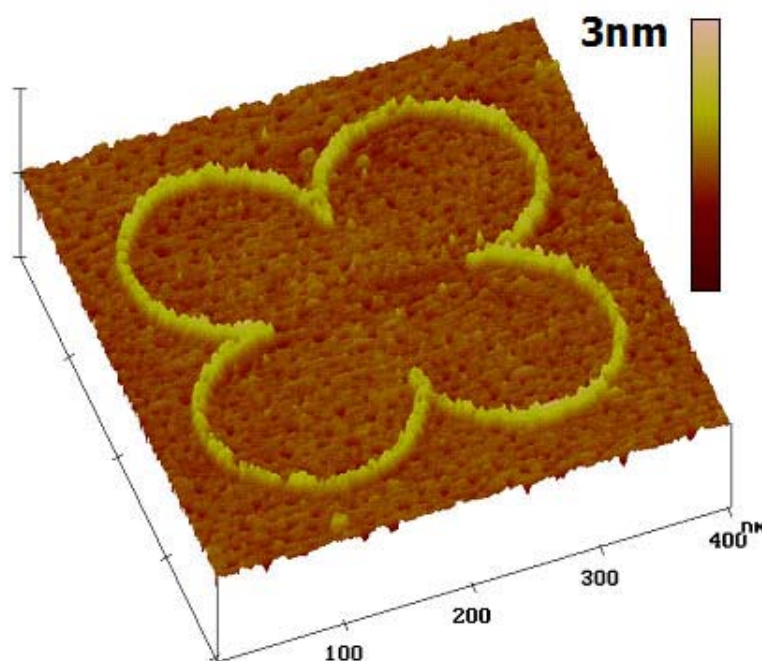


Figure 2.3: A $(400 \text{ nm})^2$ STM image of a quarterfoil pattern consisting of FcC_{11}S - replaced into a C_{12}S -SAM. (Imaging conditions: 1.2 V, 8 pA, 1 Hz, z -scale: 3 nm, Replacement conditions: 3.1 V, 8 pA, 40 nm/s, RH: 59%).

efficacy of the replacement process to be easily ascertained. This finding was believed to be from the enhanced tunneling currents through the terminal electroactive ferrocenyl moiety.

It has been demonstrated that molecules containing redox active moieties display apparent height contrast with STM imaging bias, allowing electroactive molecules to be distinguished from non-electroactive molecules.⁵⁶⁻⁵⁸ The electroactive moiety of the ferrocenyl SAM patterns used here also demonstrated this property, observed in Figure 2.4 showing three (500 nm)² STM images of the same pattern obtained at three different imaging biases. Their respective averaged line analyses shown in Panel D (the apparent height measurements were an average of three separate height measurements using the microscope image analysis software). An NC State logo^{A.2.2} was patterned under the replacement conditions of 3.0 V, 50 nm/s, 10 pA and RH of 57 %. In this patterning system, the C₁₂S-SAM (15.1 Å) and ferrocenylundecane thiol (16.8 Å) have similar film thicknesses (Table A.1). The canvas C₁₂S-SAM has been reported to have insulating properties in current-voltage measurements^{40,54,58-63} and does not display the imaging dependent contrast behavior, making it an excellent reference material to demonstrate this phenomena in a two SAM system. At the low image bias (upper Panel A, 100 mV imaging bias), the pattern is difficult to discern relative to the background C₁₂S-SAM, resulting in the monolayer appearing to have the same uniform height (0.007 nm ± 0.007 nm between C₁₂S-SAM and FcC₁₁S- pattern). Presumably, these two SAMs had comparable conductances at this imaging bias. At an intermediate bias (Panel B, 500 mV), the ferrocenyl ‘ink’ has a larger height contrast relative to the canvas C₁₂S-SAM (0.289 nm ± 0.014 nm). The highest bias (Panel C, 1500 mV imaging bias) clearly demonstrates the chemical definition of the pattern through a large apparent height contrast (0.352 nm ± 0.007 nm). The ability to vary the apparent height contrast of the ferrocenyl pattern with applied bias in STM images was a completely reversible process. At

higher bias (1500 mV), the electroactive moiety had a higher conductance allowing larger tunneling currents to pass between the tip and substrate over the patterned regions.

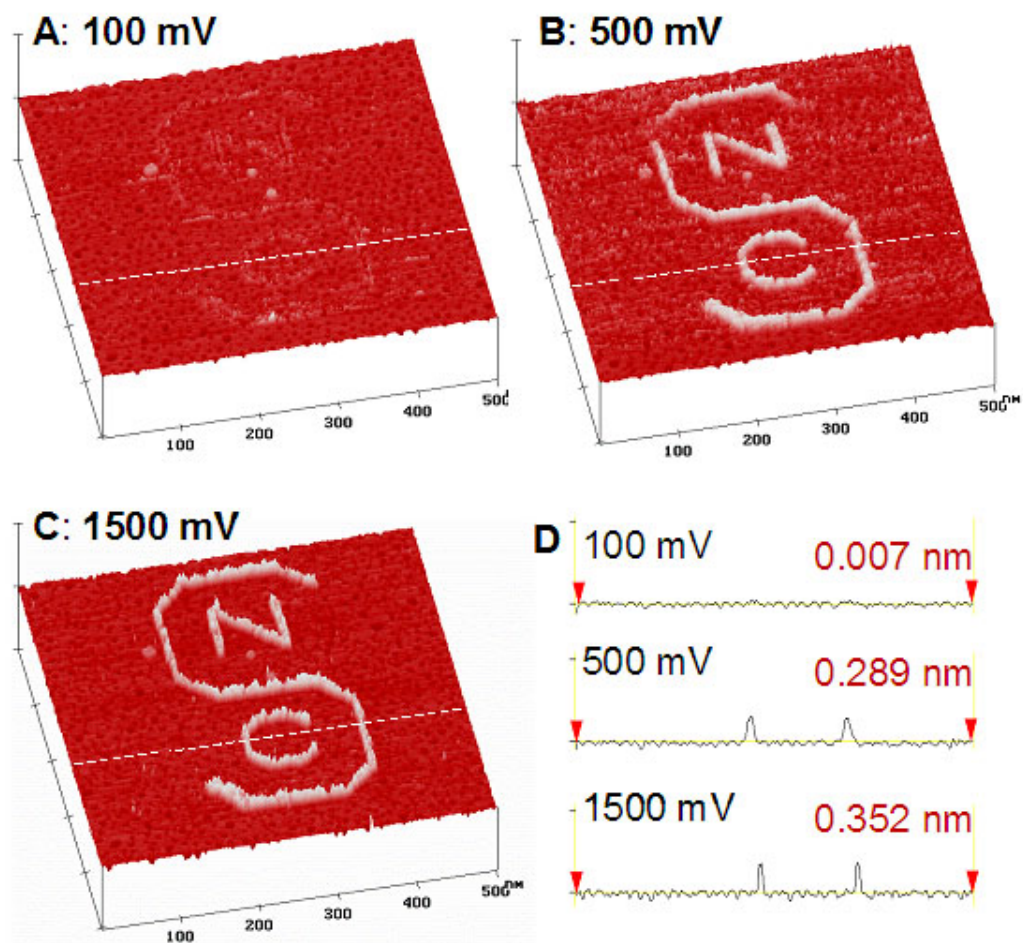


Figure 2.4: Three (500 nm)² STM images demonstrating the apparent height contrast dependence of FcC₁₁S- with imaging bias. A) Image bias 100 mV. B) Image bias 500 mV. C) Image bias 1500 mV. D) Section analysis (depicted by dotted line) showing contrast between patterned FcC₁₁S- SAM and C₁₂S-SAM. (Imaging conditions: 10 pA, 1 Hz, z-scale: 3 nm; Replacement conditions: 3.0 V, 10 pA, 50 nm/s, RH: 57%).

We hypothesized this phenomena occurred via resonant tunneling through the electroactive ferrocenyl moiety, discussed in more detail in Chapter 4. It is believed that the ferrocenyl moiety possesses an accessible molecular orbital that allows larger currents to pass through the metal-SAM-metal junction at higher image biases.⁴¹ This experiment provides an excellent example that STM images are a convolution of topography and electronic properties of a surface.

One concern when patterning systems with self-assembly components is preserving a chemical definition between the patterns. The acetyl protected ferrocenyl SAM precursor was preferentially used compared with the thiol counterpart to reduce the amount of adventitious replacement (that is, replacement not stimulated by the action of the tip) into the defect sites intrinsic to the C₁₂S-SAM. The ability to pattern the replacement thio- species into the canvas monolayer while maintaining chemical definition could occur for longer time durations. This effect can be seen qualitatively in Figure 2.5, which compares the thiol and thioacetyl terminated ferrocenyl SAM precursors adventitiously adsorbed as guests in host C₁₂S-SAMs. Panel A shows a (300 nm)² STM image of a C₁₂S-SAM that was incubated for 30 minutes in a 1 mM ethanolic solution of ferrocenyl-undecanethioacetate (Fc(CH₂)₁₁SCOCH₃), whereas Panel B shows a (300 nm)² STM image of a C₁₂S-SAM incubated in a 1 mM ethanolic solution of ferrocenylundecanethiol (Fc(CH₂)₁₁SH) for the same incubation period. The adventitious deposition procedure of the ferrocenyl species was adapted from previous literature reports of similar systems.^{54,62} The C₁₂S-SAM incubated in

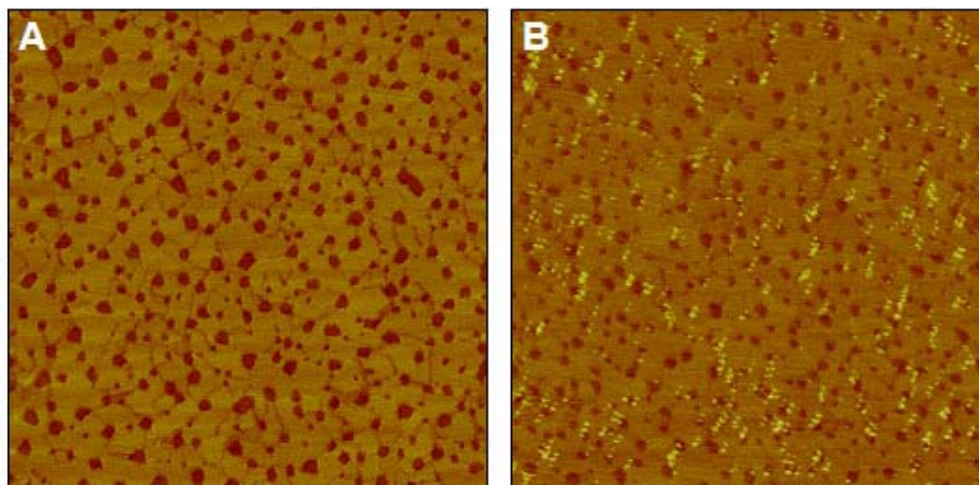


Figure 2.5: Two $(300 \text{ nm})^2$ STM images comparing the amount of adventitiously replaced FcC_{11}S - guest species into a C_{12}S -SAM after a 30 minute incubation. Below each image is a histogram representing the pixel colors contained within image. A) The SAM incubated $\text{FcC}_{11}\text{SCOCH}_3$ (thioacetate species). B) The SAM incubated FcC_{11}SH (thiol species). (Imaging conditions: 1.0 V, 10 pA, 1 Hz, z -scale: 2 nm).

the acetyl protected thiol showed very little guest ferrocenyl species adventitiously adsorbed into the host monolayer. In contrast, the SAM incubated in the thiol solution showed a pronounced amount of adventitiously adsorbed guest molecules, denoted as the bright spots in the images.

The mechanistic difference between the two thio-species remains unclear. Although there was never a deprotecting agent incorporated in the liquid STM cell during patterning, deprotection of the thioacetate occurred allowing for the chemisorption process to occur in the patterned regions in a timely fashion. Whether a small amount of thioacetate was

deprotected adventitiously in solution, or if the elevated substrate bias during the desorption event promotes deprotection has yet to be determined.

2.5 Investigation of Replacement Efficacy:

As reviewed in Chapter 1, many other SPL techniques have a lithography parameter influence on the resulting pattern features / structures. Extending an initial investigation from our group,⁴⁰ replacement lithography was observed to be dependent on three parameters: (1) the bias needed to desorb the SAM thiolates, called the ‘replacement bias’, (2) the lithographic scan rate, and (3) the relative humidity present in the atmospheric chamber surrounding the STM head. A series of experiments was performed to investigate each of these parameters and will be discussed in detail below.

Replacement Bias:

The first lithographic parameter investigated was the bias required to desorb the SAM thiolate from the substrate, which was undoubtedly one of the key events for subsequent replacement thiol adsorption to occur.³⁹ Figure 2.6 shows the resulting nanostructures obtained when systematically varying the replacement bias. The lithographic pattern shown contained two rows of six parallel lines, each 200 nm in length and separated by 100 nm.^{A.2.3} In this experiment, lithographic scan rate (50 nm/s), tunneling set point current (8 pA), and

relative humidity (57%) were kept constant, while the replacement bias was incrementally increased by 100 mV as each sequential line was drawn. At low replacement bias (2.6 to 2.8 V), no replacement of the $\text{FcC}_{11}\text{S-}$ into the $\text{C}_{12}\text{S-SAM}$ occurred, supported by no observable modification of the $\text{C}_{12}\text{S-SAM}$ in those regions of the pattern. As the replacement bias was increased, the extent of replacement increased. A bias range of 3.2 to 3.4 V gave optimal replacement of the $\text{FcC}_{11}\text{S-}$ into the background SAM, demonstrated by consistent line widths and replacement of the ferrocenyl species throughout the patterned lines. As the replacement bias was further increased, the efficacy of replacement was less controllable. At higher bias, inconsistent line widths and etching of the Au substrate beneath the monolayer occurred. The latter was suggested by the dark line parallel through the middle of the line patterned at 3.7 V.

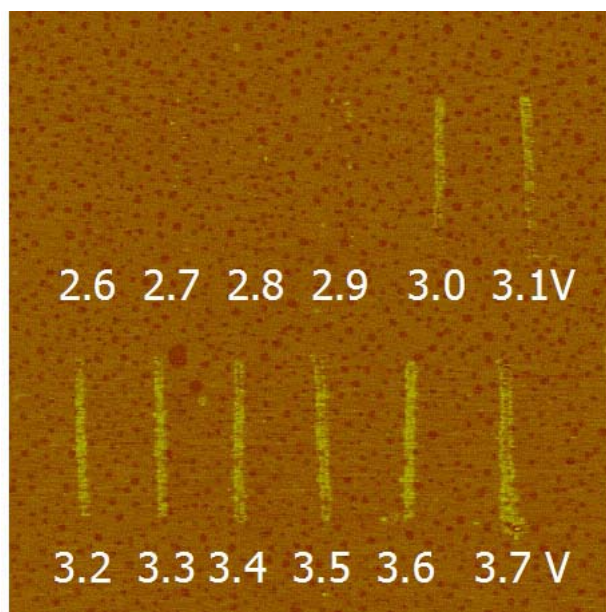


Figure 2.6: STM image (750 nm^2) demonstrating efficacy of thiol replacement with systematic variation of positive substrate replacement bias. (Imaging conditions: 1.0 V, 8 pA, 1 Hz, z -scale: 3 nm; Replacement conditions: 8 pA, 50 nm/s, RH: 57%, bias listed under each patterned line).

Crooks and coworkers suggested that the thiolate monolayer desorption under elevated substrate biases ($> 3\text{V}$) was electrochemical in nature. To support that the desorption event in replacement lithography was an oxidative process, it was hypothesized that patterning with negative substrate bias would not produce the same pattern efficacy as seen with positive substrate bias. A similar lithographic pattern was used as in the experiments with the positive substrate bias (six lines *ca.* 200 nm in length separated by *ca.* 100 nm). The results of replacement lithography under negative substrate bias can be seen in Figure 2.7.^{A.2.4} The upper panel shows an initial patterning bias (leftmost line) of -2.5 V , incrementally increasing the negative bias to an ultimate bias of -3.0 V (rightmost line), under a constant set point current (8 pA), lithographic scan rate (40 nm/s) and relative humidity (53%). The lines have poor resolution, larger widths, and low apparent height contrasts relative to the $\text{C}_{12}\text{S-SAM}$. The lower panel in Figure 2.7 shows six lines written with a slightly more negative potential range (-2.8 V to -3.3 V) under the same experimental conditions. At more negative potentials, the lines became inconsistently wider (*ca.* 35 nm) and had much lower apparent height contrasts relative to patterns produced under positive substrate bias. It was also observed that the stability of the patterned lines in this experiment with subsequent scanning was diminished substantially. The desorption of the monolayer under negative polarity and subsequent replacement of the ferrocenyl ink was incomplete along the length of the pattern. These observations suggest that the process is not the same as under of positive substrate bias conditions, and support desorption in replacement lithography was an oxidative process.

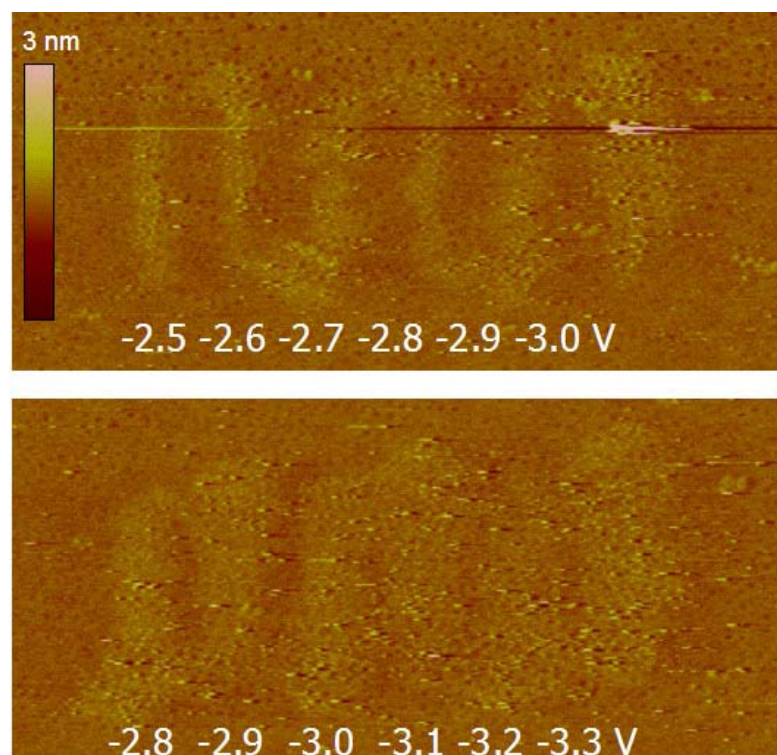


Figure 2.7: STM images (*ca.* 900 nm x 300 nm) of six replaced lines demonstrating efficacy of thiol replacement with systematic variation in negative substrate replacement bias. (Imaging conditions: -1.0 V, 8 pA, 1 Hz, *z*-scale: 3 nm; Replacement conditions: 8 pA, 40 nm/s, RH: 53%, bias listed under each patterned line).

Lithographic Scan Rate:

The lithographic scan rate was also observed to affect the degree of replacement within a pattern. Two STM images (*ca.* 950 nm x 300 nm) of a lithographic pattern that contained seven parallel lines, each 200 nm in length, spaced 100 nm apart,^{A.2.5} with the averaged horizontal line section analysis below (the averaged area is contained by the dotted line in the

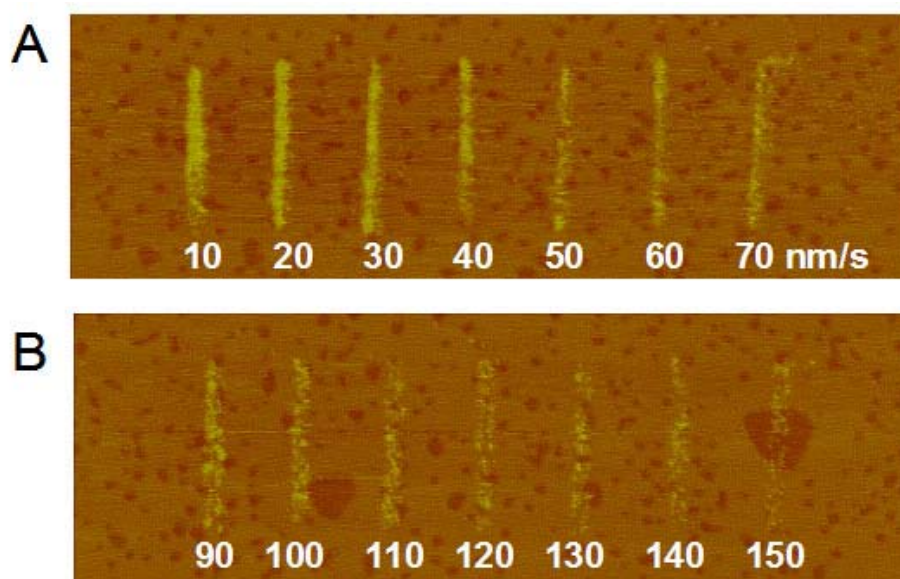


Figure 2.8: Two STM images (*ca.* 950 nm x 300 nm) demonstrating efficacy of thiol replacement with systematic variation lithographic scan rate. A horizontal averaged line analysis below each image, whose area is indicated by dotted line in the STM image. (Imaging conditions: 1.0 V, 8 pA, 1 Hz, *z*-scale: 5 nm; Replacement conditions: 3.2 V, 10 pA, RH: 58%, lithographic scan rate listed under each patterned line).

image) are displayed in Figure 2.8. In this set of experiments, the replacement bias (3.2 V), tunneling set point current (10 pA), and relative humidity (58%) were kept constant, while the lithographic scan rate was

incrementally increased by 10 nm/s for each sequential line patterned. At a low scan rate (10 nm/s), complete replacement of the FcC₁₁S- occurred, however the lines widths were larger and more inconsistent than those obtained using a slightly faster scan rate. As the scan rate was increased, 20 nm/s and 30 nm/s yielded optimal replacement with 10 to 15 nm line widths. Further increases in the

scan rate diminished the relative amount of replacement, causing the patterned lines to become blotchy. At very high scan rates (> 130 nm/s), the replacement of FcC₁₁S- within the patterned line appeared diffuse, presumably because the tip moved at a sufficiently high scan rate that did not promote complete desorption of the C₁₂S-SAM, and hence the ultimate replacement of the FcC₁₁S- species.

Effect of Relative Humidity:

The relative humidity present in the patterning environment had a pronounced effect on the degree of thiolate desorption. Other groups have observed this dependency in SPM lithography strategies involving SAM desorption, suggesting the desorption process was electrochemical in nature. Crooks *et al.* initially observed that relative humidity played a crucial role in desorption of C₁₈S-SAMs on gold. Sugimura and coworkers have reported the atmospheric moisture that condenses between SPM tip and silane SAMs created an electrochemical reaction vessel that facilitated the anodic oxidation of silicon substrates.^{29-33,37} It was hypothesized that even though our patterning technique was performed under dodecane (a non-polar hydrophobic solvent), a sufficient amount of water was somehow absorbed /adsorbed to aid in an electrochemical thiolate desorption event. To support the validity of this hypothesis, a series of lithographic experiments were performed at various relative humidities consisting of patterning of a series of lines of incrementally increasing bias while maintaining a constant setpoint current and scan rate. The upper schematic in Figure 2.9 shows the lithographic pattern^{A.2.6} used in each of the relative humidity

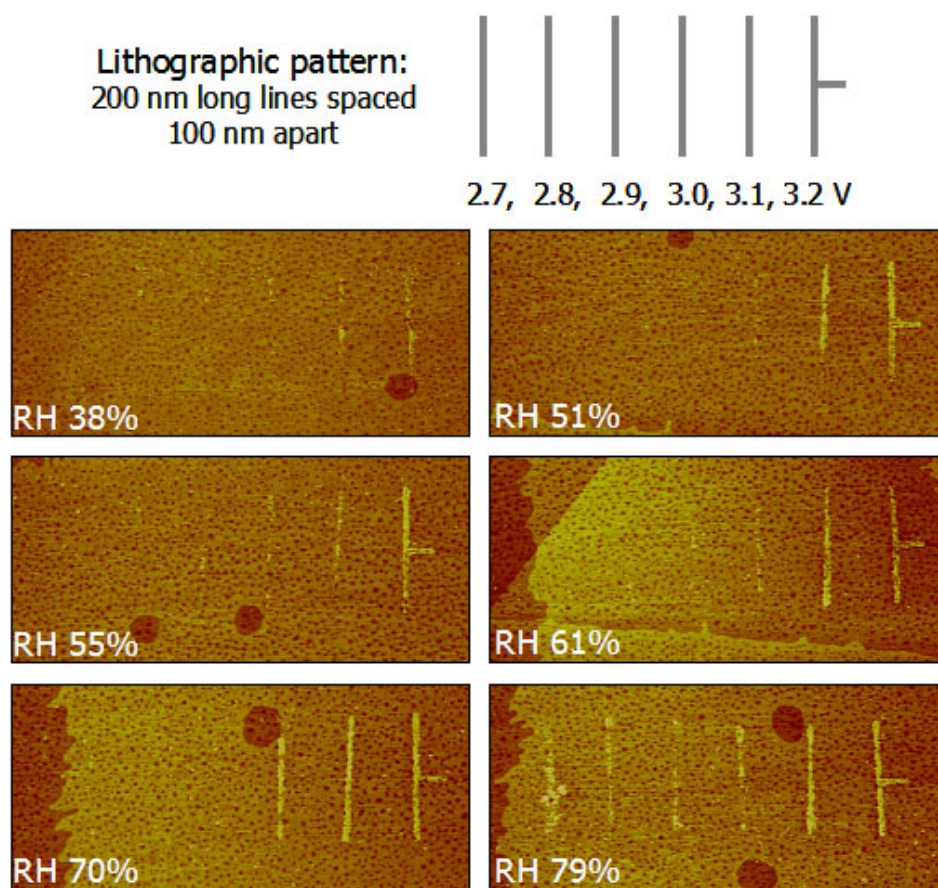


Figure 2.9: Schematic of the lithographic pattern indicating replacement bias for each line for relative humidity experiments. A series of six STM images (*ca.* 800 nm x 250 nm) demonstrating the efficacy of thiol replacement with a systematic variation in relative humidity ranging from 38% to 79%. (Imaging conditions: 1.0 V, 10 pA, 1 Hz, *z*-scale: 3 nm; Replacement conditions: 2.7 to 3.2 V, 10 pA, relative humidity listed in each image).

experiments (six parallel lines 200 nm long separated by 100 nm), starting at a replacement bias of 2.7 V and incrementally increasing by 100 mV per line to a final patterning bias of 3.2 V. The series of STM images shows that as the relative humidity incrementally increased from 38% to 79%, the degree of replacement in the lines over the range of replacement biases increased. At a relative humidity of 79%, there was less control over the replacement

of the pattern, resulting in inconsistent line widths. Through empirical experience, it has been observed that relative humidity ranges of 55% to 60% resulted in optimal lithographic results for these monolayer systems.

2.6 Patterning with Other Electroactive SAMs:

To further test our hypothesis that electroactive tethered thiols display imaging bias dependent height contrasts, another electroactive thiol species (phenoxy galvinol-substituted hexanethiol ($\text{GalC}_6\text{S-}$, 19.9 Å, Table A.1) was investigated. Electrochemical results have been reported with this molecule previously.⁶⁴⁻⁶⁶ A $(100 \text{ nm})^2$ square pattern was fabricated by decreasing the scan area, and the SAM thiolate was desorbed with a bias of 2.8 V and 10 pA, under a relative humidity of 63% (Figure 2.10). Two $(200 \text{ nm})^2$ STM images display the resulting pattern imaged at 100 mV (Figure 2.10A) and 1800 mV (Figure 2.10B) bias, with the respective average section analysis line trace below each image. The large, bulky headgroup of the galvinol terminus prevented packing of a well-ordered monolayer, as can be observed in the replaced patterned region of the low bias image (Figure 2.11A). Notably, the surface vacancy islands didn't appear to have been altered during the canvas SAM desorption, which supports that only the canvas thiolates were desorbed at this bias and replacement of the $\text{GalC}_6\text{S-}$ species did indeed occur. The averaged line section analysis shows virtually no difference in apparent height between the replaced region and the canvas SAM at the low imaging bias. However, the apparent height contrast was so large due to the

higher conductance at a higher image bias, the substrate vacancy islands cannot be discerned within the patterned region.

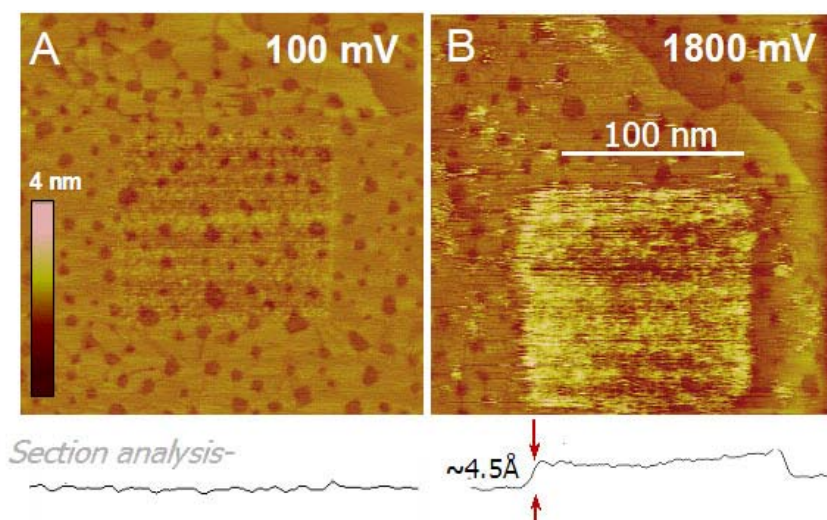


Figure 2.10: Two $(200 \text{ nm})^2$ STM images showing the imaging bias dependence of a $(100 \text{ nm})^2$ pattern containing galvinol substituted hexanethiolate replaced into C_{12}S -SAM. Averaged line analysis found below each image (Imaging conditions: 1.0 V, 10 pA, 1 Hz, z-scale: 4 nm; Replacement conditions: 2.8 V, 10 pA, 1 Hz, RH: 63%).

The section analysis shows an apparent height contrast differential of *ca.* 4.5 Å between the pattern and canvas C_{12}S -SAM. This experiment suggests that other SAMs containing electroactive moieties could show an apparent height contrast dependence on STM imaging bias.

A multiple ink patterning experiment was performed using the two electroactive inks (described above) to observe any similar apparent height contrasts at specific imaging biases

(Figure 2.11). Under a solution of *ca.* 10 μM galvinol substituted hexanethiol in dodecane, the galvinol tethered thiol was first installed into a C_{12}S -SAM in the letter pattern ‘Gal’^{A.2.7} under the replacement conditions of 3.0 V, 8 pA, 50 nm/s, RH: 59% (Figure 2.11A). The tip was retracted, the solution was removed with a syringe, the Au(111) facet rinsed twice with 120 μL aliquots of fresh dodecane, and finally exchanged with a solution of *ca.* 10 μM $\text{Fc}(\text{CH}_2)_{11}\text{SAc}$ in dodecane. The tip was reengaged, and the position of the ‘Gal’ pattern was found under normal imaging conditions. The letters ‘Fc’^{A.2.8} were patterned in close proximity under the same replacement conditions as the Gal pattern. The resulting two-ink pattern can be seen in Figure 2.12B. Although these two ‘electroactive inks’ shared similar current response at 1000 mV, the image at 250mV (Figure 2.11C) supported there were indeed two different inks replaced into the C_{12}S -SAM because of the slightly higher apparent

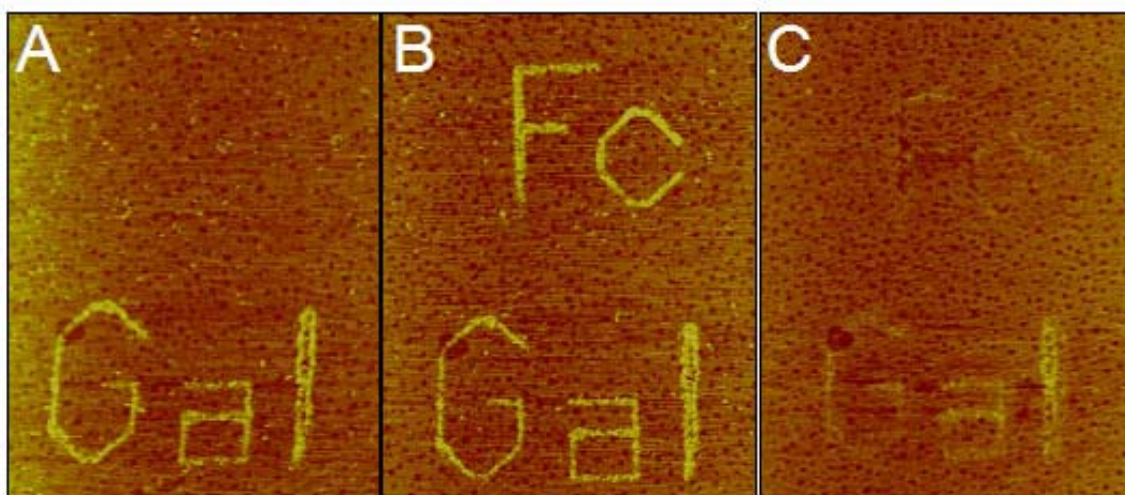


Figure 2.11: STM images (650 x 700 nm) demonstrating the process of patterning two electroactive inks in close proximity to each other. A) A galvinol thiol patterned first (in letters ‘Gal’), image bias 1000 mV, B) Image after ferrocenyl ink patterned (in letters ‘Fc’) in close proximity to the first. C) The apparent height contrast of differing inks at image bias 250 mV. (Imaging conditions: 8 pA, 1 Hz, *z*-scale: 5 nm; Replacement conditions: 3.0 V, 8 pA, 50 nm/s, RH: 59%).

height contrast of the galvinol termini. It was believed that the similar redox potentials of the two electroactive thiols (FcC₁₁S-, $E_{1/2} = +362$ mV vs. Ag/AgCl; GalC₆S-, $E_{1/2} = +381$ mV vs. Ag/AgCl)⁴¹ accounted for the similar apparent height contrasts at the various image biases investigated. Despite this, the experiment demonstrated the ability to pattern multiple inks in close proximity to each other with this lithographic technique.

2.7 Conclusion:

In conclusion, the replacement lithography technique described above selectively desorbs organothiolate SAMs in a predefined pattern, allowing a replacement thiol to adsorb onto the exposed gold in the patterned region. It has been demonstrated that determining the pattern efficacy could be aided using electroactive terminated thio- species due to their high apparent height contrasts relative to the background insulating SAMs at specific imaging biases. Using the ferrocenylthio-species, the replacement parameters were found to be dependent on replacement bias, lithographic rate of scan, and relative humidity. These results described above unambiguously demonstrate that the desorption event in replacement lithography was electrochemical in nature. By optimizing the parameters, typical line widths of *ca.* 10 nm can be achieved with this technique. In addition, this technique can pattern multiple organothiol inks in close proximity to each other.

2.8 Experimental:

Dodecane, dodecanethiol and hexadecanethiol were commercially obtained (Aldrich) and used without further purification. SAMs were formed by placing the freshly annealed Au substrates in a 1 mM C₁₂H₂₅SH ethanolic solution, refluxed for 1 hr, and allowed to cool to room temperature. The faceted ball was removed, rinsed with copious amounts of absolute ethanol and dried in a stream of N₂. Imaging and lithography was performed at room temperature with a Digital Instruments (Santa Barbara, CA) NanoScope IIIa (with low current adapter) in dodecane with mechanically cut Pt/Ir tips (90:10, 0.25 mm, Alfa Aesar). Relative humidity was introduced by bubbling N₂ through a gas dispersion tube into a closed vessel containing milliQ water (18 MΩ cm²), which fed the moist outlet gas into the atmospheric chamber containing the STM. The humidity was monitored with a hygrometer (Dickson, 0 to 95% relative humidity range).

2.9 References:

- (1) Ulman, A. *An Introduction to Ultrathin Organic Films from Langmuir-Blodgett to Self-Assembly*; Academic Press, Inc.: New York, 1991.
- (2) Whitesides, G. M.; Grzybowski, B. *Science* **2002**, *295*, 2418-2421.
- (3) Whitesides, G. M.; Boncheva, M. *Proceedings of the National Academy of Sciences* **2002**, *99*, 4769-4774.
- (4) Ulman, A. *Chemical Reviews* **1996**, *96*, 1533-1554.
- (5) Schwartz, D. K. *Annual Review of Physical Chemistry* **2001**, *52*, 107-137.
- (6) Porter, M. D.; Bright, T. B.; Allara, D. L.; Chidsey, C. E. D. *Journal of the American Chemical Society* **1987**, *109*, 3559-3568.
- (7) Poirier, G. E. *Chemical Reviews* **1997**, *97*, 1117-1127.
- (8) Tour, J. M. *Accounts of Chemical Research* **2000**, *33*, 791-804.
- (9) Mantooth, B. A.; Weiss, P. S. *Proceedings of the IEEE* **2003**, *91*, 1785-1802.
- (10) Carroll, R. L.; Gorman, C. B. *Angewandte Chemie International Edition in English* **2002**, *41*, 4378-4400.
- (11) McCord, M. A. *Journal of Vacuum Science & Technology A* **1997**, *15*, 2125-2129.
- (12) Marrian, C. R. K.; Tennant, D. M. *Journal of Vacuum Science & Technology A* **2003**, *21*, S201- S215.
- (13) Delamarche, E.; Hoole, A. C. F.; Michel, B.; Wilkes, S.; Despont, M.; Welland, M. E.; Biebuyck, H. *Journal of Physical Chemistry B* **1997**, *101*, 9263-9269.
- (14) Odom, T. W.; Love, J. C.; Wolfe, D. B.; Paul, K. E.; Whitesides, G. M. *Langmuir* **2002**, *18*, 5314-5320.
- (15) Odom, T. W.; Thalladi, V. R.; Love, J. C.; Whitesides, G. M. *Journal of the American Chemical Society* **2002**, *124*, 12112-12113.
- (16) Xia, Y.; Whitesides, G. M. *Angewandte Chemie-International Edition* **1998**, *37*, 550-575.

- (17) Xia, Y.; Whitesides, G. M. *Langmuir* **1997**, *13*, 2059-2067.
- (18) Eigler, D. M.; Schweizer, E. K. *Nature* **1990**, *344*, 524-526.
- (19) Lercel, M. J.; Craighead, H. G.; Parikh, A. N.; Seshadri, K.; Allara, D. L. *Applied Physics Letters* **1996**, *68*, 1504-1506.
- (20) Nyffenegger, R. M.; Penner, R. M. *Chemical Reviews* **1997**, *97*, 1195-1230.
- (21) Bottomley, L. A.; Coury, J. E.; First, P. N. *Analytical Chemistry* **1996**, *68*, 185R-230R.
- (22) Poggi, M. A.; Bottomley, L. A.; Lillehei, P. T. *Analytical Chemistry* **2002**, *74*, 2851-2862.
- (23) Krämer, S.; Fuierer, R. R.; Gorman, C. B. *Chemical Reviews* **2003**, *103*, 4367-4418.
- (24) Snow, E. S.; Campbell, P. M. *Science* **1995**, *270*, 1639-1626.
- (25) Snow, E. S.; Campbell, P. M. *Applied Physics Letters* **1994**, *64*, 1932-1934.
- (26) Stroschio, J. A.; Eigler, D. M. *Science* **1991**, *254*, 1319-1326.
- (27) Kim, Y. T.; Bard, A. J. *Langmuir* **1992**, *8*, 1096-1102.
- (28) Ross, C. B.; Sun, L.; Crooks, R. M. *Langmuir* **1993**, *9*, 632-636.
- (29) Sugimura, H.; Yamamoto, T.; Nakagiri, N.; Miyashita, M.; Onuki, T. *Applied Physics Letters* **1994**, *65*, 1569-1571.
- (30) Sugimura, H.; Uchida, T.; Kitamura, N.; Masuhara, H. *Journal of Physical Chemistry* **1994**, *98*, 4352-4357.
- (31) Sugimura, H.; Nakagiri, N. *Langmuir* **1995**, *11*, 3623-3625.
- (32) Sugimura, H.; Takai, O.; Nakagiri, N. *Journal of Electroanalytical Chemistry* **1999**, *473*, 230-234.
- (33) Sugimura, H.; Okiguchi, K.; Nakagiri, N.; Miyashita, M. *Journal of Vacuum Science & Technology B* **1996**, *14*, 4140-4143.
- (34) Liu, G.-Y.; Salmeron, M. B. *Langmuir* **1994**, *10*, 367-370.

- (35) Xiao, X. D.; Liu, G. Y.; Charych, D. H.; Salmeron, M. *Langmuir* **1995**, *11*, 1600-1604.
- (36) Schoer, J. K.; Ross, C. B.; Crooks, R. M.; Corbitt, T. S.; Hampden-Smith, M. J. *Langmuir* **1994**, *10*, 615-618.
- (37) Sugimura, H.; Nakagiri, N. *Journal of the American Chemical Society* **1997**, *119*, 9226-9229.
- (38) Zamborini, F. P.; Crooks, R. M. *Journal of the American Chemical Society* **1998**, *120*, 9700-9701.
- (39) Fuierer, R. R.; Carroll, R. L.; Feldheim, D. L.; Gorman, C. B. *Advanced Materials* **2002**, *14*, 154-157.
- (40) Gorman, C. B.; Carroll, R. L.; He, Y. F.; Tian, F.; Fuierer, R. R. *Langmuir* **2000**, *16*, 6312-6316.
- (41) Gorman, C. B.; Carroll, R. L.; Fuierer, R. R. *Langmuir* **2001**, *17*, 6923-6930.
- (42) Carroll, R. L. Ph.D., North Carolina State University, 2002.
- (43) Dean, J. A. *Lange's Handbook of Chemistry*; Thirteenth ed., 1985.
- (44) Hsu, T.; Crowley, J. M. *Ultramicroscopy* **1983**, *11*, 239-250.
- (45) Li, S.; Crooks, R. M. *Journal of the Electrochemical Society* **1991**, *138*, L23-L25.
- (46) Allara, D. L.; Dunbar, T. D.; Weiss, P. S.; Bumm, L. A.; Cygan, M. T.; Tour, J. M.; Reinerth, W. A.; Yao, Y.; Kozaki, M.; Jones, L. In *Molecular Electronics: Science and Technology*; NEW YORK ACAD SCIENCES: New York, 1998; Vol. 852.
- (47) Bumm, L. A.; Arnold, J. J.; Dunbar, T. D.; Allara, D. L.; Weiss, P. S. *Journal of Physical Chemistry B* **1999**, *103*, 8122-8127.
- (48) Edinger, K.; Golzhauser, A.; Demota, K.; Woll, C.; Grunze, M. *Langmuir* **1993**, *9*, 4-8.
- (49) Kawasaki, M.; Sato, T.; Tanaka, T.; Takao, K. *Langmuir* **2000**, *16*, 1719-1728.
- (50) Arce, F. T.; Vela, M. E.; Salvarezza, R. C.; Arvia, A. J. *Langmuir* **1998**, *14*, 7203-7212.
- (51) Poirier, G. E. *Langmuir* **1997**, *13*, 2019-2026.

- (52) Schöenenberger, C.; Sondag-Huethorst, J. A. M.; Jorritsma, J.; Fokkink, L. G. J. *Langmuir* **1994**, *10*, 611-615.
- (53) *Scanning Probe Microscopy and Spectroscopy: Theory, Techniques and Applications, Second Edition*; Second ed.; Bonnell, D., Ed.; John Wiley-VCH, Inc.: New York, 2001.
- (54) Bumm, L. A.; Arnold, J. J.; Cygan, M. T.; Dunbar, T. D.; Burgin, T. P.; Jones, L.; Allara, D. L.; Tour, J. M.; Weiss, P. S. *Science* **1996**, *271*, 1705-1707.
- (55) Weiss, P. S.; Bumm, L. A.; Dunbar, T. D.; Burgin, T. P.; Tour, J. M.; Allara, D. L. *Annals of the New York Academy of Sciences* **1998**, *852*, 145-168.
- (56) Tao, N. J. *Physical Review Letters* **1996**, *76*, 4066-4069.
- (57) Han, W.; Durantini, E. N.; Moore, T. A.; Moore, A. L.; Gust, D.; Rez, P.; Leatherman, G.; Seely, G. R.; Tao, N.; Lindsay, S. M. *Journal of Physical Chemistry B* **1997**, *101*, 10719-10725.
- (58) Carroll, R. L. Ph.D., North Carolina State University, 2002.
- (59) Chen, J.; Reed, M. A.; Asplund, C. L.; Cassell, A. M.; Myrick, M. L.; Rawlett, A. M.; Tour, J. M.; Van Patten, P. G. *Applied Physics Letters* **1999**, *75*, 624-626.
- (60) Bumm, L. A.; Arnold, J. J.; Charles, L. F.; Dunbar, T. D.; Allara, D. L.; Weiss, P. S. *Journal of the American Chemical Society* **1999**, *121*, 8017-8021.
- (61) Dunbar, T. D.; Cygan, M. T.; Bumm, L. A.; McCarty, G. S.; Burgin, T. P.; Reinerth, W. A.; Jones, L.; Jackiw, J. J.; Tour, J. M.; Weiss, P. S.; Allara, D. L. *Journal of Physical Chemistry B* **2000**, *104*, 4880-4893.
- (62) Cygan, M. T.; Dunbar, T. D.; Arnold, J. J.; Bumm, L. A.; Shedlock, N. F.; Burgin, T. P.; II, L. J.; Allara, D. L.; Tour, J. M.; Weiss, P. S. *Journal of American Chemical Society* **1998**, *120*, 2721-2732.
- (63) Wold, D. J.; Frisbie, C. D. *Journal of American Chemical Society* **2001**, *123*, 5549-5556.
- (64) Shultz, D. A.; Tew, G. N. *Journal of Organic Chemistry* **1994**, *59*, 6159-6160.
- (65) Sagara, T.; Midorikawa, T.; Shultz, D. A.; Zhao, Q. *Langmuir* **1998**, *14*, 3682-3690.
- (66) Finklea, H. O. In *Electroanalytical Chemistry*; Bard, A. J., Rubinstein, I., Eds.; Marcel Dekker, Inc.: New York, 1996; Vol. 19.

Chapter 3

Patterning Mesoscale Gradient Structures with Replacement Lithography



This work was done in close collaboration with Drs. R. Lloyd Carroll, Daniel L. Feldheim and Christopher B. Gorman. Their efforts are much appreciated and gratefully acknowledged. I also acknowledge the critical reading of this chapter by Drs. S. Krämer and T.L. Chasse.

This work was the subject of a publication, Ryan R. Fuieler, R. Lloyd Carroll, Daniel L. Feldheim, and Christopher B. Gorman, "Patterning Mesoscale Gradient Structures with Self-Assembled Monolayers and Scanning Tunneling Microscopy Based Replacement Lithography" *Advanced Materials*, **2002**, *14* (2) 154-157.

3.1 Introduction:

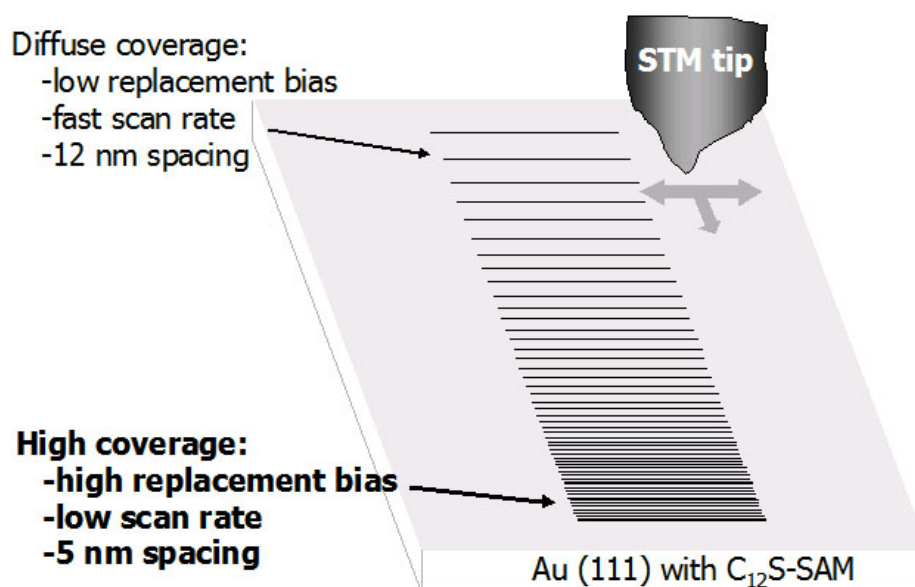
Chemical gradients are systems that possess a concentration differential of chemical functionality in one or more dimensions. They can transport materials in a directional manner, and are responsible for driving many important biological and physical processes. The growth of axons from ganglions to target tissues and the directed movement of certain bacteria toward nutrients occur in response to concentration gradients of molecules emanating from axon target or food source (chemotaxis).¹ Concentration gradients of molecules in fluids or on surfaces also affect phenomena such as osmotic swelling, surface pressure, and surface wettability. By learning to establish and manipulate these parameters, new methods of transporting fluids in microchannels are emerging which offer new transport paradigms for the fabrication of chip-based chemical devices.²

Surface-bound chemical gradients have previously been produced on millimeter to micron length scales.¹⁻¹¹ In some cases, these gradients have been used in directional transport. For example, Chaudhury and Whitesides fabricated self-assembled monolayer (SAM) gradients composed of decyltrichlorosilane on silicon substrates using a diffusion controlled vapor deposition technique. Water droplets were observed to travel uphill (15°) under the influence of the resulting spatial gradient in the surface free energy.³ Liedberg and co-workers prepared millimeter scale SAM gradients on gold surfaces by cross diffusing two different alkanethiols from opposite ends of a polysaccharide matrix.^{6,7,11} Efimenko and Genzer demonstrated the ability to tailor surface-bound gradients by fine-tuning the molecular grafting density of mechanically assembled monolayers on hydroxyl terminated silicon based substrates. They

used these gradients to demonstrate systematic control over the wettability of the resulting surfaces.⁹ Dertinger and Whitesides generated steady state solution gradients using laminar flow within microfluidic devices.¹² Krämer and Feldheim have recently demonstrated the ability to fabricate a variety of different surface bound protein gradients capable of supporting cell growth.¹³ Our approach to preparing chemical gradients was to use replacement lithography to fabricate mesoscale chemical gradients. By using the information about optimizing replacement lithography parameters needed to install one thiol into a canvas SAM, we hypothesized that we could fabricate the diffuse coverage end of a chemical gradient using sub-optimal replacement parameters, and systematically advancing them to optimal parameters in the high coverage end. With this approach, surface bound chemical gradients could be fabricated with scanning probe lithography at length scales never before demonstrated.

Using replacement lithography, surface bound chemical gradients were fabricated in which ω -substituted alkanethiolates patterned into C₁₂S-SAMs varying from diffuse coverage to more concentrated coverage over the length of the pattern. Due to the large apparent height contrast between the two SAMs, ferrocenyl-undecanethiol (FcC₁₁SAc) inserted into a dodecanethiolate C₁₂S-SAM on Au(111) was used to develop the optimal conditions needed to fabricate chemical gradients. By adjusting specific instrument parameters during replacement discussed in Chapter 2, the relative concentration of FcC₁₁S- inserted into the monolayer could be systematically varied along the pattern. These structures could be fabricated by systemically varying the replacement bias or the lithographic scan rate (or

both), while simultaneously varying the spacing between the patterned lines that constitute the overall gradient pattern. A typical approach to the line raster pattern used to fabricate the gradients is illustrated in Scheme 3.1. A line spacing of 12 nm was used in the diffuse coverage end, which was incrementally decreased to 5 nm in the high coverage end. The rationale behind this approach was based on the average line resolution of the replacement lithography technique. Line resolutions of 10 to 15 nm resulted in very little overlap of replacement lines in the diffuse coverage end, while complete overlap in the concentrated coverage end. This line spacing approach was employed for all gradient patterns described within.



Scheme 3.1: Gradient tip raster pattern. In diffuse coverage region, spacing between pattern lines was *ca.* 12 nm and either low replacement bias, fast lithographic scan rate, or both, were employed. These patterning parameters were incrementally varied across the length of the gradient to reach the high coverage region where spacing between pattern lines was *ca.* 4 nm and either higher replacement bias, slow lithographic scan rate, or both were employed. The set point current and relative humidity were kept constant.

3.2 Effect of Replacement Parameter on Gradient Fabrication:

The first approach for gradient fabrication varied the replacement bias along the length of the gradient pattern with a concomitant variation in the raster line spacing. A 200 nm x 720 nm mesoscale chemical gradient is shown in Figure 3.1¹⁸ In this experiment, the setpoint current (10 pA), lithographic scan rate (50 nm/s), and relative humidity (58%) were held constant. The structure was fabricated by beginning the lithographic pattern at a replacement bias that promoted diffuse coverage (2.6 V). The replacement bias was then incrementally increased

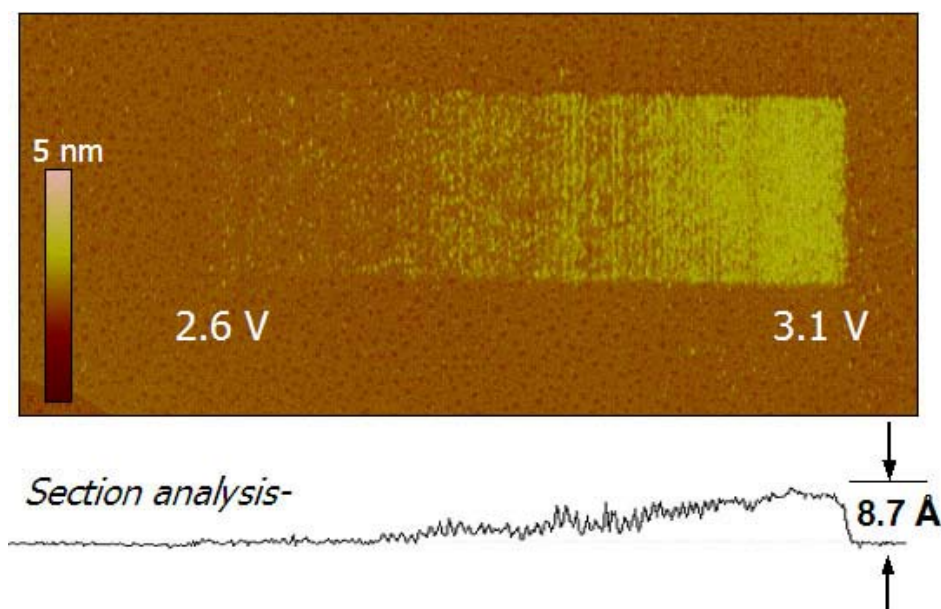


Figure 3.1; STM image (ca. 400 x 900 nm) of FcC_{11}S - mesoscale chemical gradient in C_{12}S -SAM fabricated by systematically varying the replacement bias from 2.6 V to 3.1 V while keeping the setpoint current (10 pA), scan rate (50 nm/s) and relative humidity (58%) constant. Averaged horizontal line section analysis immediately below the image demonstrating gradient nature of pattern. (Imaging conditions: 1.0 V, 10 pA, 1 Hz, z-scale: 5 nm)

by 20 mV every 3 to 5 lines drawn, arriving at the opposite end of the pattern at a bias (3.1 V) that promoted maximum degree of replacement. An average section analysis is shown below the image. This section analysis was obtained by averaging the height values of the data within a given horizontal scan line in the replaced region. It indicates an apparent height contrast differential of approximately 8.7 Å (measured between arrows) between the C₁₂S-SAM and the high coverage end of the gradient at an imaging bias of 1.0 V. As discussed previously (Chapter 2), although the two SAM molecules employed were similar in length (Table A.1), there was a distinct difference in apparent height between the FcC₁₁S-SAM and C₁₂S-SAM observed due to increased conductance at this imaging bias through the ferrocenyl headgroup.¹⁴ These systematic variations in replacement conditions promoted a gradual change in chemical heterogeneity between the FcC₁₁S- and C₁₂S-SAM along the pattern. It was also observed that the gradient mesostructure did not appreciably change in appearance over periods greater than twenty hours of continuous scanning under imaging conditions.

Alternatively, gradient structures could be constructed by systematically varying the lithographic scan rate, while maintaining all other STM parameters constant. Figure 3.2 shows a 200 nm x 600 nm gradient mesostructure fabricated by holding the replacement bias (2.8 V), set point current (10 pA) and relative humidity (60%) constant.¹⁹ Initially, a scan rate of 160 nm/s was employed to yield diffuse replacement. The scan rate was decreased incrementally by 10 nm/s every 3 to 5 raster lines in the pattern, until reaching at a final scan rate of 20 nm/s, creating a highly concentrated coverage pattern. The averaged section analysis for Figure 3.2 displayed an apparent height differential of approximately 9.9 Å

(measured between arrows) at an imaging bias of 1.0 V between the $C_{12}S$ -SAM and the concentrated (brighter) replacement side of the $FcC_{11}S$ -SAM gradient.

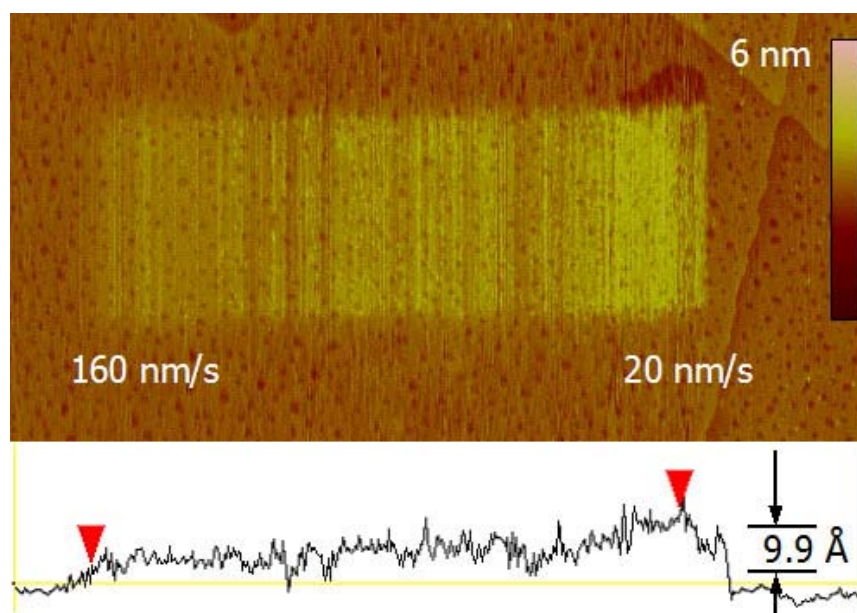


Figure 3.2: STM image (*ca.* 400 x 900 nm) of $FcC_{11}S$ - mesoscale chemical gradient in $C_{12}S$ -SAM fabricated by systematically varying the lithographic scan rate from 160 nm/s to 20 nm/s while keeping the setpoint current (10 pA), replacement bias (2.8 V) and relative humidity (60%) constant. Averaged horizontal line section analysis immediately below the image demonstrating gradient nature of pattern. (Imaging conditions: 1.0 V, 8 pA, 1 Hz, z-scale: 6 nm)

3.3 Multidirectional Gradients:

The next progression of mesoscale gradient production occurred by varying both the lithographic scan rate and replacement bias, while maintaining constant setpoint current and relative humidity. A multidirectional gradient structure (Figure 3.3) was fabricated

containing high replacement coverage at the ends of the “L” shape, and diffuse coverage in the elbow region.²⁰ This nanostructure was drawn with a constant setpoint current (10 pA) and relative humidity (58%), while systematically varying the replacement bias, lithographic scan rate, length of the pattern lines and the line spacing within the pattern. As the first (vertical) leg of the “L” was drawn, the replacement bias was decreased from 2.9

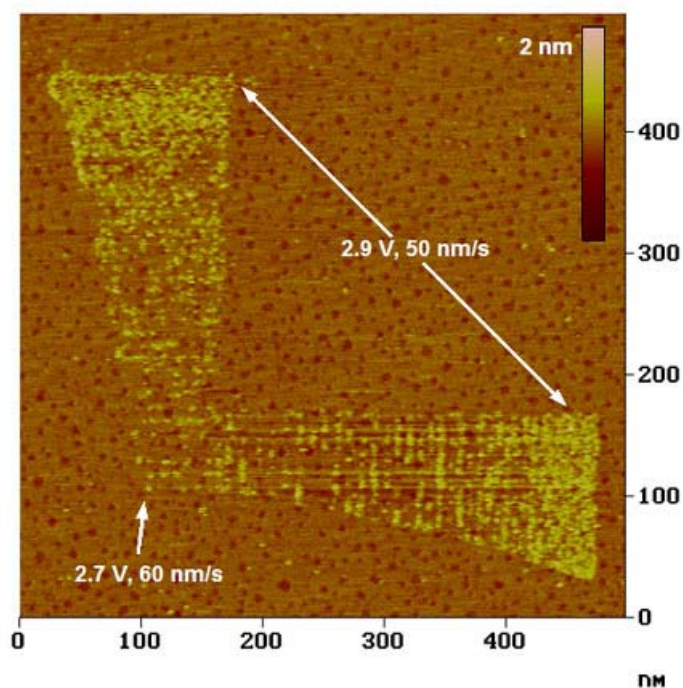


Figure 3.3: STM image of a multi-directional gradient (“L” shape) of $\text{FcC}_{11}\text{S-SAM}$ in $\text{C}_{12}\text{S-SAM}$. Structure was fabricated by systematically varying the replacement bias (from 2.95 V to 2.7 V), the lithographic scan rate (from 50 nm/s to 60 nm/s), lithographic line width (150 nm to 70 nm) and raster line spacing (4 nm to 11 nm), while maintaining constant setpoint current (10 pA) and relative humidity (58%) along each leg. (Imaging conditions: 1.0 V, 8 pA, 1 Hz, z-scale: 2 nm)

V to 2.7 V, the scan rate was increased from 50 nm/s to 60 nm/s, the line length was decreased from 150 nm to 70 nm and the raster line spacing was increased from 4 nm to 11 nm. The scan angle was then rotated 90 degrees and this process was repeated in reverse to draw the horizontal leg of the “L”.

A more complex, three-legged “Y” gradient structure was fabricated in a similar fashion to the “L” shaped gradient described above. This pattern consisted of the “L” shaped gradient described above, with an additional leg fashioned to extend from the elbow.²¹ A $(900 \text{ nm})^2$

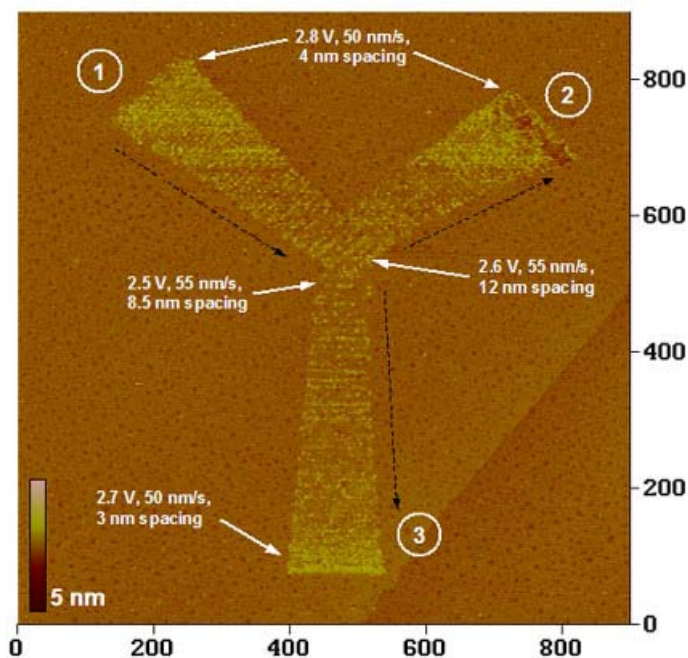


Figure 3.4: STM image of a three-legged gradient (“Y” shape) of $\text{FcC}_{11}\text{S-SAM}$ into $\text{C}_{12}\text{S-SAM}$. Structure was fabricated by systematically varying the replacement bias, the lithographic scan rate, and raster line spacing as depicted in image, while maintaining constant setpoint current (10 pA) and relative humidity (55%) along each leg. Image is annotated to depict replacement conditions along the gradient legs, fabricated in sequential order from Leg 1 to 3 following the direction of dashed arrows. (Imaging conditions: 1.0 V, 8 pA, 1 Hz, z-scale: 5 nm)

STM image is shown in Figure 3.4, which is annotated to depict how the structure was fabricated. Leg 1 of the gradient was created by decreasing the replacement bias from 2.8 V to 2.6 V, increasing the lithographic scan rate from 50 nm/s to 55 nm/s, and increasing the line spacing from 4 nm to 12 nm under a constant setpoint current of 10 pA and 55% relative humidity. Leg 2 was created perpendicular to Leg 1. The replacement commenced from a diffuse to more concentrated coverage by essentially reversing the replacement parameters found in Leg 1. Once Leg 2 was completed, Leg 3 was fashioned by moving the tip to the elbow of the “L” shape, and patterning approximately 130° with respect to leg 1 and 2. This gradient was fabricated from diffuse coverage to high coverage by increasing the bias from 2.5 to 2.7 V, decreasing the lithographic scan rate from 55 nm/s to 50 nm/s and decreasing the line spacing from 8.5 nm to 3 nm under constant setpoint current and relative humidity. It should be noted that determining the parameters for patterning was a trial and error process, consisting of many lithographic program adjustments before the finished product could be obtained. Finding the delicate interplay between replacement parameters was challenging, but once achieved, complex gradient mesostructures were fabricated.

3.4 Ex-Situ Treatment of Functionalized Gradients:

Mesostructure gradients fabricated with other ω -substituted SAM precursors were investigated to demonstrate the techniques' potential utility. A gradient structure consisting of mercaptoundecanoic acid ($\text{HS}(\text{CH}_2)_{10}\text{COOH}$, Table A.1) was fabricated using the lithographic macro used to create the replacement bias variation gradient described above.¹⁸

This structure required a diffuse coverage end created from a replacement voltage of 2.5 V that was incrementally increased to 3.0 V in the high coverage end under a constant setpoint current (10 pA), scan rate (50 nm/s) and relative humidity (51%). The resulting pattern is shown in Figure 3.5, with the averaged line section analysis depicting the gradient (sloping) nature of the pattern immediately below the image. Notably, the acid headgroups in the replaced region appear ‘darker’ than the surrounding C₁₂S-SAM. The section analysis showed an apparent height differential of -2.32 \AA from the top of the C₁₂S-SAM to the

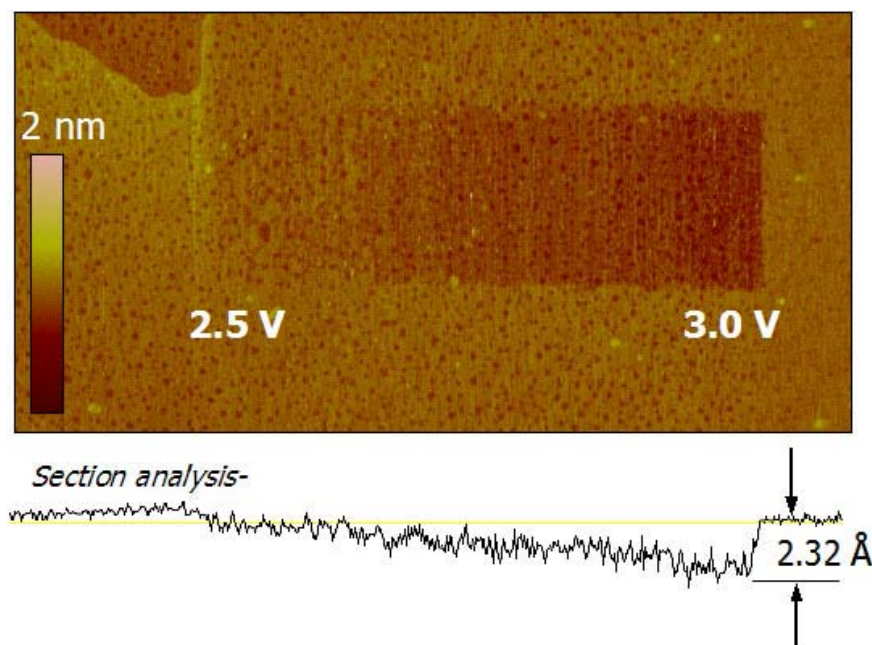


Figure 3.5: STM image (*ca.* 400 x 900 nm) of 200 nm x 720 nm HOOC(CH₂)₁₀S- mesoscale chemical gradient in C₁₂S-SAM fabricated by systematically varying the replacement bias (2.5 V to 3.0 V denoted in image) while keeping setpoint current (10 pA), scan rate (50 nm/s) and relative humidity (51%) constant. Average vertical line section analysis immediately below the image demonstrating gradient nature of pattern. (Imaging conditions: 1.0 V, 10 pA, 1 Hz, z-scale: 2nm)

lowest region of the replaced mesostructure. Padowitz and coworkers have suggested that a high oxygen content of the ω -termini alkylthiolate results in low z -scale values in the topography.¹⁵ Once again, this further demonstrates that STM images are a convolution of electronic and topographical properties.

The impetus behind construction of these mesoscale structures was to fabricate gradients consisting of a chemical terminus that could be further functionalized with other materials. By using a carboxylic acid terminus, it was hypothesized that gold nanoparticles (AuNPs) functionalized with amine terminated thiols could be introduced to the gradient in an *ex situ* step. Such an experiment would result in the amine coated particle immobilization on the gradient, the concentration of which should be proportional to the coverage of the carboxylic headgroup concentration in the gradient. Figure 3.6 demonstrates the experimental progression of this experiment. The first step was to locate an area of the $C_{12}S$ -SAM free of terraces and defects large enough to fabricate a gradient (Figure 3.6A). An equilateral triangle shaped topographical marker (a natural result from the Au(111) surface) in the upper left hand corner of the image was used to confirm the structure's location throughout the experiment. A carboxylic acid terminated SAM gradient was fabricated¹⁸ as described above (Figure 3.6B). Notably, the structure did not show a gradient from diffuse to complete coverage over the length of the pattern, but rather a diffuse to more concentrated, then a decrease in coverage towards the more concentrated part of the gradient. Although speculative, this may have been the result of lower replacement thiol concentrations after patterning multiple $-COOH$ terminated gradients on the substrate (prior to this one) to ensure

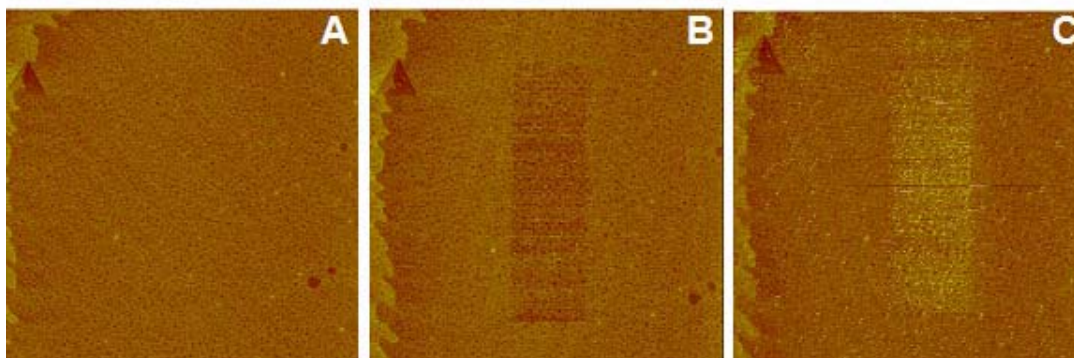


Figure 3.6: STM Image set demonstrating the successive process fabricating a $\text{HOOC}(\text{CH}_2)_{10}\text{S}$ - mesoscale chemical gradient, and installing amine terminated nanoparticles within. A) Area before gradient fabrication. B) Fabrication of an acid terminated gradient by systematically varying replacement bias and line spacing, while keeping setpoint, lithographic scan rate and relative humidity constant. C) Gradient mesostructure after aqueous incubation in $\text{H}_2\text{N}(\text{CH}_2)_7\text{S}$ - terminated 2 nm AuNPs. All imaging was carried out under dodecane. (Imaging conditions: 1.0 V, 10 pA, 1 Hz, z-scale: 2nm)

that one could be found after the post ex-situ treatment, a strategy employed for experimental efficiency. The tip was retracted and the structure (Au(111) facet) was then incubated in an aqueous solution of 2 nm AuNPs capped with $-\text{S}(\text{CH}_2)_7\text{NH}_2$ for 20 minutes. The nanoparticle solution was withdrawn from the fluid cell with a syringe, the substrate was rinsed two times with dodecane, and finally submerged in dodecane to be imaged. Figure 3.6C shows the results after nanoparticle incubation. From this image it can be seen that the AuNPs are preferentially confined to the original pattern, however, there was some non-specific binding present throughout the scan area. It was speculated this may be a result of the sweeping motion the rastering tip in the low current STM configuration imparts upon the SAM, pushing the immobilized particles from their original location. Regardless, this was a novel example of using the replacement lithography technique to fabricate a chemical

gradient on the sub-micron scale, which was subsequently used as a template to immobilize gold nanoparticles on a functionalized pattern via electrostatic interactions.

3.5 Conclusion:

In conclusion, it has been shown that replacement lithography could produce complex chemical gradient mesostructures by systematically varying the replacement bias, lithographic scan rate (either individually or in combination) and raster line spacing. The chemical gradients exhibited diffuse coverage of a ω -substituted alkanethiol into the C₁₂S-SAM on one end of the structure, intermediate coverage through the middle, and high coverage on the opposing end of the pattern. These experiments utilized SPL parameters from sub-optimal to optimal desorption conditions generating novel structures on sub-micron length scales. Gradients could be fabricated in multiple directions and/or with different terminal chemical functionality. As a result, this SPL approach enabled a variety of template patterns to be fabricated.

3.6 Experimental:

Dodecanethiol and dodecane were commercially obtained from Aldrich and used without further purification. FcC₁₁SAc was prepared in our lab from previous studies.¹⁶ Au(111) facets were annealed in a H₂ flame prior to monolayer deposition. Briefly the end of a Au wire (0.5 mm, 99.9985%, Alfa Aesar) was melted using a H₂ flame to create a small faceted

ball, and subsequently zone refined to yield Au(111) facets along the equatorial region of the ball. The freshly annealed ball was placed in a 1 mM C₁₂H₂₅SH ethanolic solution, refluxed for 1 hr,¹⁷ and allowed to cool to room temperature. The faceted ball was removed, rinsed with copious amounts of absolute ethanol (AAPER Alcohol and Chemical Co.) and dried in a stream of N₂. Imaging and lithography was performed at room temperature with a Digital Instruments NanoScope IIIa (with low current adapter) in dodecane (Aldrich) with mechanically cut Pt/Ir tips (90:10, 0.25 mm, Alfa Aesar). Relative humidity was introduced by bubbling N₂ through a gas dispersion tube into a closed vessel containing milli-Q water (18 MΩ cm²), which fed the moist outlet gas into the atmospheric chamber containing the STM. The humidity was monitored with a hygrometer (Dickson, 0 to 95% relative humidity range).

3.7 Acknowledgement:

I would like to acknowledge James P. Novak for supplying the 2 nm amine capped gold nanoparticles that were used in the immobilization experiment.

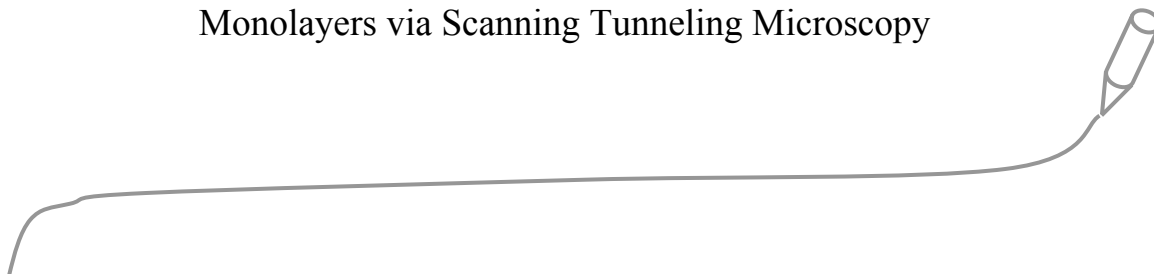
3.8 References:

- (1) Ruardy, T. G.; Scahankenraad, J. M.; van der Mei, H. C.; Busscher, H. J. *Surface Science Reports* **1997**, *29*, 3-30.
- (2) Gallardo, B. S.; Gupta, V. K.; Eagerton, F. D.; Jong, L. I.; Craig, V. S.; Shah, R. R.; Abbott, N. L. *Science* **1999**, *283*, 57-60.
- (3) Chardhury, M. K.; Whitesides, G. M. *Science* **1992**, *256*, 1539-1541.
- (4) Daniel, S.; Chaudhury, M. K. *Langmuir* **2002**, *18*, 3404-3407.
- (5) Daniel, S.; Chaudhury, M. J.; Chen, J. C. *Science* **2001**, *291*, 633.
- (6) Liedberg, B.; Wirde, M.; Tao, Y. T.; Tengvall, P.; Gelius, U. *Langmuir* **1997**, *13*, 5329-5334.
- (7) Liedberg, B.; Tengvall, P. *Langmuir* **1995**, *11*, 3821-3827.
- (8) Genzer, J.; Fischer, D. A.; Efimenko, K. *Advanced Materials* **2003**, *15*, 1545-1549.
- (9) Efimenko, K.; Genzer, J. *Advanced Materials* **2001**, *13*, 1560-1563.
- (10) Terrill, R. H.; Balss, K. M.; Zhang, Y. M.; Bohn, P. W. *Journal of the American Chemical Society* **2000**, *122*, 988-989.
- (11) Lestelius, M.; Engquist, I.; Tengvall, P.; Chaudhury, M. K.; Liedberg, B. *Colloids and Surfaces B - Biointerfaces* **1999**, *15*, 57-70.
- (12) Dertinger, S. K. W.; Chiu, D. T.; Jeon, N. L.; Whitesides, G. M. *Analytical Chemistry* **2001**, *73*, 1240-1246.
- (13) Krämer, S.; Xie, H.; Gaff, J.; Williamson, J. R.; Tkachenko, A. G.; Nouri, N.; Feldheim, D. A.; Feldheim, D. L. *Journal of the American Chemical Society* **2004**, *126*, 5388-5395.
- (14) Gorman, C. B.; Carroll, R. L.; Fuierer, R. R. *Langmuir* **2001**, *17*, 6923-6930.
- (15) Padowitz, D. F.; Messmore, B. W. *Journal of Physical Chemistry B* **2000**, *104*, 9943-9946.

- (16) Uosaki, S.; Sato, Y.; Kita, H. *Langmuir* **1991**, 7, 1510-1516.
- (17) Weiss, P. S.; Bumm, L. A.; Dunbar, T. D.; Burgin, T. P.; Tour, J. M.; Allara, D. L. *Proceeding of the New York Academy of Sciences* **1998**, 852, 145-168.

Chapter 4

Tunneling Spectroscopy Measurements of Electroactive Self-Assembled Monolayers via Scanning Tunneling Microscopy



This work was done in close collaboration with Drs. Lloyd Carroll, Grace Credo, Stephan Kramer and Drew Wassel. Their efforts are much appreciated and gratefully acknowledged. I also acknowledge the critical reading of this chapter by Drs. S. Krämer and T.L. Chasse.

This work was the subject of the publication Christopher B. Gorman, R. Lloyd Carroll, Ryan R. Fuierer, "Negative Differential Resistance in Patterned Electroactive Self-Assembled Monolayers" *Langmuir*, **2001**, *17* (22) 6923-6930.

4.1 Introduction:

One common projection regarding the future of the semiconductor industry is the inability to maintain the exponential device density growth of transistors packed on a silicon chip with time, a trend which has been enjoyed over the last thirty years.¹ This expectation is inherent due to the technological limitations in reducing the size of conventional metal/oxide/semiconductor (MOS) transistors, and the substantial concomitant increase in the costs required for manufacturing very large scale integration (VLSI) circuits. The continual demand for smaller components requires that alternative approaches to device fabrication be found, and hence the field of molecular electronics has emerged. The vision of molecular electronics is that single or small groups of molecules mounted in addressable architectures will be able to conduct and switch electrical currents in order to retain electrical bits of information for computing purposes.² The very notion implies that wires, transistors and other solid-state elements will be replaced with one or a few molecules.³ Since a molecular entity is several orders of magnitude smaller than the present-day microelectronics counterpart, it is believed that these nanoscale molecular interconnects may help minimize computer circuit dimensions and enhance performance. The main challenge is to establish that single molecules (or a finite ensemble of molecules) can perform all the basic functions of conventional electronic components.

The inevitable roadblocks for the future miniaturization of silicon microelectronics components involve physical and monetary constraints that have been projected to be deleterious to the

industry in the coming decades.^{1,2,4} From a physical standpoint, as the dimensions of the transistors reach the nanometer regime, issues like electron leakage through ultra thin oxides separating transistor gate electrodes will result in device cross talk or failure. Moreover, silicon will no longer possess its fundamental (bulk) band structure at these very small scales. Monetarily, the top-down fabrication process of the photolithographic techniques used to produce silicon devices have ever increasing costs associated with it. There are also tremendous amounts of waste generated with the iterative etching and washing procedures involved in the technique. In contrast, one popular projected approach to molecular electronic device fabrication involves the bottom-up fabrication technology employing molecular self-assembly⁵⁻⁸ to give rise to an efficient, cost effective prospect for construction of electronic circuits in a flow through manner.

There are numerous challenges that need to be solved before molecular electronics would be realized as a profitable strategy for the next generation of computing. Though molecules can be synthesized in large quantities, they are very difficult to install into an architecture that allows them to be macroscopically addressable and connected to a power supply. Other concerns involve keeping the molecular components in a static position within the architecture, and the heat dissipation necessary for the projected increased device densities. New paradigms will be essential for molecular computing to be realized. It will take an interdisciplinary effort by many scientific communities to meet these challenges. Naturally, as with any field in its infancy, fundamental research must be accomplished to learn how to address proposed molecular

electronic candidates, how they behave in an architecture and how stable they are to iterative testing.^{2,9-11}

Molecular electronics-based solid-state switches have been proposed as the active components in either nonvolatile random access memory circuits or as the configurable bits for a custom configurable logic-based computing machine.^{4,12} The basis of such devices is a two-terminal molecular tunnel junction that can be electrically switched between high- and low-conductivity states. To date, there have been numerous strategies proposed on how to address the electronic properties of molecular assemblies. A preferred approach for the assembly of molecules into devices and their connection to the macroscopic world relies on molecular self-assembly, such as the formation of self-assembled monolayers (SAMs). This strategy is favorable because substrate anchoring entities can be synthetically installed into the molecular candidate's architecture to serve as small 'alligator clips'.^{3,13} From the standpoint of molecular-device construction, wiring a molecule to two terminals appears technically more feasible than wiring to three-terminals (MOS transistors are three terminal electronic devices). This avenue of molecular electronics research has been pursued extensively because there are many approaches to measure the electronic properties of a molecular candidate in a two terminal configuration.⁹⁻¹¹ Unfortunately, it is not clear that such devices can be integrated as they do not, by themselves, offer the opportunity to introduce gain into a circuit.⁴ Thus, two-terminal devices represent a tradeoff between what is currently feasible and what offers real utility in circuit construction.

Metal-molecule-metal junctions exhibiting nonlinear current-voltage properties are currently the subject of several research efforts due to their proposed use as elements in molecule-scale electronic components. Junctions exhibiting nonlinear current-voltage properties such as negative differential resistance are desirable because they could serve as nanoscale analogs of multi-state electronic switches.¹⁴⁻¹⁶ A negative differential resistance (NDR) is characterized by a discontinuity in the monotonic increase of current as the voltage is increased. Stated otherwise, as the bias polarity increases, the current reaches a maximum, then decreases before eventually rising again. Macroscopic patriarchs to these devices are the Esaki diode¹⁵ and the resonant tunneling diode (RTD).^{15,17,18} A RTD consists of two tunnel barriers spacing a quantum well from two electrical contacts. In semiconductor devices, the quantum well is composed of a narrow layer of material characterized by accessible quantized states (as in the well/barrier system GaAs/AlGaAs).¹⁹ Upon a specific applied bias, one of the metal contact's Fermi energy (E_F) aligns with an accessible state of the quantum well material, and a phenomena known as resonant tunneling occurs, allowing an enhanced current flow across the device, creating a switching character. In resonant tunneling devices, the tunnel barriers control the probability of electrons moving from one electrode to the other through the quantum well. It was proposed that electroactive molecules could serve a similar role accessing molecular energy levels (which may be correlated with the reduction and/or oxidation potentials of the molecule) for electron tunneling. Molecules exhibiting NDR could potentially provide the electrically active components required for information processing, memory, and other electronic applications at the nanoscale.

One extensively studied candidate molecular system has been the family of conjugated phenylene ethylene oligomers (OPEs), frequently termed ‘molecular wires’.^{2,13,20} An early investigation of OPEs containing a redox center (2’-amino-4-ethynylphenyl-4’-ethynylphenyl-5’-nitro-1-benzenethiol) demonstrated NDR with a peak-to-valley ratio of 1030:1 at 60 K.¹⁶ The peak-to-valley ratio (PVR) is defined as the difference between the current at the peak maximum and the minima (valley) at higher bias polarity. Between these two points is the region that defines NDR. The peak position of NDR was temperature dependent. It was reported that control experiments using OPEs not containing amine or nitro moieties displayed no NDR responses. Later, this group showed that the system displayed NDR at room temperature, however with a considerably lower PVR that was not quantitatively given.²¹ Since this report, OPEs have been expansively studied empirically,²²⁻²⁶ and theoretically.²⁷⁻³¹ Other molecular systems that have displayed NDR have included molybdophosphates,^{32,33} cobalt phthalocyanines,³⁴ piperidine derivatives on Si(100),³⁵ terphenyl-thiols and -isonitriles,^{36,37} nitrobiphenyl molecules on graphitic carbon,³⁸ and xylyl dithiols,³⁹ to name a few.

In an early example, Han and co-workers showed that NDR correlated with redox potential in a series of metalated porphyrins.⁴⁰ They also demonstrated that electroactive porphyrins could be distinguished from non-electroactive porphyrins with STM. These observations influenced our group to hypothesize that SAMs of simple, well-studied redox active moieties (i.e. ferrocenyl) would be ideal candidates to display NDR. Moreover, we put forth the notion that we could employ replacement lithography to pattern electroactive thiols in non-

electroactive SAM matrices, allowing I(V) curves from both regions to be directly compared under the same experimental conditions.

4.2 Results and Discussion:

To test this hypothesis, our group used 11-ferrocenyldodecanethiolate ($\text{FcC}_{11}\text{S-}$) SAMs prepared on Au(111) substrates, as previously discussed in Chapters 2 and 3. Current vs. voltage (I(V)) measurements were obtained from this SAM system at room temperature under dodecane with a STM in a low current configuration using the tunneling spectroscopy mode termed continuous imaging tunneling spectroscopy (CITS). During the course of imaging in this mode, the tip is periodically stopped and an I(V) curve captured under a given set of user defined CITS parameters. This process is systematically iterated over the scan area creating an array of I(V) curves. There are many parameters that are user defined including the bias window, setpoint current and the sample period. This latter parameter is the amount of time it takes between voltage steps during the potential ramp to acquire the I(V) curve multiplied times the number of points (steps) in an I(V) curve. The scan rate of the entire I(V) curve can be calculated by dividing the sample period by bias range of the I(V) curve, which is also user defined. In this mode, large data sets of I(V) curves can be obtained in a specified voltage window and sample period under a constant set point current. Typically, data sets of 1024 curves (a 512 x 512 array) were obtained in our experiments such that a statistical representation could be generated, the advantages of which

will be discussed in more detail below. A more detailed description of this tunneling spectroscopy technique can be seen in Appendix A.1.

Typical examples of I(V) curves from a FcC₁₁S-SAM CITS data set displaying room temperature NDR can be seen in Figure 4.1A. We, and others^{16,21,40,41} have observed a variation in the peak potential of the NDR across a CITS data set. Many possible reasons for this behavior may exist, most notably the chemical environment of the molecules at each I(V) sampling point. The terminal ferrocenyl moiety was not expected to form well-ordered SAMs because of the large bulky headgroup, preventing packing of the alkylchains. This in

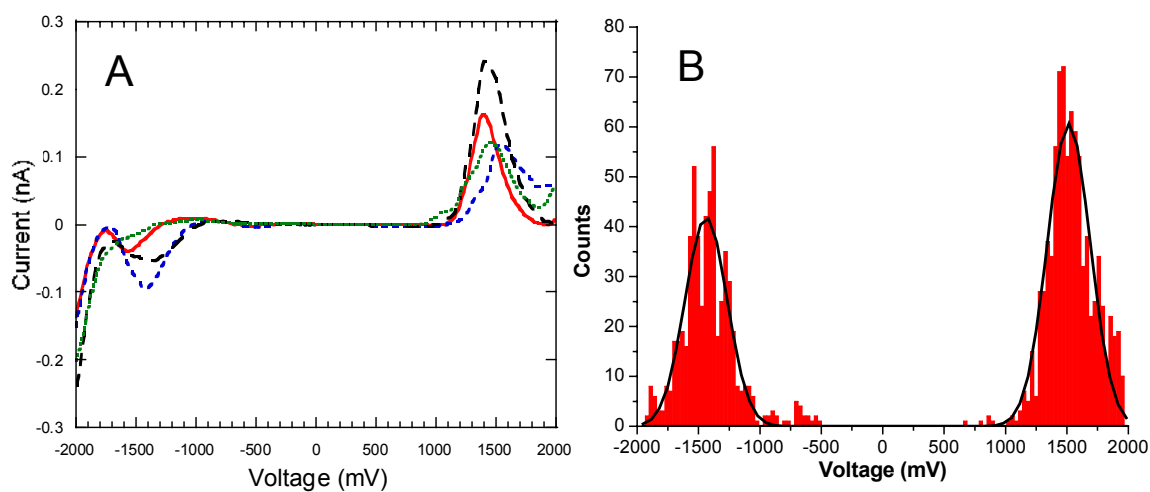


Figure 4.1: A) Typical nonlinear I(V) curves from a FcC₁₁S-SAM under dodecane displaying negative differential resistance. B) Histogram representing I-V curves that gave NDR responses in a data set of 938 curves. The histogram was fitted to a Gaussian to give NDR peak potentials: negative region -1438 mV; positive region 1539 mV. (500 nm)² scan area, I_{set}: 5 pA, 1000 μs sample period (*ca.* 15.6 V/s).

turn creates more possible degrees of freedom of the electroactive SAM species, giving non-uniformity to the SAM surface. When obtaining an I(V) curve, a variation in conformations of the electroactive headgroups in proximity of the tip can effect the sampling current, resulting in a variation of peak potential and current magnitudes. Scanning artifacts, such as current saturation (see Figure 4.2) or debris on the surface interacting with the tip, may also contribute to a peak voltage variation. Tip shape or scan rate of the voltage sweep could also be responsible for this variation. For these reasons, we developed a protocol to provide a statistical representation of the CITS data set, described in more detail in Section 4.6 (experimental). In brief, the analysis protocol rejects curves that show saturation (off-scale) or negligible currents (flat-liners) as aberrant data. Non-rejected curves are subsequently subjected to a series of algorithms to give the statistical representation. Figure 4.1B shows a histogram from a typical data set consisting of 938 curves (86 of 1024 were rejected as aberrant) using this analysis protocol. These histograms depicting the occurrences of NDR versus peak potentials suggests the observed behavior is an intrinsic electronic property of the electroactive SAM species and was reproducible from sample to sample. Fitting the histogram to a Gaussian determined an average position of NDR, resulting in a negative peak maximum at $-1439 (\pm 10)$ mV and positive peak maximum at $1515 (\pm 7)$ mV. To further survey the NDR peak potentials in this electroactive system, peak positions from sixteen separate FcC₁₁S-SAM CITS data sets were averaged to give a negative peak position at -1464 ± 21 mV, and a positive peak position at 1527 ± 33 mV. From the standard deviation of this averaging, it can be seen that the peak potentials shift across a data set, for possible reasons discussed above.

It was generally observed that the NDR response of FcC₁₁S- at the positive bias was typically larger than the response at the negative bias. The reason for this behavior is unclear, however in other surface bound systems,^{21,38,42} it has been suggested the difference in conductance between the tip film junction and the thiol gold interface can result in an asymmetry in NDR responses.^{43,44}

The relationship between NDR response and tip shape variation was investigated to determine the reproducibility in I(V) measurements. To do this, seven mechanically cut Pt/Ir (90:10) STM tips were used to obtain CITS data sets of a mono-component FcC₁₁S-SAM. The use of mechanically cut STM tips ensured that no tip shape would be identical, yet could provide atomically sharp tips. Since it is difficult to observe the apex shape of an STM tip optically, tip quality was determined by the STM image resolution of FcC₁₁S-SAMs features such as substrate vacancy islands^{26,45,46} and substrate terraces. Figure 4.2 shows an STM image of the FcC₁₁S-SAM imaged with one of these sharp tips. Notably, no domain boundaries can be seen, however, substrate vacancy islands and substrate terraces were well defined. This was expected due to the bulky ferrocenyl headgroup preventing the formation of a highly ordered SAM. Some scanning artifacts, which are generally inherent in STM images, have been highlighted in the upper portion of the image. In this experiment, six of the seven tips resolved surface features well, and also displayed NDR responses similar in peak voltage and magnitude as demonstrated in Figure 4.1A. The tip that gave poor surface feature resolution was believed to be was the result of a blunt tip, although surface or tip

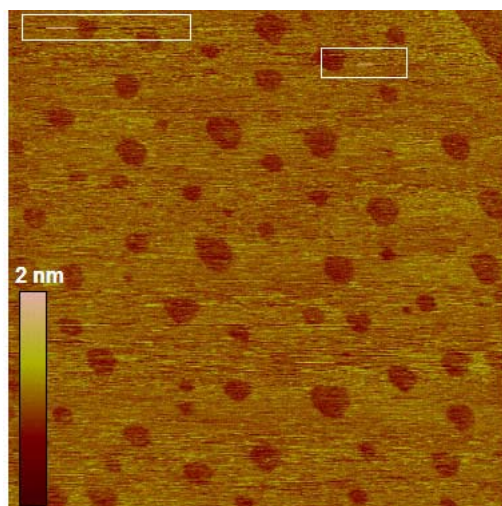


Figure 4.2: A $(500 \text{ nm})^2$ STM image of a $\text{FcC}_{11}\text{S-SAM}$ on $\text{Au}(111)$ in dodecane demonstrating the image resolution obtained from a quality tip used for $I(V)$ experiments. Surface features such as substrate vacancy islands and terraces are distinguishable. Notably, the presence of domain boundaries was expectedly absent due to the bulky headgroup of the ferrocenyl terminus, preventing an ordered SAM. The white rectangles depict scanning artifacts in the image. (Imaging conditions: 1.0 V, 5 pA, 1 Hz, z-scale: 2 nm)

contamination cannot unambiguously ruled out. $I(V)$ curves with NDR responses were not displayed with this blunt tip on a $\text{FcC}_{11}\text{S-SAM}$ that had previously displayed NDR responses with a sharper tip. This result supports a previous hypothesis that a narrow local density of states (LDOS) found in a sharp tip is necessary for the observation of NDR in metal-SAM-metal systems, in which the SAM was composed of 4-*p*-terphenylthiol in $\text{Au}(111)$.³⁶ The report further suggested that such behavior can be displayed routinely as long as a narrow LDOS is present.

It was hypothesized that the mechanism for NDR in this system may occur by an alignment of a accessible molecular energy state in the electroactive moiety and tip E_F , resulting in a

tunneling enhancement through the double tunnel junction (metal-SAM-metal). This is qualitatively illustrated in Figure 4.3. The mechanism is similar to one that has been previously defined by physicists as a resonant tunneling process in RTDs. Here, a generic I(V) trace has positions marked corresponding to the effect of increasing substrate bias on the double tunnel junction represented in Panels A-E. The double tunnel junction contains a

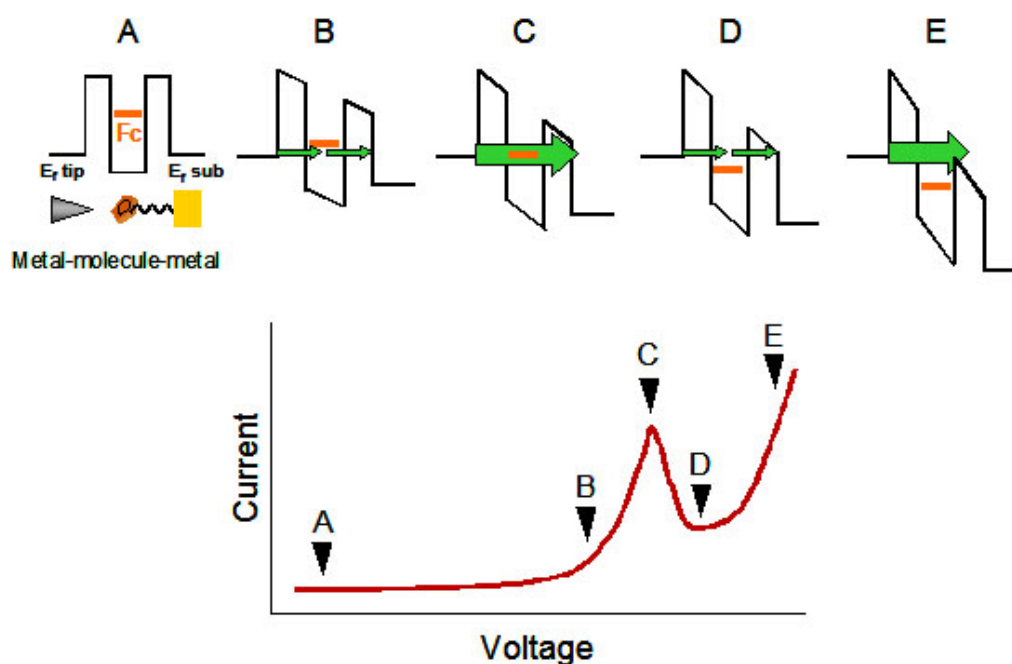


Figure 4.3: Schematic qualitatively illustrating tunneling current enhancement via molecular state and tip Fermi energy (E_F) alignment (resonant tunneling) through a double tunnel junction containing electroactive ferrocenyl moiety. The result of changing tip-substrate bias (Panels A-E) is depicted on the generic I(V) trace (above). A) The double tunnel junction at 0 V with the HOMO of the ferrocenyl moiety much higher than E_F of substrate and tip. B) An increase in substrate bias causes some overlap of the tip E_F and ferrocenyl molecular state, resulting in an increase in tunneling current. C) Optimal substrate bias gives maximum alignment (resonance) of the tip E_F and molecular state resulting in a peak maximum (NDR). D) A further increase in substrate bias moves the tip E_F and molecular state out of alignment, decreasing tunneling bias. E) A significantly large enough substrate bias causes the tip E_F to surpass the tunnel barrier height of substrate, allowing electrons to cascade over the barrier resulting in an exponential increase in tunneling current.

tunneling barrier (potential well) at the tip-SAM gap and another at the alkylchain between the ferrocenyl moiety and the sulfur – gold bond at the substrate. The relative height and width of the tunnel barriers are unlikely to be equal, and are difficult to know quantitatively. The panels in Figure 4.3 can be interpreted as follows: Panel A represents the system at 0 V, where an accessible molecular orbital energy level of the ferrocenyl headgroup lies well above the E_F of the Pt/Ir tip and Au substrate. Upon a positive increase in the Au substrate bias, the molecular energy level approaches alignment with the E_F of the tip, allowing some overlap resulting in an increase in tunneling current (Panel B). As the substrate voltage is increased, there exists an optimal alignment between the E_F and molecular energy level allowing a maximum tunneling current flow to occur (resonance, Panel C). Further increase in substrate bias moves the energy levels out of alignment, decreasing the current (Panel D). Notably, the difference in current magnitude between points C and D is defined as the peak-to-valley ratio (PVR). In Panel E, the E_F of the tip is shifted sufficiently, causing a cascade of electrons from the tip over the substrate barrier, resulting in an exponential increase in current in the $I(V)$ plot. This latter enhanced current flow may be what is often termed by physicists as thermionic emission. Considering this qualitative model, we expect that the tunnel barrier heights and position of the molecular states should influence the position of NDR in electroactive SAM systems.

To this end, experiments were performed to differentiate our hypothesized mechanism of enhanced tunneling current via molecular energy level alignment (resonant tunneling) from an adventitious electrochemical oxidation / reduction of the electroactive moiety in the tunnel

junction. To rule out an electrochemical mechanism, I(V) curves were collected at different voltage sweep rates (sample periods) varying over a decade (2.3 V/s to 60 V/s, Figure 4.4). In all cases, the position and magnitudes of the NDR response was similar to the data shown in Figure 4.1. If an electrochemical mechanism was operative, it would be expected that a shift in NDR peak position would occur with increasing scan rate. This was not observed. From

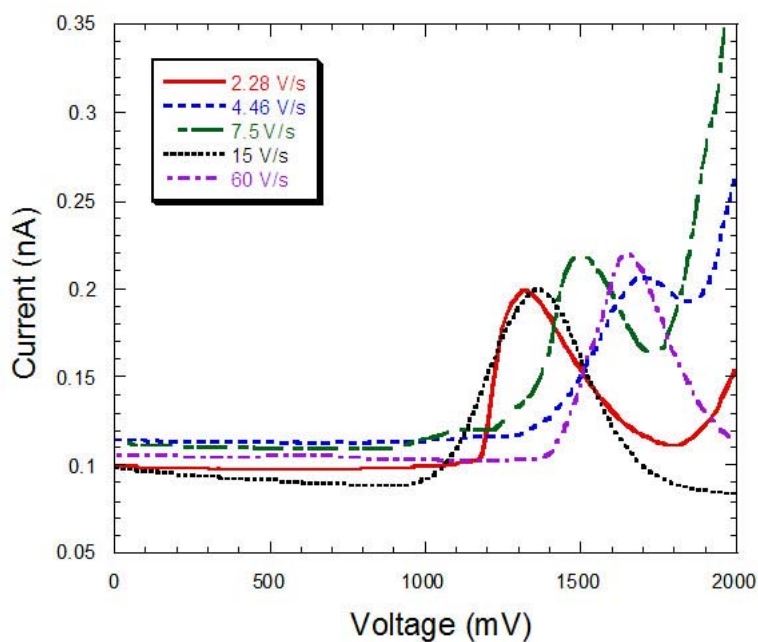


Figure 4.4: Selected I(V) curves obtained from a FeC₁₁S-SAM at various sample periods depicted in legend. No trend regarding scan rate was observed suggesting the NDR response proceeds by a resonant process.

these experiments, it was concluded that the position of NDR was not effected by the variation in sample period.

CITS data sets obtained on non-electroactive thiols that do not form well-ordered SAMs (under dodecane) were performed as control experiments. Mercapto-undecanoic acid ($\text{HS}(\text{CH}_2)_{10}\text{COOH}$) prepared as single component SAMs displayed few nonlinear $I(V)$ responses. Figure 4.5 shows a typical histogram from a CITS data set from these control experiments that contained 945 of 1024 curves that were not rejected from the algorithm procedure. The histogram data from Figure 4.1B is also displayed to directly compare this non-electroactive SAM to the electroactive ferrocenyl terminated SAM. The occasional non-linear $I(V)$ response was attributed to signal / scanning artifacts. Due to the larger dipole

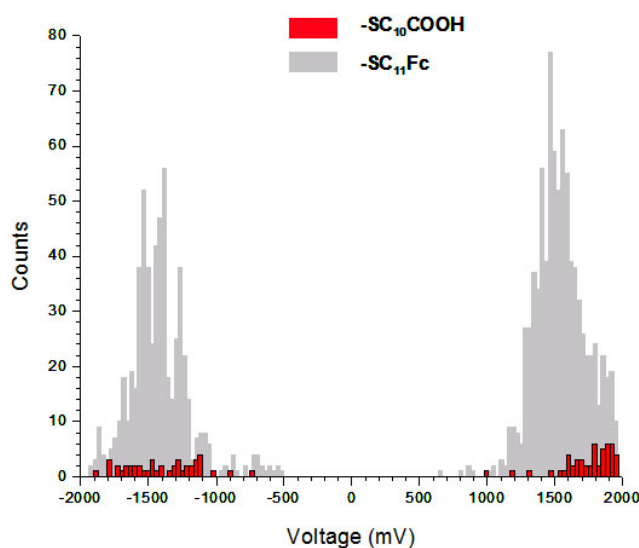


Figure 4.5: Histogram representing the number of curves containing nonlinear responses from a CITS data set of $\text{HOOC}(\text{CH}_2)_{10}\text{S}$ -SAM on Au(111) (red). This data set consisted of 945 of 1024 curves that weren't rejected from the analysis protocol as aberrant. The histogram is compared to that of the FcC_{11}S -SAM seen in Figure 4.1B.

moment associated with this SAM termini, relative to a methyl terminated SAM, it may have been more likely that contaminants could adhere to this SAM, causing these signal artifacts. This control experiment suggests that a data set of electroactive SAM is clearly different than that of a non-electroactive SAM.

4.3 Current – Voltage Measurements on Patterned FcC₁₁S-SAMs in C₁₂S-SAMs

It was hypothesized that the I(V) response of a non-electroactive SAM would not display the same behavior as the electroactive FcC₁₁S-SAM within the potential sweep window investigated. A patterned SAM system would allow the direct comparison of the two species under the same conditions. Moreover, a patterning experiment would allow the verification that the electronic properties of the patterned FcC₁₁S-SAM region are the same as monocomponent FcC₁₁S-SAMs. To this end, replacement lithography was employed to pattern FcC₁₁S-SAM within a non-electroactive C₁₂S-SAM. A description of this technique is discussed in detail in Chapter 2 (Scheme 2.1).

To obtain a significant number of curves of electroactive SAM species, it was decided that a square pattern of the electroactive SAM be fabricated with replacement lithography. A (300 nm)² square pattern of FcC₁₁S- was fabricated in a C₁₂S-SAM under a *ca.* 1 μM Fc(CH₂)₁₁SAc / dodecane solution using the replacement conditions of 3.3 V, 8 pA and 0.5 Hz (400 nm/s) in the normal imaging / raster manner at a relative humidity of 54 to 57%. The tip was retracted, the patterning solution withdrawn with a syringe from the fluid cell, the

substrate rinsed with dodecane, and finally replaced with clean dodecane to perform the CITS collection. The results of the patterning experiment can be seen in Figure 4.6A, which shows a $(500 \text{ nm})^2$ STM image of the two component SAM system. CITS was subsequently performed on a $(600 \text{ nm})^2$ area at a sample period of $160 \mu\text{s}$ and I_{set} of 8 pA . An advantage of this approach was that $I(V)$ curves within the patterned region could be separated from the $I(V)$ curves that lie outside the replaced region depending on where they occurred within the CITS data set. Figure 4.6B shows four representative $I(V)$ curves obtained from each of the two regions. Open markers represent $I(V)$ curves of the non-electroactive $\text{C}_{12}\text{S-SAM}$ from reported in the literature.^{47,48} The dashed lines represent the electroactive $\text{FcC}_{11}\text{S-SAM}$ from

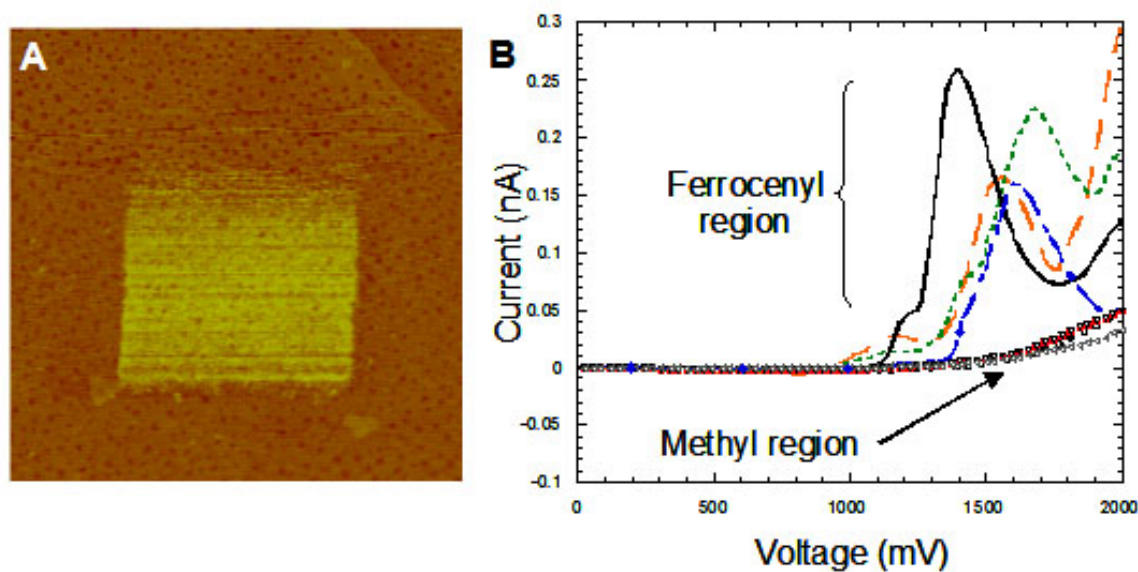


Figure 4.6: Results of a CITS experiment on a $\text{FcC}_{11}\text{S-SAM}$ patterned in a $\text{C}_{12}\text{S-SAM}$. A) $(500 \text{ nm})^2$ STM image of a $(300 \text{ nm})^2$ $\text{FcC}_{11}\text{S-SAM}$ patterned into a $\text{C}_{12}\text{S-SAM}$ using replacement lithography (Imaging conditions: 1.0 V , 8 pA , 1 Hz , $z\text{-scale: } 5 \text{ nm}$). B) Four $I(V)$ curves from inside the $\text{FcC}_{11}\text{S-SAM}$ pattern displaying NDR (lines), and four $I(V)$ curves obtained from the outside the ferrocenyl pattern displaying no NDR (open markers), CITS parameters: $(600 \text{ nm})^2$, $I_{\text{set}} = 8 \text{ pA}$, $160 \mu\text{s}$ sample period.

outside the replaced region, and did not display NDR responses. These curves were very similar to curves obtained from monocomponent C₁₂S-SAMs obtained as control experiments to compare to the monocomponent ferrocenyl SAMs, and similar to that within the pattern and did display NDR responses. As with the monocomponent FcC₁₁S-SAMs (Figure 4.1), an expected variation in peak potential and magnitude of the NDR response was observed.

4.4 Further Tunneling Spectroscopy Studies of Electroactive SAMs:

To support that other SAMs containing electroactive moieties would display NDR, I(V) spectroscopy data was obtained from galvinol terminated SAMs (phenoxy-galvinol-hexanethiolate, GalC₆S-SAM, Table A.1). Interestingly, when I(V) curves were obtained in dodecane, very low occurrences of non-linear curves displaying NDR were observed, and a large variation in NDR peak position was apparent. In contrast, when I(V) curves were obtained in air, much larger occurrences of curves displayed NDR showing a narrower distribution in peak potentials. This suggested that this electroactive SAM was sensitive to the environment in order to display NDR. It is noted that GalC₆S-SAMs shows a proton coupled redox wave in electrochemistry.^{49,50} It was speculated that the availability of water to aid in protonation of the galvinol headgroup may be the cause of the increased occurrence of NDR across a CITS data set.

The behavior of NDR in conventional semiconductor-based resonant tunneling diodes (RTDs) has been tuned by modifying the materials, dopant concentration, and the physical configuration of the device.^{19,51-53} The tunability for conventional RTDs suggests that NDR behavior in molecular-scale analogs should also exhibit predictable changes based on tunnel barrier modifications. Recent studies suggest that molecular based tunnel barriers can be rationally constructed.^{48,54-57} It was hypothesized that the NDR response in this molecular system could be attenuated by modifying the barrier height and width, analogous to tuning conventional RTDs. Recently, our group demonstrated the ability to attenuate the NDR response in FcC₁₁S-SAMs at room temperature by either coating the tip with *n*-alkylthiols, or by capping the FcC₁₁S-SAM with the bowl-shaped sugar, β -cyclodextrin.⁵⁸ In the former experiment, the double tunnel junction was modified by functionalizing the tip with *n*-alkanethiols of various chainlengths. It was observed that the peak-to-valley ratio in NDR responses decreased with increasing alkanethiol chain length. The latter set of experiments demonstrated that the double tunnel junction could also be altered by capping the ferrocenyl headgroups with β -cyclodextrin (β -CD). Electrochemical studies of Fc- β -CD complexes in solution have exhibited slowed electron-transfer kinetics following exposure of the Fc to β -CD as a result of the formation of a 1:1 host-guest inclusion complex.^{59,60} Here, it was observed that PVR ratios decreased in the β -CD/FcC₁₁S-SAM system relative to the monocomponent FcC₁₁S-SAM. Control experiments of the FcC₁₁S-SAM washed with α -CD, a sugar too small to bind to ferrocenyl headgroups, displayed NDR responses similar to that of FcC₁₁S-SAM. From these experiments, room temperature, molecular-based NDR of an electroactive SAM system was obtained in two complementary ways: one in which the tip

was functionalized with *n*-alkylthiols of various lengths, and through non-covalent encapsulation of ferrocenyl headgroups using β -cyclodextrin.

Concomitant experiments to support that the tunneling barriers affect the probability of tunneling through the double junction were performed employing current-distance tunneling spectroscopy (I-s).^{23,61-63} With this experiment, the current is measured as the STM tip retracts from the surface, enabling an apparent tunneling barrier (ϕ) to be approximated from the slope of the exponential decay in the tunneling current. It is important to note that since the exact location of the tip was not known during this experiment, an accurate tunneling barrier could not be calculated. However, a comparison could be made when performing I-s experiments between the different SAMs systems investigated (FcC₁₁S-, β -CD/FcC₁₁S-, α -CD/FcC₁₁S- and C₁₂S-SAMs). To provide a statistical representation, 50 curves of each SAM system were obtained. The FcC₁₁S-SAM system displayed I-s curves representing a lower ϕ , suggesting a higher conductance through the film. The β -CD/FcC₁₁S-SAM system displayed a broader range of ϕ , which suggests that many of the ferrocenyl headgroups were capped to give higher ϕ , while lower ϕ may have been the result of incomplete capping from the sugar. Control experiments on the α -CD/FcC₁₁S-SAM systems showed similar results as the mono-component FcC₁₁S-SAM as expected. C₁₂S-SAMs showed higher ϕ , indicative of a more resistive film. From these experiments, the modification of the tunneling barrier was demonstrated as a potential means to tune molecular based tunnel barriers.

4.5 Conclusion:

In conclusion, negative differential resistance has been displayed in current-voltage curves obtained with STM over SAMs containing electroactive moieties (ferrocene and galvinoxyl) as measured in a tip-SAM-substrate junction. Large data sets of I(V) curves were generated using CITS, and these data treated with an analysis protocol to statistically demonstrate the reproducibility of such a measurement. Variation in peak position and current magnitude were observed, believed to be caused by the different conformations of the bulky ferrocenyl headgroup in the local environment of the tip during I(V) sampling. A mechanism describing a tunneling current enhancement through an accessible molecular energy level of the electroactive group and tip E_F has been hypothesized to explain this electronic behavior. Studies to rule out an electrochemical mechanism were performed by varying the scan rate of the potential window. From these results, it was clear that further work must be done before the phenomena of NDR can be fully understood. Control experiments consisting of I(V) curves obtained over non-electroactive acid terminated SAM systems did not show appreciable NDR responses across large CITS data sets. Moreover, patterned ferrocenyl SAMs systems fabricated via replacement lithography also displayed reproducible NDR responses, similar to those obtained with the mono-component ferrocenyl terminated SAMs. Other SAMs containing electroactive moieties (GalC₆S-) were observed to display NDR responses, further supporting that electroactivity and NDR may be correlated. It was also observed that the double tunneling junction could be modified to attenuate NDR response in ferrocenyl SAMs in two complementary ways. One approach involved coating the STM tip

with alkanethiols of various lengths, and the other involved capping the ferrocenyl termini with β -cyclodextrin.

4.6 Experimental:

11-Ferroceneundecanethiol was prepared as previously described in the literature. The synthesis of which can be seen in Appendix 4. Dodecanethiol and dodecane were purchased from Aldrich and used as received. Absolute ethanol was purchased from AAPER Alcohol and Chemical Co. and used without further purification. Au(111) substrates were prepared by melting the end of a gold wire in a flame to produce a bead, which was subsequently zone refined to produce (111) facets along the equatorial region of the bead, as previously described in Chapter 2. FcC₁₁S-SAMs were produced by incubating the freshly annealed Au beads in 5 mM ethanolic solutions for 12 to 24 hours, rinsed with ethanol and dried in a stream of N₂. Samples were mounted in a stainless steel and Kel-F fluid imaging cell, and imaged immediately after preparation.

All STM experiments were carried out on a Nanoscope IIIa or NSe Multimode SPM in low current configuration (Digital Instruments, Santa Barbara, CA). Mechanically cut Pt-Ir (90:10) tips were used for all experiments. Standard imaging conditions (SIC) were +1 V substrate bias, 5-10 pA tunneling current, and 0.5-1 Hz scan rate or a slight variation thereof as noted in figure captions.

Aberrant data in CITS data, such as current responses out of measurable range or excessively noisy curves, were thought to be due to either the tip with the surface or localized tip / sample contamination. Algorithms were constructed to discard these ‘aberrant curves’ in the analysis of a data set. Aberrant curves were defined as those that show saturated current response at either positive or negative potentials. In addition, curves displaying negligible currents (flat-liners) throughout the voltage sweep were also removed from the data set. All curves retained were set to zero current at zero bias to account for internal offsets generated by the microscope. These internal offsets were verified to occur sometimes when the tip was well out of range of the sample, indicating that they are the result of an instrumental artifact.

The voltage at which NDR occurred was determined by derivatizing the $I(V)$ curve with a 7 point derivative. That is, for point n , a regression line was determined for the points $n-3, n-2, n-1, n, n+1, n+2, \text{ and } n+3$ and the slope of the regression line was recorded as the derivative of point n . This procedure had the additional advantage of minimizing the effects of noise on the curve. At positive potentials, the NDR peak position was determined by the algorithm as the point at which slope goes from positive to negative, and at negative potentials, the reverse was true. The voltage at this point was tabulated, then all voltage values were binned to give a histogram representation of peak position.^{40,41} The voltage distribution was fit to a Gaussian curve, of the formula:

$$\text{Count} = A \exp [-(V-V_p)^2 / B^2] + C$$

where V_p is the peak voltage, and B is related to the width at half-height, ΔV , by $\Delta V = 1.175B$.^{40,64}

4.7 References:

- (1) Stan, M. R.; Franzon, P. D.; Goldstein, S. C.; Lach, J. C.; Ziegler, M. M. *Proceedings of the IEEE* **2003**, *91*, 1940-1957.
- (2) Joachim, C.; Gimzewski, J. K.; Aviram, A. *Nature* **2000**, *408*, 541-548.
- (3) Tour, J. M. *Accounts of Chemical Research* **2000**, *33*, 791-804.
- (4) Carroll, R. L.; Gorman, C. B. *Angewandte Chemie International Edition in English* **2002**, *41*, 4378-4400.
- (5) Ulman, A. *An Introduction to Ultrathin Organic Films from Langmuir-Blodgett to Self-Assembly*; Academic Press, Inc.: New York, 1991.
- (6) Ulman, A. *Chemical Reviews* **1996**, *96*, 1533-1554.
- (7) Whitesides, G. M.; Grzybowski, B. *Science* **2002**, *295*, 2418-2421.
- (8) Whitesides, G. M.; Boncheva, M. *Proceedings of the National Academy of Sciences* **2002**, *99*, 4769-4774.
- (9) Mantooth, B. A.; Weiss, P. S. *Proceedings of the IEEE* **2003**, *91*, 1785-1802.
- (10) Rawlett, A. M.; Hopson, T. J.; Amlani, I.; Zhang, R.; Tresek, J.; Nagahara, L. A.; Tsui, R. K.; Goronkin, H. *Nanotechnology* **2003**, *14*, 377-384.
- (11) Reed, M. A.; Zhou, C.; Deshpande, M. R.; Muller, C. J.; Burgin, T. P.; Jones II, L.; Tour, J. M. *Annals of the New York Academy of Sciences* **1998**, *852*, 133-144.
- (12) Aviram, A.; Ratner, M. *Chemical Physics Letters* **1974**, *29*, 277-283.
- (13) Kusmerick, J. G.; Pollack, S. K.; Yang, J. C.; Naciri, J.; Holt, D. B.; Ratner, M. A.; Shashidhar, R. *Annals of the New York Academy of Sciences* **2003**, *1006*, 277-290.
- (14) Selzer, Y.; Salomon, A.; Ghabboun, J.; Cahen, D. *Angewandte Chemie International Edition in English* **2002**, *41*, 827-830.
- (15) Sze, S. M. *Physics of Semiconductor Devices*; Second ed.; John Wiley and Sons: New York, 1981.

- (16) Chen, J.; Reed, M. A.; Rawlett, A. M.; Tour, J. M. *Science* **1999**, *286*, 1550-1551.
- (17) Mathews, R. H.; Sage, J. P.; Sollner, T. C. L. G.; Calawa, S. D.; Chen, C.-L.; Mahoney, L. J.; Maki, P. A.; Molvar, K. M. *Proceedings of the IEEE* **1999**, 596-605.
- (18) Mazumder, P. K., S.; Bhattacharya, M.; Jian Ping Sun; Haddad, G.I. *Proceedings of the IEEE* **1998**, *86*, 664-686.
- (19) Sun, J. P.; Haddad, G. I.; Mazumder, P.; Schulman, J. N. *Proceedings of the IEEE* **1998**, *86*, 641-661.
- (20) Tour, J. M.; Kozaki, M.; Seminario, J. M. *Journal of American Chemical Society* **1998**, *120*, 8486-8493.
- (21) Rawlett, A. M.; Hopson, T. J.; Nagahara, L. A.; Tsui, R. K.; Ramachandran, G. K.; Lindsay, S. M. *Applied Physics Letters* **2002**, *81*, 3043-3045.
- (22) Chen, J.; Wang, W.; Reed, M. A.; Rawlett, A. M.; Price, D. W.; Tour, J. M. *Applied Physics Letters* **2000**, *77*, 1224-1226.
- (23) Fan, F. F.-R.; Yang, J.; Cai, L.; Price, J., D.W.; Dirk, S. M.; Kosynkin, D. V.; Yao, Y.; Rawlett, A. M.; Tour, J. M.; Bard, A. J. *Journal of American Chemical Society* **2002**, *124*, 5550-5560.
- (24) Fan, F. R. F.; Lai, R. Y.; Cornil, J.; Karzazi, Y.; Bredas, J. L.; Cai, L. T.; Cheng, L.; Yao, Y. X.; Price, D. W.; Dirk, S. M.; Tour, J. M.; Bard, A. J. *Journal of American Chemical Society* **2004**, *126*, 2568-2573.
- (25) Walzer, K.; Marx, E.; Greenham, N. C.; Less, R. J.; Raithby, P. R.; Stokbro, K. *Journal of the American Chemical Society* **2004**, *126*, 1229-1234.
- (26) Donhauser, Z. J.; Mantooth, B. A.; Kelly, K. F.; Bumm, L. A.; Monnell, J. D.; Stapleton, J. J.; Price, D. W.; Rawlett, A. M.; Allara, D. L.; Tour, J. M.; Weiss, P. S. *Science* **2001**, *292*, 2303-2307.
- (27) Karzazi, Y.; Cornil, J.; Brédas, J. L. *Nanotechnology* **2003**, *14*, 165-171.
- (28) Karzazi, Y.; Cornil, J.; Brédas, J. L. *Journal of American Chemical Society* **2001**, *123*, 10076-10084.
- (29) Seminario, J. M.; Zacarias, A. G.; Tour, J. M. *Journal of American Chemical Society* **2000**, *122*, 3015-3020.

- (30) Seminario, J. M.; Derosa, P. A.; Bastos, J. L. *Journal of American Chemical Society* **2002**, *124*, 10266-10267.
- (31) Zangmeister, C. D.; Robey, S. W.; van Zee, R. D.; Yao, Y. X.; Tour, J. M. *Journal of the American Chemical Society* **2004**, *126*, 3420-3421.
- (32) Song, I. K.; Kaba, M. S.; Coulston, G.; Kourtakis, K.; Barteau, M. A. *Chemistry of Materials* **1996**, *8*, 2352-2358.
- (33) Kaba, M. S.; Song, I. K.; Barteau, M. A. *Journal of Physical Chemistry* **1996**, *100*, 19577-19581.
- (34) Mazur, U.; Hipps, K. W. *Journal of Physical Chemistry* **1995**, *99*, 6684-6688.
- (35) Guisinger, N. P.; Greene, M. E.; Basu, R.; Baluch, A. S.; Hersam, M. C. *Nano Letters* **2004**, *4*, 55-59.
- (36) Xue, Y. Q.; Datta, S.; Hong, S.; Reifenberger, R.; Henderson, J. I.; Kubiak, C. P. *Physical Review B* **1999**, *59*, R7852-R7855.
- (37) Hong, S.; Reifenberger, R.; Tian, W.; Datta, S.; Henderson, J. I.; Kubiak, C. P. *Superlattices and Microstructures* **2000**, *28*, 289-303.
- (38) Solak, A. O.; Ranganathan, S.; Itoh, T.; McCreery, R. L. *Electrochemical and Solid-State Letters* **2002**, *5*, E43-E46.
- (39) Datta, S.; Tian, W. D.; Hong, S.; Reifenberger, R.; Henderson, J. I.; Kubiak, C. P. *Physical Review Letters* **1997**, *79*, 2530-2533.
- (40) Han, W.; Durantini, E. N.; Moore, T. A.; Moore, A. L.; Gust, D.; Rez, P.; Leatherman, G.; Seely, G. R.; Tao, N.; Lindsay, S. M. *Journal of Physical Chemistry B* **1997**, *101*, 10719-10725.
- (41) Kinne, M.; Barteau, M. A. *Surface Science* **2000**, *447*, 105-111.
- (42) Wong, E. W.; Collier, C. P.; Behloradsky', M.; Raymo, F. M.; Stoddart, J. F.; Heath, J. R. *Journal of American Chemical Society* **2000**, *122*, 5831-5840.
- (43) Cui, X. D.; Primak, A.; Zarate, X.; Tomfohr, J.; Sankey, O. F.; Moore, A. L.; Moore, T. A.; Gust, D.; Harris, G.; Lindsay, S. M. *Science* **2001**, *294*, 571-574.
- (44) Collier, C. P.; Jeppesen, J. O.; Luo, Y.; Perkins, J.; Wong, E. W.; Heath, J. R.; Stoddart, J. F. *Journal of American Chemical Society* **2001**, *123*, 12632-12641.

- (45) Schoenenberger, C.; Sondag-Huethorst, J. A. M.; Jorritsma, J.; Fokkink, L. G. J. *Langmuir* **1994**, *10*, 611-615.
- (46) Touzov, I.; Gorman, C. B. *Langmuir* **1997**, *13*, 4850-4854.
- (47) Lee, T.; Wang, X. D.; Reed, M. A. *Annals of the New York Academy of Sciences* **2003**, *1006*, 21-35.
- (48) Wold, D. J.; Frisbie, C. D. *Journal of American Chemical Society* **2001**, *123*, 5549-5556.
- (49) Sagara, T.; Midorikawa, T.; Shultz, D. A.; Zhao, Q. *Langmuir* **1998**, *14*, 3682-3690.
- (50) Shultz, D. A.; Tew, G. N. *Journal of Organic Chemistry* **1994**, *59*, 6159-6160.
- (51) Zhao, P.; Cui, H. L.; Woolard, D.; Jensen, K. L.; Buot, F. A. *Journal of Applied Physics* **2000**, *87*, 1337-1349.
- (52) Xue, Y.; Datta, S.; Ratner, M. A. *Journal of Chemical Physics* **2001**, *115*, 4292-4299.
- (53) Schulman, J. N.; Santos, H. J. D. L.; Chow, D. H. *IEEE Electronic Device Letters* **1996**, *17*, 220-222.
- (54) Holmlin, R. E.; Ismagilov, R. F.; Haag, R.; Mujica, V.; Ratner, M. A.; Rampi, M. A.; Whitesides, G. M. *Angewandte Chemie International Edition in English* **2001**, *40*, 2316-2320.
- (55) Holmlin, R. E.; Haag, R.; Chabynyc, M. L.; Ismagilov, R. F.; Cohen, A. E.; Terfort, A.; Rampi, M. A.; Whitesides, G. M. *Journal of American Chemical Society* **2001**, *123*, 5075-5085.
- (56) Wold, D. J.; Frisbie, C. D. *Journal of the American Chemical Society* **2000**, *122*, 2970-2971.
- (57) Boulas, C.; Davidovits, J. V.; Rondelez, F.; Vuillaume, D. *Physical Review Letters* **1996**, *76*, 4797-4800.
- (58) Wassel, R. A.; Credo, G. M.; Fuierer, R. R.; Feldheim, D. L.; Gorman, C. B. *Journal of American Chemical Society* **2003**, *126*, 295-300.
- (59) Isnin, R.; Salam, C.; Kaifer, A. E. *Journal of Organic Chemistry* **1991**, *56*, 35-41.
- (60) Schönherr, H.; Beulen, M. W. J.; Bügler, J.; Huskens, J.; van Veggel, F.; Reinhoudt, D. N.; Vancso, G. J. *Journal of the American Chemical Society* **2000**, *122*, 4963-4967.

- (61) Moresco, F.; Meyer, G.; Rieder, K. H. *Physical Review Letters* **2001**, *86*, 672-675.
- (62) Yamada, Y.; Sinsarp, A.; Sasaki, M.; Yamamoto, S. *Japanese Journal of Applied Phycis Part 1 -Regular Papers Short Notes & review* **2002**, *41*, 5003–5007.
- (63) *Scanning Probe Microscopy and Spectroscopy: Theory, Techniques and Applications, Second Edition*; Second ed.; Bonnell, D., Ed.; John Wiley-VCH, Inc.: New York, 2001.
- (64) Carroll, R. L. Ph.D., North Carolina State University, 2002.

Chapter 5

Stochastic Variation in Appearance of Electroactive Guest Molecules in Insulating Host SAMs.



This work was done in close collaboration with Drew Wassel. His efforts are much appreciated and gratefully acknowledged. I gratefully acknowledge Sofi Bin-Salamon for synthesizing the Ruthenium tris(bipyridine)hexanethiol used in this study, and Dr. Stephan Krämer for his critical review of this chapter.

This work was the subject of the publication “Stochastic Variation in Conductance on the Nanometer Scale: A General Phenomenon.” Ronald A. Wassel, Ryan R. Fuierer, Namjin Kim, Christopher B. Gorman, *Nano Letters*, **2002**, 3 (11) 1617-1620.

5.1 Introduction:

Conductance switching has been proposed as the basis for potential molecular electronic memory devices, and has been the focus of many research endeavors. Switching between a high and low conductance state by some outside stimulus would make molecular scale logic devices and memory elements possible. The phenomena of negative differential resistance (NDR) in molecular scale systems is an example of molecular switching from high to low resistance states in an applied electric field, then back to a high resistance state as the bias polarity is increased further. There have been many examples of molecular based NDR reported displaying bistability in nanopore junctions,^{1,2} and scanning tunneling spectroscopy experiments.³⁻¹⁴ These experiments all involve a two-electrode configuration that swept through a potential window to initiate the bistability in the respective system. Our group has recently demonstrated room temperature NDR responses in self-assembled monolayers containing terminal electroactive moieties,^{15,16} and later showed the ability to tune the NDR response in these systems by modifying the tunnel junction by two complementary ways.¹⁷

Besides instances of NDR, the conductance of a nanometer-scale, metal-molecule-metal junction is dependent on other factors. Notable among these is the orientation of the molecules in a metal-SAM-metal junction, and any conformational changes that these molecules may experience with respect to the metallic contacts. When considering the dynamics of an electroactive molecule adsorbed to a substrate, stochastic switching between

various conductance states can occur by a change in conformation of a molecule in a junction. This phenomenon has recently been observed using a scanning tunneling microscope (STM) tip in contact with a self-assembled monolayer (SAM) adsorbed on Au(111). Weiss *et al.* observed stochastic conductance changes over time in phenylene ethynylene oligomer (OPE)¹⁸ guests isolated in alkanethiol host SAMs.^{19,20} The length of these rigid molecules was slightly taller than the host SAM they were isolated in, so they could be topographically distinguished in STM images. However, since these guests were fully conjugated systems and that convolution between electronic and topographic properties of the surface occurs in STM images, large apparent height contrasts between high conductance states ('On') and low conductance states ('Off') were observed temporally from these isolated guest species. These stochastic switching events were consequently termed 'blinking'. The proposed switching mechanism in these systems has been explained in terms of strong coupling between relative angular displacements of the aromatic rings and molecular conductivity.^{19,21,22} The researchers observed the occurrence of switching was dependent on the packing density of the surrounding host SAM matrix.^{19,21}

Ramachandran *et al.* observed stochastic switching in non-conjugated *n*-alkanedithiols (of various lengths) isolated in alkanemonothiol host SAMs of the same chain length. It was suggested that the conductivity fluctuations was from the uppermost part of the dithiol guest becoming intermittently buried in the host monolayer through a orientation change in the chain.¹¹ They subsequently hypothesized that attachment of a gold nanoparticle atop a alkyldithiol guest species, would help inhibit the possibility of the guest becoming

intermittently buried within the host SAM because of its relative size. The nanoparticle would also serve to be a larger top contact, aiding in the ability for the SPM tip to address it. However, conductance changes were still observed in the alkanedithiol systems over time.¹¹ In this system, the ‘blinking’ behavior was attributed to changes in the bonding sites between the thiol anchoring group and the gold substrate. It was suggested that the adventitious insertion strategy may cause the guest to select more labile bonding sites on the gold surface.

Fundamental research regarding the dynamics and behavior of molecules in a junction is imperative in developing an understanding of systems for / towards the realization of viable molecular electronic configurations. After contemplating some of these early reports, we hypothesized that stochastic variation in the relative conductance of molecules is likely a completely general phenomenon.¹⁷ This behavior is most simply rationalized as conformational and/or orientation changes of one or a small collection of molecules over time. When considering a bulk SAM with a mesoscopic (> 100 nm) two-dimensional area, these conformation / orientation changes will effectively cancel out over the entire area of the SAM. However, in cases relevant to molecular-scale electronics, these changes will not be averaged out over a large collection of molecules. While the work presented here does not indicate how many molecules will be required to create a junction with a consistent conductance, it does illustrate the importance of addressing this issue in molecular-scale electronics studies.

Many recent research endeavors investigating the electronic properties of molecular electronic candidates have sandwiched them between two electrodes, creating a metal-SAM-metal junction. Devices / junctions to probe I(V) behavior such as nanopore,^{1,2} or mercury drop-SAM-metal junctions^{23,24} are often difficult to reproducibly fabricate, and offer the concomitant possibility of failure due to short circuiting. Scanning probe microscopy techniques have often been employed to probe the electronic properties of SAM systems.^{4-7,12-14,25-33} In particular, STM seems particularly well suited to study stochastic conductance changes of molecular guests in host matrices for several reasons. The ability to achieve atomic resolution offers the advantage of investigating single or small bundles of molecular entities that differ from their surrounding matrix. Also, SAM systems to be investigated are more easily prepared because the STM tip serves as the second electrode in a metal-SAM-metal configuration. Hence, the SAM can be prepared on the desired conductive substrate, and mounted in the STM for imaging. As the current used in STM feedback is based on tunneling, an increase in the dimensions of the tip-substrate gap at a given bias is expected to result in an exponential change in the current.

$$I \propto \exp(-2\kappa z)$$

where κ is a constant relating the tunneling barrier and energy of an electron, and z is the tip-substrate gap distance (Appendix A.1 discusses this in more detail). This phenomenon translates into order of magnitude change in tunneling current for an Ångstrom change in the gap dimensions. Given that any metal-molecule-metal junction is likely to have enough

variability on this length scale, conductance changes in these junctions (and thus stochastic switching) are likely to be completely general in this type of system.

5.2 Results and Discussion:

To demonstrate our hypothesis, we used STM to investigate alkylthiolate SAMs terminated with electroactive moieties as guest molecules, which were adventitiously inserted into host dodecanethiol SAMs ($C_{12}S$ -SAMs) by a process previously described in the literature.^{11,19,34,35} Briefly, after the host SAM is prepared, the substrate is incubated in an ethanolic solution of the guest for a given period of time (dependent on guest adsorption rates) to allow adventitious adsorption into the disordered regions / defect sites (i.e. domain boundaries and step edges) of the host SAM. These SAM systems were monitored with low current STM which allows the tip to reside just above the SAM, as suggested by Weiss and coworkers.^{36,37} The electroactive molecules investigated were 11-ferrocenylundecanethiol ($FcC_{11}SH$), galvinoxylhexanethiol ($GalC_6SH$) and Ruthenium tris(bipyridine)-hexanethiol ($Ru(bpy)_3C_6SH$). The impetus behind their use is that the electroactive terminated SAM guests have similar lengths as the surrounding host matrix, but give large apparent height contrasts under standard imaging conditions (1 to 1.3 V, 10 pA) allowing them to be more easily distinguished in STM images.

Due to thermal drift and creep in the STM piezoelectric imaging system, it was difficult to monitor small regions over the time scales needed track the stochastic switching. To remedy

this, large areas ($(200 \text{ nm})^2$ to $(300 \text{ nm})^2$) were scanned to simultaneously monitor multiple guest species within the host matrix, from which data for individual guest regions could be extracted. Images were continuously captured under normal imaging conditions (1 Hz) to monitor the variation in the apparent height of guest species, resulting in an image acquisition every 8.5 minutes. Figure 5.1 shows a typical C_{12}S -SAM containing multiple FcC_{11}S - species adventitiously adsorbed into the matrix. The guest FcC_{11}S - species appear as bright spots relative to the C_{12}S -SAM. A white square marks region containing a guest that

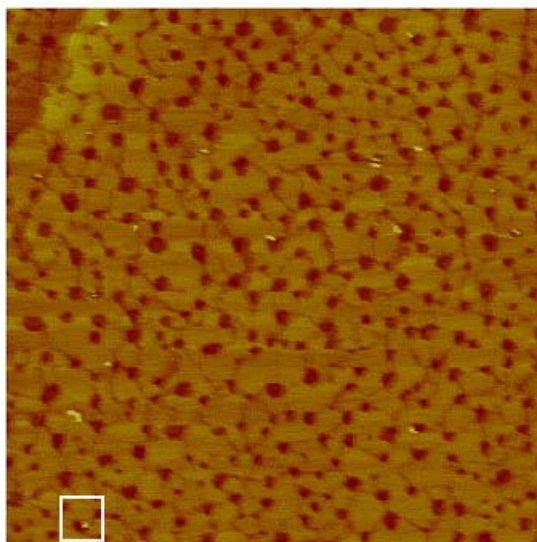


Figure 5.1: A $(250 \text{ nm})^2$ STM image of a C_{12}S - host SAM containing adventitiously adsorbed FcC_{11}S - guest species. The region marked with the square was tracked over time to generate the data seen in Figure 5.3. (Imaging conditions: 1 V, 9 pA, 1 Hz, z-scale: 2 nm)

was tracked over time, and the apparent height data from subsequent images extracted for Figure 5.3. This particular spot was chosen based on the amount of stochastic switching it

displayed over the data set, and because it remained in all the images despite the amount of drift that occurred in the images. The apparent heights of the guest species were measured by obtaining cross sectional analysis of four lines (vertical, horizontal and two diagonally) through the center of the guest(s) in question. This protocol is shown in Figure 5.2, which shows a guest species (bright spot) isolated in the host SAM. These four measurements for each guest were subsequently averaged, and plotted with error bars, as seen below.

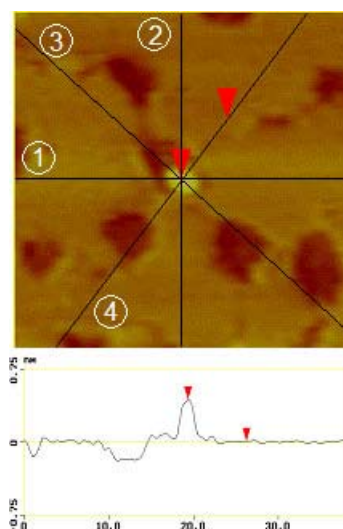


Figure 5.2: Analysis protocol used to determine apparent height contrast of guest species in host SAM. Section analysis of vertical, horizontal and diagonal section analysis were obtained and averaged to give an apparent height.

5.3 Stochastic conductance variation in FcC_{11}S - guests isolated in C_{12}S -SAMs:

A series of STM images displaying stochastic switching of a small collection of FcC_{11}S - guests in a C_{12}S -SAM is shown in Figure 5.3. The guest species appears as a bright spot at the edge of a substrate vacancy island. This was a common location for the guest species

adsorption because the bulky headgroup restricted the insertion into well-ordered regions of the *n*-alkanethiol host SAM. Below the images, the apparent height is tracked per frame number. It can be seen that the apparent height contrast fluctuates through the series of images in a manner similar to these seen in the stochastic switching reports described in the introduction. We believe this observation was because of conformation and / or orientation changes of the guest species. Notably, the bright spots also appear to vary in diameter / size

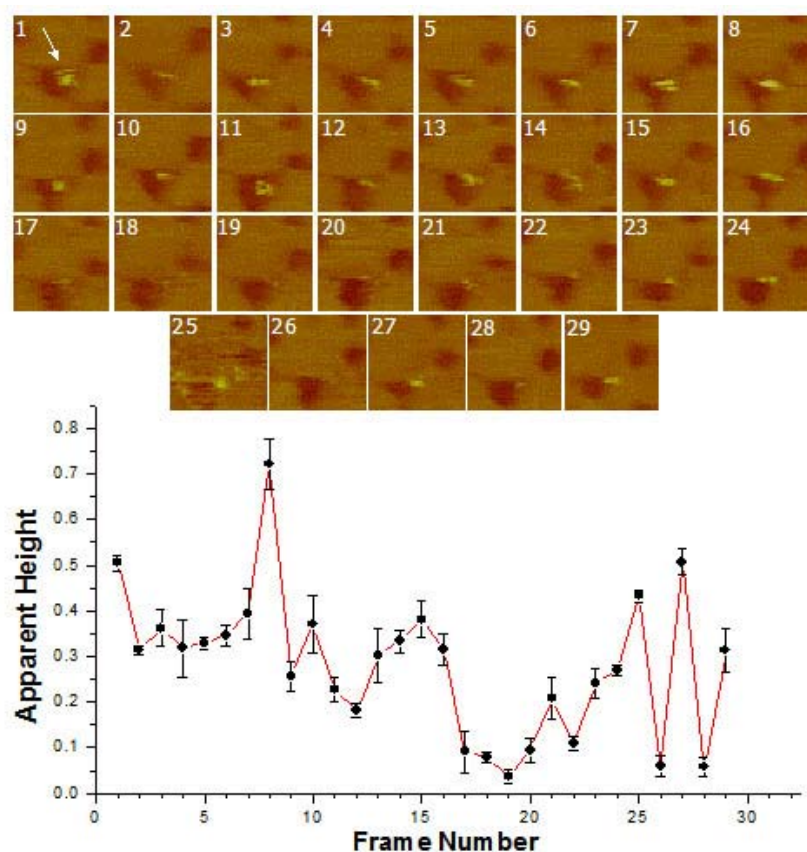


Figure 5.3: A) Time-lapse series of images of a collection of FcC_{11}S -guests in C_{12}S -SAM. Each image size is *ca.* $(20 \text{ nm})^2$. (Imaging conditions: 1.0 V, 9 pA, 1 Hz, z-scale: 2 nm). B) Apparent height contrast variation with frame number. Time between frames was 8.5 minutes.

as well as apparent height contrast. This is presumably because small groups (or bundles) of molecules occupy these guest regions, and their collective dynamic behavior results in the variation in apparent height contrasts and diameter depicted in the STM image. It is difficult to determine exactly how many guest species are actually contained within this bundle because the resolution of the image is not sufficient. Another series of STM images from a different sample containing the guest ferrocenyl terminated SAM guests (seen in Figure 5.4)

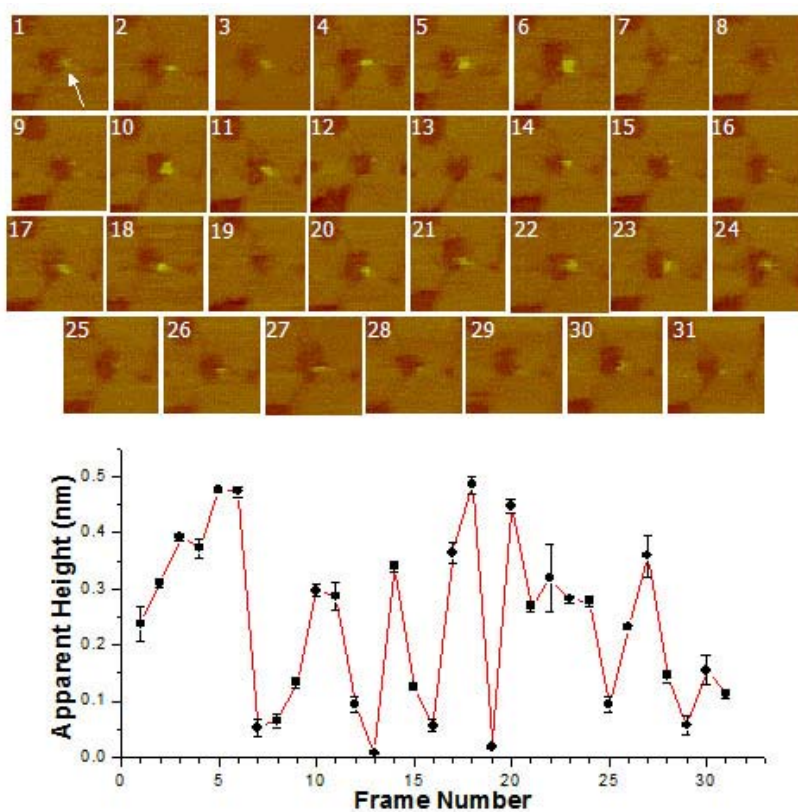


Figure 5.4: A) Time-lapse series of images of FcC₁₁S-SAM guest in C₁₂S-SAM. Each image size is *ca.* (20 nm)². (Imaging conditions: 1.0 V, 9 pA, 1 Hz, z-scale: 2 nm). B) Apparent height contrast variation with frame number. Time between frames was 8.5 minutes.

displayed a similar behavior. These examples clearly show that stochastic switching does occur in this host – guest SAM system.

The results from these stochastic switching investigations can be explained in terms of conformational or orientation changes within the guest species. A schematic of our hypothesized apparent height variation is shown in Figure 5.5, depicting a guest molecule inserted into a domain boundary at the edge of a substrate terrace. Here, the electroactive moiety is depicted as a pentagon atop an undecanethiol SAM. Since the alkyl tether is composed of sp^3 hybridized carbon centers, there are many degrees of freedom that could allow a considerable amount of movement. In Panel A, the electroactive guest is fully extended, causing the STM feedback response to give a large apparent height due to the

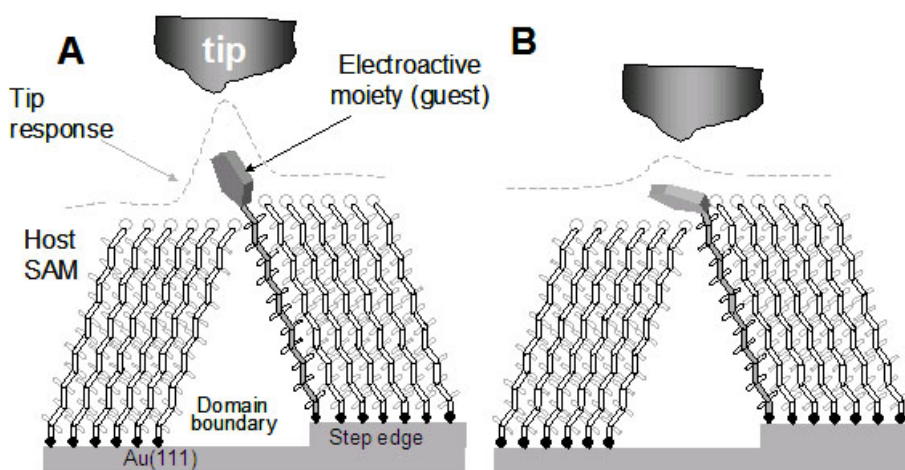


Figure 5.5: Schematic illustrating conformation changes (A & B) of a host electroactive containing SAM in an insulating guest SAM, resulting in different apparent height contrasts.

enhanced tunneling current that typically occurs over electroactive species. In panel B, a slight conformation change of the electroactive moiety causes the apparent height to decrease. These two panels offer a very simple depiction of what could occur at the molecular level by a small change in the electroactive headgroup orientation, resulting in a observable change in apparent height contrast in STM images. In extreme cases, it is possible that the headgroup could be intermittently buried in the host SAM, causing the apparent height contrast of the guest to decrease substantially, or temporarily disappear altogether.

5.4 Stochastic conductance variation in GalC₆S- guests isolated in C₁₂S-SAMs:

To further test our hypothesis that electroactive terminated SAMs will display stochastic switching behavior, other electroactive containing species were inserted into C₁₂S-SAMs and monitored over time with STM. To this end, GalC₆S- was inserted in C₁₂S-SAM according to the procedure described in section 5.6 (experimental). It was more difficult to find regions containing this guest species in C₁₂S-SAMs than with the FcC₁₁S- guest. Presumably, the large bulky headgroup and short alkylthiol tethering chain made it difficult for the guest to adsorb into the host matrix, even into most disordered regions. In the cases where a guest was tracked temporally, it was common that the apparent height contrast variation would appear to cease early on during the time scale surveyed, and often resulting in the disappearance of the guest altogether. An example of this can be seen in Figure 5.6. Here, the apparent height variation appears to decrease after frame eleven, and doesn't display a higher conductance during the rest of the frames. The reasons for this remain unclear. This occurrence may have

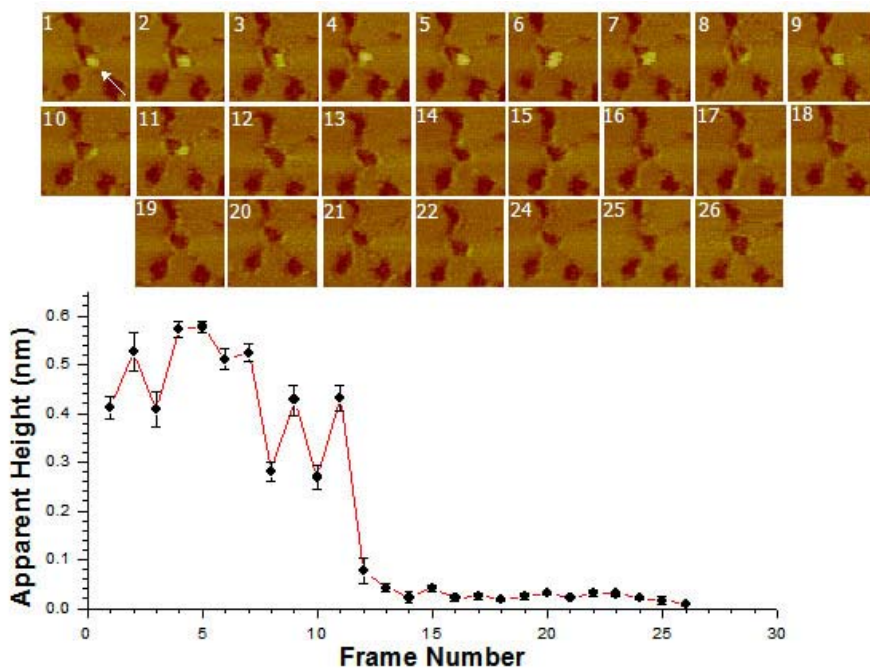


Figure 5.6: A) Time-lapse series of images of GalC₆S-SAM guest in C₁₂S-SAM. Each image size is (15.3 nm)². (Imaging conditions: 1.3 V, 10 pA, 1 Hz, z-scale: 1.5 nm). B) Apparent height contrast variation with frame number. Time between frames was 8.5 minutes.

been because the head group became buried within the host monolayer, or the guest species was desorbed from the substrate initiated by interaction with the tip and its bulky terminal headgroup.

5.5 Stochastic conductance variation in Ru(bpy)₃C₆S- guests isolated in C₁₂S-SAMs:

The third electroactive thiol investigated in this series was Ruthenium tris(bipyridine)-hexanethiol (Ru(bpy)₃C₆S-), shown in a series of STM images in Figure 5.7. This guest was also found at the periphery of a substrate vacancy island in a region of higher local disorder

due to its bulky headgroup. This data set showed similar results as the GalC₆S- guest, however with a slightly larger variation in stochastic behavior. A second series of images shows the Ru(Bpy)₃C₆S- guest isolated in a domain boundary away from a substrate vacancy island. In this series, the guest species did not appear to display large apparent contrast differentials across the data set relative to the host SAM, presumably because of the influence of the packing density of the surrounding matrix. This effect has been previously reported.¹⁹ In the latter images, a low apparent height contrast is displayed, possibly due to

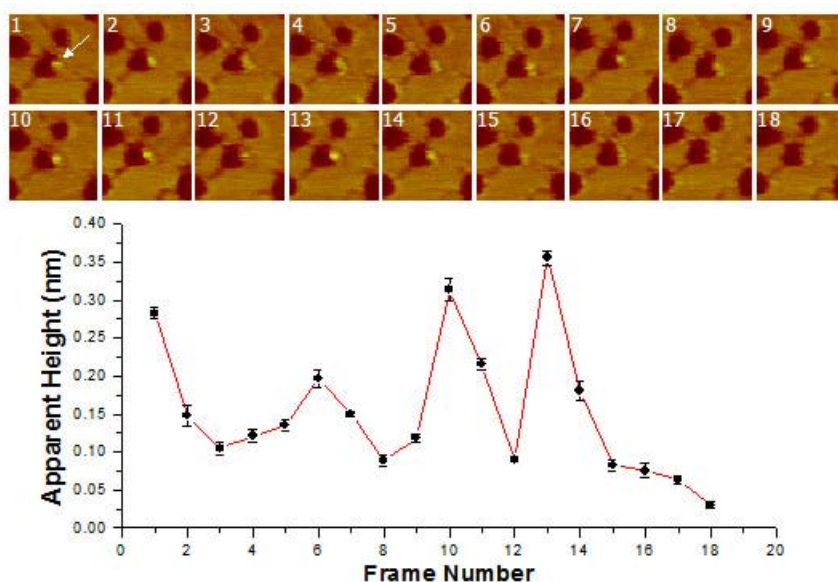


Figure 5.7: A) Time-lapse series of images of Ru(bpy)₃C₆S-SAM guest in C₁₂S-SAM. Each image size is (22.9 nm)². (Imaging conditions: 1.0 V, 10 pA, 1 Hz, z-scale: 2 nm). B) Apparent height contrast variation with frame number. Time between frames was 8.5 minutes.

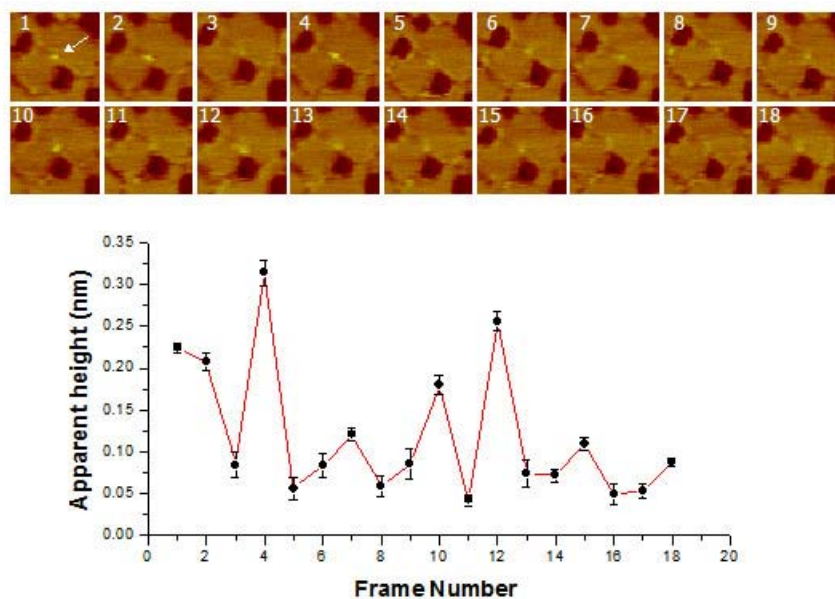


Figure 5.8: A) Time-lapse series of images of $\text{Ru}(\text{bpy})_3\text{C}_6\text{S}$ -SAM guest in C_{12}S -SAM. Each image size is $(24.1 \text{ nm})^2$. (Imaging conditions: 1.0 V, 10 pA, H1 z, z-scale: 2 nm). B) Apparent height contrast variation with frame number. Time between frames was 8.5 minutes.

the guest species headgroup being buried in the domain boundary of the host SAM. As with the other guest species investigated, this one also clearly displayed stochastic switching events.

5.6 Conclusion:

Stochastic variation in the apparent height contrast of molecules in a metal-SAM-metal junction was hypothesized to be a completely general phenomenon. Using STM, temporal investigations monitoring the conductance of electroactive containing SAM guest species isolated in host SAM matrices were extracted from the apparent height of these species in

STM images. Three different electroactive terminated alkylthiolates studied displayed this switching behavior over time. This behavior was most simply rationalized as being due to conformational and/or orientational changes of one or a small collection of molecules over time. With the more bulky candidates, the presence of the guest seemed to disappear, the reason for which remain unclear. It may have become buried into the host SAM by an orientation change, or desorbed from the substrate altogether from perturbation by the STM tip. The observations from these data may lend insight to how molecular electronic candidates might behave when sandwiched in a two-electrode configuration (metal-SAM-metal junction).

Acknowledgements: I gratefully acknowledge Sofi Bin-Salamon for synthesizing the Ruthenium tris(bipyridine)-hexanethiol used in these investigations, and Dr. David Shultz for providing the galvinoxylhexanethiol.

5.7 Experimental:

SAM Preparation:

Sample substrates were flame-annealed Au(111) facets on a gold bead formed at the end of a gold wire (Alfa Aesar, 99.999%). The wire was alloyed to a platinum foil (Alfa Aesar)

base.¹⁶ Prior to monolayer deposition the substrates were cleaned in piranha solution (3:1 H₂SO₄:H₂O₂ (30%) by volume). *n*-Alkanethiolate SAMs were prepared on gold by refluxing Au(111) facets in 1 mM dodecanethiol ethanolic solutions for 1 hour, allowed to cool, and then briefly exposed them to 1 mM ethanolic solutions of an electroactive guest species (FcC₁₁SH, GalC₆SH or Ru(bpy)₃C₆SH) for a few minutes. This allowed small groups of the guest species to insert into the defects sites in the host matrix.^{11,19,20,35,37} After copious rinsing in ethanol, the sample holder was mounted in a custom Kel-F fluid cell in preparation for scanning. After samples were placed in the STM, the environmental chamber was purged with dry N₂ for a minimum of 30 minutes before images were captured.

STM Imaging:

All STM experiments employed a Digital Instruments (Santa Barbara, CA) Nanoscope IIIa equipped with an E-scanner in low-current mode to obtain STM images at room temperature in dry nitrogen. Standard imaging conditions consisted of a setpoint current of 8 to 10 pA and a bias of 1.0 to 1.3V.

5.8 References:

- (1) Chen, J.; Reed, M. A.; Rawlett, A. M.; Tour, J. M. *Science* **1999**, *286*, 1550-1551.
- (2) Chen, J.; Wang, W.; Reed, M. A.; Rawlett, A. M.; Price, D. W.; Tour, J. M. *Applied Physics Letters* **2000**, *77*, 1224-1226.
- (3) Datta, S.; Tian, W. D.; Hong, S.; Reifenberger, R.; Henderson, J. I.; Kubiak, C. P. *Physical Review Letters* **1997**, *79*, 2530-2533.
- (4) Fan, F. R. F.; Lai, R. Y.; Cornil, J.; Karzazi, Y.; Bredas, J. L.; Cai, L. T.; Cheng, L.; Yao, Y. X.; Price, D. W.; Dirk, S. M.; Tour, J. M.; Bard, A. J. *Journal of American Chemical Society* **2004**, *126*, 2568-2573.
- (5) Fan, F. F.-R.; Yang, J.; Cai, L.; Price, J., D.W.; Dirk, S. M.; Kosynkin, D. V.; Yao, Y.; Rawlett, A. M.; Tour, J. M.; Bard, A. J. *Journal of American Chemical Society* **2002**, *124*, 5550-5560.
- (6) Han, W.; Durantini, E. N.; Moore, T. A.; Moore, A. L.; Gust, D.; Rez, P.; Leatherman, G.; Seely, G. R.; Tao, N.; Lindsay, S. M. *Journal of Physical Chemistry B* **1997**, *101*, 10719-10725.
- (7) Hong, S.; Reifenberger, R.; Tian, W.; Datta, S.; Henderson, J. I.; Kubiak, C. P. *Superlattices and Microstructures* **2000**, *28*, 289-303.
- (8) Le, J. D.; He, Y.; Hoye, T. R.; C.C., M.; Kiehl, R. A. *Applied Physics Letters* **2003**, *83*, 5518-5520.
- (9) Rawlett, A. M.; Hopson, T. J.; Nagahara, L. A.; Tsui, R. K.; Ramachandran, G. K.; Lindsay, S. M. *Applied Physics Letters* **2002**, *81*, 3043-3045.
- (10) Selzer, Y.; Salomon, A.; Ghabboun, J.; Cahen, D. *Angewandte Chemie International Edition in English* **2002**, *41*, 827-830.
- (11) Ramachandran, G. K.; Hopson, T. J.; Rawlett, A. M.; Nagahara, L. A.; Primak, A.; Lindsay, S. M. *Science* **2003**, *300*, 1413-1416.
- (12) Song, I. K.; Kaba, M. S.; Coulston, G.; Kourtakis, K.; Barteau, M. A. *Chemistry of Materials* **1996**, *8*, 2352-2358.
- (13) Walzer, K.; Marx, E.; Greenham, N. C.; Less, R. J.; Raithby, P. R.; Stokbro, K. *Journal of the American Chemical Society* **2004**, *126*, 1229-1234.

- (14) Xue, Y. Q.; Datta, S.; Hong, S.; Reifenberger, R.; Henderson, J. I.; Kubiak, C. P. *Physical Review B* **1999**, *59*, R7852-R7855.
- (15) Carroll, R. L.; Fuierer, R. R.; Gorman, C. B. *Using Probe Lithography and Self-Assembled Monolayers to Investigate Potential Molecular Electronics Systems*; American Chemical Society, 2003.
- (16) Gorman, C.; Carroll, R. L.; Fuierer, R. R. *Langmuir* **2001**, *17*, 6923-6930.
- (17) Wassel, R. A.; Credo, G. M.; Fuierer, R. R.; Feldheim, D. L.; Gorman, C. B. *Journal of American Chemical Society* **2003**, *126*, 295-300.
- (18) Tour, J. M. *Accounts of Chemical Research* **2000**, *33*, 791-804.
- (19) Donhauser, Z. J.; Mantooh, B. A.; Kelly, K. F.; Bumm, L. A.; Monnell, J. D.; Stapleton, J. J.; Price, D. W.; Rawlett, A. M.; Allara, D. L.; Tour, J. M.; Weiss, P. S. *Science* **2001**, *292*, 2303-2307.
- (20) Donhauser, Z. J.; Mantooh, B. A.; Pearl, T. P.; Kelly, K. F.; Nanayakkara, S. U.; Weiss, P. S. *Japanese Journal of Applied Physics Part 1-Regular Papers Short Notes & Review Papers* **2002**, *41*, 4871-4877.
- (21) Seminario, J. M.; Derosa, P. A.; Bastos, J. L. *Journal of American Chemical Society* **2002**, *124*, 10266-10267.
- (22) Solak, A. O.; Ranganathan, S.; Itoh, T.; McCreery, R. L. *Electrochemical and Solid-State Letters* **2002**, *5*, E43-E46.
- (23) Holmlin, R. E.; Haag, R.; Chabynyc, M. L.; Ismagilov, R. F.; Cohen, A. E.; Terfort, A.; Rampi, M. A.; Whitesides, G. M. *Journal of American Chemical Society* **2001**, *123*, 5075-5085.
- (24) Holmlin, R. E.; Ismagilov, R. F.; Haag, R.; Mujica, V.; Ratner, M. A.; Rampi, M. A.; Whitesides, G. M. *Angewandte Chemie International Edition in English* **2001**, *40*, 2316- 2320.
- (25) Carroll, R. L.; Gorman, C. B. *Angewandte Chemie International Edition in English* **2002**, *41*, 4378-4400.
- (26) Hipps, K. W.; Xing, L.; Wang, X. D.; Mazur, U. *Journal of Physical Chemistry* **1996**, *100*, 11207-11210.
- (27) Joachim, C.; Gimzewski, J. K.; Aviram, A. *Nature* **2000**, *408*, 541-548.

- (28) Mantooth, B. A.; Weiss, P. S. *Proceedings of the IEEE* **2003**, *91*, 1785-1802.
- (29) Lindsay, S. M. *Japanese Journal of Applied Physics Part 1 -Regular Papers Short Notes & review* **2002**, *41*, 4867-4870.
- (30) Tao, N. J. *Physical Review Letters* **1996**, *76*, 4066-4069.
- (31) Wold, D. J.; Frisbie, C. D. *Journal of the American Chemical Society* **2000**, *122*, 2970-2971.
- (32) Wold, D. J.; Frisbie, C. D. *Journal of American Chemical Society* **2001**, *123*, 5549-5556.
- (33) Allara, D. L.; Dunbar, T. D.; Weiss, P. S.; Bumm, L. A.; Cygan, M. T.; Tour, J. M.; Reinerth, W. A.; Yao, Y.; Kozaki, M.; Jones, L. In *Molecular Electronics: Science and Technology*; NEW YORK ACAD SCIENCES: New York, 1998; Vol. 852.
- (34) Bumm, L. A.; Arnold, J. J.; Cygan, M. T.; Dunbar, T. D.; Burgin, T. P.; Jones, L.; Allara, D. L.; Tour, J. M.; Weiss, P. S. *Science* **1996**, *271*, 1705-1707.
- (35) Cygan, M. T.; Dunbar, T. D.; Arnold, J. J.; Bumm, L. A.; Shedlock, N. F.; Burgin, T. P.; II, L. J.; Allara, D. L.; Tour, J. M.; Weiss, P. S. *Journal of American Chemical Society* **1998**, *120*, 2721-2732.
- (36) Weiss, P. S.; Bumm, L. A.; Dunbar, T. D.; Burgin, T. P.; Tour, J. M.; Allara, D. L. *Annals of the New York Academy of Sciences* **1998**, *852*, 145-168.
- (37) Bumm, L. A.; Arnold, J. J.; Dunbar, T. D.; Allara, D. L.; Weiss, P. S. *Journal of Physical Chemistry B* **1999**, *103*, 8122-8127.

Appendix A.1: Operation of STM:

This appendix describes the basic operation of scanning tunneling microscopy, and the instrumentation used in this work. A more detailed description can be found in numerous sources.¹⁻³

The majority of this work was completed with a scanning tunneling microscope (STM), a probe microscopy technique in which a voltage is applied between an atomically sharp tip and conducting substrate that is spaced sufficiently close to each other to allow electrons to tunnel between the tip-substrate gap.⁴ The tip is attached to a computer controlled piezo-positioning element, which allows the tip to be moved independently in three dimensions with atomic scale precision. Variation in the current results from either a change in tip-substrate separation or a change in the local density of states in the substrate, or a combination of the two. A feedback loop monitors the tunneling current across the x -, y - plane and adjusts the height of the tip (in the z -direction) to maintain a constant setpoint tunneling current (i.e. constant current mode). This information is plotted to give a three dimensional relief that is a convolution of the topographic and electronic properties of the surface. A schematic of an STM can be seen in Figure A.1.

Electron tunneling occurs when the tip and substrate are close enough in space (several Ångstroms) that their surface waves overlap. The gap between these two electrodes imposes an energy barrier. As a bias is applied between these two electrodes, the shape of the energy barrier is changed and there is a driving force for electrons to move across the barrier. Figure A.2

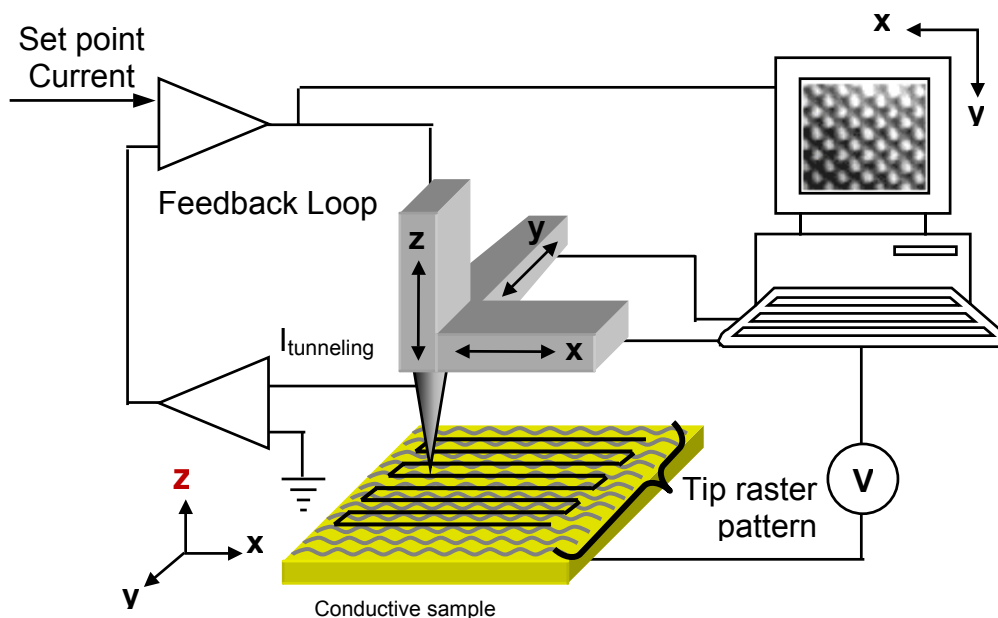


Figure A.1: Schematic of a scanning tunneling microscope (STM).

depicts this process schematically. Quantum mechanical treatment allows a finite number of electrons to traverse this barrier if the thickness (z) is small. The solution of the Schrödinger equation inside the barrier is:

$$\Psi(z) = \Psi(0) \exp(-2\kappa z) \quad \text{Equation (A.1)}$$

where κ is

$$\kappa = (2m(V-E)/\hbar^2)^{1/2} \quad \text{Equation (A.2)}$$

Where m is the mass of an electron, V is the potential in the barrier, E is the energy of the electron and \hbar is plank's constant. The probability that an electron will cross the barrier is the tunneling current, I

$$I \propto \exp(-2\kappa z) \quad \text{Equation (A.3)}$$

A decrease in wave overlap results in a decrease in the probability of electron tunneling, and ultimately a decrease in the tunneling current flow between the two electrodes at a given applied bias. As the tip and substrate are moved away from one another, the overlap of the surface waves will decay exponentially.

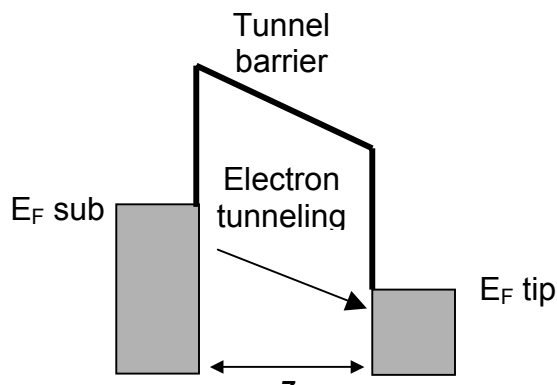


Figure A.2: Schematic illustrating the energy levels in the tip and substrate separated by a energy (tunnel) barrier with an applied bias. Energies of the electrons in the electrodes are indicated by the shaded regions. The applied bias is equal to the difference in the Fermi energies (E_F) of the two electrodes.²

The relation between the tip-substrate separation (z) as a function of tunneling current with constant applied bias can be seen in Figure A.3.A, and the separation as a function of applied bias while constant tunneling current is maintained Figure A.3.B. Equation A.1, dictates both the bias and current are exponential functions with respect to the distance. Larger tip-substrate

distances can be obtained by either increasing the STM operating bias, or lowering the operating setpoint current. These plots must always be considered when assigning experimental parameters, or blindly assigning empirical observations from an increase in tip-substrate separation.

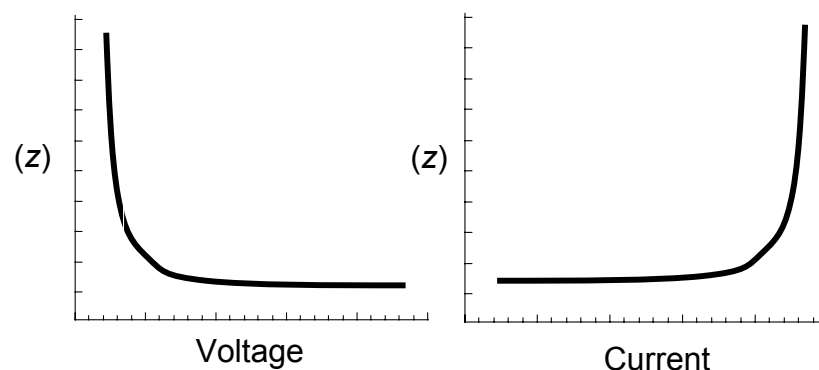


Figure A.3: Exponential dependency of voltage and current (respectively) as a function of tip-substrate distance (z).

Continuous Imaging Tunneling Spectroscopy:

As described briefly in Chapter 4, the current-voltage tunneling spectroscopy data were obtained in the mode known as continuous imaging tunneling spectroscopy (CITS).⁵ During the course of imaging the tip is periodically stopped in which the feedback loop disabled maintaining a constant tip-substrate separation, the bias swept to collect an $I(V)$ curve under a given set of user defined CITS parameters. This process is systematically iterated over the x -, y - scan area, creating an array of $I(V)$ sampling points. The user can define the bias range, number of $I(V)$ curves collected, number of sample points within a $I(V)$ curve, and the time between each

sample within the spectra (sample period). However, the user cannot define the bias direction or where the I(V) curves within the image can be collected. The sample period is the amount of time it takes for between voltage steps in the bias ramp during the I(V) curve acquisition (Figure A.4).⁶ The time it takes to acquire a single I(V) curve can be calculated by multiplying the

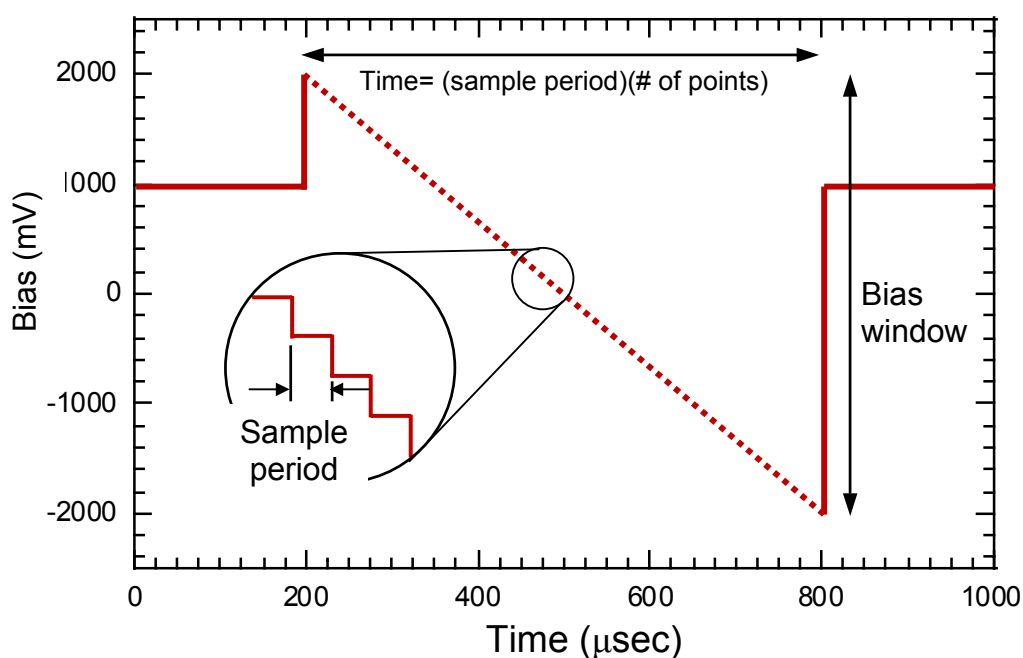


Figure A.4: Schematic illustrating the relation between the CITS parameters.
Figure adaptation courtesy of Drs. S. Krämer & W.P. McConnell

sample period by number of points contained in the I(V) curve,

$$\text{Time} = (\# \text{ samples})(\text{sample period}) \quad \text{Equation (A.4)}$$

The scan rate of the I(V) curve can be calculated by dividing time by the bias range,

$$\text{Scan Rate} = ((\# \text{ samples})(\text{sample period})/\text{bias range}) \quad \text{Equation (A.5)}$$

Typically, data sets of 1024 curves (a 512 x 512 array) were obtained in our experiments, such that a statistical representation could be generated. The details of the statistical protocol is discussed in Section 4.6, and elsewhere.^{7,8}

Another important consideration when collecting I(V) curves in CITS is the bandwidth of the low current electronics used in our STM configuration. These electronics have limited bandwidth due to noise compression filters that are required for these low current ranges. It is advisable that the signal one wants to collect under a specific set of parameters lies within the bandwidth of the measurement electronics. All of the I(V) data within was collected with a Digital Instruments Nanoscope NSe with booster box (low current electronics) that had a maximum filter cut-off frequency of 1.5 kHz. When expecting to observe a NDR response with a peak width of 1000 mV, within a voltage window of 4000 mV (-2 V to 2 V) with CITS parameters of 256 points and sample period of 1000 μ s, a series of quick calculations should first be executed. Using the empirical parameters given above, the total time of the voltage sweep is:

$$(256 \text{ points})(1000 \mu\text{s} / \text{point}) = 2.56 \times 10^5 \mu\text{s}$$

After conversion from μ s to s, the scan rate can be calculated for a 4000 mV window:

$$4 \text{ V} / 0.256 \text{ s} = 15.625 \text{ V} / \text{s}$$

The final calculation converts the voltage scale to frequency by dividing by the peak width:

$$(15.625 \text{ V} / \text{s}) / 1 \text{ V} = 15.625 \text{ s}^{-1}$$

This means that an NDR response with peak width of 1000 mV will have a frequency of 0.0156 kHz, which falls under the cut-off frequency of the electronics in the low current booster box.

A plot of peak width versus cut-off frequency as a function of sample period can be seen in Figure A.5. This figure was generated to determine if an NDR response collected at a specific sample period over a 4000 mV bias range would fall under the cut-off frequency of 1.5 kHz used in our experiments. As can be seen from the plot, I(V) curves collected with a sample period of 20 μ s fall outside the cut-off frequency of the low current electronics.

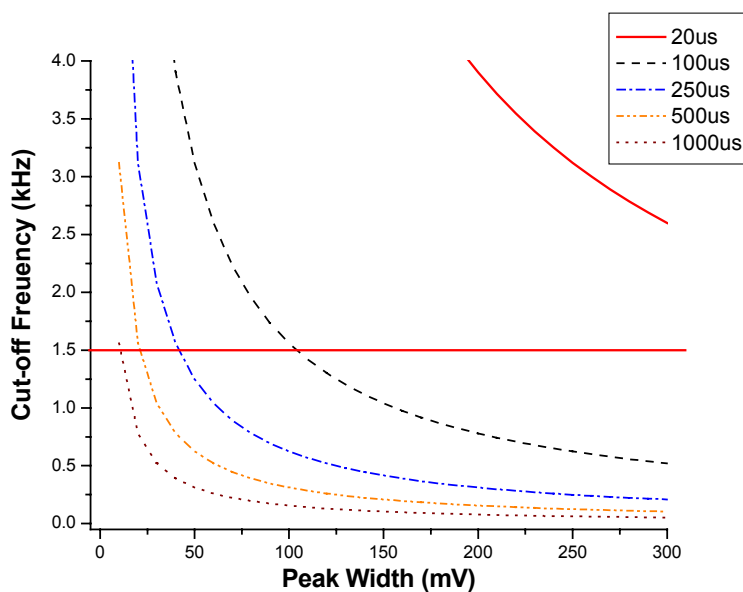


Figure A.5: Peak width vs. cut-off frequency plot as a function of sample period of the CITS experiment. Curves below the cut-off frequency of 1.5 kHz fall within bandwidth of the low current electronics.

References:

- (1) Bai, C. *Scanning Tunneling Microscopy and Its Applications*; Second ed.; Springer: Shanghai, 2000.
- (2) Bonnell, D.; Huey, B. D. In *Scanning Probe Microscopy and Spectroscopy: Theory, Techniques and Applications*; Second ed.; Bonnell, D., Ed.; John Wiley-VCH, Inc.: New York, 2001, pp 7-42.
- (3) Chung, Y.-W.; Academic Press: San Diego, 2001.
- (4) Binnig, G.; Rohrer, H. *IBM Journal of Research and Development* **1986**, *30*, 355-369.
- (5) Hamers, R. J.; Tromp, R. M.; Demuth, J. E. *Physical Review Letters* **1986**, *56*, 1972-1975.
- (6) McConnell, W. P. In *The Role of Surface Chemistry in Defining the Energetics and Kinetics of Single Electron Tunneling Through Individual Gold Nanoparticles*. Chemistry Department, North Carolina State University: Raleigh, NC, 2003, p 157.
- (7) Carroll, R. L. In *Studies of Structural and Electronic Properties of Self-assembled Monolayers - Towards Molecular Electronics*; Chemistry Department, North Carolina State University: Raleigh, NC, 2002.
- (8) Gorman, C. B.; Carroll, R. L.; Fuierer, R. R. *Langmuir* **2001**, *17*, 6923-6930.

Appendix 2.1

“Quarterfoil pattern” for Figure 2.3

```
#include <litho.h>

void main()
{
  LITHO_BEGIN
  // this macro writes a four leaf clover; “quarterfoil” pattern
  //has 100 steps takes about 15 seconds
  double rate = 0.04; //move tip in x-y at this value um/s
  double bias = 3.1; // move to starting point where the letter is scribed
  LithoTranslate (0, 0.07, rate);

  LithoSetOutput (aoBias, bias);

  //start at crotch

  //part 1 - crotch
  LithoTranslate ( 0.002, 0.018, rate);
  LithoTranslate ( 0.004, 0.012, rate);
  LithoTranslate ( 0.006, 0.012, rate);
  LithoTranslate ( 0.012, 0.014, rate);
  LithoTranslate ( 0.014, 0.012, rate);
  LithoTranslate ( 0.012, 0.006, rate);
  LithoTranslate ( 0.014, 0.004, rate);
  LithoTranslate ( 0.016, 0.002, rate);
  //part 2 - top of arc (repeat part 1)

  LithoTranslate ( 0.016, -0.002, rate);
  LithoTranslate ( 0.003, -0.004, rate);
  LithoTranslate ( 0.012, -0.006, rate);
  LithoTranslate ( 0.014, -0.012, rate);
  LithoTranslate ( 0.012, -0.014, rate);
  LithoTranslate ( 0.006, -0.012, rate);
  LithoTranslate ( 0.004, -0.012, rate);
  LithoTranslate ( 0.002, -0.018, rate);
  // part 3 - inverse of part 2

  LithoTranslate ( -0.002, -0.018, rate);
  LithoTranslate ( -0.004, -0.012, rate);
  LithoTranslate ( -0.006, -0.012, rate);
  LithoTranslate ( -0.012, -0.014, rate);
  LithoTranslate ( -0.014, -0.012, rate);
  LithoTranslate ( -0.012, -0.006, rate);
  LithoTranslate ( -0.014, -0.004, rate);

  LithoTranslate ( -0.016, -0.002, rate);

  // part 4 - repeat part 3
  LithoTranslate ( 0.016, -0.002, rate);
```

```
LithoTranslate ( 0.003, -0.004, rate);
LithoTranslate ( 0.012, -0.006, rate);
LithoTranslate ( 0.014, -0.012, rate);
LithoTranslate ( 0.012, -0.014, rate);
LithoTranslate ( 0.006, -0.012, rate);
LithoTranslate ( 0.004, -0.012, rate);
LithoTranslate ( 0.002, -0.018, rate);

// part 5

LithoTranslate ( -0.002, -0.018, rate);
LithoTranslate ( -0.004, -0.012, rate);
LithoTranslate ( -0.006, -0.012, rate);
LithoTranslate ( -0.012, -0.014, rate);
LithoTranslate ( -0.014, -0.012, rate);
LithoTranslate ( -0.012, -0.006, rate);
LithoTranslate ( -0.014, -0.004, rate);
LithoTranslate ( -0.016, -0.002, rate);

//part 6 -
LithoTranslate ( -0.016, 0.002, rate);
LithoTranslate ( -0.003, 0.004, rate);
LithoTranslate ( -0.012, 0.006, rate);
LithoTranslate ( -0.014, 0.012, rate);
LithoTranslate ( -0.012, 0.014, rate);
LithoTranslate ( -0.006, 0.012, rate);
LithoTranslate ( -0.004, 0.012, rate);
LithoTranslate ( -0.002, 0.018, rate);

// part 7 -
LithoTranslate ( -0.002, -0.018, rate);
LithoTranslate ( -0.004, -0.012, rate);
LithoTranslate ( -0.006, -0.012, rate);
LithoTranslate ( -0.012, -0.014, rate);
LithoTranslate ( -0.014, -0.012, rate);
LithoTranslate ( -0.012, -0.006, rate);
LithoTranslate ( -0.014, -0.004, rate);
LithoTranslate ( -0.016, -0.002, rate);

// part 8 -
LithoTranslate ( -0.016, 0.002, rate);
LithoTranslate ( -0.003, 0.004, rate);
LithoTranslate ( -0.012, 0.006, rate);
LithoTranslate ( -0.014, 0.012, rate);
LithoTranslate ( -0.012, 0.014, rate);
LithoTranslate ( -0.006, 0.012, rate);
LithoTranslate ( -0.004, 0.012, rate);
LithoTranslate ( -0.002, 0.018, rate);

//part 9
LithoTranslate ( 0.002, 0.018, rate);
LithoTranslate ( 0.004, 0.012, rate);
LithoTranslate ( 0.006, 0.012, rate);
```

```
LithoTranslate ( 0.012, 0.014, rate);  
LithoTranslate ( 0.014, 0.012, rate);  
LithoTranslate ( 0.012, 0.006, rate);  
LithoTranslate ( 0.014, 0.004, rate);  
LithoTranslate ( 0.016, 0.002, rate);
```

```
//part 10
```

```
LithoTranslate ( -0.016, 0.002, rate);  
LithoTranslate ( -0.003, 0.004, rate);  
LithoTranslate ( -0.012, 0.006, rate);  
LithoTranslate ( -0.014, 0.012, rate);  
LithoTranslate ( -0.012, 0.014, rate);  
LithoTranslate ( -0.006, 0.012, rate);  
LithoTranslate ( -0.004, 0.012, rate);  
LithoTranslate ( -0.002, 0.018, rate);
```

```
// part 11
```

```
LithoTranslate ( 0.002, 0.018, rate);  
LithoTranslate ( 0.004, 0.012, rate);  
LithoTranslate ( 0.006, 0.012, rate);  
LithoTranslate ( 0.012, 0.014, rate);  
LithoTranslate ( 0.014, 0.012, rate);  
LithoTranslate ( 0.012, 0.006, rate);  
LithoTranslate ( 0.014, 0.004, rate);  
LithoTranslate ( 0.016, -0.002, rate);
```

```
//part 12 -
```

```
LithoTranslate ( 0.016, -0.002, rate);  
LithoTranslate ( 0.003, -0.004, rate);  
LithoTranslate ( 0.012, -0.006, rate);  
LithoTranslate ( 0.014, -0.012, rate);  
LithoTranslate ( 0.012, -0.014, rate);  
LithoTranslate ( 0.006, -0.012, rate);  
LithoTranslate ( 0.004, -0.012, rate);  
LithoTranslate ( 0.002, -0.018, rate);  
LithoSetOutput ( aoBias, 1.0);
```

```
LITHO_END
```

```
}
```

Appendix 2.2

“NC State Logo” for Figure 2.4

```
#include <litho.h>
```

```
void main()
```

```
LITHO_BEGIN
```

```
// this draws the NCS logo, where N & C are within the S
```

```
double rate=0.05; //move the tip in x-y at 100nm/s
```

```
double bias=3.0;
```

```
//move to the startingpoint where the letter is scribed
```

```
LithoTranslate (-0.1,-0.16,rate);
```

```
//set the Bias voltage to 3.0 volts
```

```
LithoSetOutput (aoBias,bias);
```

```
//scribe the letter S
```

```
LithoTranslate ( 0.04, -0.04, rate);
```

```
LithoTranslate ( 0.12, 0, rate);
```

```
LithoTranslate ( 0.04, 0.04, rate);
```

```
LithoTranslate ( 0, 0.12, rate);
```

```
LithoTranslate (-0.04, 0.04, rate);
```

```
LithoTranslate (-0.12, 0, rate);
```

```
LithoTranslate (-0.04, 0.04, rate);
```

```
LithoTranslate ( 0, 0.12, rate);
```

```
LithoTranslate ( 0.04, 0.04, rate);
```

```
LithoTranslate ( 0.12, 0, rate);
```

```
LithoTranslate ( 0.04, -0.04, rate);
```

```
LithoSetOutput ( aoBias,1.0);
```

```
//scribe letter N inside S
```

```
LithoTranslate (-0.06, -0.02, rate);
```

```
LithoSetOutput ( aoBias, bias);
```

```
LithoTranslate ( 0, -0.08, rate);
```

```
LithoTranslate (-0.08, 0.08, rate);
```

```
LithoTranslate ( 0, -0.08, rate);
```

```
LithoSetOutput ( aoBias, 1.0);
```

```
//scribe the letter C inside S
```

```
LithoTranslate (0.08, -0.14, rate);
```

```
LithoSetOutput (aoBias,bias);
```

```
LithoTranslate (-0.02, 0.02, rate);
```

```
LithoTranslate (-0.04, 0, rate);
```

```
LithoTranslate (-0.02, -0.02, rate);
```

```
LithoTranslate ( 0, -0.04, rate);
```

```
LithoTranslate ( 0.02, -0.02, rate);
```

```
LithoTranslate ( 0.04, 0, rate);
```

```
LithoTranslate ( 0.02, 0.02, rate);
```

```
LithoSetOutput ( aoBias, 1.0);
```

```
LITHO_END
```

Appendix 2.3

“12 lines” for Figure 2.6

```
#include <litho.h>

void main()
{
  LITHO_BEGIN
  // writes two rows of 6 vertical lines 100nm apart at incrementally different biases
  double rate = 0.05; //move tip in x-y at this rate in um/s
  double startvoltage = 2.5; //voltage of first line etch
  double increment = 0.1; //increment of voltage

  LithoTranslate (-0.25, +0.05, rate); //move to starting point
  LithoSetOutput (aoBias, startvoltage); // turn on at startvoltage
  LithoTranslate ( 0, 0.2, rate); //scribes line up
  LithoSetOutput (aoBias, 1.0); //turn off
  LithoTranslate ( 0.1, 0, rate); // move
  LithoSetOutput (aoBias, startvoltage+1*increment); // turn on and etch
  LithoTranslate ( 0, -0.2, rate); //scribe line down
  LithoSetOutput ( aoBias, 1.0); // turn off
  LithoTranslate ( 0.1, 0, rate); // move
  LithoSetOutput (aoBias, startvoltage+2*increment); //turn on and etch
  LithoTranslate ( 0, 0.2, rate); //scribe line up
  LithoSetOutput ( aoBias, 1.0); // turn off
  LithoTranslate ( 0.1, 0, rate); // move
  LithoSetOutput ( aoBias, startvoltage+3*increment); // turn on and etch
  LithoTranslate ( 0, -0.2, rate); // scribe line down
  LithoSetOutput ( aoBias, 1.0); // turn off
  LithoTranslate ( 0.1, 0, rate); // move
  LithoSetOutput (aoBias, startvoltage+4*increment); // turn on and etch
  LithoTranslate ( 0, 0.2, rate); // scribe line up
  LithoSetOutput ( aoBias, 1.0); // turn off
  LithoTranslate ( 0.1, 0, rate); // move
  LithoSetOutput ( aoBias, startvoltage+5*increment); // turn on and etch
  LithoTranslate ( 0, -0.2, rate); // scribe line Down, reference line
  LithoTranslate ( 0.07, 0, rate); //makes reference line on last (RHS) line
  LithoSetOutput (aoBias, 1.0);
  LithoTranslate (-0.57, -0.3, rate); //move to starting point
  LithoSetOutput (aoBias, startvoltage+6*increment); // turn on at startvoltage
  LithoTranslate ( 0, 0.2, rate); //scribes line up
  LithoSetOutput (aoBias, 1.0); //turn off
  LithoTranslate ( 0.1, 0, rate); // move
  LithoSetOutput (aoBias, startvoltage+7*increment); // turn on and etch
  LithoTranslate ( 0, -0.2, rate); //scribe line down
  LithoSetOutput ( aoBias, 1.0); // turn off
  LithoTranslate ( 0.1, 0, rate); // move
  LithoSetOutput (aoBias, startvoltage+8*increment); //turn on and etch
  LithoTranslate ( 0, 0.2, rate); //scribe line up
  LithoSetOutput ( aoBias, 1.0); // turn off
  LithoTranslate ( 0.1, 0, rate); // move
```

```
LithoSetOutput ( aoBias, startvoltage+9*increment); // turn on and etch
LithoTranslate ( 0, -0.2, rate); // scribe line down
LithoSetOutput ( aoBias, 1.0); // turn off
LithoTranslate ( 0.1, 0, rate); // move
LithoSetOutput (aoBias, startvoltage+10*increment); // turn on and etch
LithoTranslate ( 0, 0.2, rate); // scribe line up
LithoSetOutput ( aoBias, 1.0); // turn off
LithoTranslate ( 0.1, 0, rate); // move
LithoSetOutput ( aoBias, startvoltage+11*increment); // turn on and etch
LithoTranslate ( 0, -0.2, rate); // scribe line Down, reference line
LithoTranslate ( 0.07, 0, rate); //makes reference line on last (RHS) line
LithoSetOutput (aoBias, 1.0);
LITHO_END
}
```

Appendix 2.4

“6 lines” for Figure 2.7

```

void main()
{
LITHO_BEGIN
// write 6 vertical lines 100nm apart at different (-) bias'
// has 29 instructions
double rate = 0.02; //move tip in x-y at this rate in um/s
double startvoltage = -2.7;
double increment = -0.10;

LithoTranslate (-0.26, -0.1, rate); //move to starting point
LithoSetOutput (aoBias, startvoltage);
LithoTranslate ( 0, 0.2, rate); //scribes line up
LithoSetOutput (aoBias, 1.0); //turn off
LithoTranslate ( 0.1, 0, rate); // move
LithoSetOutput (aoBias, startvoltage+1*increment); // turn on
LithoTranslate ( 0, -0.2, rate); //scribe line down
LithoSetOutput ( aoBias, 1.0); // turn off
LithoTranslate ( 0.1, 0, rate); // move
LithoSetOutput (aoBias, startvoltage+2*increment); //turn on
LithoTranslate ( 0, 0.2, rate); //scribe line up
LithoSetOutput ( aoBias, 1.0); // turn off
LithoTranslate ( 0.1, 0, rate); // move
LithoSetOutput ( aoBias, startvoltage+3*increment); // turn on
LithoTranslate ( 0, -0.2, rate); // scribe line down
LithoSetOutput ( aoBias, 1.0); // turn off
LithoTranslate ( 0.1, 0, rate); // move
LithoSetOutput (aoBias, startvoltage+4*increment); // turn on a
LithoTranslate ( 0, 0.2, rate); // scribe line up
LithoSetOutput ( aoBias, 1.0); // turn off
LithoTranslate ( 0.1, 0, rate); // move
LithoSetOutput ( aoBias, startvoltage+5*increment); // turn on at 2.8V
LithoTranslate ( 0, -0.2, rate); // scribe line Down, reference line
LithoSetOutput (aoBias, 1.0);
LithoTranslate ( 0, 0.1, rate);
LithoSetOutput ( aoBias, startvoltage+5*increment);
LithoTranslate ( 0.04, 0, rate);
LithoSetOutput ( aoBias, 1.0); // turn off

LITHO_END}

```

Appendix 2.5

“7 lines” for Figure 2.8

```
#include <litho.h>

void main()
{
  LITHO_BEGIN
  // write 7 vertical lines 100nm apart at different bias'
  double rate = 0.05; //move tip in x-y at this rate in um/s

  LithoTranslate (-0.3, -0.1, rate); //move to starting point
  LithoSetOutput (aoBias, 2.7); // turn on at 2.5V
  LithoTranslate ( 0, 0.2, rate); //scribes line up at 2.5V
  LithoSetOutput (aoBias, 1.0); //turn off
  LithoTranslate ( 0.1, 0, rate); // move
  LithoSetOutput (aoBias, 2.8); // turn on at 2.6
  LithoTranslate ( 0, -0.2, rate); //scribe line down at 2.6V
  LithoSetOutput ( aoBias, 1.0); // turn off
  LithoTranslate ( 0.1, 0, rate); // move
  LithoSetOutput (aoBias, 2.9); //turn on at 2.7V
  LithoTranslate ( 0, 0.2, rate); //scribe line up
  LithoSetOutput ( aoBias, 1.0); // turn off
  LithoTranslate ( 0.1, 0, rate); // move
  LithoSetOutput ( aoBias, 3.0); // turn on at 2.8V
  LithoTranslate ( 0, -0.2, rate); // scribe line down
  LithoSetOutput ( aoBias, 1.0); // turn off
  LithoTranslate ( 0.1, 0, rate); // move
  LithoSetOutput (aoBias, 3.1); // turn on at 3.1V
  LithoTranslate ( 0, 0.2, rate); // scribe line up
  LithoSetOutput ( aoBias, 1.0); // turn off
  LithoTranslate ( 0.1, 0, rate); // move
  LithoSetOutput ( aoBias, 3.2); // turn on at 3.2V
  LithoTranslate ( 0, -0.2, rate); // scribe line Down
  LithoSetOutput ( aoBias, 1.0); // turn off
  LithoTranslate ( 0.1, 0, rate); // move
  LithoSetOutput ( aoBias, 3.3); // turn on at 3.3V
  LithoTranslate ( 0, 0.2, rate); //scribe line up
  LithoTranslate ( 0.04, 0, rate); // finished reference line
  LithoSetOutput ( aoBias, 1.0); //turn off

  LITHO_END
}
```

Appendix 2.6

“RH lines” for Figure 2.9

```
#include <litho.h>

void main()
{
  LITHO_BEGIN
  // write 6 vertical lines 100nm apart at different (-) bias'
  // has 29 intructions
  double rate = 0.02; //move tip in x-y at this rate in um/s
  double startvoltage = -2.7;
  double increment = -0.10;

  LithoTranslate (-0.26, -0.1, rate); //move to starting point
  LithoSetOutput (aoBias, startvoltage);
  LithoTranslate ( 0, 0.2, rate); //scribes line up
  LithoSetOutput (aoBias, 1.0); //turn off
  LithoTranslate ( 0.1, 0, rate); // move
  LithoSetOutput (aoBias, startvoltage+1*increment); // turn on
  LithoTranslate ( 0, -0.2, rate); //scribe line down
  LithoSetOutput ( aoBias, 1.0); // turn off
  LithoTranslate ( 0.1, 0, rate); // move
  LithoSetOutput (aoBias, startvoltage+2*increment); //turn on
  LithoTranslate ( 0, 0.2, rate); //scribe line up
  LithoSetOutput ( aoBias, 1.0); // turn off
  LithoTranslate ( 0.1, 0, rate); // move
  LithoSetOutput ( aoBias, startvoltage+3*increment); // turn on
  LithoTranslate ( 0, -0.2, rate); // scribe line down
  LithoSetOutput ( aoBias, 1.0); // turn off
  LithoTranslate ( 0.1, 0, rate); // move
  LithoSetOutput (aoBias, startvoltage+4*increment); // turn on a
  LithoTranslate ( 0, 0.2, rate); // scribe line up
  LithoSetOutput ( aoBias, 1.0); // turn off
  LithoTranslate ( 0.1, 0, rate); // move
  LithoSetOutput ( aoBias, startvoltage+5*increment); // turn on at 2.8V
  LithoTranslate ( 0, -0.2, rate); // scribe line Down, reference line
  LithoSetOutput (aoBias, 1.0);
  LithoTranslate ( 0, 0.1, rate);
  LithoSetOutput ( aoBias, startvoltage+5*increment);
  LithoTranslate ( 0.04, 0, rate);
  LithoSetOutput ( aoBias, 1.0); // turn off

  LITHO_END}
```

Appendix 2.7

“Gal” letters for Figure 2.10

```
#include <litho.h>

void main()
{
LITHO_BEGIN

double rate = 0.03; // move tip in x-y at 100nm/s
double bias = 3.1; // move to starting point where the letter is scribed
// writes g in opposite direction as galvinol macro
LithoTranslate (-0.1, 0.06, rate);

// set the Bias Voltage to 3.0 volts
LithoSetOutput (aoBias, bias);

//scribe the letter G
LithoTranslate (-0.04, 0.04, rate);
LithoTranslate (-0.02, 0, rate);
LithoTranslate (-0.04, -0.04, rate);
LithoTranslate ( 0, -0.12, rate);
LithoTranslate ( 0.04, -0.04, rate);
LithoTranslate ( 0.02, 0, rate);
LithoTranslate ( 0.04, 0.04, rate);
LithoTranslate ( 0, 0.06, rate);
LithoTranslate ( -0.04, 0, rate);
LithoSetOutput (aoBias, 1.0);

//scribe the letter a
LithoTranslate (0.1, 0, rate);
LithoSetOutput (aoBias, bias);
LithoTranslate (0.08, 0, rate);
LithoTranslate (0, -0.1, rate);
LithoTranslate ( -0.08, 0, rate);
LithoTranslate ( 0, 0.06, rate);
LithoTranslate ( 0.08, 0, rate);
LithoSetOutput (aoBias, 1.0);

//scribe the letter l
LithoTranslate (0.06, -0.06, rate);
LithoSetOutput (aoBias, bias);
LithoTranslate (0, 0.2, rate);
LithoSetOutput (aoBias, 1.0);

LITHO_END

}
```

Appendix 2.8

“Fc” letters for Figure 2.11

```
#include <litho.h>

void main()
{
LITHO_BEGIN

double rate = 0.05; //move tip in x-y at this value in um/s
double bias = 2.9;
// move to starting point where the letter is scribed
LithoTranslate (-0.1, -0.08, rate);

// set the Bias Voltage to 3.0 volts
LithoSetOutput (aoBias, bias);

//scribe the F
LithoTranslate ( 0, 0.2, rate);
LithoTranslate ( 0.1, 0, rate);
LithoSetOutput (aoBias, 1.0);
LithoTranslate ( -0.1, -0.08, rate);
LithoSetOutput (aoBias, bias);
LithoTranslate ( 0.06, 0, rate);
LithoSetOutput (aoBias, 1.0);
//scribe the letter c
LithoTranslate ( 0.14, -0.02, rate);
LithoSetOutput (aoBias, bias);
LithoTranslate ( -0.04, 0.04, rate);
LithoTranslate ( -0.02, 0, rate);
LithoTranslate ( -0.04, -0.04, rate);
LithoTranslate ( 0, -0.04, rate);
LithoTranslate ( 0.04, -0.04, rate);
LithoTranslate ( 0.02, 0, rate);
LithoTranslate ( 0.04, 0.04, rate);
LithoSetOutput (aoBias, 1.0);

LITHO_END
}
```

Appendix 3.1

“Replacement bias gradient” for Figure 3.1

```
#include <litho.h>
```

```
void main()
{
LITHO_BEGIN
// has 184 steps,takes a few minutes
double rate = 0.05; // move tip in x-y at 50nm/s
double startvoltage = 2.5;
double increment = 0.02;

LithoTranslate (-0.1, 0.3, rate);

LithoSetOutput ( aoBias, startvoltage);
LithoTranslate ( 0.2, 0, rate); // scribe line
LithoTranslate ( 0, -0.012, rate);
LithoTranslate ( -0.2, 0, rate); // scribe line
LithoTranslate ( 0, -0.012, rate);
LithoTranslate ( 0.2, 0, rate); //scribe line
LithoTranslate ( 0, -0.012, rate);
LithoSetOutput ( aoBias, startvoltage+1*increment);
LithoTranslate ( -0.2, 0, rate); //scribe line
LithoTranslate ( 0, -0.012, rate);
LithoTranslate ( 0.2, 0, rate); // scribe line
LithoTranslate ( 0, -0.012, rate);
LithoTranslate (-0.2, 0, rate); // scribe line
LithoTranslate ( 0, -0.012, rate);
LithoSetOutput ( aoBias, startvoltage+2*increment);
LithoTranslate ( 0.2, 0, rate); // scribe line
LithoTranslate ( 0, -0.012, rate);
LithoTranslate ( -0.2, 0, rate); // scribe line
LithoTranslate ( 0, -0.012, rate);
LithoTranslate ( 0.2, 0, rate); // scribe line
LithoTranslate ( 0, -0.012, rate);
LithoSetOutput ( aoBias, startvoltage+3*increment);
LithoTranslate ( -0.2, 0 , rate); // scribe line
LithoTranslate ( 0, -0.012, rate);
LithoTranslate ( 0.2, 0, rate); //scribe line
LithoTranslate ( 0, -0.012, rate);
LithoTranslate ( -0.2, 0, rate);
LithoTranslate ( 0, -0.012, rate);
LithoSetOutput ( aoBias, startvoltage+4*increment);
LithoTranslate ( 0.2, 0, rate);
LithoTranslate ( 0, -0.012, rate);
LithoTranslate ( -0.2, 0, rate);
LithoTranslate ( 0, -0.012, rate);
LithoTranslate ( 0.2, 0, rate); // scribe line
LithoTranslate ( 0, -0.012, rate);
LithoSetOutput ( aoBias, startvoltage+5*increment);
LithoTranslate ( -0.2, 0, rate);
LithoTranslate ( 0, -0.012, rate);
```

```
LithoTranslate ( 0.2, 0, rate);
LithoTranslate ( 0, -0.012, rate);
LithoTranslate ( -0.2, 0, rate);
LithoTranslate ( 0, -0.01, rate);
LithoSetOutput ( aoBias, startvoltage+6*increment);
LithoTranslate ( 0.2, 0, rate);
LithoTranslate ( 0, -0.01, rate);
LithoTranslate ( -0.2, 0, rate);
LithoTranslate ( 0, -0.01, rate);
LithoTranslate ( 0.2, 0, rate);
LithoTranslate ( 0, -0.01, rate);
LithoSetOutput ( aoBias, startvoltage+7*increment);
LithoTranslate ( -0.2, 0, rate);
LithoTranslate ( 0, -0.01, rate);
LithoTranslate ( 0.2, 0, rate); // scribe line
LithoTranslate ( 0, -0.01, rate);
LithoTranslate ( -0.2, 0, rate);
LithoTranslate ( 0, -0.01, rate);
LithoSetOutput ( aoBias, startvoltage+8*increment);
LithoTranslate ( 0.2, 0, rate);
LithoTranslate ( 0, -0.01, rate);
LithoTranslate ( -0.2, 0, rate);
LithoTranslate ( 0, -0.01, rate);
LithoTranslate ( 0.2, 0, rate);
LithoTranslate ( 0, -0.01, rate);
LithoSetOutput ( aoBias, startvoltage+9*increment);
LithoTranslate ( -0.2, 0, rate);
LithoTranslate ( 0, -0.01, rate);
LithoTranslate ( 0.2, 0, rate);
LithoTranslate ( 0, -0.01, rate);
LithoTranslate ( -0.2, 0, rate);
LithoTranslate ( 0, -0.01, rate);
LithoSetOutput ( aoBias, startvoltage+10*increment);
LithoTranslate ( 0.2, 0, rate);
LithoTranslate ( 0, -0.01, rate);
LithoTranslate ( -0.2, 0, rate);
LithoTranslate ( 0, -0.01, rate);
LithoTranslate ( 0.2, 0, rate);
LithoTranslate ( 0, -0.01, rate);
LithoSetOutput ( aoBias, startvoltage+11*increment);
LithoTranslate ( -0.2, 0, rate);
LithoTranslate ( 0, -0.01, rate);
LithoTranslate ( 0.2, 0, rate);
LithoTranslate ( 0, -0.01, rate);
LithoTranslate ( -0.2, 0, rate);
LithoTranslate ( 0, -0.01, rate);
LithoSetOutput ( aoBias, startvoltage+12*increment);
LithoTranslate ( 0.2, 0, rate);
LithoTranslate ( 0, -0.01, rate);
LithoTranslate ( -0.2, 0, rate);
LithoTranslate ( 0, -0.01, rate);
LithoTranslate ( 0.2, 0, rate);
LithoTranslate ( 0, -0.01, rate);
```

```
LithoSetOutput ( aoBias, startvoltage+13*increment);
LithoTranslate ( -0.2, 0, rate);
LithoTranslate ( 0, -0.01, rate);
LithoTranslate ( 0.2, 0, rate);
LithoTranslate ( 0, -0.01, rate);
LithoTranslate ( -0.2, 0, rate);
LithoTranslate ( 0, -0.01, rate);
LithoSetOutput ( aoBias, startvoltage+14*increment);
LithoTranslate ( 0.2, 0, rate);
LithoTranslate ( 0, -0.01, rate);
LithoTranslate ( -0.2, 0, rate);
LithoTranslate ( 0, -0.01, rate);
LithoTranslate ( 0.2, 0, rate);
LithoTranslate ( 0, -0.01, rate);
LithoSetOutput ( aoBias, startvoltage+15*increment);
LithoTranslate ( -0.2, 0, rate);
LithoTranslate ( 0, -0.0075, rate);
LithoTranslate ( 0.2, 0, rate);
LithoTranslate ( 0, -0.0075, rate);
LithoTranslate ( -0.2, 0, rate);
LithoTranslate ( 0, -0.0075, rate);
LithoSetOutput ( aoBias, startvoltage+16*increment);
LithoTranslate ( 0.2, 0, rate);
LithoTranslate ( 0, -0.0075, rate);
LithoTranslate ( -0.2, 0, rate);
LithoTranslate ( 0, -0.0075, rate);
LithoTranslate ( 0.2, 0, rate);
LithoTranslate ( 0, -0.0075, rate);
LithoSetOutput ( aoBias, startvoltage+17*increment);
LithoTranslate ( -0.2, 0, rate);
LithoTranslate ( 0, -0.0075, rate);
LithoTranslate ( 0.2, 0, rate);
LithoTranslate ( 0, -0.0075, rate);
LithoTranslate ( -0.2, 0, rate);
LithoTranslate ( 0, -0.0075, rate);
LithoSetOutput ( aoBias, startvoltage+18*increment);
LithoTranslate ( 0.2, 0, rate);
LithoTranslate ( 0, -0.0075, rate);
LithoTranslate ( -0.2, 0, rate);
LithoTranslate ( 0, -0.0075, rate);
LithoTranslate ( 0.2, 0, rate);
LithoTranslate ( 0, -0.0075, rate);
LithoSetOutput ( aoBias, startvoltage+19*increment);
LithoTranslate ( -0.2, 0, rate);
LithoTranslate ( 0, -0.0075, rate);
LithoTranslate ( 0.2, 0, rate);
LithoTranslate ( 0, -0.0075, rate);
LithoTranslate ( -0.2, 0, rate);
LithoTranslate ( 0, -0.0075, rate);
LithoSetOutput ( aoBias, startvoltage+20*increment);
LithoTranslate ( 0.2, 0, rate);
LithoTranslate ( 0, -0.005, rate);
LithoTranslate ( -0.2, 0, rate);
```

```
LithoTranslate ( 0, -0.005, rate);
LithoTranslate ( 0.2, 0, rate);
LithoTranslate ( 0, -0.005, rate);
LithoSetOutput ( aoBias, startvoltage+21*increment);
LithoTranslate ( -0.2, 0, rate);
LithoTranslate ( 0, -0.005, rate);
LithoTranslate ( 0.2, 0, rate);
LithoTranslate ( 0, -0.005, rate);
LithoTranslate ( -0.2, 0, rate);
LithoTranslate ( 0, -0.005, rate);
LithoSetOutput ( aoBias, startvoltage+22*increment);
LithoTranslate ( 0.2, 0, rate);
LithoTranslate ( 0, -0.005, rate);
LithoTranslate ( -0.2, 0, rate);
LithoTranslate ( 0, -0.005, rate);
LithoTranslate ( 0.2, 0, rate);
LithoTranslate ( 0, -0.005, rate);
LithoSetOutput ( aoBias, startvoltage+23*increment);
LithoTranslate ( -0.2, 0, rate);
LithoTranslate ( 0, -0.005, rate);
LithoTranslate ( 0.2, 0, rate);
LithoTranslate ( 0, -0.005, rate);
LithoTranslate ( -0.2, 0, rate);
LithoTranslate ( 0, -0.005, rate);
LithoSetOutput ( aoBias, startvoltage+24*increment);
LithoTranslate ( 0.2, 0, rate);
LithoTranslate ( 0, -0.005, rate);
LithoTranslate ( -0.2, 0, rate);
LithoTranslate ( 0, -0.005, rate);
LithoTranslate ( 0.2, 0, rate);
LithoTranslate ( 0, -0.005, rate);
LithoSetOutput ( aoBias, startvoltage+25*increment);
LithoTranslate ( -0.2, 0, rate);
LithoTranslate ( 0, -0.005, rate);
LithoTranslate ( 0.2, 0, rate);
LithoTranslate ( 0, -0.005, rate);
LithoTranslate ( -0.2, 0, rate);
LithoSetOutput ( aoBias, 1.0); // turn OFF
```

```
LITHO_END
```

```
}
```

Appendix 3.2

“Lithographic scan rate gradient“ for Figure 3.2

```
#include <litho.h>

void main()
{
LITHO_BEGIN
// has 184 steps,takes a few minutes
double rate = 0.02; // move tip in x-y at 50nm/s
double bias = 3.0;

LithoTranslate (-0.1, 0.3, rate);

LithoSetOutput ( aoBias, bias);
LithoTranslate ( 0.2, 0, rate*10); // scribe line
LithoTranslate ( 0, -0.012, rate*10);
LithoTranslate ( -0.2, 0, rate*10); // scribe line
LithoTranslate ( 0, -0.012, rate*10);
LithoTranslate ( 0.2, 0, rate*10); //scribe line
LithoTranslate ( 0, -0.012, rate*10);
//
LithoTranslate ( -0.2, 0, rate*9.5); //scribe line
LithoTranslate ( 0, -0.012, rate*9.5);
LithoTranslate ( 0.2, 0, rate*9.5); // scribe line
LithoTranslate ( 0, -0.012, rate*9.5);
LithoTranslate (-0.2, 0, rate*9.5); // scribe line
LithoTranslate ( 0, -0.012, rate*9.5);
//
LithoTranslate ( 0.2, 0, rate*9); // scribe line
LithoTranslate ( 0, -0.012, rate*9);
LithoTranslate ( -0.2, 0, rate*9); // scribe line
LithoTranslate ( 0, -0.012, rate*9);
LithoTranslate ( 0.2, 0, rate*9); // scribe line
LithoTranslate ( 0, -0.012, rate*9);
//
LithoTranslate ( -0.2, 0 , rate*8.5); // scribe line
LithoTranslate ( 0, -0.012, rate*8.5);
LithoTranslate ( 0.2, 0, rate*8.5); //scribe line
LithoTranslate ( 0, -0.012, rate*8.5);
LithoTranslate ( -0.2, 0, rate*8.5);
LithoTranslate ( 0, -0.012, rate*8.5);
//
LithoTranslate ( 0.2, 0, rate*8);
LithoTranslate ( 0, -0.012, rate*8);
LithoTranslate ( -0.2, 0, rate*8);
LithoTranslate ( 0, -0.012, rate*8);
LithoTranslate ( 0.2, 0, rate*8);
LithoTranslate ( 0, -0.012, rate*8);
//
LithoTranslate ( -0.2, 0, rate*7.5);
LithoTranslate ( 0, -0.012, rate*7.5);
```

```
LithoTranslate ( 0.2, 0, rate*7.5);
LithoTranslate ( 0, -0.012, rate*7.5);
LithoTranslate ( -0.2, 0, rate*7.5);
LithoTranslate ( 0, -0.01, rate*7.5);
//
LithoTranslate ( 0.2, 0, rate*7);
LithoTranslate ( 0, -0.01, rate*7);
LithoTranslate ( -0.2, 0, rate*7);
LithoTranslate ( 0, -0.01, rate*7);
LithoTranslate ( 0.2, 0, rate*7);
LithoTranslate ( 0, -0.01, rate*7);
//
LithoTranslate ( -0.2, 0, rate*6.5);
LithoTranslate ( 0, -0.01, rate*6.5);
LithoTranslate ( 0.2, 0, rate*6.5);
LithoTranslate ( 0, -0.01, rate*6.5);
LithoTranslate ( -0.2, 0, rate*6.5);
LithoTranslate ( 0, -0.01, rate*6.5);
//
LithoTranslate ( 0.2, 0, rate*6);
LithoTranslate ( 0, -0.01, rate*6);
LithoTranslate ( -0.2, 0, rate*6);
LithoTranslate ( 0, -0.01, rate*6);
LithoTranslate ( 0.2, 0, rate*6);
LithoTranslate ( 0, -0.01, rate*6);
//
LithoTranslate ( -0.2, 0, rate*5.5);
LithoTranslate ( 0, -0.01, rate*5.5);
LithoTranslate ( 0.2, 0, rate*5.5);
LithoTranslate ( 0, -0.01, rate*5.5);
LithoTranslate ( -0.2, 0, rate*5.5);
LithoTranslate ( 0, -0.01, rate*5.5);
//
LithoTranslate ( 0.2, 0, rate*5);
LithoTranslate ( 0, -0.01, rate*5);
LithoTranslate ( -0.2, 0, rate*5);
LithoTranslate ( 0, -0.01, rate*5);
LithoTranslate ( 0.2, 0, rate*5);
LithoTranslate ( 0, -0.01, rate*5);
//
LithoTranslate ( -0.2, 0, rate*4.5);
LithoTranslate ( 0, -0.01, rate*4.5);
LithoTranslate ( 0.2, 0, rate*4.5);
LithoTranslate ( 0, -0.01, rate*4.5);
LithoTranslate ( -0.2, 0, rate*4.5);
LithoTranslate ( 0, -0.01, rate*4.5);
//
LithoTranslate ( 0.2, 0, rate*4);
LithoTranslate ( 0, -0.01, rate*4);
LithoTranslate ( -0.2, 0, rate*4);
LithoTranslate ( 0, -0.01, rate*4);
LithoTranslate ( 0.2, 0, rate*4);
LithoTranslate ( 0, -0.01, rate*4);
```

```

//
LithoTranslate ( -0.2, 0, rate*3.5);
LithoTranslate ( 0, -0.01, rate*3.5);
LithoTranslate ( 0.2, 0, rate*3.5);
LithoTranslate ( 0, -0.01, rate*3.5);
LithoTranslate ( -0.2, 0, rate*3.5);
LithoTranslate ( 0, -0.01, rate*3.5);
//
LithoTranslate ( 0.2, 0, rate*3);
LithoTranslate ( 0, -0.01, rate*3);
LithoTranslate ( -0.2, 0, rate*3);
LithoTranslate ( 0, -0.01, rate*3);
LithoTranslate ( 0.2, 0, rate*3);
LithoTranslate ( 0, -0.01, rate*3);
//
LithoTranslate ( -0.2, 0, rate*2.5);
LithoTranslate ( 0, -0.0075, rate*2.5);
LithoTranslate ( 0.2, 0, rate*2.5);
LithoTranslate ( 0, -0.0075, rate*2.5);
LithoTranslate ( -0.2, 0, rate*2.5);
LithoTranslate ( 0, -0.0075, rate*2.5);
//
LithoTranslate ( 0.2, 0, rate*2);
LithoTranslate ( 0, -0.0075, rate*2);
LithoTranslate ( -0.2, 0, rate*2);
LithoTranslate ( 0, -0.0075, rate*2);
LithoTranslate ( 0.2, 0, rate*2);
LithoTranslate ( 0, -0.0075, rate*2);
//
LithoTranslate ( -0.2, 0, rate*1.5);
LithoTranslate ( 0, -0.0075, rate*1.5);
LithoTranslate ( 0.2, 0, rate*1.5);
LithoTranslate ( 0, -0.0075, rate*1.5);
LithoTranslate ( -0.2, 0, rate*1.5);
LithoTranslate ( 0, -0.0075, rate*1.5);
//
LithoTranslate ( 0.2, 0, rate);
LithoTranslate ( 0, -0.0075, rate);
LithoTranslate ( -0.2, 0, rate);
LithoTranslate ( 0, -0.0075, rate);
LithoTranslate ( 0.2, 0, rate);
LithoTranslate ( 0, -0.0075, rate);
//

LithoSetOutput ( aoBias, 1.0); // turn OFF

LITHO_END

}

```

Appendix 3.3

“L grad” for Figure 3.3

```
#include <litho.h>

void main()
{
LITHO_BEGIN
//this writes and L shaped symmetrical gradient, a little bigger than lgrad4
double rate = 0.04; //move tip in x-y at this value in um/s
double startvoltage = 2.9;
double increment = 0.05;
// 178 steps
// move to starting point where the letter is scribed
LithoTranslate (-0.155, 0.20, rate);

LithoSetOutput (aoBias, startvoltage);
LithoTranslate ( 0.150, 0, rate);
LithoTranslate ( 0, -0.004, rate);
LithoTranslate (-0.148, 0, rate);
LithoTranslate ( 0.002, -0.004, rate);
LithoTranslate ( 0.146, 0, rate);
LithoTranslate ( 0, -0.004, rate);
LithoTranslate (-0.144, 0, rate);
LithoTranslate ( 0.002, -0.005, rate);
LithoTranslate ( 0.142, 0, rate);
LithoSetOutput ( aoBias, startvoltage-1*increment);
LithoTranslate ( 0, -0.005, rate);
LithoTranslate (-0.14, 0, rate);
LithoTranslate ( 0.002, -0.005, rate);
LithoTranslate ( 0.138, 0, rate);
LithoTranslate ( 0, -0.005, rate);
LithoTranslate (-0.136, 0, rate);
LithoTranslate ( 0.002, -.005, rate);
LithoTranslate ( 0.134, 0, rate);
LithoTranslate ( 0, -0.005, rate);
LithoTranslate (-0.132, 0, rate);
LithoSetOutput ( aoBias, startvoltage-2*increment);
LithoTranslate ( 0.002, -0.005, rate);
LithoTranslate ( 0.130, 0, rate);
LithoTranslate ( 0, -0.006, rate);
LithoTranslate (-0.128, 0, rate);
LithoTranslate ( 0.002, -0.006, rate);
LithoTranslate ( 0.126, 0, rate);
LithoTranslate ( 0, -0.006, rate);
LithoTranslate (-0.124, 0, rate);
LithoTranslate ( 0.002, -0.006, rate);
LithoTranslate ( 0.122, 0, rate);
LithoSetOutput ( aoBias, startvoltage-3*increment);
LithoTranslate ( 0, -0.006, rate);
LithoTranslate (-0.122, 0, rate);
LithoTranslate ( 0.002, -0.007, rate);
```

```
LithoTranslate ( 0.120, 0, rate);
LithoTranslate ( 0, -0.007, rate);
LithoTranslate ( -0.118, 0, rate);
LithoTranslate ( 0.002, -0.007, rate);
LithoTranslate ( 0.116, 0, rate);
LithoTranslate ( 0, -0.007, rate);
LithoTranslate ( -0.114, 0, rate);
LithoTranslate ( 0.002, -0.007, rate);
LithoTranslate ( 0.112, 0, rate);
LithoSetOutput ( aoBias, startvoltage-4*increment);
LithoTranslate ( 0, -0.007, rate);
LithoTranslate ( -0.110, 0, rate);
LithoTranslate ( 0.002, -0.008, rate-0.005);
LithoTranslate ( 0.108, 0, rate-0.005);
LithoTranslate ( 0, -0.008, rate-0.005);
LithoTranslate ( -0.106, 0, rate-0.005);
LithoTranslate ( 0.002, -0.008, rate-0.005);
LithoTranslate ( 0.104, 0, rate-0.005);
LithoTranslate ( 0, -0.008, rate-0.005);
LithoTranslate ( -0.102, 0, rate-0.005);
LithoTranslate ( 0.002, -0.008, rate-0.005);
LithoTranslate ( 0.100, 0, rate-0.005);

LithoTranslate ( 0, -0.008, rate-0.005);
LithoTranslate ( -0.098, 0, rate-0.005);
LithoTranslate ( 0.002, -0.008, rate-0.005);

LithoTranslate ( 0.096, 0, rate-0.005);
LithoTranslate ( 0, -0.009, rate-0.005);
LithoTranslate ( -0.094, 0, rate-0.005);
LithoTranslate ( 0.002, -0.009, rate-0.005);
LithoTranslate ( 0.092, 0, rate-0.005);
LithoTranslate ( 0, -0.009, rate-0.005);
LithoTranslate ( -0.090, 0, rate-0.005);
LithoTranslate ( 0.002, -0.009, rate-0.005);
LithoTranslate ( 0.088, 0, rate-0.005);
LithoTranslate ( 0, -0.009, rate-0.005);
LithoTranslate ( -0.086, 0, rate-0.005);
LithoTranslate ( 0.002, -0.010, rate-0.005);
LithoTranslate ( 0.084, 0, rate-0.005);
LithoTranslate ( 0, -0.010, rate-0.005);
LithoTranslate ( -0.082, 0, rate-0.005);
LithoTranslate ( 0.002, -0.010, rate-0.005);
LithoTranslate ( 0.080, 0, rate-0.005);

LithoTranslate ( 0, -0.011, rate);
LithoTranslate ( -0.078, 0, rate);
LithoTranslate ( 0, -0.011, rate);
LithoTranslate ( 0.076, 0, rate);
LithoTranslate ( 0.002, -0.011, rate);
LithoTranslate ( -0.074, 0, rate);
LithoTranslate ( 0, -0.012, rate);
LithoTranslate ( 0.072, 0, rate);
```

```

LithoTranslate ( 0.002, -0.012, rate);
LithoTranslate ( -0.070, 0, rate);

// keep going a little more at diffuse conditions

LithoTranslate ( 0.002, -0.012, rate);
LithoTranslate ( 0.068, 0, rate);
LithoTranslate ( 0.002, -0.012, rate);
LithoTranslate ( -0.066, 0, rate);
LithoTranslate ( 0.002, -0.012, rate);
LithoTranslate ( 0.064, 0, rate);
LithoTranslate ( 0.002, -0.012, rate);
LithoTranslate ( -0.062, 0, rate);
LithoTranslate ( 0.002, -0.012, rate);
LithoTranslate ( 0.065, 0, rate);

// start rhs gradient

LithoTranslate ( 0.0, 0.070, rate);
LithoTranslate ( 0.011, 0, rate);
LithoTranslate ( 0, -0.072, rate);
LithoTranslate ( 0.011, -0.002, rate);
LithoTranslate ( 0.0, 0.074, rate);
LithoTranslate ( 0.010, 0, rate);
LithoTranslate ( 0, -0.076, rate);
LithoTranslate ( 0.010, -0.002, rate);
LithoTranslate ( 0.0, 0.078, rate);
LithoSetOutput ( aoBias, startvoltage-5*increment);
LithoTranslate ( 0.010, 0, rate);
LithoTranslate ( 0, -0.08, rate);
LithoTranslate ( 0.009, -0.002, rate);
LithoTranslate ( 0.0, 0.082, rate);
LithoTranslate ( 0.009, 0, rate);
LithoTranslate ( 0, -0.084, rate);
LithoTranslate ( 0.009, -0.002, rate);
LithoTranslate ( 0.0, 0.086, rate);
LithoTranslate ( 0.009, 0, rate);
LithoTranslate ( 0, -0.088, rate);
LithoSetOutput ( aoBias, startvoltage-4*increment);
LithoTranslate ( 0.009, -0.002, rate);
LithoTranslate ( 0.0, 0.09, rate);
LithoTranslate ( 0.009, 0, rate);
LithoTranslate ( 0, -0.092, rate);
LithoTranslate ( 0.008, -0.002, rate);
LithoTranslate ( 0.0, 0.094, rate);
LithoTranslate ( 0.008, 0, rate);
LithoTranslate ( 0, -0.096, rate);
LithoTranslate ( 0.008, -0.002, rate);
LithoTranslate ( 0.0, 0.098, rate);
LithoTranslate ( 0.008, 0, rate);
LithoTranslate ( 0, -0.100, rate);
LithoSetOutput ( aoBias, startvoltage-3*increment);

```

```

LithoTranslate ( 0.007, -0.002, rate);
LithoTranslate ( 0.0, 0.102, rate);
LithoTranslate ( 0.007, 0, rate);
LithoTranslate ( 0, -0.104, rate);
LithoTranslate ( 0.007, -0.002, rate);
LithoTranslate ( 0.0, 0.106, rate);
LithoTranslate ( 0.007, 0, rate);
LithoTranslate ( 0, -0.108, rate);
LithoTranslate ( 0.007, -0.002, rate);
LithoTranslate ( 0.0, 0.110, rate);
LithoSetOutput ( aoBias, startvoltage-2*increment);
LithoTranslate ( 0.007, 0, rate);
LithoTranslate ( 0, -0.112, rate);
LithoTranslate ( 0.006, -0.002, rate);
LithoTranslate ( 0.0, 0.114, rate);
LithoTranslate ( 0.006, 0, rate);
LithoTranslate ( 0, -0.116, rate);
LithoTranslate ( 0.006, -0.002, rate);
LithoTranslate ( 0.0, 0.118, rate);
LithoTranslate ( 0.006, 0, rate);
LithoTranslate ( 0, -0.120, rate);
LithoTranslate ( 0.006, -0.002, rate);
LithoTranslate ( 0.0, 0.122, rate);
LithoSetOutput ( aoBias, startvoltage-1*increment);
LithoTranslate ( 0.006, 0, rate);
LithoTranslate ( 0, -0.124, rate);
LithoTranslate ( 0.006, -0.002, rate);
LithoTranslate ( 0.0, 0.126, rate);
LithoTranslate ( 0.005, 0, rate);
LithoTranslate ( 0, -0.128, rate);
LithoTranslate ( 0.005, -0.002, rate);
LithoTranslate ( 0.0, 0.130, rate);
LithoTranslate ( 0.005, 0, rate);
LithoSetOutput ( aoBias, startvoltage);
LithoTranslate ( 0, -0.132, rate);
LithoTranslate ( 0.005, -0.002, rate);
LithoTranslate ( 0.0, 0.134, rate);
LithoTranslate ( 0.005, 0, rate);
LithoTranslate ( 0, -0.136, rate);
LithoTranslate ( 0.005, -0.002, rate);
LithoTranslate ( 0.0, 0.138, rate);
LithoTranslate ( 0.005, 0, rate);
LithoTranslate ( 0, -0.140, rate);

```

```

LithoSetOutput (aoBias, 1.0);

```

```

LITHO_END
}

```

Appendix 3.4

“Y” gradient for Figure 3.4

```
#include <litho.h>

void main()
{
LITHO_BEGIN
//this writes and L shaped symmetrical gradient, a little bigger than lgrad4
double rate = 0.05; //move tip in x-y at this value in  $\mu\text{m/s}$ 
double startvoltage = 2.8;
double increment = 0.05;
// 178 steps
// move to starting point where the letter is scribed
LithoTranslate (-0.155, 0.20, rate);

LithoSetOutput (aoBias, startvoltage-1*increment);
LithoTranslate ( 0.150, 0, rate);
LithoTranslate ( 0, -0.004, rate);
LithoTranslate (-0.148, 0, rate);
LithoTranslate ( 0.002, -0.004, rate);
LithoTranslate ( 0.146, 0, rate);
LithoTranslate ( 0, -0.004, rate);
LithoTranslate (-0.144, 0, rate);
LithoTranslate ( 0.002, -0.005, rate);
LithoTranslate ( 0.142, 0, rate);
LithoSetOutput ( aoBias, startvoltage-1*increment);
LithoTranslate ( 0, -0.005, rate);
LithoTranslate (-0.14, 0, rate);
LithoTranslate ( 0.002, -0.005, rate);
LithoTranslate ( 0.138, 0, rate);
LithoTranslate ( 0, -0.005, rate);
LithoTranslate (-0.136, 0, rate);
LithoTranslate ( 0.002, -0.005, rate);
LithoTranslate ( 0.134, 0, rate);
LithoTranslate ( 0, -0.005, rate);
LithoTranslate (-0.132, 0, rate);
LithoSetOutput ( aoBias, startvoltage-2*increment);
LithoTranslate ( 0.002, -0.005, rate);
LithoTranslate ( 0.130, 0, rate);
LithoTranslate ( 0, -0.006, rate);
LithoTranslate (-0.128, 0, rate);
LithoTranslate ( 0.002, -0.006, rate);
LithoTranslate ( 0.126, 0, rate);
LithoTranslate ( 0, -0.006, rate);
LithoTranslate (-0.124, 0, rate);
LithoTranslate ( 0.002, -0.006, rate);
LithoTranslate ( 0.122, 0, rate);
LithoSetOutput ( aoBias, startvoltage-3*increment);
LithoTranslate ( 0, -0.006, rate);
LithoTranslate (-0.122, 0, rate);
LithoTranslate ( 0.002, -0.007, rate);
```

```
LithoTranslate ( 0.120, 0, rate);
LithoTranslate ( 0, -0.007, rate);
LithoTranslate ( -0.118, 0, rate);
LithoTranslate ( 0.002, -0.007, rate);
LithoTranslate ( 0.116, 0, rate);
LithoTranslate ( 0, -0.007, rate);
LithoTranslate ( -0.114, 0, rate);
LithoTranslate ( 0.002, -0.007, rate);
LithoTranslate ( 0.112, 0, rate);
LithoSetOutput ( aoBias, startvoltage-4*increment);
LithoTranslate ( 0, -0.007, rate);
LithoTranslate ( -0.110, 0, rate);
LithoTranslate ( 0.002, -0.008, rate-0.005);
LithoTranslate ( 0.108, 0, rate-0.005);
LithoTranslate ( 0, -0.008, rate-0.005);
LithoTranslate ( -0.106, 0, rate-0.005);
LithoTranslate ( 0.002, -0.008, rate-0.005);
LithoTranslate ( 0.104, 0, rate-0.005);
LithoTranslate ( 0, -0.008, rate-0.005);
LithoTranslate ( -0.102, 0, rate-0.005);
LithoTranslate ( 0.002, -0.008, rate-0.005);
LithoTranslate ( 0.100, 0, rate-0.005);

LithoTranslate ( 0, -0.008, rate-0.005);
LithoTranslate ( -0.098, 0, rate-0.005);
LithoTranslate ( 0.002, -0.008, rate-0.005);

LithoTranslate ( 0.096, 0, rate-0.005);
LithoTranslate ( 0, -0.009, rate-0.005);
LithoTranslate ( -0.094, 0, rate-0.005);
LithoTranslate ( 0.002, -0.009, rate-0.005);
LithoTranslate ( 0.092, 0, rate-0.005);
LithoTranslate ( 0, -0.009, rate-0.005);
LithoTranslate ( -0.090, 0, rate-0.005);
LithoTranslate ( 0.002, -0.009, rate-0.005);
LithoTranslate ( 0.088, 0, rate-0.005);
LithoTranslate ( 0, -0.009, rate-0.005);
LithoTranslate ( -0.086, 0, rate-0.005);
LithoTranslate ( 0.002, -0.010, rate-0.005);
LithoTranslate ( 0.084, 0, rate-0.005);
LithoTranslate ( 0, -0.010, rate-0.005);
LithoTranslate ( -0.082, 0, rate-0.005);
LithoTranslate ( 0.002, -0.010, rate-0.005);
LithoTranslate ( 0.080, 0, rate-0.005);

LithoTranslate ( 0, -0.011, rate);
LithoTranslate ( -0.078, 0, rate);
LithoTranslate ( 0, -0.011, rate);
LithoTranslate ( 0.076, 0, rate);
LithoTranslate ( 0.002, -0.011, rate);
LithoTranslate ( -0.074, 0, rate);
LithoTranslate ( 0, -0.012, rate);
LithoTranslate ( 0.072, 0, rate);
```

```

LithoTranslate ( 0.002, -0.012, rate);
LithoTranslate ( -0.070, 0, rate);

// keep going a little more at diffuse conditions

LithoTranslate ( 0.002, -0.012, rate);
LithoTranslate ( 0.068, 0, rate);
LithoTranslate ( 0.002, -0.012, rate);
LithoTranslate ( -0.066, 0, rate);
LithoTranslate ( 0.002, -0.012, rate);
LithoTranslate ( 0.064, 0, rate);
LithoTranslate ( 0.002, -0.012, rate);
LithoTranslate ( -0.062, 0, rate);
LithoTranslate ( 0.002, -0.012, rate);
LithoTranslate ( 0.065, 0, rate);

// start rhs gradient

LithoTranslate ( 0.0, 0.070, rate);
LithoTranslate ( 0.011, 0, rate);
LithoTranslate ( 0, -0.072, rate);
LithoTranslate ( 0.011, -0.002, rate);
LithoTranslate ( 0.0, 0.074, rate);
LithoTranslate ( 0.010, 0, rate);
LithoTranslate ( 0, -0.076, rate);
LithoTranslate ( 0.010, -0.002, rate);
LithoTranslate ( 0.0, 0.078, rate);
LithoSetOutput ( aoBias, startvoltage-5*increment);
LithoTranslate ( 0.010, 0, rate);
LithoTranslate ( 0, -0.08, rate);
LithoTranslate ( 0.009, -0.002, rate);
LithoTranslate ( 0.0, 0.082, rate);
LithoTranslate ( 0.009, 0, rate);
LithoTranslate ( 0, -0.084, rate);
LithoTranslate ( 0.009, -0.002, rate);
LithoTranslate ( 0.0, 0.086, rate);
LithoTranslate ( 0.009, 0, rate);
LithoTranslate ( 0, -0.088, rate);
LithoSetOutput ( aoBias, startvoltage-4*increment);
LithoTranslate ( 0.009, -0.002, rate);
LithoTranslate ( 0.0, 0.09, rate);
LithoTranslate ( 0.009, 0, rate);
LithoTranslate ( 0, -0.092, rate);
LithoTranslate ( 0.008, -0.002, rate);
LithoTranslate ( 0.0, 0.094, rate);
LithoTranslate ( 0.008, 0, rate);
LithoTranslate ( 0, -0.096, rate);
LithoTranslate ( 0.008, -0.002, rate);
LithoTranslate ( 0.0, 0.098, rate);
LithoTranslate ( 0.008, 0, rate);
LithoTranslate ( 0, -0.100, rate);
LithoSetOutput ( aoBias, startvoltage-3*increment);

```

```

LithoTranslate ( 0.007, -0.002, rate);
LithoTranslate ( 0.0, 0.102, rate);
LithoTranslate ( 0.007, 0, rate);
LithoTranslate ( 0, -0.104, rate);
LithoTranslate ( 0.007, -0.002, rate);
LithoTranslate ( 0.0, 0.106, rate);
LithoTranslate ( 0.007, 0, rate);
LithoTranslate ( 0, -0.108, rate);
LithoTranslate ( 0.007, -0.002, rate);
LithoTranslate ( 0.0, 0.110, rate);
LithoSetOutput ( aoBias, startvoltage-2*increment);
LithoTranslate ( 0.007, 0, rate);
LithoTranslate ( 0, -0.112, rate);
LithoTranslate ( 0.006, -0.002, rate);
LithoTranslate ( 0.0, 0.114, rate);
LithoTranslate ( 0.006, 0, rate);
LithoTranslate ( 0, -0.116, rate);
LithoTranslate ( 0.006, -0.002, rate);
LithoTranslate ( 0.0, 0.118, rate);
LithoTranslate ( 0.006, 0, rate);
LithoTranslate ( 0, -0.120, rate);
LithoTranslate ( 0.006, -0.002, rate);
LithoTranslate ( 0.0, 0.122, rate);
LithoSetOutput ( aoBias, startvoltage-1*increment);
LithoTranslate ( 0.006, 0, rate);
LithoTranslate ( 0, -0.124, rate);
LithoTranslate ( 0.006, -0.002, rate);
LithoTranslate ( 0.0, 0.126, rate);
LithoTranslate ( 0.005, 0, rate);
LithoTranslate ( 0, -0.128, rate);
LithoTranslate ( 0.005, -0.002, rate);
LithoTranslate ( 0.0, 0.130, rate);
LithoTranslate ( 0.005, 0, rate);
LithoSetOutput ( aoBias, startvoltage);
LithoTranslate ( 0, -0.132, rate);
LithoTranslate ( 0.005, -0.002, rate);
LithoTranslate ( 0.0, 0.134, rate);
LithoTranslate ( 0.005, 0, rate);
LithoTranslate ( 0, -0.136, rate);
LithoTranslate ( 0.005, -0.002, rate);
LithoTranslate ( 0.0, 0.138, rate);
LithoTranslate ( 0.005, 0, rate);
LithoTranslate ( 0, -0.140, rate);
LithoSetOutput (aoBias, 1.0);

LithoTranslate (-0.33, 0.08, rate);//move to 3 diagonal leg start point

LithoSetOutput ( aoBias, startvoltage-6*increment);
LithoTranslate (-0.050, 0.050, rate+0.005);
LithoTranslate (-0.0085, -0.0085, rate+0.005);
LithoTranslate (0.051, -0.051, rate+0.005);
LithoTranslate (-0.0085, -0.0085, rate+0.005);
LithoTranslate (-0.052, 0.052, rate+0.005);

```

```
LithoTranslate (-0.0085, -0.0085, rate+0.005);
LithoTranslate (0.053, -0.053, rate+0.005);
LithoTranslate (-0.0085, -0.0085, rate+0.005);
LithoTranslate (-0.054, 0.054, rate+0.005);
LithoSetOutput ( aoBias, startvoltage-5.5*increment);
LithoTranslate (-0.008, -0.008, rate+0.005);
LithoTranslate (0.055, -0.055, rate+0.005);
LithoTranslate (-0.008, -0.008, rate+0.005);
LithoTranslate (-0.056, 0.056, rate+0.005);
LithoTranslate (-0.008,-0.008, rate+0.005);
LithoTranslate (0.057,-0.057, rate+0.005);
LithoTranslate (-0.008,-0.008, rate+0.005);
LithoTranslate (-0.058, 0.058, rate+0.005);
LithoTranslate (-0.0075,-0.0075, rate+0.005);
LithoTranslate (0.060, -0.060, rate+0.005);
LithoTranslate (-0.0075,-0.0075, rate+0.005);
LithoTranslate (-0.061, 0.061, rate+0.005);
LithoTranslate (-0.0075,-0.0075, rate);
LithoSetOutput ( aoBias, startvoltage-5*increment);
LithoTranslate (0.062, -0.062, rate);
LithoTranslate (-0.0075,-0.0075, rate);
LithoTranslate (-0.063, 0.063, rate);
LithoTranslate (-0.0075,-0.0075, rate);
LithoTranslate (0.064, -0.064, rate);
LithoTranslate (-0.007,-0.007, rate);
LithoTranslate (-0.065,0.065, rate);
LithoTranslate (-0.007,-0.007, rate);
LithoTranslate (0.066, -0.066, rate);
LithoTranslate (-0.007,-0.007, rate);
LithoTranslate (-0.067, 0.067, rate);
LithoTranslate (-0.0064,-0.0064, rate);
LithoTranslate (0.068, -0.068, rate);
LithoSetOutput ( aoBias, startvoltage-4.5*increment);
LithoTranslate (-0.0064,-0.0064, rate);
LithoTranslate (-0.069, 0.069, rate);
LithoTranslate (-0.0064,-0.0064, rate);
LithoTranslate (0.070, -0.070, rate);
LithoTranslate (-0.0064,-0.0064, rate);
LithoTranslate (-0.071, 0.071, rate);
LithoTranslate (-0.006,-0.006, rate);
LithoTranslate (0.072, -0.072, rate);
LithoTranslate (-0.006,-0.006, rate);
LithoTranslate (-0.073, 0.073, rate);
LithoTranslate (-0.006,-0.006, rate);
LithoSetOutput ( aoBias, startvoltage-4*increment);
LithoTranslate (0.074, -0.074, rate);
LithoTranslate (-0.0057,-0.0057, rate);
LithoTranslate (-0.075, 0.075, rate);
LithoTranslate (-0.0057,-0.0057, rate);
LithoTranslate (0.076, -0.076, rate);
LithoTranslate (-0.005,-0.005, rate);
LithoTranslate (-0.077, 0.077, rate);
LithoTranslate (-0.005,-0.005, rate);
```

```
LithoTranslate (0.078, -0.078, rate);
LithoTranslate (-0.005,-0.005, rate);
LithoTranslate (-0.079, 0.079, rate);
LithoSetOutput ( aoBias, startvoltage-3.5*increment);
LithoTranslate (-0.005,-0.005, rate);
LithoTranslate (0.080, -0.080, rate);
LithoTranslate (-0.005,-0.005, rate);
LithoTranslate (-0.081, 0.081, rate);
LithoTranslate (-0.0047,-0.0047, rate);
LithoTranslate (0.082, -0.082, rate);
LithoTranslate (-0.0047,-0.0047, rate);
LithoTranslate (-0.083, 0.083, rate);
LithoTranslate (-0.0045,-0.0045, rate);
LithoTranslate (0.084, -0.084, rate);
LithoTranslate (-0.0045,-0.0045, rate);
LithoTranslate (-0.085, 0.085, rate);
LithoSetOutput ( aoBias, startvoltage-3*increment);
LithoTranslate (-0.0045,-0.0045, rate);
LithoTranslate (0.086, -0.086, rate);
LithoTranslate (-0.0045,-0.0045, rate);
LithoTranslate (-0.087, 0.087, rate);
LithoTranslate (-0.0043,-0.0043, rate);
LithoTranslate (0.088, -0.088, rate);
LithoTranslate (-0.0043,-0.0043, rate);
LithoTranslate (-0.089, 0.089, rate);
LithoSetOutput ( aoBias, startvoltage-2*increment);
LithoTranslate (-0.0036,-0.0036, rate);
LithoTranslate (0.090, -0.090, rate);
LithoTranslate (-0.0036,-0.0036, rate);
LithoTranslate (-0.091, 0.091, rate);
LithoTranslate (-0.003,-0.003, rate);
LithoTranslate (0.092, -0.092, rate);
LithoTranslate (-0.003,-0.003, rate);
LithoTranslate (-0.093, 0.093, rate);
LithoTranslate (-0.003,-0.003, rate);
LithoTranslate (0.094, -0.094, rate);
LithoTranslate (-0.003,-0.003, rate);
LithoTranslate (-0.095, 0.095, rate);

LithoSetOutput (aoBias, 1.0);

LITHO_END
}
```

Appendix 4:

Synthesis of 11-Ferrocenylundecane thiol

Br(CH₂)₁₀COCl (11-bromoundecanoyl chloride) RF 8,83

10.7 mL (0.15 mole) of freshly distilled thionyl chloride (Acros) was added to 3.985 g (0.015 mole) of 11-bromoundecanoic acid (Br(CH₂)₁₀COOH, Acros) dropwise via cannulation at 25 °C and stirred for 3.5 hrs under N₂. The excess SOCl₂ was removed by rotary evaporation, followed by bulb-to-bulb distillation, producing a clear light yellow oil. Product was carried on to next step with yield determination.

FcCO(CH₂)₁₀Br (ferrocenyl-10-bromodecyl ketone) RF 8, 84

The freshly prepared Br(CH₂)₁₀COCl was added dropwise via cannulation to 2.88 g (0.0152 mole) ferrocene (Aldrich) at 0 °C, the ice water bath removed, and stirred for 3.5 hrs under N₂. This produced a dark orange-brown reaction mixture. The reaction was quenched with cold deionized water until bubbling ceased (*ca.* 10 mL), causing the reaction to turn an opaque navy blue color. The reaction mixture was poured into a separatory funnel and extracted with diethyl ether. The organic layer was washed three times with water. The blue aqueous layers were discarded, while the dark orange organic layer was dried with magnesium sulfate, gravity filtered and concentrated via rotary evaporation. The crude product was purified via flash chromatography with 5% ethyl acetate/ hexanes to give an orange solid. (91% yield; R_f = 0.23); ¹HNMR (400 MHz) CDCl₃: 1.308 (broad, 12 H, CH₂), 1.703 (m, 2H, Fe(Cp)₂COCH₂CH₂), 1.855 (m, 2H, CH₂CH₂Br), 2.694 (t, *J* = 7.6 Hz, 2H, Fe(Cp)₂COCH₂), 3.409 (t, *J* = 6.8 Hz, 2H, CH₂Br), 4.192 (s, 5H, C₅H₅), 4.489 (t, *J* = 1.8 Hz, 2H, C₅H₅), 4.778 (t, *J* = 2.4 Hz, 2H, C₅H₄).

Fc(CH₂)₁₁Br (1-bromo-11-ferrocenylundecane) RF 9, 80

To reduce the aryl ketone under Clemmenson reduction conditions, a zinc - mercury amalgam was prepared by dissolving 1.397 g (0.0051 mole) mercuric chloride (Aldrich) in 10 mL 6 N HCl, which was chilled to 0 °C in an ice water bath. 10.493 g (0.161 mole) of Zn dust (Aldrich) was added to this solution, *slowly* (add in *ca.* 1 g portions, wait several minutes before next addition) with continuous stirring, to prepare small spheres (*ca.* 6 mm in diameter). Once the amalgam was prepared, roughly half the solution was drawn off the top to allow the organic layer to interact with the amalgam. 0.5533 g (0.0013 mole) FcCO(CH₂)₁₀Br was dissolved in *ca.* 5 mL freshly distilled toluene was added to the flask containing the amalgam, and stirred under N₂ for *ca.* 24 hrs. The reaction was monitored with thin layer chromatography (100 % hexanes). Once the reaction was complete, the solution was extracted with diethyl ether, and washed four times with water. The orange organic layer was dried with magnesium sulfate, gravity filtered and concentrated via rotary evaporation.

The crude product was purified via flash chromatography with 1% ethyl acetate hexanes. Product is a yellow / orange solid. (83% yield; $R_f = 0.62$); $^1\text{H NMR}$ (400 MHz) CDCl_3 : 1.287 (broad, 12 H, CH_2), 1.427 (m, 2H, $\text{Fe}(\text{Cp})_2\text{CH}_2\text{CH}_2$), 1.495 (m, 2H, $\text{CH}_2\text{CH}_2\text{CH}_2\text{Br}$), 1.858 (m, 2H, $\text{CH}_2\text{CH}_2\text{Br}$), 2.312 (t, $J = 7.6$ Hz, 2H, $\text{Fe}(\text{Cp})_2\text{CH}_2$), 3.412 (t, $J = 7.0$ Hz, 2H, CH_2Br), 4.037 (d, 2H, $J = 2$ Hz, C_5H_4), 4.053 (d, $J = 1.2$ Hz, 2H, C_5H_4), 4.085 (s, 5H, C_5H_5).

$\text{Fc}(\text{CH}_2)_{11}\text{SCOCH}_3$ (11-ferrocenylundecyl thioacetate) RF 8, 49

0.5097 g (0.0012 mole) of $\text{Fc}(\text{CH}_2)_{11}\text{Br}$ and 0.3341 g (0.0029 mole) of potassium thioacetate (Aldrich) were added to a reaction flask, and fitted with condenser and purged with N_2 . To this flask, 60 mL of freshly distilled 100% ethanol (AAPER) was added under N_2 . The solution was refluxed under nitrogen for 4 to 5 hrs under N_2 . The excess ethanol was removed via rotary evaporation. The crude product was transferred to a separatory funnel, extracted with diethyl ether and washed three times with D.I. water. The yellow-orange organic layer was dried with magnesium sulfate, gravity filtered and concentrated. The crude product was purified via flash chromatography with 1.5% ethyl acetate / hexanes. Product is a yellow / orange solid. (92% yield, $R_f = 0.1$); $^1\text{H NMR}$ (400 MHz) CDCl_3 : 1.267 (broad, 14 H, CH_2), 1.474 (m, 2H, $\text{Fe}(\text{Cp})_2\text{CH}_2\text{CH}_2$), 1.564 (m, 2H, $\text{CH}_2\text{CH}_2\text{S}$), 2.310 (t, $J = 7.8$ Hz, 2H, $\text{Fe}(\text{Cp})_2\text{CH}_2$), 2.865 (t, $J = 7.4$ Hz, 2H, CH_2S), 3.324 (s, 3H, SCOCH_3), 4.031 (d, $J = 1.6$ Hz, 2H, C_5H_4), 4.053 (d, $J = 1.6$ Hz, 2H, C_5H_4), 4.082 (s, 5H, C_5H_5).

$\text{Fc}(\text{CH}_2)_{11}\text{SH}$ (11-ferrocenylundecane thiol) RF 9, 89

0.306 g (0.739 mMole) of $\text{Fc}(\text{CH}_2)_{11}\text{SCOCH}_3$ and 0.1866 g (0.0033 mole) of potassium hydroxide (KOH (Fisher) ground to fine powder) was added to a reaction flask, fitted with condenser and purged with N_2 for 20 minutes. To this flask, 20 mL of freshly distilled 100% Ethanol (AAPER) was added to the reaction vessel under N_2 . The solution was refluxed under N_2 for 1 to 1.5 hrs. The excess ethanol was removed via rotary evaporation. The crude product was transferred to a separatory funnel, extracted with diethyl ether, washed three times with cold 0.5 N HCl and one time with D.I. water. The organic layer was dried with magnesium sulfate, gravity filtered and concentrated. The crude product was purified via flash chromatography with 1% ethyl acetate / hexanes. Product is a yellow / light orange solid. (45% yield, $R_f = 0.37$); $^1\text{H NMR}$ (400 MHz) CDCl_3 : 1.278 (broad, 14H, CH_2), 1.394 (t, 1H, SH), 1.494 (m, 2H, $\text{Fe}(\text{Cp})_2\text{CH}_2\text{CH}_2$) 1.608 (m, 2H, $\text{CH}_2\text{CH}_2\text{SH}$), 2.311 (t, $J = 7.8$ Hz, 2H, $\text{Fe}(\text{Cp})_2\text{CH}_2$), 2.523 (q, 2H, $J = 7.3$, 2H, CH_2SH), 4.032 (d, 2H, $J = 2.2$ Hz, C_5H_4), 4.052 (d, $J = 1.8$ Hz, 2H, C_5H_4), 4.083 (s, 5H, C_5H_5).

References:

- (1) Chidsey, C. E. D.; Bertozzi, C. R.; Putvinski, T. M.; Muijsce, A. M. *Journal of the American Chemical Society* **1990**, *112*, 4301-4306.
- (2) Miller, R. L. In *Investigating the Effects of the Incorporation of Functional Elements into Adlayers*; North Carolina State University, Raleigh, NC 27695, 1997, p 126.

